Alma Mater Studiorum – Università di Bologna

DOTTORATO DI RICERCA IN

NANOSCIENZE PER LA MEDICINA E PER L'AMBIENTE

Ciclo 34

Settore Concorsuale: 03/B1 - FONDAMENTI DELLE SCIENZE CHIMICHE E SISTEMI INORGANICI

Settore Scientifico Disciplinare: CHIM/03 - CHIMICA GENERALE E INORGANICA

SYNTHESIS AND ELECTRONIC PROPERTIES OF LUMINESCENT SILICON NANOCRYSTALS AND COPPER INDIUM SULPHIDE QUANTUM DOTS

Presentata da: Giacomo Morselli

Coordinatore Dottorato
Prof. Dario Braga

Supervisore
Prof.ssa Paola Ceroni

Co-supervisore
Prof. Giacomo Bergamini

Esame finale anno 2022

"Quare etiam atque etiam sunt venti corpora caeca,
quandoquidem factis et moribus aemula magnis
amnibus inveniuntur, aperto corpore qui sunt.
Tum porro varios rerum sentimus
odores nec tamen ad naris venientis cernimus umquam,
nec calidos aestus tuimur nec frigora quimus
usurpare oculis nec voces cernere suemus;
quae tamen omnia corporea constare necessest
natura, quoniam sensus impellere possunt.
Tangere enim et tangi, nisi corpus, nulla potest res.
Denique fluctifrago suspensae in litore vestes
uvescunt, eaedem dispansae in sole serescunt.
At neque quo pacto persederit umor aquai
visum est nec rursum quo pacto fugerit aestu.
In parvas igitur partis dispergitur umor
quas oculi nulla possunt ratione videre."

Lucretius, *De Rerum Natura* (I, 294-310)

Table of Contents

1. Introduction 1

1.1. Introductory notes of semiconductor physics 1

1.1.1. The band theory 1

1.1.2. Useful concepts 2

1.2. Nanomaterials and quantum dots 4

1.2.1. Synthesis of conventional quantum dots 8

1.2.2. Core-shell systems 13

1.3. Silicon Nanocrystals (SiNCs): an overview 16

1.3.1. Synthesis and functionalisation of silicon nanocrystals 17

1.3.2. Photophysical properties of silicon nanocrystals 28

1.3.3. Electrochemistry and electrochemiluminescence of silicon nanocrystals 39

1.4. Applications of Silicon Nanocrystals 43

1.4.1. Luminescent solar concentrators 43

1.4.2. Biomedical applications and bioimaging 44

1.5. Copper Indium Sulphide (CIS) Quantum Dots: an overview 51

1.5.1. Crystallography of CIS QDs 51

1.5.2. General synthesis of CIS QDs and phase transfer into water 53

1.5.3. Photophysical properties of CIS QDs 56

1.5.4. Applications of CIS QDs 59

2. Functionalisation of Silicon Nanocrystals with acetylides 63

2.1. Introduction 63

2.2. Results and Discussion 65

2.3. Conclusions 69

2.4. Experimental Section 70

2.4.1. Materials and methods 70

2.4.2. Synthesis of Si-DPA 70

3. Functionalisation of Silicon Nanocrystals with amines 75

3.1. Introduction 75

3.2. Results and Discussion 75

3.3. Conclusions 88

3.4. Experimental Section 88

3.4.1. Synthesis of amine-functionalised SiNCs 89

4. Functionalisation of Silicon Nanocrystals *via* click-chemistry 93

4.1. Introduction 93

4.2. Results and Discussion 94
4.3. Conclusions 98
4.4. Experimental Section 99
4.4.1. Synthesis of Si-PEG 99
5. Functionalisation of Silicon Nanocrystals with carboxylic acids 101
5.1. Introduction 101
5.2. Results and Discussion 101
5.2.1. Amide coupling *via* formation of acyl chlorides 106
5.2.2. Determination of the number of ligands per nanocrystal 110
5.3. Conclusions 112
5.4. Experimental Section 112
5.4.1. Functionalisation of silicon nanocrystals with carboxylic acids 112
5.4.2. Functionalisation of silicon nanocrystals with amides *via* acyl chloride 115
6. ECL of chromophore-functionalised SiNCs 117
6.1. Introduction 117
6.2. Results and Discussion 118
6.3. Conclusions 125
6.4. Experimental Section 126
6.4.1. Synthesis of silicon nanocrystals 126
6.4.2. ECL apparatus and ECL measurements 128
7. Light-harvesting antennae based on CIS@ZnS QDs 131
7.1. Introduction 131
7.2. Results and Discussion 132
7.3. Conclusions 140
7.4. Experimental Section 141
7.4.1. Materials and methods 141
7.4.2. Synthesis of CIS-py and CIS@ZnS-py QDs 141
Final considerations and perspectives 145
Appendix – Experimental techniques 147
A.1. Electronic Absorption Spectroscopy 147
Computation of the number of chromophores per nanoparticle 148
A.2. Emission Spectroscopy 149
Emission Quantum Yield 150
Evaluation of the enhancement of the brightness 151
Evaluation of the sensitisation efficiency 152

A.3. Lifetime Measurements 152
Gated Sampling 154
Time-Correlated Single-Photon Counting 154
Computation of the quenching efficiency of a fluorophore 156
A.4. Dynamic Light Scattering 156
A.5. Nuclear Magnetic Resonance 158
A.6. Mass spectrometry 159
A.7. Cyclic Voltammetry and Chronoamperometry 161
A.8. Transmission Electron Microscopy 162
Bibliography **163**

Abstract

In the last decades, nanomaterials, and in particular semiconducting nanoparticles (or quantum dots), have gained increasing attention due to their controllable optical properties and potential applications.

Silicon nanoparticles (also called silicon quantum dots, SiQDs, or silicon nanocrystals, SiNCs, due to the presence of organised crystalline lattice) have been extensively studied in the last years, due to their physical and chemical properties which render them a valid alternative to conventional quantum dots. Even though their research began in the late Eighties, with the discovery of the photoluminescence of mesoporous silicon by Leigh Canham, initially they weren't assumed to overwhelm the other types of nanoparticles, because one of their features, the indirect nature of silicon band gap, worsens its optical properties. Only in the last few years, new synthetical approaches and functionalisation strategies have overcome some of these drawbacks, rendering SiNCs more appropriate for their applications. Several organic molecules, for instance, have been linked to the surface of the quantum dot enhancing its optical features. Moreover, some applications have been proposed exploiting the other consequences of the indirect band gap: therefore, the long emission lifetimes are now under study for sensing or time-gated detection applications.

During my PhD studies I have planned new synthetical routes to obtain SiNCs functionalised with molecules which could ameliorate the properties of the nanoparticle. However, this was certainly challenging, because SiNCs are very susceptible to many reagents and conditions that are often used in organic synthesis. They can be irreversibly quenched in the presence of alkalis, they can be damaged in the presence of oxidants, they can modify their optical properties in the presence of many nitrogen-containing compounds, metal complexes or simple organic molecules. If their surface is not well-passivated, the oxygen can introduce defect states, or they can aggregate and precipitate in several solvents.

Therefore, I was able to functionalise SiNCs with different ligands: chromophores, amines, carboxylic acids, poly(ethylene)glycol, even ameliorating functionalisation strategies that already existed. I performed these reactions aiming at particular photophysical properties or at certain applications, combining the organic synthesis,

the inorganic one, the knowledges in photochemistry, the ones in electrochemistry and a subject which is usually unfamiliar to a chemist, that is nanomedicine.

Consequently, this thesis will collect the experimental procedures used to synthesize silicon nanocrystals, the strategies adopted to functionalise effectively the nanoparticle with different types of organic molecules, and the characterisation of their surface, physical properties and luminescence (mostly photogenerated, but also electrochemigenerated).

I also spent a period of 7 months in Leeds (UK), which was, unfortunately, affected by Covid-19 outbreak in the spring of 2020. Although I was kept away from the laboratory for most of the time, I managed to learn how to synthesize other cadmium-free quantum dots made of copper, indium and sulphur (CIS QDs). During my last year of PhD, I focused on their functionalisation by ligand exchange techniques, yielding the first example of light-harvesting antenna based on those quantum dots. Part of this thesis is dedicated to them.

Acknowledgements

First of all, I have to thank my supervisor, professor Paola Ceroni, who gave me the opportunity to experience research, believed in me and made me feel more self-confident, which is a great help for an introverted person like me.

I want to thank also the group of the Photochemistry and Nanoscience Laboratory in Bologna, for the joyful moments spent together as well as the scientific discussions held at lunchtime (thank you also for being the victims of my puns and jokes: a Nobel Peace Prize or a beatification process is waiting for you).

Thank you to my old friends, who made the years at the University unforgettable (and thank you for being my first victims, see above).

Also, thank you to Dr. Kevin Critchley and the Molecular and Nanoscale Physics group in Leeds, for hosting me and who made me feel at home even in a different country during a difficult period.

A special thank you to my girlfriend, who makes me feel really special and who makes the time spent together extraordinary.

But the biggest thank goes to (drumroll…) my family: my parents, my sister, my grand-parents (who are watching me from Heaven) and my aunt who supported me in so many ways that unfortunately I can't list, or this acknowledgements section will cover half of my thesis, making it surely more innovative but also too boring.

And thank also to the one who's reading my thesis. Hope you enjoy it!

1. Introduction

1.1. Introductory notes of semiconductor physics

1.1.1. The band theory

The nanoparticles that have been studied during this three-year period and that will be considered in this thesis are composed of semiconducting materials. Therefore, it is worth devoting a chapter to the physical properties of semiconductors, spanning from the bulk to the nanostructured ones.

Treating the argument of crystalline bulk semiconductors (just as metals), it is convenient considering at first single atoms that interact with each other. Their atomic orbitals, if a symmetrical requirement is achieved, can interact, combining in delocalized orbitals separated by a certain energy gap. If n orbitals of the first atom interact with n orbitals of the second atom, 2n combinations (e.g. molecular orbitals as linear combination of atomic orbitals) are formed, usually with n new orbitals at lower energy than the first ones (stabilized) and n at higher energy (destabilized). If the overall electrons of the two atoms occupy more stabilized new orbitals, the interaction is favourable with respect to the situation in which the atoms are separated.

Enhancing the number of interacting atoms in the lattice, and therefore the number of atomic orbitals interacting, a higher number of new delocalized orbitals will be formed, and their separation in energy will be narrowed. In a solid bulk material, supposing an infinite number of atoms, this difference will be negligible, yielding a continuum of orbitals, called band.[1,2]

The bands generated by the atomic orbitals completely occupied by the electrons will be filled, as the bands generated by the emptied atomic orbitals will be un-filled. The position of those bands can define the type of the material accordingly with its electric conductivity (Figure 1.1.1).

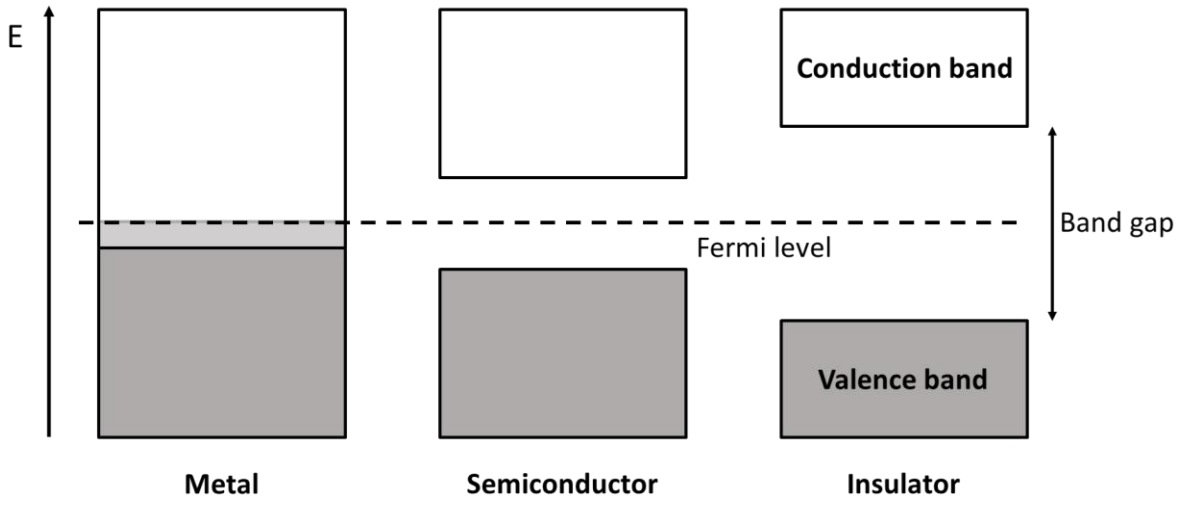

Figure 1.1.1 – Illustration of the positions of the bands for metals, intrinsic semiconductors and insulators.

If they overlap with each other, the absence of an energy gap will allow to the electrons of the filled band to be easily promoted to the un-filled one even at low temperatures: in other words, the electrons have a high mobility in the solid lattice. As a consequence, an excellent electric conductivity is achieved, and the material is called metal.

If the filled band (or valence band, VB) is separated from the empty band (conduction band, CB) by a large energy gap (usually higher than 4 eV), the migration of an electron from one band to the other one cannot easily occur at room temperature and the material is an electric insulator.

If the band gap has a value of few electronvolts, an intermediate situation occurs: the material is a semiconductor. Among their peculiar property, their electric conductivity can vary with the temperature: the thermal energy can allow the electron from the valence band to migrate to the conduction band and so, the conductivity enhances. Moreover, the electric features can ameliorate by doping the semiconducting materials with elements with a higher number of valence electrons (n-type doping) or lower (p-type). Those "extrinsic" semiconductors are commonly used in electronic systems (solar cells, LEDs, transistors, *et cetera*).

1.1.2. Useful concepts

Dealing with metals and semiconductors, it is useful to introduce an equation (attributed to Fermi and Dirac) which measures the probability $P(E_i)$ for an electron (at thermodynamic equilibrium) to be in a state with energy E_i, which is:

$$P(E_i) = \frac{1}{\exp\left(\frac{E_i - E_F}{k_B T}\right) + 1}$$

in which k_B is the Boltzmann constant, T the absolute temperature and E_F the Fermi energy level, which symbolizes the amount of energy required to add an electron to the system.[3] This last quantity represents the energetic level in which the probability to find an electron is 50%. It is an actual level for metals (in a hypothetical situation at 0 Kelvin it would represent the highest occupied molecular level), but it is virtual for semiconductors, laying between the VB and the CB (it occurs exactly in the middle for intrinsic semiconductors, but the presence of dopants can influence its position).

Other useful concepts that are needed to treat the semiconductors' physics are the *exciton* and the *phonon*.

The *exciton* can be considered as the equivalent of the excited state of the molecules but for solid materials. Briefly, if a photon of energy equal or superior to the band gap of the semiconductor (resonance rule) is absorbed by the material, an electron can be promoted from the VB to the CB. The fictitious positive charge left by the missing electron in the VB is generally called *hole*. The overall neutral situation generated by the couple "electron in the CB – hole in the VB" is the *exciton*. Depending on the dimensions of the semiconductor (if bulk or nanostructured), the aim of the exciton can be different (*vide infra*).

The *phonon* is defined as a quasi-particle at which is associated a collective movement of the atoms of the lattice. It can be associated with the equivalent of the vibrations in molecules.

In order to deal with the photophysical properties of the semiconductors that will be considered in this work, it is necessary to introduce also a further distinction due to the relative position of the valence band and the conduction band with respect to the momentum of the crystal lattice (k). If the maximum energy of the valence band and the minimum of the conduction band share the same value of k, the semiconductor is characterized by a *direct band gap*. On the contrary, if the bands are shifted at different k values, it is the case of an *indirect band gap* (Figure 1.1.2).[4] Crystalline silicon and germanium are indirect band gap semiconductors, while GaAs, CdTe, ZnS, $CuInS_2$ and

many others are direct band gap semiconductors. At the nanoscale, some important consequences arise.

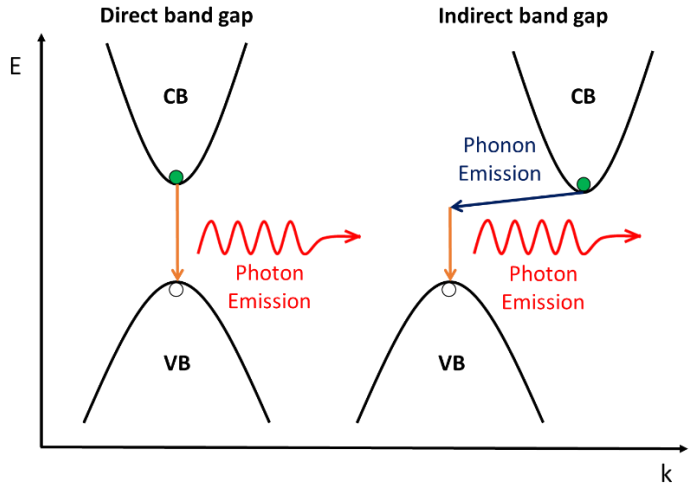

Figure 1.1.2 – Schematic representation of the position of the valence band (VB) and the conduction band (CB) in direct and indirect band gap semiconductors. The implication on the emission will be discussed in a following chapter.

1.2. Nanomaterials and quantum dots

Nanotechnology can be defined as a branch of technology which studies the phenomena and the manipulation of materials at the nanometre scale.[5] This is approximately the range between 1 and 100 nm (1 nm = 1 billionth of metre, 10^{-9} m), which is the intermediate zone between molecules and bulk materials. A nanostructured material (or nanomaterial) in the same way is defined as a solid material characterized by at least one dimension in the nanometre range.[6] Therefore, particles with 3 dimensions on the nanometre range (such as nanocrystals and quantum dots), wires with 2 dimensions (nanotubes), sheets with 1 dimension (thin films, surfaces…) or even macroscopic materials with nanometre-sized cavities (zeolites, molecular organic frameworks…) fall under the definition of nanomaterials.

A peculiar and fascinating characteristic of nanomaterials is the effect of the size on different physical and chemical properties. If the size of the nanomaterial varies, while remaining in the nanometre scale, some features such as melting point, chemical reactivity, photophysical and electrochemical properties change accordingly.[7] This is due to two main effects:

1) The number of the atoms exposed to the surface is high if compared to the inner atoms. This “surface to volume” ratio decreases with the size of the material: it is

paramount for nanomaterials, while it is negligible for macroscopic ones. This aspect is important because the atoms on the surface have different properties and chemistry (e.g. due to defects or lower coordination number) and can affect surface properties such as catalysis and reactivity.

2) The rising of quantum confinement effects.[8,9] The properties of a material depend on the type of motion its electrons can perform, which depends on the space available for them. Therefore, the properties of a material are characterized by a specific "length scale", delimited by their wave-function, which is usually on the nanometre dimension. If the physical size of the material is reduced below this length scale, the wave-function is confined to it and its properties change and become sensitive to size and shape.[9] Moreover, semiconducting nanoparticles, which are subject to the quantum confinement, are called *quantum dots*.

In particular, the quantum confinement effect drastically influences the optical properties of the quantum dot. After the absorption of a photon and the formation of the exciton (as described in Paragraph 1.1.2), the two charge carriers, the electron in the conduction band and the hole in the valence band, are separated by a specific distance which includes a certain number of atoms or ions in the crystal lattice. The mean distance between the charge carriers in the exciton is called *Bohr radius*, and it is dependent on the material which composes the semiconductor (it is usually in the order of few nanometres).

In a bulk semiconductor the binding energy between the electron and the hole is small (furthermore, the exciton is called *Wannier-Mott exciton*)[10] and this allows the charges to migrate along the material until they are trapped, annihilated by another exciton or relaxed (e.g. it is the principle of semiconductor solar cells, in which the charges are channelled to an external conductive wire generating an electric current).

However, if the dimensions of the semiconductor are reduced to the nanometre scale and are comparable to twice the Bohr radius, the exciton is confined to the size of the quantum dot itself. The higher electrostatic interaction between the electron and the holes leads to a rapid thermal deactivation of the charge carriers to the band edges. Then, a radiative recombination called *band edge luminescence* can occur (Figure 1.2.1).[7] This is the reason why semiconductors such as silicon display a relevant photoluminescence only if nanostructured.

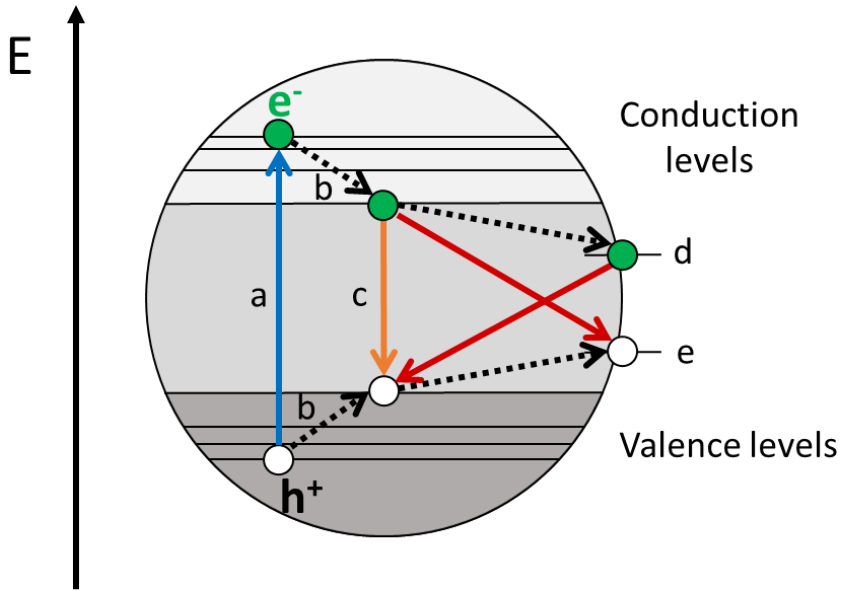

Figure 1.2.1 – Schematic representation of the principal processes in a quantum dot. After the absorption (a) of a photon with an energy equal or superior to the band gap, an electron is promoted from the valence band to the conduction band, generating an exciton. Due to strong electrostatic interactions, a rapid thermal relaxation (b) occurs, leading the charge carriers to the band edges. Then, a radiative recombination (c) can happen. The presence of defects on the surface (d, oxidizing surface state, e, reducing surface state) can trap the charge carriers and cause a non-radiative relaxation (lowering the emission quantum yield) or a defected redshifted emission (red arrows). Adapted from reference [7] with permission of the Royal Society of Chemistry.

For quantum dots of different sizes, quantum confinement effect causes other two important consequences.

Firstly, the edges of the valence band and the conduction band are not continuous anymore (Figure 1.2.2). A discretization of the levels (which is more evident with smaller nanoparticles) occurs,[8] and this is visible especially from the absorption spectra, where it is possible to notice the absorption bands associated to single transitions between discrete levels. Those bands are quite sharp and well-defined. The inner of the CB and VB, due to the high density of states, maintain their continuity, and therefore, the transitions in absorption from the valence band to the inner states of the conduction band lose their structuration and the molar absorption coefficient is increasingly higher due to degeneration of the final state.[11] Because the photoluminescence involves only the frontiers levels, it appears as one bell-shaped band even narrower than the organic chromophores' one (Figure 1.2.3) and the Stokes Shift, defined as the difference in energy between the maxima in absorption and in emission for the same transition, is low.

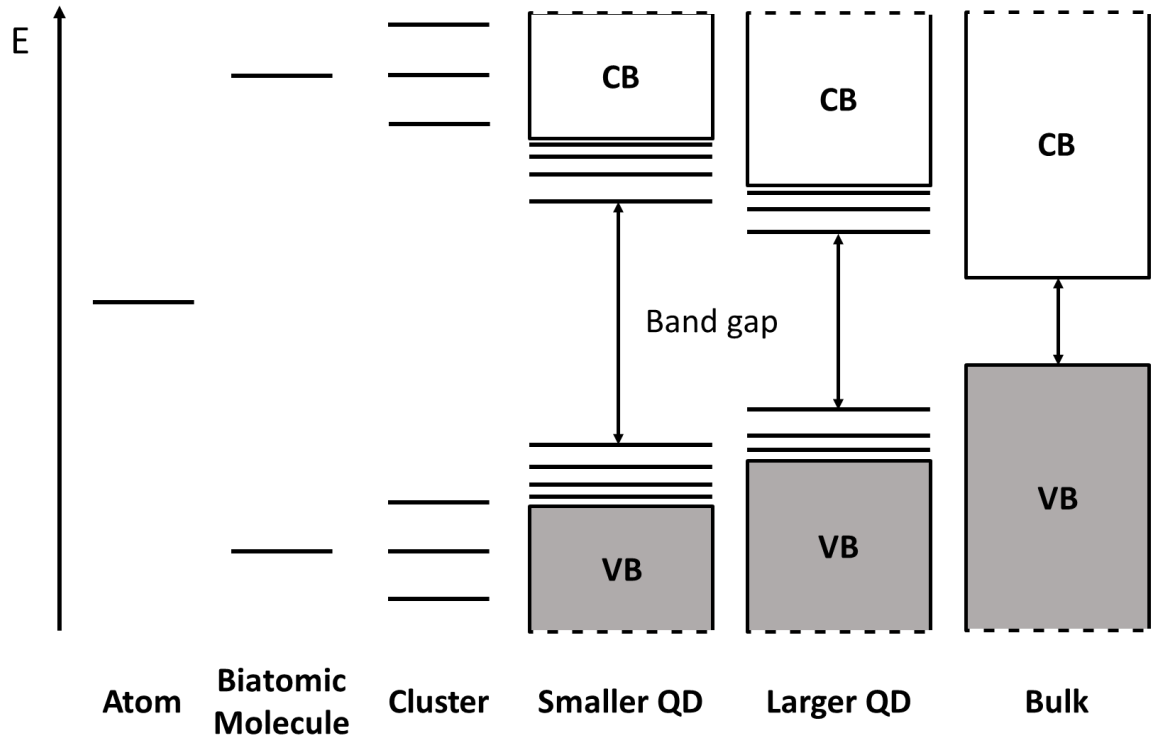

Figure 1.2.2 – Schematic representation of orbital diagrams in energy increasing the number of atoms, supposing that each atom contributes with one atomic orbital. Increasing the number of atoms, the separation between the levels decreases, leading to the band structures discussed in Chapter 1.1. An intermediate situation between the cluster of atoms and a bulk material is given by quantum dots (and nanomaterials in general). It is possible to notice that it is still present a discretization of the levels in the edges of the valence band (VB) and conduction band (CB), which diminishes while enhancing the size of the nanoparticle and fades in the bulk semiconductor. Moreover, the band gap decreases accordingly with the dimensions.

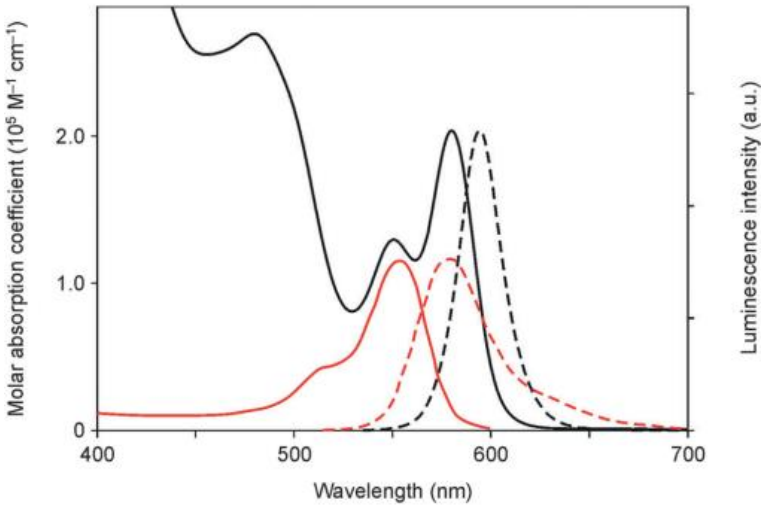

Figure 1.2.3 – Absorption (black solid line) and emission (black dashed line, exciting at 500 nm) of CdSe quantum dots (diameter = 3.8 nm) in chloroform compared to the absorption and the emission (red lines) of Rhodamine B in methanol. It is possible to notice the structuration of the absorption spectrum of the quantum dot, due to the discretization of the band edge levels. Reproduced from reference [7] with permission of the Royal Society of Chemistry.

Moreover, the band gap of the semiconducting nanoparticles is influenced by the size of the nanocrystal itself. Bigger nanoparticles are associated to smaller band gaps (Figure 1.2.2). Consequently, increasing the size of the nanoparticle, the absorption and the emission spectra (as it is possible to see in Figure 1.2.4) are shifted towards higher wavelengths.

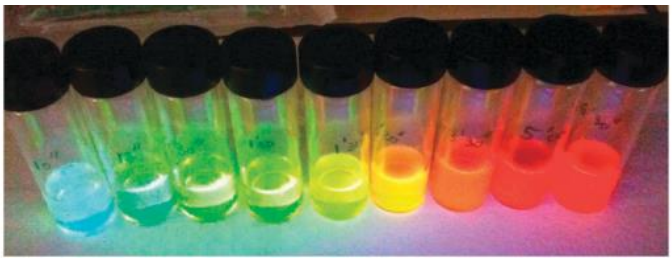

Figure 1.2.4 – Photograph of chloroform suspensions of CdSe-ZnS quantum dots of different sizes (smaller to larger from left to right) under UV excitation. Reproduced from reference [7] with permission of the Royal Society of Chemistry.

Since their discovery in the Eighties[12], quantum dots have gained increasing attention for their peculiar optical properties which render them "ideal luminophores": besides the absorption and the narrow emission that can be modulated according to the size of the nanoparticle, quantum dots are usually characterized by emission quantum yield and photostability equal or even superior to those of the conventional organic fluorophores.[7] Moreover, thanks to the development of appropriate synthetical strategies,[13] it is possible to achieve a good control over the size of the nanoparticle and to perform a functionalisation of the surface with a wide variety of molecules. Therefore, quantum dots have been proposed as replacements of molecules and bulk semiconductor for different purposes: in photovoltaic solar cells,[14–18] in LEDs,[19,20] in photocatalysis,[21–23] as sensors[7,24] or for biomedical applications (diagnostic or therapeutic).[25–29]

1.2.1. Synthesis of conventional quantum dots

Since the properties of the quantum dot are heavily determined by the size and the shape of the nanoparticle, the synthetical strategies represent an important process. Those procedures have been more and more investigated and ameliorated in order to obtain nanocrystals at a desired dimension with a narrow size distribution.[8,30–33]

Usually, the main methods used to synthesize nanoparticles are classified in "top-down" or "bottom-up" approaches.

Top-down refers to the techniques that focusses on macroscopic bulk semiconductors as starting material which, by lithographic methods, laser ablations, etching procedures, *et cetera*, is reduced to the nanometre scale. Those methods, anyway, do not allow to obtain a high number of nanoparticles and are mainly used to study the physical properties of the single quantum dot.

The "more chemical" approach consists in *bottom-up* strategies, using molecules or ionic compounds as precursors and obtaining the desired quantum dots after actual chemical reactions. In contrast to physical methodologies, *bottom-up* strategies permit to synthesize high quantities, even grams of nanoparticles.[34–36] In this case, the size (and the shape) of the nanomaterial is mostly determined by the amount and ratio of precursors, capping molecules, solvent, temperatures and time of reaction and the presence of a template (such as micelles).[37–40]

In this paragraph, the thermodynamic and kinetic aspects and general procedure of the synthesis of conventional quantum dots will be considered. Therefore, the synthesis of nanostructured semiconductors composed of elements II-VI (e.g. cadmium chalcogenides), IV-VI (lead chalcogenides), III-V (e.g. InAs) and also $CuInS_2$ quantum dots. Regarding the synthesis of silicon quantum dots, the procedures are different and will be exposed in Chapter 1.3.

1.2.1.1. The thermodynamics of Quantum Dots nucleation

The growth of a crystalline semiconductor (both bulk and nanostructured) involves the process of precipitation of a solid phase from a supersaturated solution.[8] In this condition, if an energetic barrier is overcome, the ions (e.g. Cd^{2+} and S^{2-}) start to assembly in a small solid cluster. This first step of crystallisation is called (homogeneous) *nucleation*. In order to occur, the thermodynamic must be favourable: to assess this, the variation of free energy for the nucleation process (ΔG_n) should be considered.

It is possible to express ΔG_n as the sum of two free energy variations: one due to the formation of a new volume (ΔG_v which is a stabilising component, because in a super-saturated solution the solid is more stable, i.e. negative) and the other due to the new surface created (ΔG_s, de-stabilising, therefore positive, because it considers the cost of

the creation of a solid-liquid interface).[41] For a spherical particle, is valid the following equation:[8]

$$\Delta G_n = \Delta G_v + \Delta G_s = -\frac{4}{3V}\pi r^3 k_B T ln(S) + 4\pi r^2 \gamma$$

where V is the molecular volume of the precipitated species, r is the radius of the spherical particle, k_B the Boltzmann constant, S the saturation ratio and γ the free energy per unit surface area. It is worth noting that the cubic exponentiation of r increases more rapidly than the square if r>1. This means that for lower values of r, ΔG_n will be positive and de-stabilizing, while for higher values of r, ΔG_n will decrease more and more and the nucleation will be favourable.

In particular, for supersaturated solutions (S>1), it is possible to compute the maximum for the curve ΔG_n in function of the size, yielding a certain value of r called *critical size* (r^*):

$$\frac{d\Delta G_n}{dr} = 0 \Rightarrow r = r^* = \frac{2V\gamma}{3k_B T ln(S)}$$

This means that nuclei larger than the critical size will further decrease their free energy for growth and form stable nuclei that grow to form particles.

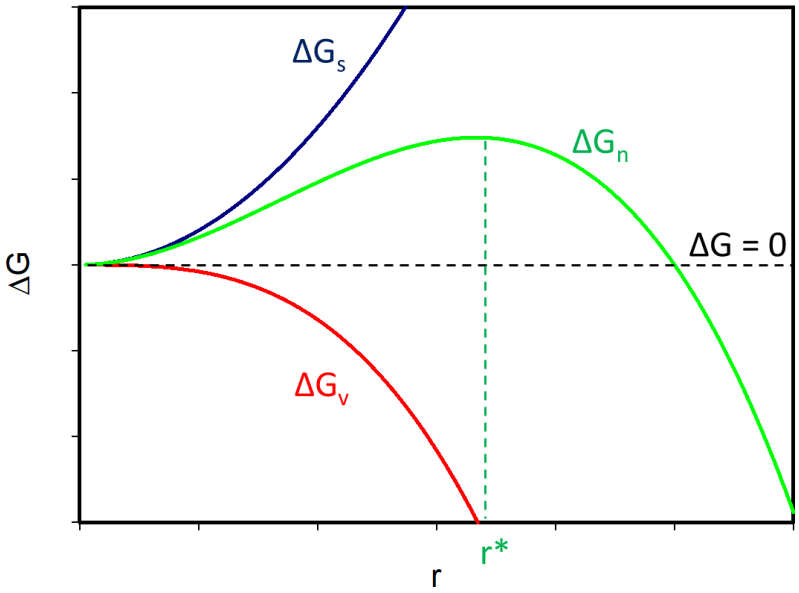

Figure 1.2.5 – Representation of the equation of the variation of free energy in function of the nucleus radius. The blue curve is the surface component, while the red one is the volume one. The sum, ΔG_n is the green line. Its maximum appears when the radius equals the critical size, r.*

Once the nucleation has occurred, the second step concerns the growth of the stable crystals.

1.2.1.2. The Quantum Dots growth and the size focussing regime

The addition of subsequent layers of material onto the surface of the nuclei occurs and the growth of the nanoparticle begins. This step is dependent on the diffusion of the precursor to the forming quantum dot, whose kinetic is well-described by the Fick's law of diffusion:

$$\vec{J} = -D\nabla C$$

where J represents the flux of reagents towards the nanocrystals (the upper arrow denotes the vector), D is the diffusion coefficient and ∇C the gradient of concentration. Solving this equation for a monodimensional case ($\nabla C = dC/dx$) and expressing the derivative of the growing size of the nanoparticle with respect to the time (i.e. the growth rate of the radius, r) it is possible to obtain the following equation:[41,42]

$$\frac{dr}{dt} = K\left(\frac{1}{r} - \frac{1}{\delta}\right)\left(\frac{1}{r^*} - \frac{1}{r}\right)$$

where K is a constant proportional to the diffusion constant of the reagents, δ represents the thickness of the diffusion layer and r^* the critical size. The resulting plot of the previous equation is represented in Figure 1.2.6.

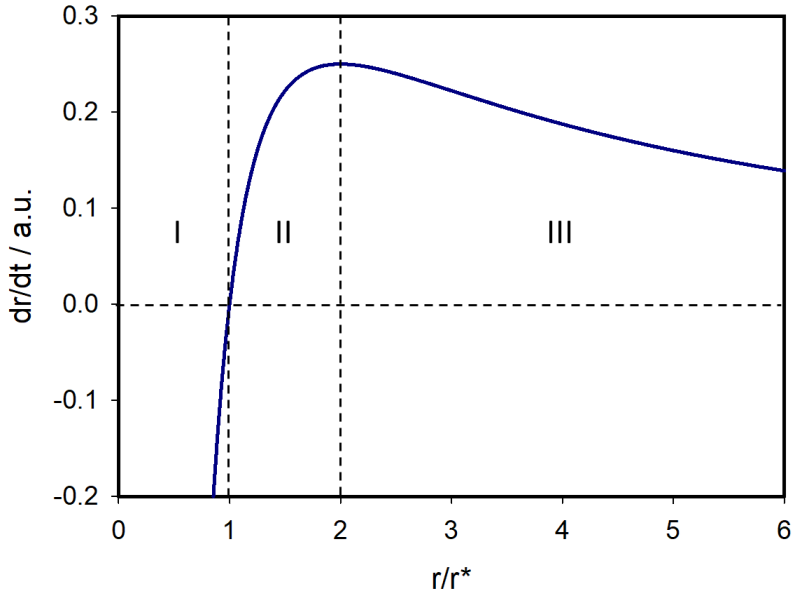

Figure 1.2.6 – Representation of the trend of the crystal growth rate (dr/dt) with respect to the ratio r (radius of the nanoparticle) over r (critical size), with the three zones highlighted (the explanation can be found in the text).*

It is possible to notice that there is a maximum and three key zones, which are highlighted in the figure. Zone I refers to the particles that have a radius inferior to the critical size ($r/r^* < 1$). The crystal growth is negative, and this means that the nuclei dissolves, as assessed by the thermodynamics. When the radius equals the critical size ($r/r^* = 1$), the overall growth rate is zero and the solution and the solid phase are in equilibrium. Zone II represents the growth rate of the particles with a radius intermediate between 1 and 2 critical sizes ($r^* < r < 2r^*$). In this case, the larger nanoparticles grow faster than the smaller ones, which leads to a size-broadening of the dispersion. When the radius overcomes twice the value of the critical size ($r > 2r^*$), encroaching upon the zone III, the situation reverses, and the crystal growth rate decreases with respect to the size. In this case, the bigger nanoparticles enlarge more slowly than the smaller ones and the nanocrystals narrowing the size distribution. When this occurs, it is said that the nanocrystals have reached the *size-focussing regime*.

Ideally, in order to obtain nanocrystals of the same size (a monodispersed sample), the nucleation and the growth of all the crystals should occur at the same time. However, while the reaction is carried out and the concentration of the reactants diminishes (and so does the saturation ratio S), the value of the critical size *r** increases. Moreover, the particles that had already been formed with a size inferior to the resulting *r** are not thermodynamically stable anymore, melt and the "lost" material is incorporated in the larger nanoparticles, leading to a process (called *Ostwald ripening*) that reduces the mono-dispersion of the sample. In order to avoid this, it is possible either to continue supplying reagents, maintaining the typical level of saturation,[42] or to quench the reaction while in the size focussing regime. One synthetical method generally used to achieve this is the *hot-injection*.

1.2.1.3. Hot-injection method

As discussed previously, in order to obtain a sufficiently monodisperse sample, it is necessary to separate definitely the phases of nucleation and growth: the crystals should nucleate at the same time and should grow with the same rate. A general scheme for preparing monodisperse nanoparticles requires a rapid, single nucleation event followed by a slower growth of the new-formed nuclei.[8,13] This can be achieved by the *hot-injection* method. In principle, a solution of one component of the aimed quantum dot is heated up to high temperatures, in the presence of a high-boiling

solvent and the ligand molecule. Then, a room-temperature solution of the second component is rapidly injected into the reaction mixture. The high temperature of the solution of the first component leads to a rapid single nucleation, which is immediately quenched by the lowering of the temperature due to the injected solution of the second component. Therefore, a low process of growth begins, and the particles will be maintained at the size-focussing regime until the desired size are reached. The reaction will be quenched at very low temperature, and the isolation and purification of the quantum dots can be performed.

In order to better explain this process, the *hot injection* method for the synthesis of CdSe quantum dots is reported.[8] The precursor of cadmium, e.g. CdO, is mixed together with stearic acid and heated to about 130 °C for the activation (i.e. solubilisation) of the metal under inert atmosphere. The mixture is then allowed to cool to room temperature and a stabilising agent (e.g. trioctyl phosphine oxide, TOPO) is added. The temperature of the system is raised up to 360 °C. A room temperature solution of selenium in toluene and trioctyl phosphine is quickly injected into the reaction flask. A nucleation burst happens, but it is rapidly quenched due to the temperature, which decreases to 300 °C upon injection. This temperature is maintained during the growth of the nanocrystals. After the reaction is complete (i.e. the desired size of the quantum dot is reached), the reaction flask is allowed to cool to room temperature and the quantum dots purified.

1.2.2. Core-shell systems

It has been previously explained how the properties of the quantum dots depend on the size of the nanoparticle. In particular, the photophysical properties vary accordingly with the dimension of the nanocrystal, due to a different magnitude of the band gap. Therefore, the emission of larger quantum dots occurs at higher wavelengths with respect to the luminescence of smaller ones. This behaviour is predicted by a theory called the *effective mass approximation*.[43] However, it is possible that the presence of defects on the surface suppresses the typical emission that is due to the band-edge and a new emission, which is not dependent on the size anymore, arises. Usually, these defects are trap states for the electron promoted by the excitation process to the conduction band (which is an oxidising surface state) or for the hole left in the valence band (a reducing surface state), as it can be stated from Figure 1.2.1.[7]

The subsequent recombination (if radiative) of the charge carriers result in a new emission that is shifted towards higher wavelengths (a higher Stokes Shift results), broad, and independent of the size of the quantum dot.[11] For many applications, this new emission is disadvantageous.

In order to preserve the band edge emission, it is essential to avoid the formation of surface trap states, for instance passivating the surface of the nanocrystal by chemically binding a capping agent.

Another approach consists in coating the surface of the semiconducting nanoparticle with a layer of a different semiconducting material. Those systems are known as *core-shell nanoparticles*.[44,45]

In particular, if the semiconductor composing the shell is characterized by a larger band gap and its band edges lies outside those of the core's ones, the core-shell system is called *type I*. One example is given by ZnS shells grown on CdSe[46] or $CuInS_2$ quantum dots. In this case, the shell avoids the presence of surface trap states, therefore enhancing the photoluminescence quantum yield of the inner semiconductor and, moreover, the core's band edge emission is maintained, because the exciton is confined in it (Figure 1.2.7 a).

A different class of *core-shell* nanoparticles, called *type II*, refers to systems in which the band situation of the semiconductor components is staggered. For instance, the valence and the conduction bands of the core semiconductor are at lower energies with respect to the shell's ones, or *vice versa* (Figure 1.2.7 b). In this case, after creating the exciton by absorption, because of a different favourable energetic situation (i.e. the electron will be delocalized in the conduction band that lies at lower energy and the hole in the valence band of higher energy) the recombination can occur at the interface of the two components.[44] In this way it is possible to engineer systems in which the emission is red-shifted with respect to the core one's, and controlled due to the type of the semiconductor that composes the shell.

The synthesis of the shell coating usually occurs by an epitaxial and successive deposition of layers around the core seed. Therefore, it does not undergo a separate nucleation.[46]

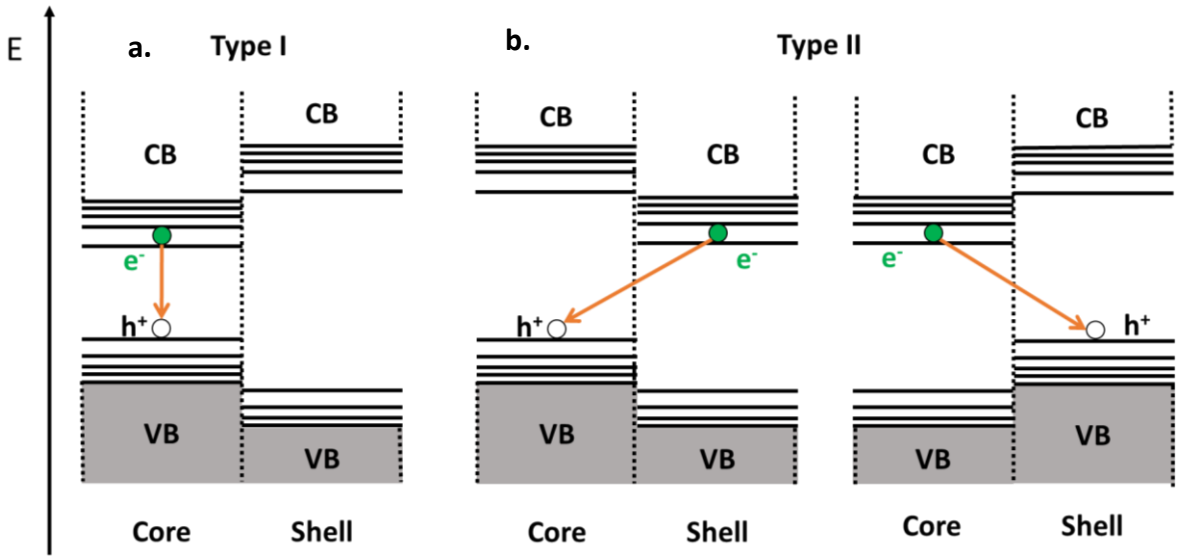

Figure 1.2.7 – Schematic representation of the energetic situation for (a) type I and (b) type II core-shell semiconductor nanoparticles. While the recombination of the exciton is localized in the core for type I QDs, it occurs at the interface for type II core-shell systems.

Also for core-shell systems, a coating of the surface with organic molecules is necessary to accomplish stability, dispersibility of the nanoparticle in various solvents and new properties.[7]

1.3. Silicon Nanocrystals (SiNCs): an overview

Conventional quantum dots are composed of group II-VI, IV-VI and III-V type semiconductors.[7–9] Despite their unique optimal photophysical properties which render them interesting substitutes to many organic and inorganic molecular luminophores for multiple applications, some ethical and practical problems have been rising due to the elements that are contained in those nanomaterials. As a matter of fact, toxic heavy metals, such as cadmium, mercury, lead and arsenic, or rare and scarce elements, like indium or selenium, mostly constitute those typical quantum dots.[47]

Silicon seems to be a valid alternative, due to its non-toxicity (it is biocompatible)[48] and its availability (it is, after the oxygen, the second most abundant element on the Earth's crust).[49] Moreover, it is also a very well-known material, which has been dominating the microelectronics industry for over half a century.[47] However, despites its advantageous semiconducting characteristics, bulk silicon possesses scarce optical properties, i.e. a limited absorption and negligible emission quantum yield at room temperature. This is mostly due to the indirect nature of its bandgap that renders the radiative transitions less likely to occur (see Paragraph 1.3.2).

Nevertheless, when reduced to the nanoscale, to sizes comparable to its Bohr radius (about 5 nm),[50] quantum confinement effects arise and silicon acquires new interesting optical properties, including emission quantum yields high up to 70% (Figure 1.3.1).[51] Therefore, since the discovery of the photoluminescence in porous silicon by Leigh Canham in the early Nineties,[52] the attention of many research groups has been focussed on silicon quantum dots (also called *silicon nanocrystals*, SiNCs), on their synthesis, functionalisation techniques, optical and electrochemical properties and applications.[47,53–58]

Figure 1.3.1 – Photographs of vials containing a toluene suspension of 4 nm sized silicon nanocrystals under ambient (on the left) or 365 nm UV (on the right) light.

1.3.1. Synthesis and functionalisation of silicon nanocrystals

Many types of strategies have been reported so far for the synthesis of silicon nanocrystals.[47] Omitting the *top-down* approaches, i.e. the methods that reduce bulk silicon to the nanoscale,[59,60] this chapter will focus on several *bottom-up* routes, highlighting one in particular, the *thermal decomposition of hydrogen silsesquioxane*, which has been extensively performed during my PhD studies. Moreover, an essential synthetical step to obtain stable silicon quantum dots with new characteristic is the passivation and functionalisation of their surface with organic molecules. Therefore, a relevant emphasis will be given also to those processes.

1.3.1.1. General synthetical methods for SiNCs' production

A wide spectrum of methods has been reported for preparing silicon nanocrystals. Many of them produce nanoparticles with various size ranges and also with different and unexpected optical properties.[53] The reason why this is happening is still on debate and will be treated in Paragraph 1.3.2.1.[50] Moreover, different studies and researches have severely criticized several accepted synthetical routes, claiming that there is no real proof of the production of silicon nanoparticles.[61–63]

It is possible to classify the recognized methodologies[47] in reduction of silicon halides,[64–67] oxidation of metal silicides[68,69] and decomposition of silanes in the presence of plasma or high temperatures (see Figure 1.3.2).[70,71] However, one method in particular, which provides a proper control of the size of the silicon nanoparticles with a good mono-dispersion and does not require sophisticated apparatuses, is the *thermal decomposition* of silicon-rich oxides. Developed by Hessel in the laboratory of professor Jonathan Veinot in 2006,[72] and then proposed and deeply investigated in professor Brian Korgel's group,[73] this method has been adopted also by our research group since 2014.[74–76]

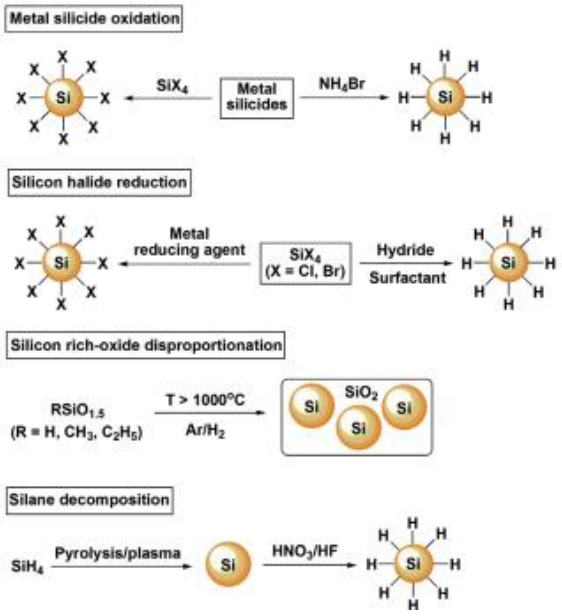

Figure 1.3.2 – General bottom-up methods for preparing silicon nanocrystals. Reprinted with permission from reference [47] (John Wiley and Sons).

1.3.1.2. Thermal decomposition of silicon-rich oxides (i.e. HSQ) and etching

Silsesquioxanes are cage-structured compounds with empirical formula $RSiO_{3/2}$.[77] If the R group is replaced with a hydrogen atom, the resulting oxide is called *hydrogen silsesquioxane* (abbreviated HSQ). HSQ has been widely investigated for the production of high purity silica,[78] which is known to be synthesized upon oxidative conditions at high temperatures.

Only in 2006, HSQ was studied for the formation of silicon nanocrystals.[72] It was noticed that at temperature higher than 1000 °C, in the presence of a slightly reducing atmosphere, the inorganic compound decomposes, releasing silane and hydrogen gases, silicon dioxide and silicon nanoparticles. Therefore, SiNCs embedded in a silica matrix are produced. This method allows a strict control over the size of the quantum dots, accordingly with the temperature (and the time) of the process. At higher temperatures, larger SiNCs are produced. For instance, at 1100 °C, 3-4 nm sized silicon nanocrystals are formed, while at 1200 °C, 5-6 nm sized silicon nanocrystals appear.[79] This is probably due to the higher facility with which silicon atoms reach the nucleus of the growing nanoparticle. A proof of that is given substituting the H of $(HSiO_{3/2})_n$ with a methyl group $(CH_3SiO_{3/2})_n$. The enhanced hindrance of the substituting group creates an inorganic network with larger cavities. Therefore, the silicon atoms can

penetrate more easily in the inner of the structure and, at equal temperature, larger SiNCs are produced.[80]

The accepted mechanism with which the production of SiNCs occurs through the thermal decomposition of HSQ in inert atmosphere is here reported:[72]

a) HSQ decomposes into silicon dioxide and silane:

$$4HSiO_{3/2} \rightarrow 3SiO_2 + SiH_4$$

b) Cleavage of Si-H bond occurs for silane:

$$SiH_4 \rightarrow Si + 2H_2$$

A typical procedure for thermal decomposition of HSQ is here described: the precursor is inserted in a quartz reactor vessel and heated in a high temperature furnace under a slightly reducing atmosphere (usually 95% nitrogen, 5% hydrogen) at a rate of 20 °C/minute. Once reached, the desired annealing temperature (e.g. 1100 °C) is maintained for an hour. Afterwards, the sample is slowly cooled down to room temperature. The obtained dark solid is grinded manually and mechanically, yielding a brownish powder.

Hydrogen silsesquioxane is a commercially available compound. It was usually sold as FOx-n® by *Dow Corning* as a solution in methyl isobutyl ketone.[72] However, it is a valuable material and can be very expensive. Consequently, many efforts have been done to search for a cheaper alternative. It was shown that it is possible to synthesize sol-gel precursors with the same empirical formula of HSQ, which can be used for the same purpose.[81,82] In the presence of oleum, toluene and trichlorosilane, the sol-gel polymer is produced. Once dried, it can be decomposed in the furnace.

Anyway, silicon nanocrystals trapped in a silicon dioxide matrix are produced (SiNCs@SiO_2). In order to extract the SiNCs, an etching of the oxide must be performed in the presence of hydrofluoric acid with hydrochloric acid[73] or ethanol.[79] This process leads to hydride-terminated silicon nanocrystals (H-SiNCs, see Figure 1.3.3).

Usually, 100 mg of SiNCs@SiO_2 are introduced in a plastic reactor container with a Teflon coated magnetic stir bar. 1 mL of distilled water and 1 mL of absolute ethanol are then introduced. While stirring slowly, 1 mL of 49% HF is carefully dropped. The reaction mixtures then stirred vigorously for 1 hour and 30 minutes at room temperature, ambient light and atmosphere. The nanocrystals are extracted in toluene,

purified by several centrifugation cycles in toluene and immediately transferred in an inert gas-filled flask or vial and the passivation of the surface of H-SiNCs is performed.

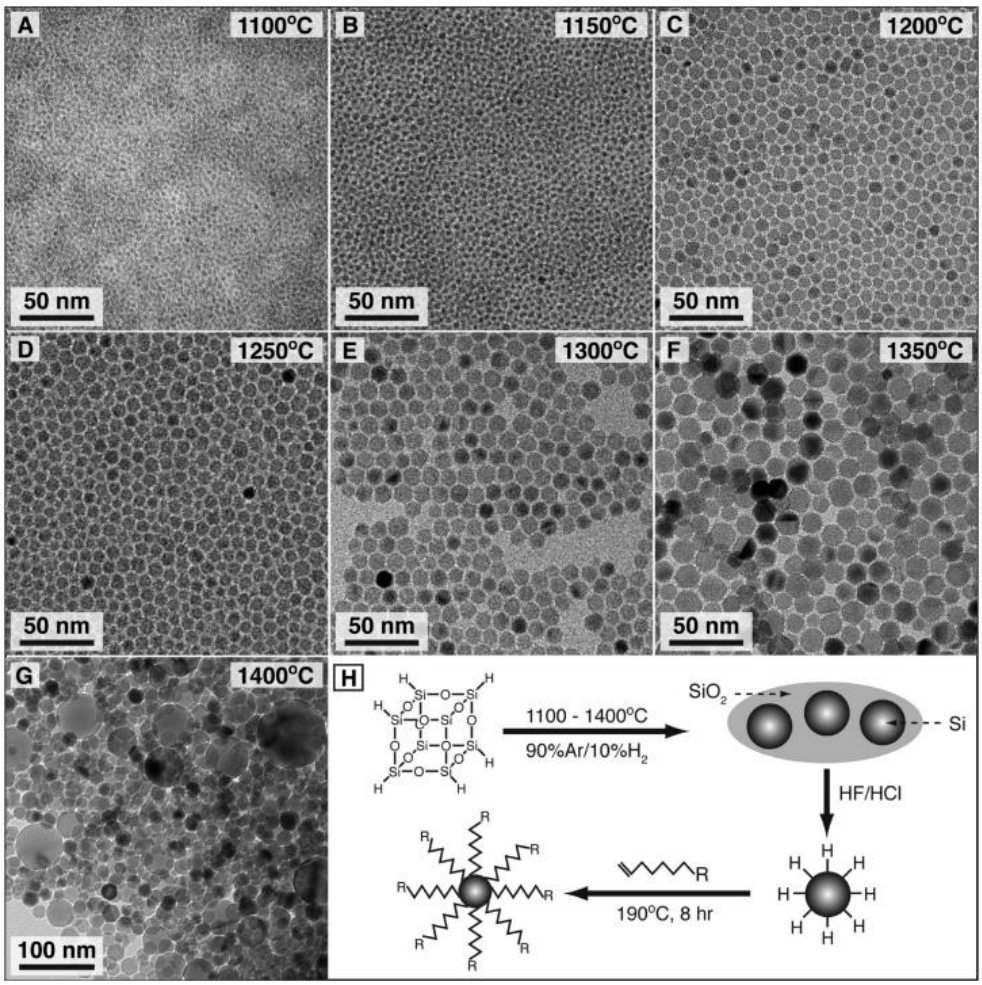

Figure 1.3.3 – (A to G) High- resolution TEM images of silicon nanocrystals annealed at different temperatures and (H) general method for the synthesis of H-SiNCs and their passivation with terminal alkenes (this process will be explained in the next paragraphs). Reprinted with permission from reference [73]. Copyright 2012, American Chemical Society.

1.3.1.3. Several silicon nanocrystals passivation techniques

The most of the synthetical techniques described above (among which the thermal decomposition of silicon-rich oxides) yields to hydride-terminated silicon nanocrystals. These nanoparticles are very sensitive to oxidation, susceptible to aggregation and not dispersible in any kind of solvents. In order to overcome those limitations, a passivation of the surface with organic molecules is required.[47]

The functionalisation techniques that have been studied so far are numerous. In some of them, alkyl lithium reagents are directly attached onto the surface of silicon nanoparticles, producing alkyl-silicon and lithium-silicon bonds (the latter, unstable,

can undergo a further substitution).[83] Others contemplate the reaction with carbon dioxide, amines or alkylphosphine oxides,[84] as shown in Figure 1.3.4a. Further interesting methods involve the substitution of the overexposed hydrogen atom with a halogen[85], which is reactive towards nucleophiles Figure 1.3.4b.

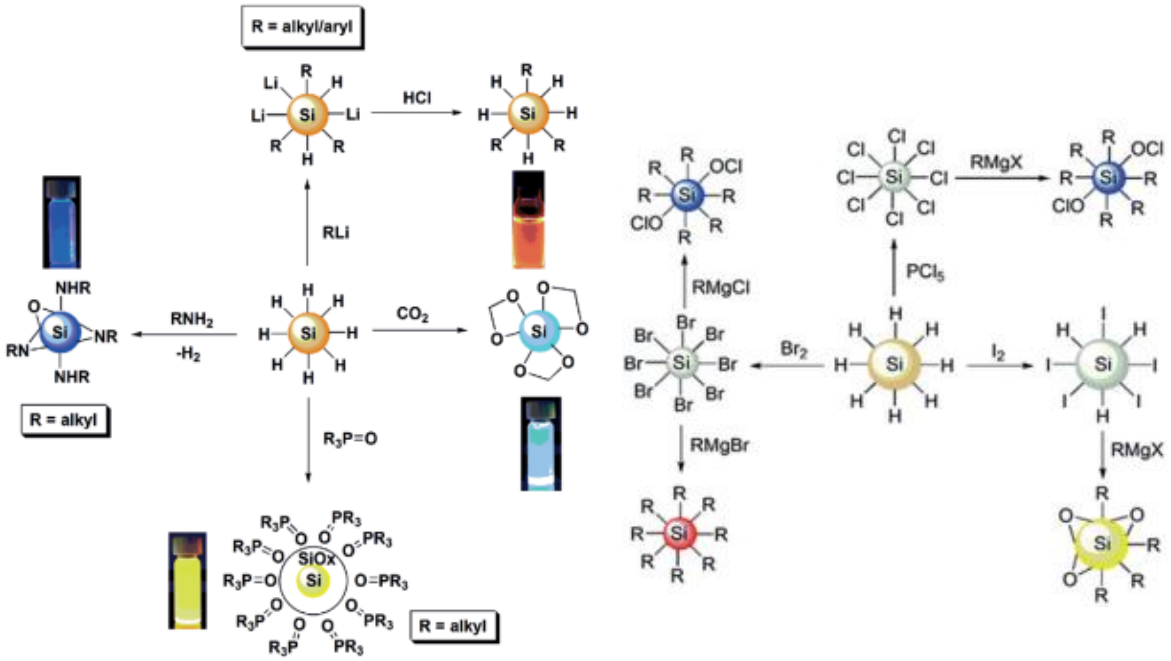

Figure 1.3.4 – (a) Reactivity of H-SiNCs with organolithium (RLi) reagents, carbon dioxide, amines and alkylphosphine oxides. (b) Substitution of hydrogen atoms with halogens and reactivity with nucleophiles. The resulting SiNCs display different emissions, as shown by the photographs or by the colours (if any) of the sphere representing the SiNC. Reprinted with permission from reference [47] (John Wiley and Sons) and from reference [85]. Copyright 2015, American Chemical Society.

As it is possible to see from Figure 1.3.4, the modification of the surface is of paramount importance also for the photophysical properties: a different functionalisation leads to different emissive properties (i.e. emission spectra, lifetimes, quantum yields, as Paragraph 1.3.2 will consider in detail).[83–85] However, in many cases, the photoluminescence that rises from those functionalised silicon nanocrystals is not directly associated to the band edge luminescence, but to defect states which are introduced by the ligands. It is known that the intrinsic emission of the nanocrystal is maintained when the surface is passivated with silicon-carbon bonds, i.e. silicon nanocrystals are passivated with unsaturated hydrocarbons, in particular terminal alkenes and alkynes. One effective strategy for tethering them to SiNCs is the hydrosilylation reaction.

1.3.1.4. Hydrosilylation reaction

Hydrosilylation is defined as the reaction that enables the addition of silicon hydrides across carbon-carbon double or triple bonds.[86,87] It is a well-known methodology for the synthesis of organosilicon compounds and it is one of the most important reactions in silicon chemistry and in silicone industry. It usually requires a catalyst to occur: metal-containing compounds such as platinum (hexachloroplatinic acid, Karstedt's catalyst), rhodium, iridium, ruthenium, iron complexes, *et cetera* have been studied for this purpose.[86,88] In those cases, the silicon-hydrogen bond of a silane is substituted with a silicon-carbon bond (in Figure 1.3.5 a catalytic cycle of a platinum-mediated hydrosilylation between an alkene and an organosilane is represented).

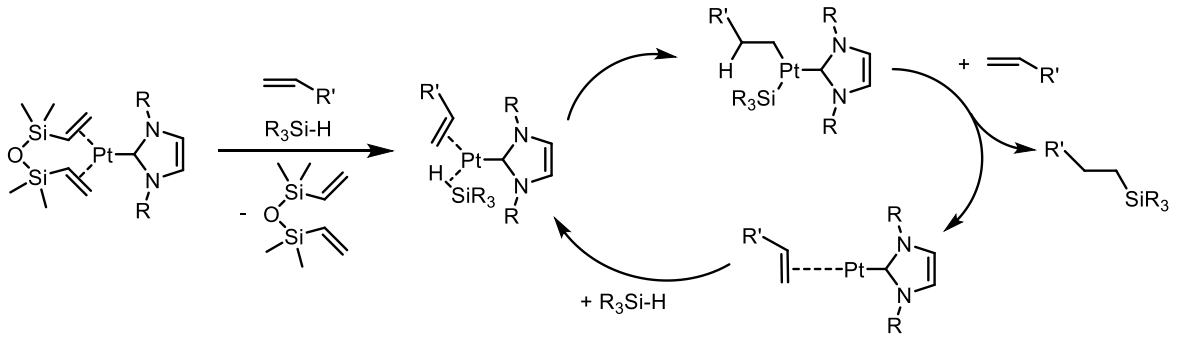

Figure 1.3.5 – Schematic hydrosilylation mechanism using a platinum complex.

The hydrosilylation reaction was subsequently proposed for the passivation of H-SiNCs. The first attempts involved the use of platinum complexes for smaller hydride-terminated silicon nanoparticles.[66,89,90] However, the resulting nanoparticles were characterised by scarce optical properties, with a low-bright (emission quantum yield inferior to 10%), short-lived (on the nanosecond range) blue emission. In addition, the problem of purification of the sample from traces of the metal catalyst is considerable.

Afterwards, new methods of hydrosilylation processes were exploited. Instead of using metal complexes, the addition of the Si-H bond to the unsaturated C-C bond was proved to be achieved also at high temperatures (thermal hydrosilylation),[91] upon exposure at UV light,[92] or in the presence of Lewis acids[93] or radical initiators.[94] Therefore, all these methods were tested on silicon nanocrystals.[47]

Thermal hydrosilylation consists in the homolytic cleavage of the silicon-hydrogen bond present on the surface of the nanoparticle occurring at temperatures higher than 150 °C. The so-formed silyl radicals react with the unsaturated C-C bond, propagating

in a chain reaction along the surface of the nanoparticle, in a mechanism accepted also for bulk silicon.[95] This method has been used also by our group for the functionalization of silicon nanocrystals with chromophores.[74,76,96] The main drawbacks of thermal hydrosilylation consist in the impossibility to link temperature-labile molecules or alkenes with low-boiling point, and an oligomerisation of the ligand alkenes on the surface of the nanoparticle can happen.[79,97]

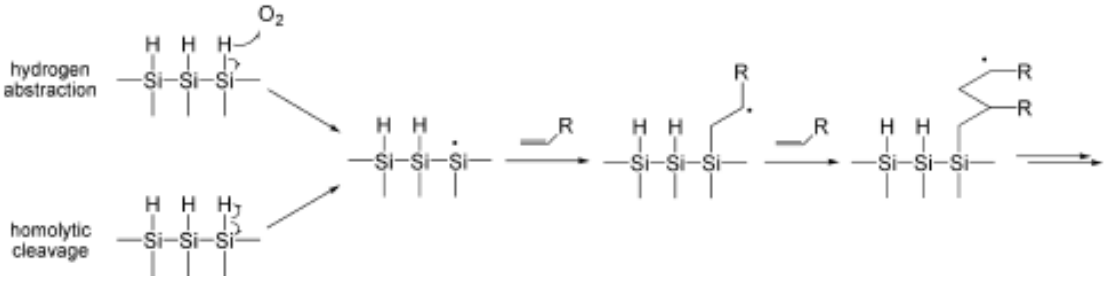

Figure 1.3.6 – Proposed mechanism for the oligomerisation of alkenes on the surface of hydride-terminated silicon nanocrystals. Reprinted with permission from reference [97]. Copyright 2013, American Chemical Society.

The *UV-assisted hydrosilylation* involves the formation of the silyl radicals upon exposure at UV light.[98] It is interesting, because it does not require other reagents but silicon nanocrystals and the ligands. However, this method does not allow to link chromophores, which could absorb the light, instead, lowering the efficiency of the desired hydrosilylation process. Moreover, it is strictly dependent on the size (and therefore the surface reactivity) of the nanoparticle and requires long reaction times to occur.[79,99]

Room temperature hydrosilylation can be accomplished also in the presence of Lewis acid catalysts, among which boranes have been extensively studied by Purkait *et al* (Figure 1.3.7).[100] The proposed mechanisms for this reaction are reported in Figure 1.3.8. In each case, the electrophilic borane is assumed to react (hydroboration, case A) or to activate directly (case B) the nucleophilic multiple bond of the ligand; consequently, the insertion of the Si-H (A) or the interaction with a silyl cation (B) occurs, forming the Si-C bond. Despite its high reaction yields,[100] this strategy is limited to non-nucleophilic ligands (alcohols and amines could deactivate the borane).[79]

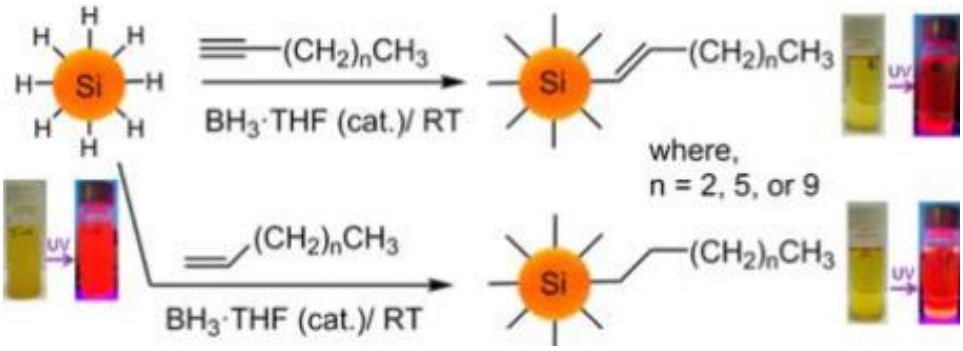

Figure 1.3.7 – Borane-catalysed functionalisation of H-SiNCs to yield alkyl or alkenyl-passivated SiNCs. Reprinted with permission from reference [100]*. Copyright 2015, American Chemical Society.*

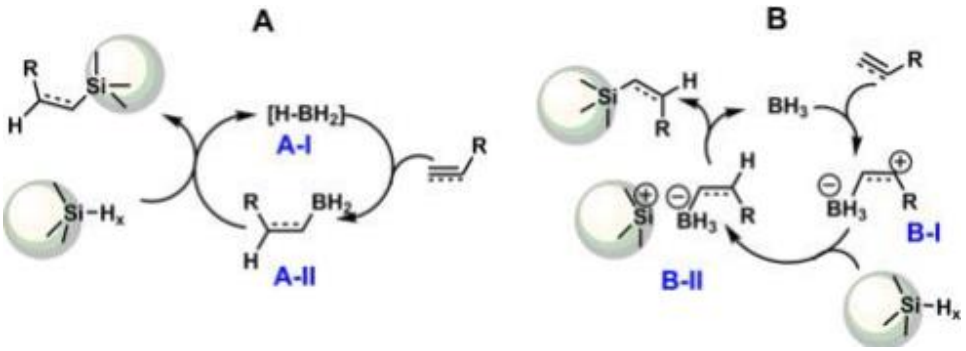

Figure 1.3.8 – Proposed mechanisms for the functionalisation of H-SiNCs with alkenes or alkynes through borane-catalysed hydrosilylation. Reprinted with permission from reference [100]*. Copyright 2015, American Chemical Society.*

Another interesting room-temperature hydrosilylation was introduced by Korgel *et al.*[101] In this work, the considered ligands were bi-functional alkenes, in which one extremity of the molecule is a carboxyl group (carboxylic acid or ester). The carboxyl moiety acts as a catalyst, activating the overexposed Si-H bond rendering it more nucleophilic towards the olefin. When in proximity, the electron-deficient C-C double bond accepts the hydride and facilitates the formation of the silicon-carbon bond (as shown in Figure 1.3.9). It is worth noting that carboxyl groups with higher resonance strength are more reactive towards the H-SiNC. Moreover, smaller nanocrystals are more reactive (due to the higher surface atoms over volume atoms ratio, see Chapter 1.2). Alkenes bearing a carboxylic moiety have also been used in co-presence of other alkenes in order to ameliorate the chemical yield in thermal hydrosilylations.[102]

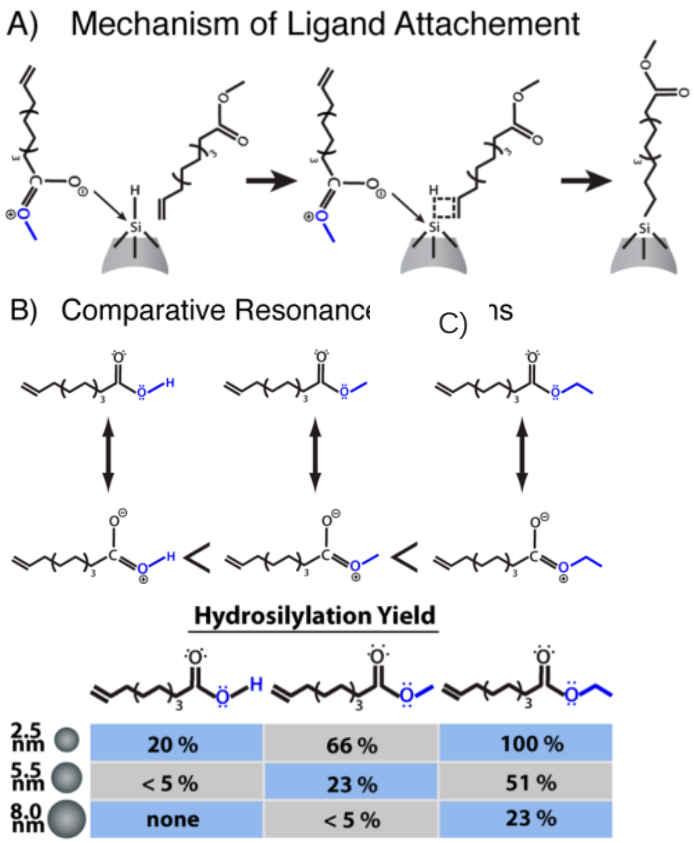

Figure 1.3.9 – Room temperature hydrosilylation of Silicon Nanocrystals with bifunctional terminal alkenes. (A) Mechanism of ligand attachment, (B) comparative resonance strength of the considered alkenes and (C) hydrosilylation yields based on the type of alkene or the size of the nanocrystal. Adapted with permission from reference [101]. Copyright 2013, American Chemical Society.

A valid alternative to the methods mentioned above is the hydrosilylation assisted by radical initiators.[103] In particular, one kind of initiator that has been widely used also by our research group[104–106] is an amphiphilic aryl diazonium salt called 4-decyl diazobenzene tetrafluoroborate (4-DDB, Figure 1.3.10).[107] The main characteristics that render this compound particularly interesting are:

a) The lower aggressivity towards the silicon structure compared to other radical initiators (such as hydrogen peroxide);
b) The presence of tetrafluoroborate as counter anion, which render it less safety hazardous than halide diazonium salts and stable if stored at -10 °C;
c) The presence of a decyl chain, which enhances the solubility of the salt in apolar solvents (e.g. toluene), where the most of the reaction on silicon nanoparticles are performed;
d) The lower oligomerisation yield compared to thermal hydrosilylation.[79]

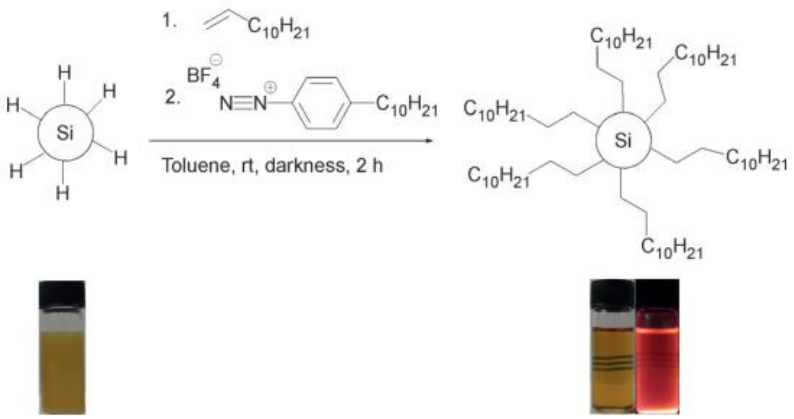

Figure 1.3.10 – General reaction scheme for radical initiator (4-DDB)-assisted hydrosilylation of H-SiNCs with 1-dodecene. It is possible to notice that the functionalisation leads to a good dispersibility in a solvent (photographs below, under ambient or UV light). Reprinted with permission from reference [107] *(John Wiley and Sons).*

As for thermal hydrosilylation, this reaction proceeds through a radical chain mechanism, as reported in Figure 1.3.11.[107] In particular:

1) The diazonium salt oxidizes the surface of the silicon nanoparticles, generating an aryl radical. The driving force of this process is the release of stable nitrogen gas;
2) The counter anion of the salt deprotonates the oxidized Si-H, producing a silyl radical (Figure 1.3.11A);
3) The silyl radical acts as an initiator for the alkene's chain propagation along the surface of the nanoparticle: silicon-carbon bonds are formed in this process (Figure 1.3.11B);
4) The aryl radicals derived from the diazonium salts acts as terminating agents for the chain reaction.

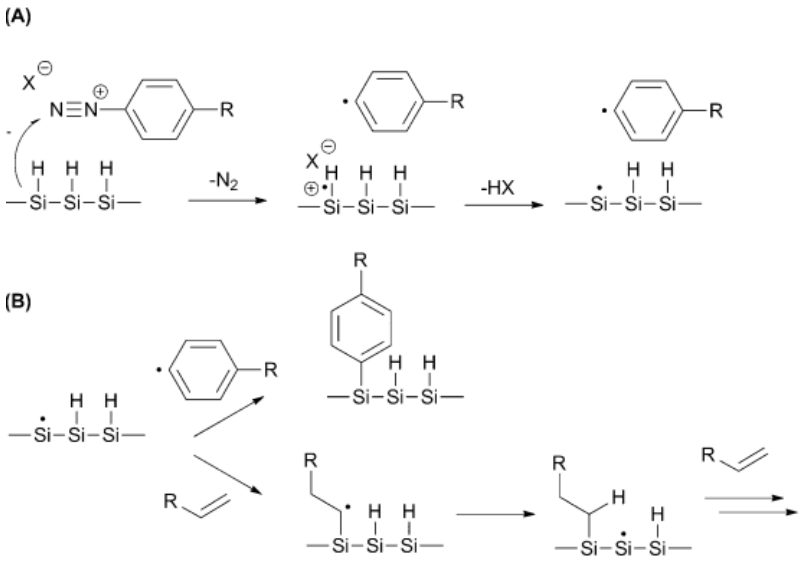

Figure 1.3.11 – Mechanism of the diazonium salt-assisted hydrosilylation. Reprinted with permission from reference [107] *(John Wiley and Sons).*

Despite its numerous advantages, this method has several important drawbacks:

a) Alcohols, amines and carboxylic acids seem to hamper the hydrosilylation reaction and cannot be directly linked to silicon nanocrystal's surface with this strategy;[107]
b) Molecules containing conjugated systems, such as chromophores, are neither tethered specifically (e.g. the radicals distort the conjugated system) nor linked at all (this issue seems to be overcome if the diazonium salt is replaced by other radical initiators such as AIBN[108]).

In order to surmount the problems listed above, a new synthetical strategy has been associated with the diazonium salt-assisted radical hydrosilylation: it consists in passivating the surface of H-SiNCs with alkenes bearing chlorosilane moieties (e.g. chloro(dimethyl)vinylsilane).[109] This reaction leads to chlorosilane-passivated silicon nanocrystals, i.e. silicon nanocrystals possessing an organic electrophilic shell. The passivation allows the SiNCs to be stable in anhydrous degassed solvent and permits a new reaction (called post-functionalisation) with nucleophilic reagents (e.g. alcohols, silanols, organolithium compounds, *et cetera*, see Figure 1.3.12).

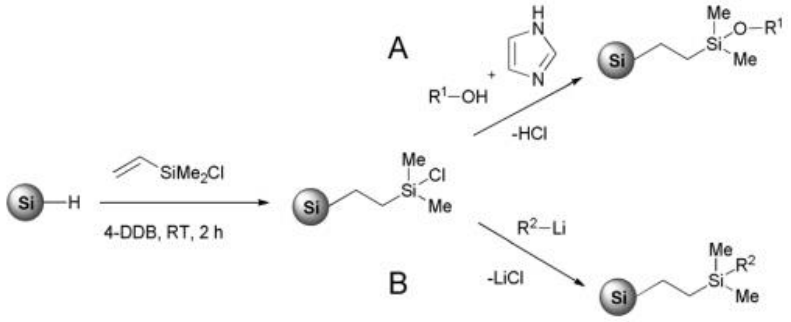

Figure 1.3.12 – Passivation of H-SiNCs with chloro(dimethyl)vinyl silane in the presence of diazonium salts and post-functionalisation with (A) alcohols and silanols or (B) organolithium reagents. Reprinted from reference [109] *with permission from the Royal Society of Chemistry.*

In this way, our group was able to functionalise silicon nanocrystals with chromophores[106] or amines.[105] Those procedures have been developed during my PhD studies and the relative discussions will be treated in the Results and Discussion and Experimental Sections of this thesis.

1.3.2. Photophysical properties of silicon nanocrystals

With few exceptions, which will be considered in a following paragraph (1.3.2.1), the photophysical properties of silicon nanocrystals are determined by the nature of the semiconductor's band gap. As reported in Paragraph 1.1.2, silicon is characterised by an indirect band gap, which influences the radiative transitions. Because of the difference in the momentum of the crystal lattice, the migration of an electron from a band to the other must involve the absorption (if the electron migrate from the VB to the CB) or the emission (*vice versa* from the CB to the VB) of a photon of energy at least equal to the band gap accompanied by the absorption or emission of a phonon. In other words, an overall rearrangement of the crystal lattice must occur in order to promote the electron or relax the exciton radiatively (see Figure 1.1.2). This renders the radiative transitions (both in absorption and in emission) less probable to occur with respect to direct band gap semiconductors.[53]

The scarce absorption qualities of silicon are also evident in bulk silicon for applications in which the interaction with light is required (e.g. solar cells): in order to remedy the problem, more thick (or numerous) layers of material are used to ameliorate the absorption.

In silicon nanocrystals, the molar absorption coefficient is lower than conventional direct band gap semiconducting nanoparticles. In particular, it is not visible the peak

relative to the band edge transition (compare with Figure 1.2.3) and the absorption spectrum appears as a continuous curve lacking in inflection point with negative first derivative (i.e. decreasing with the wavelength) and positive second derivative (concave upwards).[53,73]

In Figure 1.3.13 the absorption spectra of silicon nanocrystals with diameter of 3 (green line), 4 (orange line) and 5 nm (red line) are reported. As stated in Chapter 1.2, the spectra are size-dependent: larger nanocrystals are associated to smaller band gaps, and the resulting absorption spectrum appears red-shifted. Moreover, as anticipated in the previous chapter, lower wavelengths are associated to higher absorbances: this is due to the increased number of degenerative states that lie in the inner of the bands and that are involved in the transitions with more energetic photons.

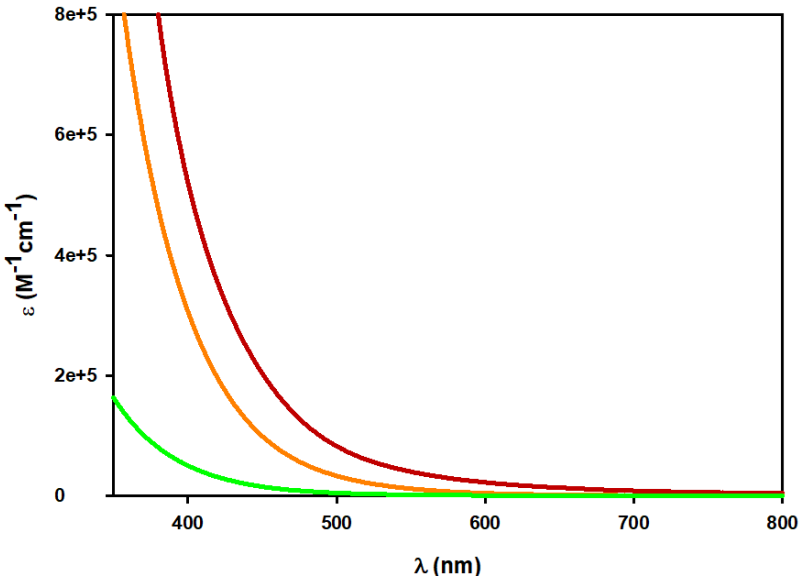

Figure 1.3.13 – Absorption spectra of dodecyl-passivated SiNCs with core diameter of 3 (green line), 4 (orange line) and 5 (red line) nm in distilled air-equilibrated toluene.

Despite the quantum confinement effect ameliorate the emissive properties of silicon if compared to the bulk semiconductor,[110] emission quantum yield (PLQY) and luminescence lifetimes (τ_{em}) are undoubtedly affected by indirect band gap. The PLQY is lower with respect to direct-band gap semiconductors (the mean value reported in this study is 20% for 4 nm sized SiNCs, while core-shell cadmium-based QDs reach values even superior to 60%)[7], while the emission lifetimes are far longer (tens or hundreds of microseconds compared to tens of nanoseconds of conventional quantum dots' lifetimes).[53] Moreover, both PLQY and emission lifetime values increase with the

size of the nanoparticle, suggesting that non-radiative recombinations are less dominant in larger SiNCs.[111,112]

Regarding the photoluminescence spectrum, the emission wavelength spans the orange to near-infrared spectral range accordingly with the size of the nanoparticle (from about 2 nm to 12 nm), as shown in Figure 1.3.14.[73] As it is possible to notice (comparing with Figure 1.2.3), the emission profile appears broader than direct-band gap quantum dots' ones. This is probably due to an effect of the temperatures that enhances vibrations in the particle, resulting in structures with different crystal lattice momentum in the emission process.[113]

Another factor that seems to affect the emissive properties of SiNCs is the crystallinity of the sample.[114] Despite the structure of the lattice has been described as diamond-like cubic, it is noteworthy knowing that amorphous zones are still present.[115] Recent studies have shown that nanoparticles with same core size, but different amount of crystalline phase show different emissions, as they were characterised by different sizes.[116]

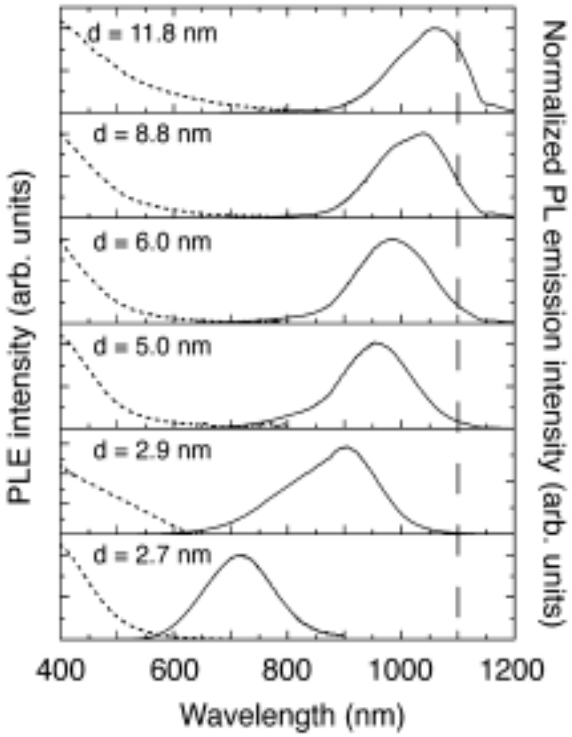

Figure 1.3.14 – Photoluminescence excitation spectra (dashed lines, measured at emission maximum) and emission spectra (solid lines, recorded at 420 nm) of alkyl-passivated silicon nanocrystals of different dimensions dispersed in toluene. Reprinted with permission from reference [73]. Copyright 2012, American Chemical Society.

Despite the efforts of the scientific community, however, the origin of the typical long-lived photoluminescence of silicon nanocrystals is still debated.

1.3.2.1. EMA theory and defected emission in Silicon Nanocrystals

The photophysical properties described so far are closely associated with silicon nanocrystals with size superior to 2 nm (usually synthesized at high temperature through thermal decomposition of silicon-rich oxides or plasma-assisted methods, see Paragraph 1.3.1) with a carbon functionalisation of the surface. For this kind of SiNCs, the emission is strictly dependent on the band gap (i.e. on the size of the nanoparticle in absence of defects). In other terms, this emission follows the effective mass approximation (EMA), which allows to correlate the quantum confined band gap with the size of the quantum dot:

$$E(d) = E_g + \frac{h^2\pi^2}{2d^2}\left(\frac{1}{m_e^*} + \frac{1}{m_h^*}\right) - \frac{1.786e^2}{\epsilon_r d}$$

where E_g is the band gap energy of the bulk semiconductor (1.1 eV in cubic silicon), e is the electron charge, ϵ_r is the relative permittivity of Si (11.68), d the diameter of the nanoparticle and m_e^* and m_h^* are the effective masses of the conduction band electrons and valence band holes.

In the case of (1) nanocrystals synthesized by low-temperature (< 150 °C) methods, (2) smaller nanoparticles or (3) quantum dots characterised by defects on the surface, a new photoluminescence that deviates from the behaviour provided by the EMA arises.[53,58]

Figure 1.3.15 collects the peak photoluminescence energy for silicon nanocrystals synthesized at high temperature (red symbols) and with low-temperature procedures (such as reduction of metal silicides and oxidation of silicon halides, see Paragraph 1.3.1, blue symbols) by several research groups.[53,73] It is possible to notice that only the latter behave as expected from EMA calculations (black line).

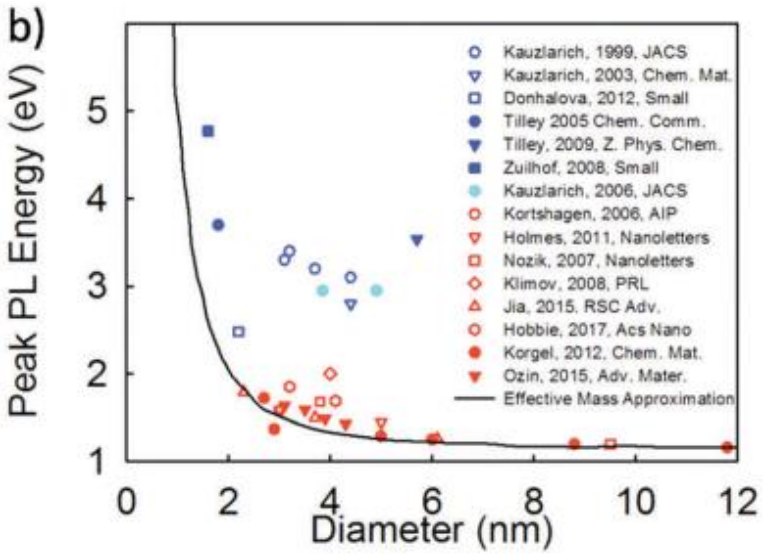

Figure 1.3.15 – PL peak emission versus the diameter of alkyl-functionalised SiNCs prepared by low temperature methods: Mg_2Si reduction[68,117,118] (empty blue symbols), $SiCl_4$ reduction[89,119,120] (solid blue symbols) and NaSi reaction with ammonium bromide[121] (light blue symbols) compared to SiNCs prepared by a plasma-assisted reaction[122–127] (empty red symbols) and by high temperature nucleation[73,128] (solid red symbols). The black line corresponds to the equation reported above. Reprinted from reference [53] with permission of the Royal Society of Chemistry.

The former nanoparticles are characterised by a short-lived (on the nanosecond range) less bright (PLQY inferior than 20%) blue emission which is not dependent on the size of the quantum dot.[53]

A similar behaviour occurs for silicon nanocrystals smaller than 1.9 nm. In a recent study,[50] the photophysical properties of different sized silicon nanoparticles obtained by thermal decomposition of silicon-rich oxide and different etching times have been compared. It is shown that smaller nanoparticles display a blue-shifted short-lived (hundreds of picoseconds) luminescence instead of the orange-to-near infrared long-lived emission. According to the authors, this is probably associated to a different electronic structure: beneath 1.9 nm, silicon quantum dots would be characterised by molecule-like energy states rather than the typical electronic structure of an indirect-band gap semiconductor. This should explain their diverse photophysical behaviour.

More interesting influences on the photoluminescence of silicon nanocrystals are consequences of the direct interaction of the silicon crystal lattice with heteroatoms such as halogens, oxygen and nitrogen.[53]

The presence of chlorine, bromine or iodine on the surface of the quantum dot is responsible for the complete quenching of the luminescence.[85] However, if the halogen is substituted with an alkyl chain, the emissive properties are partially restored.

The effects of the presence of oxygen atoms (i.e. the oxidation of the surface of the nanoparticle) have been extensively debated. According to several researchers,[110,129] this presence is fundamental for the rising of the long-lived luminescence. In other studies,[130] it is reported that the oxidation of the surface produces a trap state which causes a slight blue-shifted emission (contrary to what happens for conventional quantum dots, see Paragraph 1.2), even maintaining long emission lifetimes (in the microsecond range) with high photoluminescence quantum yields. It has been noticed that this change in the photophysics occurs[53] if the surface is not well-passivated (therefore the oxygen can react with the defects, yielding Si-O single or double bonds), if the nanoparticle is stored in air-equilibrated solutions[102,105] or in the presence of alcohols[131] or carboxylic acids.[132]

Furthermore, many SiNCs researchers' interests are focussed on the functionalisation of silicon nanocrystals with nitrogen-based ligands. It seems that the interaction between even traces of nitrogen atoms and the silicon crystal lattice creates a charge-transfer state which is responsible for a short-lived blue emission dependent on the excitation wavelength.[130,133,134] It has been noticed that this photoluminescence (also called F-band) can either co-exist with the long-lived red one (S-band)[131,135,136] or suppress it.[133,137] Because of several exceptions, in which nitrogen-containing ligands functionalised silicon nanocrystals or SiNCs exposed to nitrogen-containing reactive compounds display red long-lived emission,[76,105,138,139] the origin of this behaviour is still debated.

Figure 1.3.16 collects the emissive mechanisms proposed by Veinot[130] for alkyl-passivated silicon nanocrystals (in which the emission is due to the core), silicon nanocrystals with oxidized surface (which involves a trap state for the electron at high energies) and nitrogen containing silicon nanocrystals (where the emission is due to the exciton recombination which entirely occurs at a surface charge-transfer state laying at higher energies than the bang gap).

During my PhD studies, functionalisation strategies with amines or carboxylic acids have been developed in order to maintain the typical core emission. The results and discussions will be addressed in a following chapter.

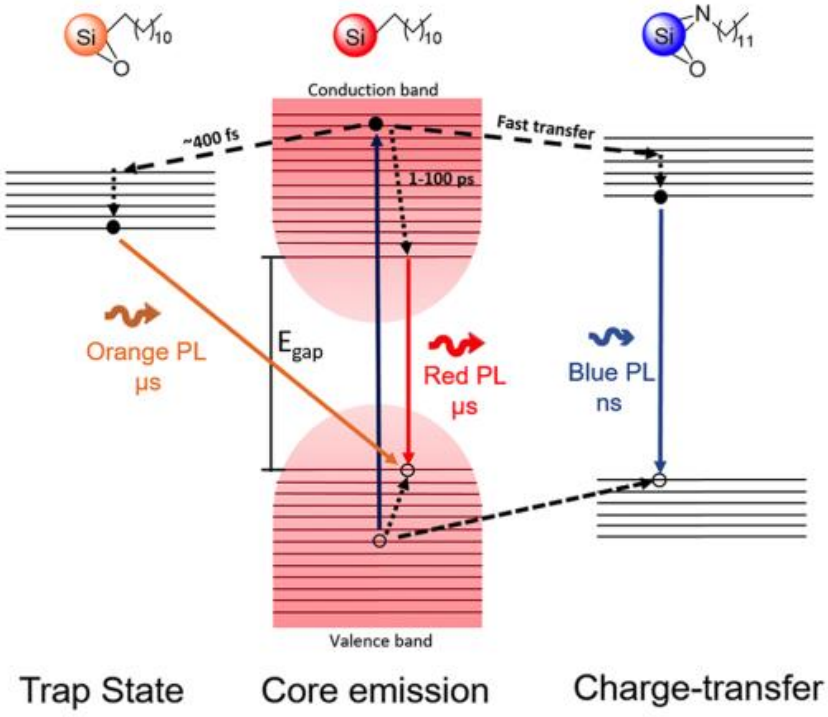

Figure 1.3.16 – Proposed emission mechanisms for SiNCs bearing oxygen or nitrogen impurities. Reprinted with permission from reference [130]. Copyright 2017, American Chemical Society.

1.3.2.2. Photophysical properties of chromophore-functionalised silicon nanocrystals

As stated in the previous paragraphs, the main disadvantage of silicon nanocrystals is correlated to their scarce absorption properties, especially in the range spanning green to near-infrared light. As a consequence, the brightness, defined as the product between the molar absorption coefficient (at the excitation wavelength) and the emission quantum yield of the sensitised system, is limited. Therefore, the photon required to create the exciton is far more energetic than the emitted one. In other words, in order to achieve a reasonable emissive signal, highly energetic excitation light must be employed.

In order to enhance the absorption of SiNCs, the surface of the quantum dot can be decorated with chromophores. More chromophores are linked, higher the absorption at the correlated wavelengths is (for the additive property of absorbance). If the fate of

the excited state of the chromophore is the energy transfer to the silicon core, a *light-harvesting antenna* is produced.[53]

Despite this approach is quite interesting for ameliorating the optical properties and therefore the applications (and as it will be discussed in a following paragraph), only few research groups have realized such systems.[140]

For instance, our group at first studied the properties of pyrene-functionalised silicon nanocrystals.[74,75] The organic chromophore was introduced via a thermal hydrosilylation reaction as 1-(allyloxy)methylpyrene or 1-((undec-10-enyloxy)methyl)pyrene (Figure 1.3.17) in co-presence of 1-dodecene.

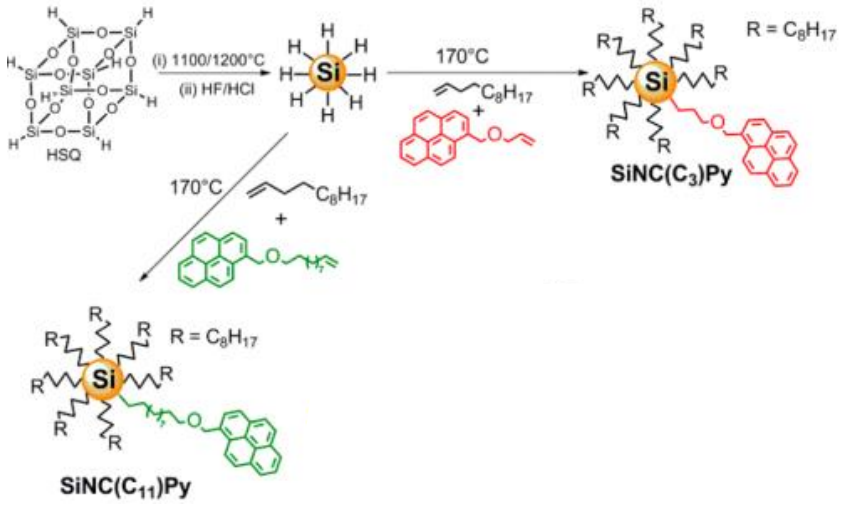

Figure 1.3.17 – General preparation scheme of pyrene-functionalised silicon nanocrystals. Adapted with permission from reference [75]. Copyright 2015, American Chemical Society.

The so-obtained silicon nanocrystals with an average diameter core of 3 nm displayed an absorption spectrum which is the superimposition of the absorption profile of the inner silicon nanocrystals and the spectrum of the pyrene moieties (Figure 1.3.18b). This means that no interaction between the organic shell and the inorganic core occurs at the ground state.

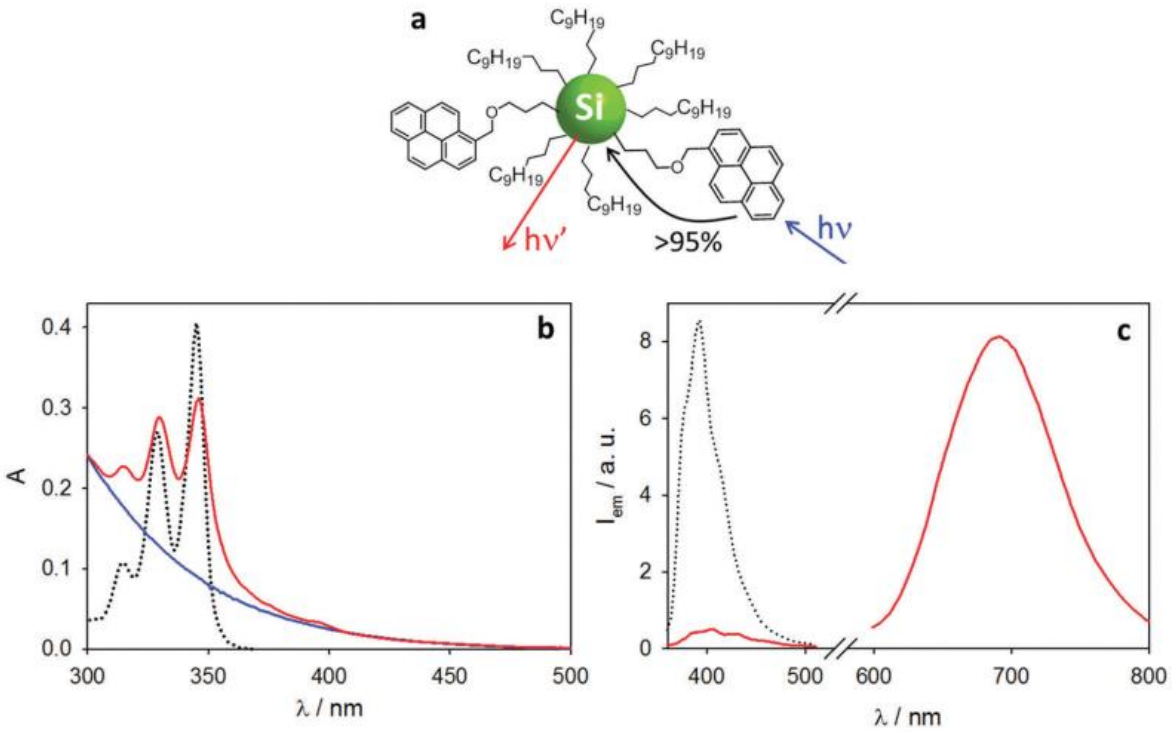

Figure 1.3.18 – (a) Schematic representation of the light-harvesting antenna based on pyrene chromophores attached to SiNCs with an average diameter of 3 nm. (b) Absorption spectra of 3 nm-SiNCs capped with dodecyl ligands (blue) or pyrene and dodecyl ligands (red line), and pyrene model compound (black dotted line) in air-equilibrated toluene. (c) Emission spectra of SiNCs schematically presented in panel (a) (solid red line) and optically matched solutions of free pyrene (dotted black line) in air-equilibrated toluene. λ_{exc} = 345 nm.[53,74] *Reprinted from reference* [53] *with permission of the Royal Society of Chemistry. Adapted with permission from reference* [74]*. Copyright 2014, American Chemical Society.*

Regarding the emission spectrum (Figure 1.3.18c), it is possible to distinguish the photoluminescence of the silicon core centred at about 700 nm and the quenched emission of pyrene at 396 nm. Lifetime measurements and excitation spectra can confirm the formation of a light-harvesting system: exciting the pyrene-moieties, the absorbed energy is funnelled to the silicon core with an efficiency superior to 95% (as it is schematised in Figure 1.3.18a). Silicon, therefore, performs a brighter sensitised emission.

Another case of silicon nanocrystal-based light harvesting antenna studied by our group consists in Zn(II)tetraphenylporphyrin-functionalised 5 nm sized-quantum dots.[76] The absorption bands in visible range of the complex are added to the silicon core's profile and the emission consists in two bands: one (centred at about 650 nm) is due to the quenched porphyrin, the other (~ 1000 nm) to the sensitised inorganic core (Figure 1.3.19).

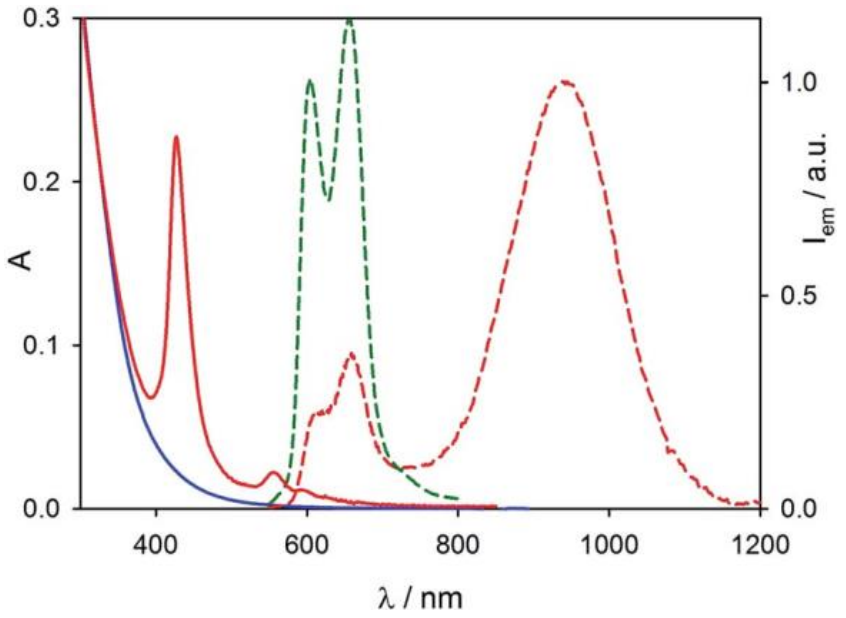

Figure 1.3.19 – Absorption spectra (solid lines) of 5 nm SiNCs functionalised with a Zn(II)tetraphenylporphyrin (red line) and 5 nm alkyl-capped SiNC (blue line) in toluene. Emission spectra (dashed lines) of the porphyrin functionalised SiNCs (red line) in air-equilibrated toluene at room temperature. For comparison purposes, the emission spectrum (green line) of a mixture of alkyl-passivated SiNCs and the detached porphyrin in the correct ratio to match the absorption spectrum of the hybrid system is reported. λ_{exc} = 427 nm. Reproduced from reference [76] with the permission of the Royal Society of Chemistry.

Because of the more limited absorption in the orange-to-near infrared spectral range, many efforts have been addressed to the development of hybrid organic-inorganic silicon nanocrystals in which the chromophore could provide the absorption of photons with an energy inferior to 2.5 eV. An example of these systems are the SiNCs functionalised with 4,7-di(2-thienyl)-2,1,3-benzothiadiazole.[96] This organic chromophore can absorb light at 480 nm and transfer the energy to the emitting silicon. Moreover, it exhibits also a good two-photon absorption (2PA) cross section with band maxima at 730 and 960 nm, as measured by recording its fluorescence in toluene solution upon excitation with a continuous train of femtosecond pulses from a tuneable Ti:sapphire laser oscillator. While the two-photon absorption cross section of SiNCs is rather poor, upon excitation of the benzothiadiazole moieties at 960 nm a sensitised anti-Stokes luminescence of the silicon core in the NIR spectral region is observed (Figure 1.3.20).[53,96]

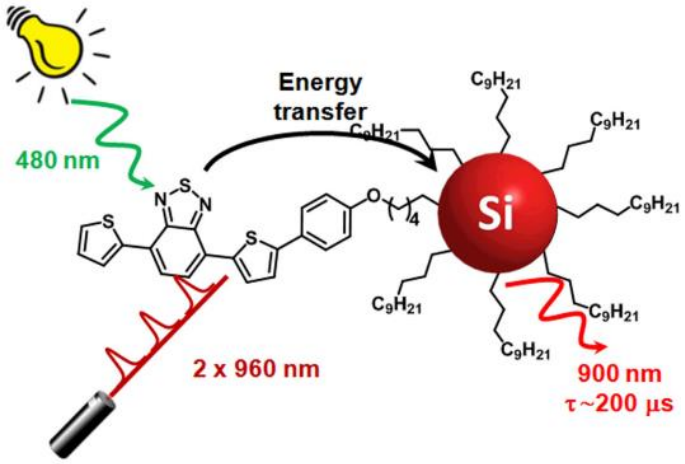

Figure 1.3.20 – Schematic representation of 4,7-di(2-thienyl)-2,1,3-benzothiadiazole functionalised silicon quantum dots where the organic chromophore is either excited by one photon at 480 nm or two simultaneous photons at 960 nm and the energy transfer occurs resulting in a sensitised emission of the silicon core at 900 nm. Reproduced with permission from reference [96] (Elsevier).

Other recent examples of light-harvesting systems are based on SiNCs linked to perylene and BODIPY, where the functionalisation is microwave-assisted.[141] Conversely, a different situation is offered by anthracene tethered to SiNCs,[142] in which the energy transfer occurs in the opposite way. In this study, the excited state of the organic chromophore is able to generate the triplet excited state of freestanding diphenylanthracene molecules. The triplet-triplet annihilation of the latter results in a delayed fluorescence (Figure 1.3.21).

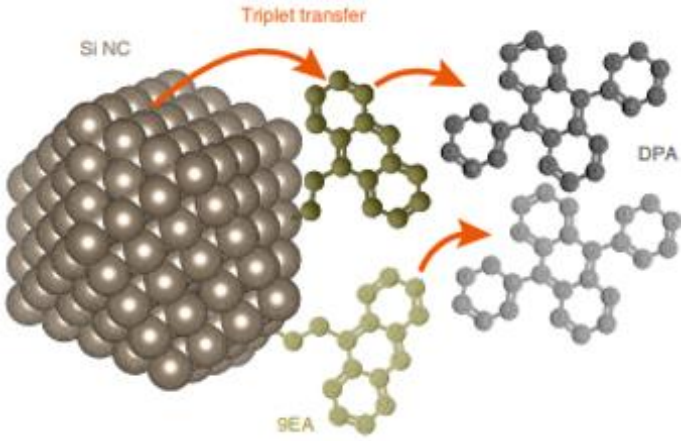

Figure 1.3.21 – General mechanism for the sensitization of diphenylanthracene through excitation of silicon nanocrystals functionalised with anthracene. Reprinted with permission from reference [142] (Springer Nature).

During my PhD project, new synthetical strategies and new chromophores were tested to produce light-harvesting antennae based on hybrid silicon nanocrystals. The results and discussions will be addressed to a following chapter.

1.3.3. Electrochemistry and electrochemiluminescence of silicon nanocrystals

Electrochemiluminescence (ECL) is defined as the generation of light by electron transfer between species generated electrochemically.[143,144] It is an electrogenerated chemiluminescence which has been extensively studied for sensing, *in vitro* diagnosis and light-emitting devices[145]. Thanks to the absence of excitation light, ECL owns unique properties such as very low background and high sensitivity. In particular, it has been a great success in the biosensor fields, thanks to the unique signal-to-noise ratio also in real and very complex matrixes. One of the main mechanisms of ECL involves a coreactant. It is known, for instance, that tripropylamine (TrPA) can act as coreactant in the presence of $[Ru(bpy)]^{2+}$.[146] The radical species formed when subject to oxidation (TrPA·) can reduce $[Ru(bpy)]^{3+}$ generated at the anode, leading to the excited state of the complex, which emits. This technique is useful for sensing applications:[147] for instance, if the coreactant is a target molecule, the application of the potential generates an ECL signal which is dependent on its concentration.[148]

In addition to metal complexes, aromatic compounds, such as rubrene, anthracene and diphenylanthracene[149], carbon dots,[150] polymer dots,[151] dye-doped nanoparticles.[152,153] or quantum dots[144,154] are known to produce electrochemiluminescence. In particular, nanomaterials are very attractive for these applications due to (i) the efficiency of electron transfer process[155] and (ii) the number of ECL dyes or the ECL efficiency for recognition event.[147,156] For instance, Cao *et al.* recently showed the advantages of core/shell cadmium-based quantum dots over conventional emitters, including an enhancement in ECL efficiency and the size-dependent emission.[157] Among them, silicon nanocrystals were the first quantum dots studied for ECL.[54]

Firstly, Bard *et al.* analysed the electrochemical properties of different-sized silicon nanocrystals dispersed in N,N-dimethylformamide and acetonitrile. Cyclic (CV) and differential pulse voltammetry (DPV) showed discrete steps associated to single-electron charging, which is similar to the Coulomb blockade phenomenon observed for metal nanoparticles.[158] Briefly, for metal nanoparticles, the addition of electrons is

quantized and occurs at specific potentials that allow to overcome the Coulombic repulsion with the already introduced charges.

Moreover, the DPV (Figure 1.3.22) shows a large central gap between the onset of oxidation and reduction, characteristic of the energy difference between the highest occupied and lowest unoccupied molecular orbitals. It is worth noting that a study from our group[159] treated the valence and the conduction band positions, based on the analysis, within the Marcus theory, of the rate constants of photoinduced electron transfer processes with electron donors (ferrocene derivatives) and electron acceptors (quinone derivatives). Interestingly, this study highlights that the rate constants seem to be influenced by the reduction potential of the quenchers, the size of the nanoparticle, the solvent polarity, but not by the surface capping layer of the SiNCs, suggesting that quencher molecules can penetrate within the protecting layer.[53,159]

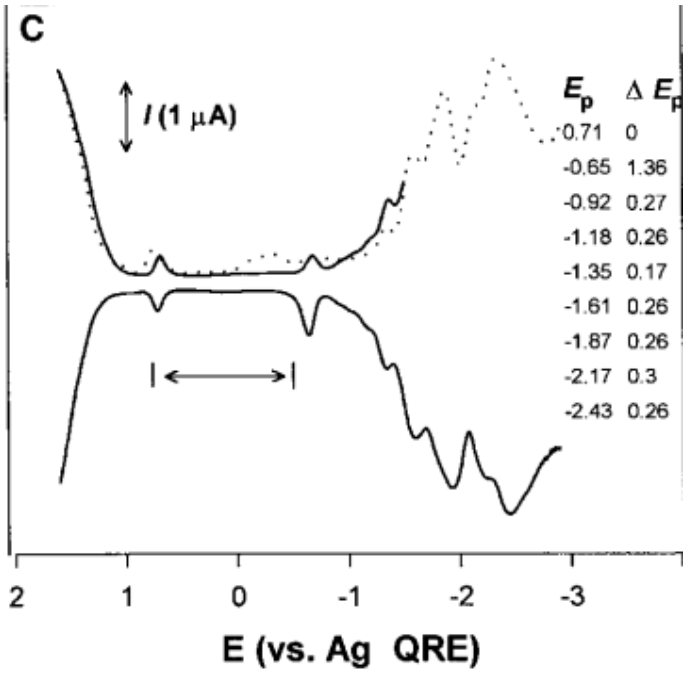

Figure 1.3.22 – Differential pulse voltammogram for SiNCs with a diameter of 1.7 nm in 0.1 M tetrahexylammonium perchlorate DMF solution. I *is the current,* E *the potential, on the right side are reported* E_p, *the current peak potential, and* Δ E_p, *the potential difference between two consecutive peaks. From reference* [54]. Reprinted with permission from AAAS.

Therefore, in their work,[54] Bard and co-workers reported the electrochemiluminescence of SiNCs, discovering that two main mechanisms can be responsible of it: annihilation or the presence of coreactant.

Annihilation mechanism occurs when the same species (in this case, SiNCs) are subject to potential cycling between oxidizing and reducing potentials. In this case, both oxidised ($SiNCs^{+\cdot}$) and reduced ($SiNCs^{-\cdot}$) nanoparticles are formed in the medium. The overall energetic situation is higher than the energy of the exciton. Therefore, an electron transfer between the two species generated at the electrodes can result in the formation of an excited nanoparticle (*SiNC) which emits:

$SiNC + e^- \rightarrow SiNC^{-\cdot}$ at the cathode

$SiNC - e^- \rightarrow SiNC^{+\cdot}$ at the anode

$SiNC^{-\cdot} + SiNC^{+\cdot} \rightarrow *SiNC + SiNC$ electron-transfer reaction

$*SiNC \rightarrow SiNC + h\upsilon$ electrochemigenerated luminescence

The ECL mechanism requires only one type of potential at the working electrode (oxidizing or reducing) in the presence of coreactants. In particular, Bard observed that oxalate ($C_2O_4^{2-}$) and persulfate ($S_2O_8^{2-}$) can act as coreactants for SiNCs at positive and negative potentials respectively, generating reducing and oxidising species correspondingly. The mechanisms are reported below.

For oxalate assisted ECL:

$SiNC - e^- \rightarrow SiNC^{+\cdot}$ at the anode

$C_2O_4^{2-} - e^- \rightarrow CO_2 + CO_2^-$ at the anode (the generated $C_2O_4^-$ is unstable)

$SiNC^{+\cdot} + CO_2^- \rightarrow *SiNC + CO_2$ electron-transfer reaction

$*SiNC \rightarrow SiNC + h\upsilon$ electrochemigenerated luminescence

For persulfate assisted ECL:

$SiNC + e^- \rightarrow SiNC^{-\cdot}$ at the cathode

$S_2O_8^{2-} + e^- \rightarrow SO_4^{2-} + SO_4^-$ at the cathode (the generated $S_2O_8^{3-}$ is unstable)

$SiNC^{-\cdot} + SO_4^- \rightarrow *SiNC + SO_4^{2-}$ electron-transfer reaction

$*SiNC \rightarrow SiNC + h\upsilon$ electrochemigenerated luminescence

In each case, an emission at higher wavelength with respect to the photoluminescence (640 nm versus 420 nm) is observed. This is probably because photoluminescence is a core phenomenon, while ECL is attributed to hole-electron recombination processes occurring on the surface, therefore generating a different emission (as Figure 1.3.23 shows). Interestingly, the reported ECL was not size-dependent, unlike other electrochemiluminescent quantum dots.[157]

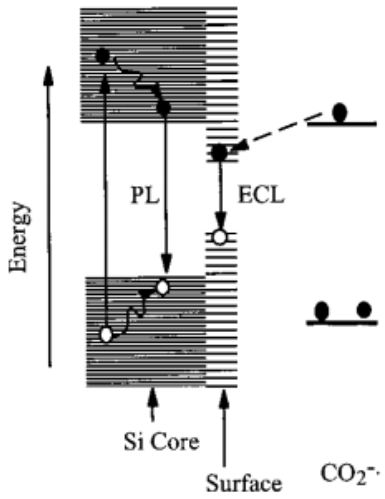

Figure 1.3.23 – Schematic representation of the mechanisms for oxalate assisted ECL and photoluminescence (PL) of SiNCs. The emitting states are different: the core is responsible for the PL, while surface states for the ECL. From reference [54]. Reprinted with permission from AAAS.

Despite the rising interest for sensing applications,[48,53,160–162] the ECL of silicon nanocrystals was investigated only in few studies[163,164]. The behaviour of chromophore functionalised SiNCs was examined during my research period.[165]

1.4. Applications of Silicon Nanocrystals

Due to the properties of the composing element, their unique optical features and the possibility to functionalise them with different types of molecules through stable covalent bond, silicon nanocrystals have been considered interesting materials for different applications.[47,53] Among them it is worthy to recall photovoltaic systems,[166–168] in which silicon nanoparticles act as the active material responsible for the absorption of light, the charge separation and their injection in a conductive circuit (conversion of light in electric energy). Some solar cells take also advantage of the *multiple exciton generation*: if a photon of energy equal or superior to 2 times the energy band gap, two excitons can be formed, thus increasing the efficiency of the cell.[123,169,170] Moreover, silicon quantum dots have also been exploited for the opposite process, i.e. the conversion of electric energy to light, in light-emitting diode devices (LEDs)[19,171,172] or lasers.[173–175] Other interesting applications were proposed, for instance catalysis,[21,176,177] sensing[160–162,178] and quantum computing.[179,180]

Anyway, this chapter will focus mostly on two kinds of applications: luminescent solar concentrators and bioimaging which were the main purposes of the SiNCs synthesized during my PhD programme.

1.4.1. Luminescent solar concentrators

The first time luminescent solar concentrators (LSCs) were proposed was in the Seventies.[181–183] The aim was to suggest a cheaper alternative to traditional solar panels. LSCs consist in luminophores that are embedded in a thin sheet of a material characterised by a high refractive index, such as poly(methylmethacrylate) or glass. The luminophore should absorb efficiently the solar light and emit it at wavelengths at which conventional photovoltaic cells are characterised by high efficiency of power conversion. Due to the particular structure and optical properties of the host sheet, which acts as a waveguide, the emitted light undergoes a total internal reflection and is directed mostly towards the edges of the layer, instead of the faces (as shown in Figure 1.4.1).

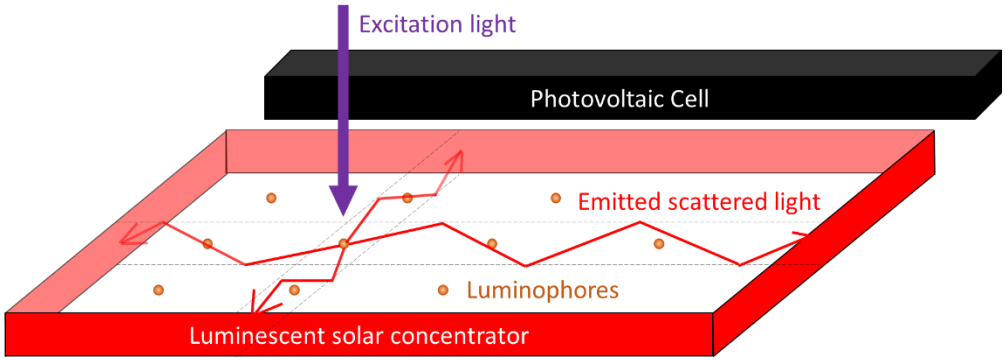

Figure 1.4.1 – General scheme of a luminescent solar concentrator.

If small area, band gap matched, and highly efficient conventional photovoltaic cells are put in contact with the borders of the LSC, the directed emitted light can be collected and converted into electricity. The main idea is that the LSCs could be installed in buildings' facades acting as *solar harvesting window*.[184–187]

Among the typical luminophores, silicon nanocrystals seem to be suitable for the purpose, because of their apparent large Stokes Shift due to the indirect band gap of silicon (see Paragraph 1.3.2 for further details). This fact permits to avoid the re-absorption of the emitted photons typical of organic fluorophores, which lowers the efficiency of the LSC[188] and allows to maintain an uncoloured device (which is useful, if the aim is to obtain a window).

Therefore, many studies focussed on LSCs made of SiNCs.[189–191] Amid them, also our group exploited this application, and the synthesis of the nanocrystals was developed and ameliorated during my research.[106]

1.4.2. Biomedical applications and bioimaging

Before proceeding with the writing of this thesis, I feel obliged to dedicate part of this introduction to nanomedicine, being a PhD candidate in Nanoscience for Medicine and the Environment myself.

"Nanomedicine" can be defined as the application of nanotechnology to medicine.[192] It aims to use the properties, physical and chemical characteristics of nanomaterials for the diagnosis and treatment of diseases at the molecular level.[193] With respect to conventional medicine that takes advantage of low molecular weights agents, nanomedicine shows undoubted benefits.[194] First of all, nanoparticles can be used as carriers for contrast agents or pharmaceutical molecules, protecting the

payload from premature clearance, enzymatic degradation, and/or exposure to potentially harmful physiological conditions. Moreover, due to the possibility to functionalise their surface with specific markers, nanoparticles can improve the biodistribution and target site accumulation of drugs and imaging agents, enhancing the *in vivo* efficacy of diagnostic and therapeutic interventions and reducing the incidence and intensity of side effects.[195,196] Furthermore, nanoparticles, if properly engineered, can overcome the typical biological barriers (e.g. the reticulo-endothelial system, i.e. the cells belonging to the immune system of the patient, or the blood-brain barrier) which are known to hinder the efficacy of several pharmaceutical molecules or contrast agents. Nanomedicine is also believed to ameliorate the existing techniques, because it allows to combine diagnostic techniques either with other ones (i.e. multi-modal imaging) or with therapeutic ones (theranostics). What renders this science so interesting is its interdisciplinarity: engineers, physicists, chemists, biochemists, biologists, clinicians, and toxicologists work together sharing their knowledge.

Regarding the diagnostic techniques, nanoparticles, and in particular quantum dots, due to their appropriate optical properties, have been investigated for biosensing and bioimaging.[25,197,198]

Bioimaging is defined as the ensemble of techniques used to acquire, process and visualize structural or functional images of living objects or systems.[199] It can operate on cell lines (*in vitro*) or in a body (*in vivo*). Several well-known bioimaging techniques are magnetic resonance imaging (MRI), positron emission tomography (PET), computed tomography (CT), ultrasound (US), optical imaging (OI), *et cetera*. In OI, the light is the investigational tool; luminescence imaging is a particular type of OI in which the emitted light from a contrast agent present in a tissue or organ is detected in order to accomplish the diagnosis.[200–203] Therefore, it is understandable why quantum dots have been proposed as devices for optical imaging: their colour-tuneable emission and photostability renders them optimal contrast agents. However, as stated previously, many concerns are rising due to their toxicity.

Silicon nanocrystals seem to be a valid alternative to conventional quantum dots for biomedical applications.[204–208] Many studies have been addressed on the harmfulness and pharmacokinetics of SiNCs both *in vitro* and *in vivo*. Besides there is no universal agreement on this topic, SiNCs are assumed to be essentially a

biocompatible and biodegradable material.[48,57,209,210] Those assessments should be carried out considering also several factors, including (i) the size, (ii) the functionalisation of the nanocrystal and (iii) its colloidal stability in a biological environment.

Concerning the dimensions, nanoparticles with a lower hydrodynamic volume are preferred for the renal excretion, due to the filtration-size threshold in kidneys.[211] However, it is also well-known that usually smaller nanoparticles (e.g. silica or gold nanoparticles) are considered to be more toxic towards certain cells, probably because of the high surface over volume atoms ratio (see Chapter 1.2) which overexposes more reactive surface sites.[212–214]

Additionally, the functionalisation of the surface plays a key role on the cytotoxicity: amine functionalised SiNCs are shown to be less toxic than epoxy-terminated ones with respect to hepatoma cells,[215] but more toxic than carboxylic acid or dextran functionalised nanoparticles on rat or human cells.[216] This clearly means that every SiNCs batch studied for biomedical applications exhibits different behaviours towards cells and tissues and an investigation on the cytotoxicity should be performed in any case.

Obviously, a necessary requirement for *in vivo* applications is the dispersibility of silicon nanocrystals in aqueous solutions. To accomplish this, silicon nanocrystals have been encapsulated within water-soluble carriers (e.g. micelles or amphiphilic polymers).[206,217] The main issue of this approach is the formation of nanoaggregates with sizes that can exceed the renal excretion filter. Based on the possibility to functionalise silicon nanocrystals through covalent bonds (see Paragraph 1.3.1), different polar groups have been grafted onto the surface of the nanoparticles. Poly(ethylene glycol),[102,104,132,218] poly(acrylic) acid,[219,220] carboxylic acids,[101,221,222] sugars[223,224] and amines[105,225] were tethered for this purpose, but in some cases damaging the optical properties.

On that note, the less harmfulness than cadmium-containing QDs is undoubted: in a study,[206] researchers compared the behaviour *in vitro* of Cd based quantum dots encapsulated in polymer micelles and Si nanostructures with similar surface

composition. The experiments showed a 50% cell viability (IC50) equal to 20 and 11 µg/mL for CdTe and CdHgTe, respectively, but superior to 500 µg/mL for SiNCs.

Also clearance of silicon nanocrystals is still debated: SiNCs are assumed to act as silica nanoparticles, being degraded into silicic acid and excreted rapidly through renal filtration.[226] However, other studies shows an accumulation of silicon nanocrystals in liver.[104]

The photophysical properties of silicon nanocrystals are very suitable for luminescence bioimaging.[48,53] Silicon nanocrystals are indeed characterised by a high photostability, an emission that spans the red to near infrared spectral range (therefore, the photons that most penetrate biological tissues, as seen in Figure 1.4.2), high emission quantum yields and long emission lifetimes (up to hundreds of microseconds) which are not effectively affected by dioxygen (see Paragraph 1.3.2 for further details).

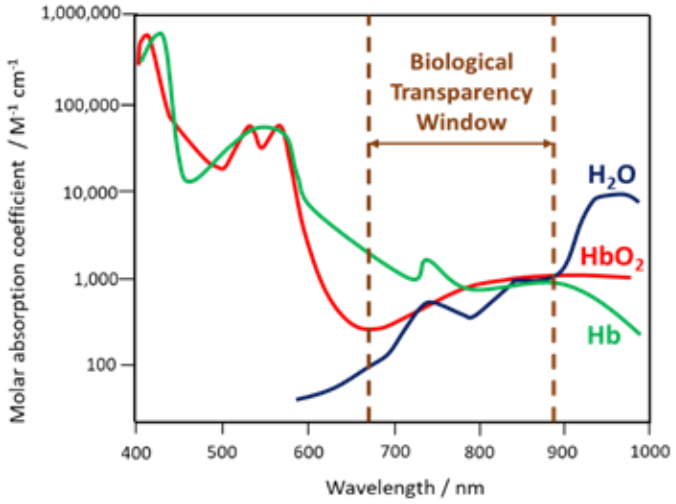

Figure 1.4.2 – Absorption profile of water and haemoglobin. The lesser absorption occurs in the red/near infrared window (in particular, approximately between 650 and 900 nm). Reprinted from the reference [227] with permission of the Royal Society of Chemistry.

This last characteristic has been extensively investigated for the enhancement of the signal to noise ratio of *in vitro* and *in vivo* bioimaging techniques thanks to the *time-gated detection*. It consists in delaying the detection of the emitted light from the sample, so that the short-lived emitting components of the biological matrix (the so-called autofluorescence) are not emitting anymore, while the luminescence of the long-lived components (SiNCs) is still present. In other words, the recorded light will be due mostly to the silicon nanocrystals, as explained by Figure 1.4.3.

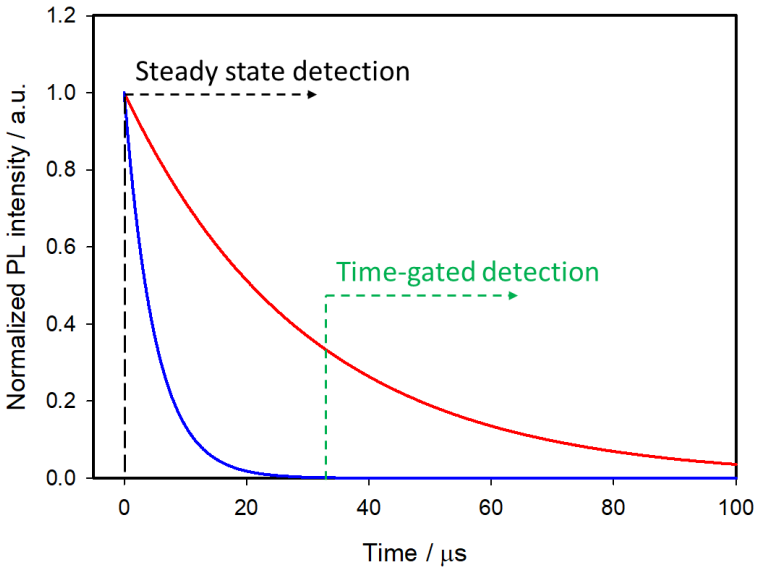

Figure 1.4.3 – Comparison between steady state (or continuous) detection and time-gated detection. A continuous detection from the excitation pulse at time = 0 includes the emission of short-living components (whose decay in time is represented by the solid blue line) and long-living ones (red line). A delayed detection is clean from the first ones.

It is a technique already used for lanthanide nanoparticles[228–230] and it has been assessed also for nanoaggregates of silicon nanocrystals for sentinel lymph node mapping[206] or cancer cells[231], porous silicon and other large silicon-based materials.[231–233] The application of small silicon nanocrystals for time-gated detection luminescence bioimaging *in vivo* and *ex vivo* was firstly reported by us.[104]

A particular technique which applies the principles of luminescence bioimaging to the therapy and for which SiNCs have been studied during my project is the fluorescence-guided surgery.

1.4.2.1. Fluorescence-guided surgery

Cancer is one of the leading causes of death worldwide. Only in 2016, in the USA, 1.6 million tumour cases and about 600,000 deaths were reported.[234] Besides chemotherapy and radiotherapy, oncologic surgery represents one of the current best operative options. The success of the operative surgery is based on the accurate removal of cancer tissue while preserving healthy tissue:[235] if the resection leaves some cancer tissue (*positive margins*), a recurrence of the tumour can occur,[201] as if some healthy tissue was removed (blood vessels, nerves…), this could lead to serious complications.[236]

The current bioimaging techniques, such as MRI or CT, despite allowing the physician to precisely screen the patient and identify or localize the cancer, do not allow a specific differentiation on tissues nor a real-time imaging during the surgery: the operation should be interrupted and the patient subject to diagnostic techniques. These modalities are expensive in time and money.[234]

Fluorescence (or *light*) *guided surgery* (LGS) takes advantage of the light emitted by fluorophores previously injected and targeting tumours to obtain a real-time visualization of the considered tissue.[237] In other words, a fluorophore is injected, it proceeds towards the tissue, the surgeon excites it with a laser and receives the emitted light which guides the operation. LGS is used also to assess the vascular flow in grafted tissues and for sentinel lymph node removal.[238–240]

So far, many IR emitters have been employed as contrast agents for LGS. This choice is due to the reduced scattering of excitation light, minimal absorption and negligible autofluorescence by tissues, affording a higher signal to noise ratio and image contrast. One of the most used molecules is indocyanine green (ICG, Figure 1.4.4),[237,241,242] an oligo-methylene chromophore emitting in NIR spectral range. It is worth noting that the surgeon must possess camera systems and detectors which are sensitive to these photons and convert them in visible light.

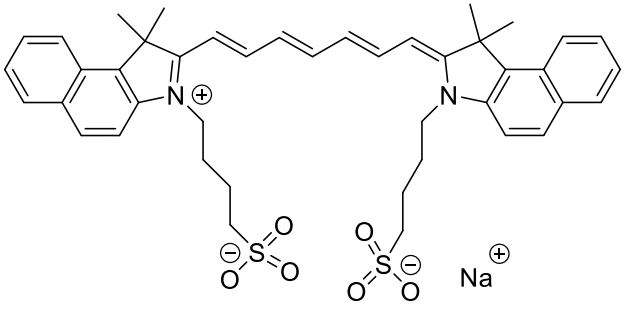

Figure 1.4.4 – Indocyanine green (ICG).

Other investigated systems are NIR-II emitters[200,243,244] (NIR-II is defined as the spectral range included between 1000 and 1700 nm) or lanthanide nanoparticles absorbing in NIR spectral window.[245–247]

Nanoparticles, in particular, have reached increasingly attention due to the possibility to target a specific tissue. They can be headed to a tumour due to EPR effect (enhanced-permeation and retention) or active targeting.[248]

EPR effect is the basis of the passive targeting of nanoparticles on tumours. Due to their high metabolic activity, tumours usually generate blood vessels that drain the nutrition from the vascular system of the host, in a process called angiogenesis. The newly generated vessels are leaky, so that the drainage can be more efficient. In this way, the circulating agents, among which the nanoparticles, can extravasate more easily in the tumour.[249]

Contrary, the *active targeting* is based on the recognition between the nanocrystal and the tumour. This is usually achieved functionalising the surface of the nanoparticle with a receptor able to tag and link biomarker overexpressed in tumour cells.

This technique has been implemented with robotic surgery (Da Vinci System®, Intuitive Surgical Inc.), using mechanical systems characterised by lasers as excitation source, cameras for the detection and operative tools equipped in robotic arms driven by a remote-controlled laparoscopic operation.

1.5. Copper Indium Sulphide (CIS) Quantum Dots: an overview

During the period I spent at the university of Leeds, and precisely at Molecular and Nanoscale Physics Laboratory under the supervision of Dr. Kevin Critchley, I got in contact with other quantum dots whose properties and applications are under study in the group I was hosted in.

Copper indium disulphide quantum dots ($CuInS_2$ or CIS QDs) are ternary I-III-VI_2 semiconducting nanoparticles which have been intensively investigated since 00s as a non-toxic and bright alternative to cadmium and lead based quantum dots.[250–252] The direct nature of their band gap allows to reach higher molar absorption coefficients and emission quantum yields with respect to indirect band gap SiNCs,[253] although several optical properties closely match silicon nanocrystals' ones, such as long emission lifetimes and an emission that covers the biological window characterised by a large Stokes shift.[254–257]

In this chapter, I will briefly consider some aspects regarding the crystallography, the synthesis, the photophysical and electrochemical properties and several applications. Part of this chapter has been reproduced or adapted from reference [227] with permission of the Royal Society of Chemistry.

1.5.1. Crystallography of CIS QDs

There are several differences between the crystallographic structures of bulk CIS and CIS QDs. Firstly, bulk copper indium sulphide, at room temperature crystallizes only in the tetragonal structure of chalcopyrite (CP, $CuFeS_2$), in which the cations occupy ordered positions. At higher temperatures, a random distribution of In^{3+} and Cu^{+} is more likely to occur and the stoichiometry of the compound becomes more flexible. Therefore, at 980 °C, CIS can achieve a zinc blende (ZB)-like structure, which is similar to CP one, but with a random swap of the cations, and at 1045 °C, an hexagonal wurtzite (WZ)-like structure.[258] The crystallographic structures are reported in Figure 1.5.1.

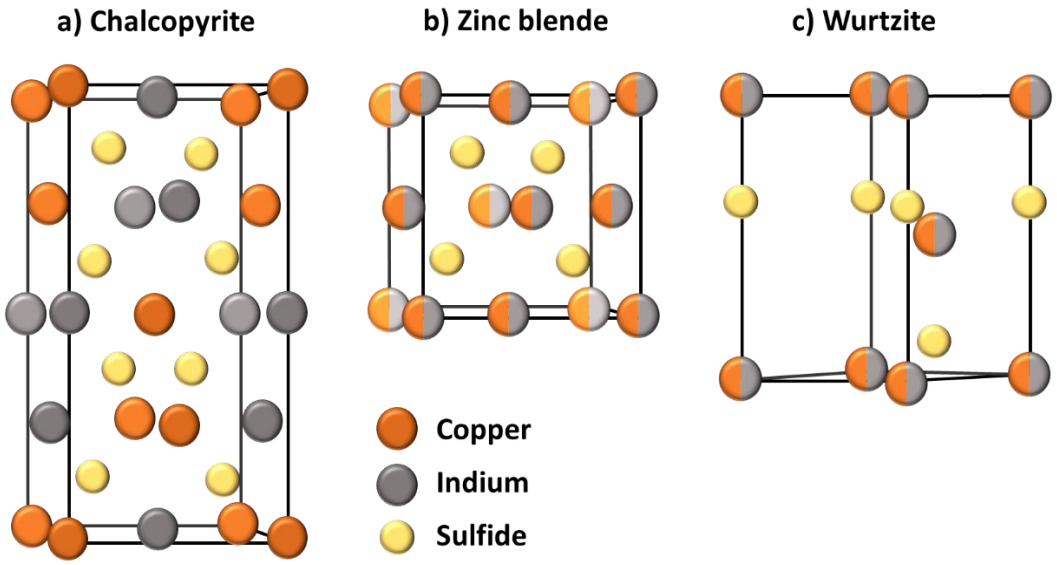

Figure 1.5.1 – Crystallographic structures of (a) chalcopyrite, (b) zinc blende and (c) wurtzite CIS.

At the nanoscale, CIS can crystallize in each structure at the same temperature, depending on the adopted synthetical methodology.[259,260] CP structure exhibits a cation ordering in which each sulphide ion is surrounded by two In^{3+} and two Cu^{+} ions (Figure 1.5.1a). Despite the atomic radii of the cations are similar (about 80 pm), the Cu-S and In-S bond lengths are quite different and this causes a tetragonal distortion of the crystal lattice. This results in a low band gap energy, an abundance of intrinsic defects and a broader emission if compared to cadmium-based quantum dots.[250,252,261] As stated before, ZB structure (Figure 1.5.1b) is comparable to CP and it is also difficult to distinguish due to their similar XRD and electron diffraction patterns. For CP and ZB structures, the displacement of the cations can lead to a non-stoichiometric CIS compound which could be useful for photovoltaic applications because of the formation of n-type and p-type nanocrystals (see Applications paragraph).[262] WZ structure (Figure 1.5.1c) is characterized by a superior order in which an anionic lattice is interlaced with domains of ordered cations sublattices.[263] The mechanism of its formation is more defined with respect to CP CIS QDs: it is well-known that CIS QDs with a WZ-like structure will grow if a Cu_2S intermediate is formed first.[264,265] However, their emissive properties are reported to be usually worse than both CP and ZB CIS QDs, and therefore this requires attention during the synthetic process, if the scope is to obtain highly emitting nanoparticles.[250]

1.5.2. General synthesis of CIS QDs and phase transfer into water

The synthesis of CIS quantum dots is usually considered challenging because of the different reactivity of the two cations with respect to the anion. As a matter of fact, according to the HSAB (which stands for "hard/soft acid/base") theory, Cu^+ is a soft Lewis acid, while In^{3+} is a hard Lewis acid. Therefore, copper has a higher affinity with S^{2-}, which is a soft Lewis base. If the reaction's conditions are not adjusted, the formation of binary copper sulphides can occur instead of ternary $CuInS_2$. To balance the reactivity of the reactants, three main strategies have been developed. The reactivity of copper and indium cations can be simultaneously adjusted by including different types of ligands in the reaction mixture, for instance thiols (i.e. soft Lewis bases, therefore stabilizing Cu^+) together with carboxylates (hard Lewis bases, to control the reactivity of In^{3+}).[35,255] As an alternative, an excess of thiol can be introduced, to accomplish the triple function of sulfur source, solvent and copper stabilizer.[257] Another option is provided by the use of a precursor containing both the cations, namely $(PPh_3)_2CuIn(SCH_3CH_2)_4$:[266,267] in the reaction mixture, its decomposition releases the same quantities of copper and indium, therefore avoiding the formation of binary compounds.

Many synthetical strategies have been reported.[251,268] These differ from each other on the type and ratio of precursors, stabilizers and conditions, allowing to obtain nanocrystals with a great variety of sizes, shapes, morphologies and stoichiometry and, consequently, optical properties. Usually, the syntheses are conducted in non-aqueous solvents, with few exceptions.[269–271] This is the reason why for biological applications, CIS QDs are usually functionalised with hydrophobic ligands during the synthesis, which provide stability in non-polar solvents, and afterwards a ligand exchange with a polar molecule is performed. Phase transfer into water can also be accomplished encapsulating the apolar quantum dot in amphiphilic polymers[272] or using inorganic ligands.[273]

Besides the high number of strategies, it is well-accepted that the methods which provide a better control over the size and shape are the hot-injection (see Paragraph 1.2.1) and heating-up procedures. One of these, which has been used and adapted by Critchley group and by different groups allowed to obtain tetragonal CIS QDs.[35,257,274]

This non-injection synthesis uses as precursors an equimolar amount of indium acetate and copper(I) iodide dissolved in 1-dodecanethiol (DDT) or 1-octanethiol, which acts both as stabilizer and reaction solvent. The reaction mixture is purged under inert atmosphere in order to remove oxygen, which could incorporate in sulphur vacancies. The flask is first heated to 120 °C to dissolve the components (the solubility can be enhanced by adding little amounts of high-boiling point molecules, e.g. octadecene). At high temperatures (ca. 180 °C), the alkanethiol molecules decompose and release sulphide ions, which provides the anions for the CIS crystal growth. Enhancing the temperature (over 200 °C), the colour of the suspension varies from yellow to dark red, indicating the nucleation and subsequent growth of the QDs (Figure 1.5.2). When the desired sizes are reached, the reaction is quenched by decreasing the temperature with a cold-water bath.[257]

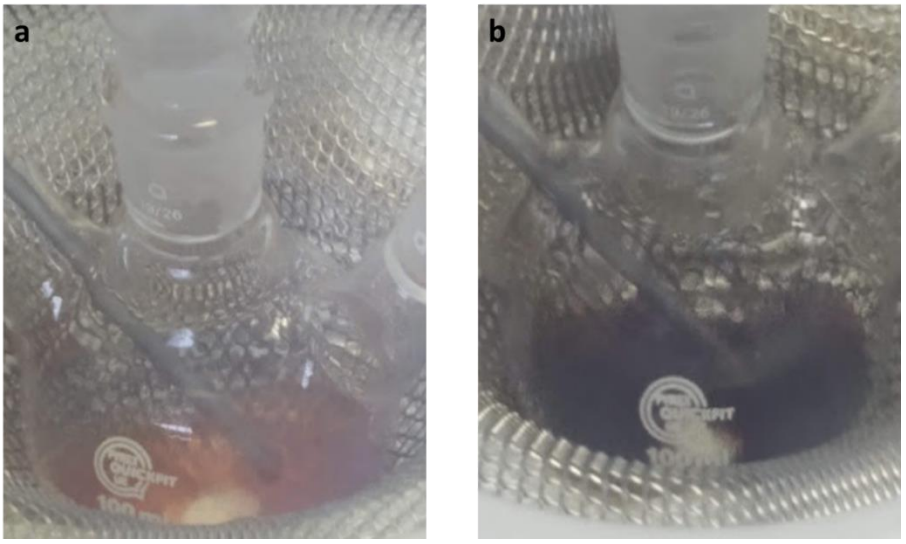

Figure 1.5.2 – Photographs of a suspension of CIS QDs during (a) nucleation at 230 °C and growth (b) at 200 °C after 25 minutes.

As it will be discussed in the next Paragraph, the formation of an alloy or a shell containing zinc can help ameliorating the optical properties of CIS QDs. Doping the QD with additional cations (as zinc,[275] silver,[276] gallium,[277] tin,[278] gadolinium,[279] *et cetera*), thus forming alloyed systems, is made possible due to the high tolerance of CIS QDs towards lattice defects and their non-stoichiometry. Usually, in the syntheses, the precursor of the extra cation is added in the reaction mixture together with copper and indium before the crystallization occurs, but it is also possible to perform a partial cation exchange on already formed CIS QDs.[280] The emissive properties of CIS QDs, as well as their chemical stability, drastically enhance by covering the nanoparticles with

a shell of a suitable semiconductor. Zinc(II) sulfide is a stable, non-toxic, semiconductor with a wide bandgap (3.5 eV), that shows a low lattice mismatch (ca. 2%) with copper indium sulfide, which permits an epitaxial growth. Zinc(II) sulfide, thanks to these properties, is one of the best choices to obtain a type-I core-shell system.[257] Despite several procedures being developed,[251] the zinc precursor is usually added to the preformed CIS QD synthesis solution and the temperature raised to 210 °C to initiate the shell formation. The temperature is typically maintained for 0.5 to 2 h. Nonetheless, it has been noticed that this reaction is also accompanied by other processes, such as the diffusion of Zn(II) into the lattice, or a partial cation exchange, which can further modify the optical properties, including a blue-shift of the emission peak.[281]

The method examined so far is performed in organic medium, and the resulting nanoparticles are stabilized by an organic hydrophobic shell. Certainly, for various applications, including bioimaging, the nanoparticles must be transferred in aqueous solutions. Several approaches allow to synthesize directly CIS QDs in aqueous phase.[282–285] In this case, the syntheses are carried out in presence of water-soluble thiol derivatives, such as thioglycolic acid, mercaptopropionic acid, thiol-derivatized poly(ethylene)glycol or glutathione. For instance, it is possible to synthesize the CIS core by mixing $CuCl_2$ and $InCl_3$ in the presence of an aqueous solution of sodium citrate and L-glutathione. Then, sodium sulfide is injected as sulfur source, while zinc acetate and thiourea are used to make the shell grow.[282] Microwave-assisted methods have also been introduced to improve the synthesis.[286]

Despite the low cost and toxicity of those methods, the so-obtained nanoparticles are reported not to possess high quality properties;[281] therefore, it is common to perform the synthesis of CIS QDs in organic phase and then transfer the nanoparticles in water.

Phase transfer could be accomplished by three main methodologies of surface modification: ligand exchange, encapsulation in amphiphilic molecules or in a silica shell.

Ligand exchange consists in replacing the original ligands stabilizing the nanoparticles in organic phase with hydrophilic organic ligands. When thiols are used as ligands during the synthesis, their replacement can occur if the substituting

molecule possesses a superior number of anchoring groups. For instance, dodecanethiol can be exchanged with dihydrolipoic acid (DHLA, 2 thiol moieties).[287] As an alternative it is possible to introduce long chain amines (such as oleylamine)[288,289] or phosphines[265] in a mixture with the thiols as stabilizers during the synthesis of the nanoparticles. The bonding between those molecules and the surface of the QD is more labile than the one with thiols. This allows to efficiently substitute them with other water-solubilizing thiols (i.e. mercaptopropionic acid) at a lower temperature. Unfortunately, ligand exchange is reported to lower the PLQY due to the reduction of the ZnS shell and consequent increase in surface trap states.

A different option consists in maintaining the apolar ligands utilized during the synthesis in the organic phase and encapsulating the nanoparticle in an amphiphilic polymer or micelles.[272,290,291] The hydrophobic groups present on the molecule interact in a non-covalent way with the apolar ligands of the QD, while the polar moieties allow a good dispersibility in water. For instance, it is reported[272] the coating of DDT capped CIS/ZnS core-shell QDs with an amphipol poly(maleic anhydride-*alt*-1-tetradecene), 3-(dimethylamino)-1-propylamine derivative, yielding water-suspendable systems stable at various pH. On the other hand, by silanisation, it is possible to realize biocompatible water-suspendable silica-embedded CIS/ZnS QDs.[274,292]

1.5.3. Photophysical properties of CIS QDs

As stated in a previous paragraph, CIS quantum dots display interesting optical properties, due to the fact that $CuInS_2$ is a direct band gap semiconductor, but certain characteristics are halfway between cadmium-based QDs' and silicon nanocrystals' ones.

Bulk CIS' band gap is 1.45 eV and the Bohr radius is about 4.1 nm. Therefore, quantum confinement effects occur at dimensions inferior to 8 nm.[251] The absorption spectrum, related to the promotion of an electron from the valence band to the conduction band, can be tuned accordingly with the size of the nanoparticle. The typical profile of the spectrum is reported in Figure 1.5.3a.[255]

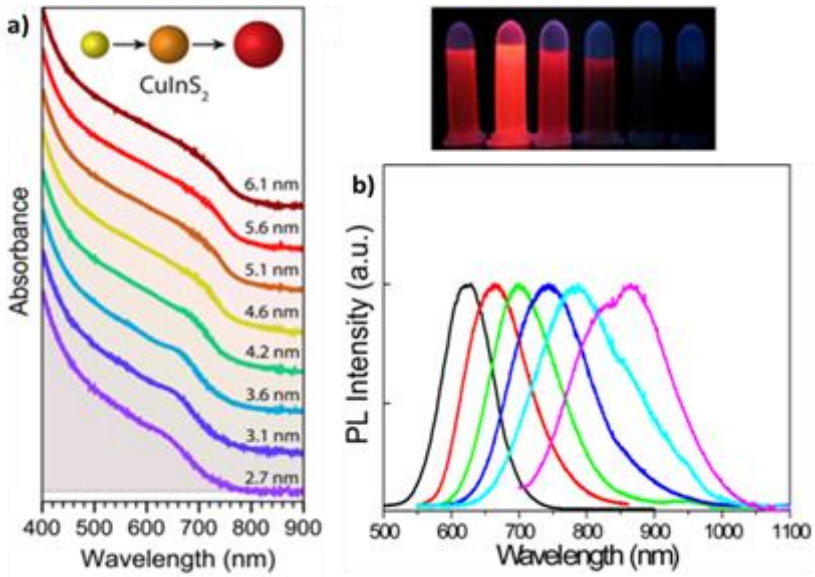

Figure 1.5.3 – (a) Absorption spectra (plus offset) of WZ CIS QDs ranging from 2.7 to 6.1 nm in size. Adapted from reference [293]. Copyright 2018, American Chemical Society. https://doi.org/10.1021/acsnano.8b03641. (b) Emission spectra (and digital photographs under UV light) of CIS QDs with different size. Reprinted (adapted) with permission from reference [256]. Copyright 2012, American Chemical Society.

Contrary to conventional quantum dots, the absorption profile does not display a sharp peak related to the transition HOMO-LUMO (compare with Chapter 1.2), but a shoulder, which could be due to inhomogeneities of the size, shape and composition of the sample. At very long wavelengths, the absorption shows tails which can be related to the contribution of intra-band states or plasmon resonance bands.[294]

Critchley *et al.* reported the determination of the molar absorption coefficient (ε) for CIS QDs or core-shell systems CIS-ZnS of different sizes.[253] In particular, they assessed this value at two wavelengths, the one corresponding to the first excitonic transition (E_1) and 400 nm (3.1 eV), yielding to the size-dependent equations described below.

$$\varepsilon_{CIS\ QD}(E_1) = (830 \pm 660)d^{3.7\pm0.6}$$

$$\varepsilon_{CIS\ QD}(3.1\ eV) = (2123 \pm 109)d^{3.8\pm0.3}$$

Following the absorption, a radiative recombination of the charges can occur, yielding the characteristic photoluminescence of CIS QDs. Unlike conventional quantum dots, however, this emission is not associated to the *band edge luminescence*. Despite there is no universal agreement about the origin of CIS QDs photoluminescence, researchers believe that it generates from intrinsic defect states in

the lattice. The main intra-band defects include copper vacancies, indium-copper anti-sites and oxygen-sulphur anti-sites. Some groups suggest this emission arises from a recombination from a donor-acceptor pair. [262,295,296] This theory is supported by the evidence that PLQY is higher for CIS QDs which are richer in indium and poorer in copper.[262]

The size-dependent emission of CIS QDs can be varied within the spectral region spanning the red to near-infrared range (Figure 1.5.3b).[256] This is an interesting feature for bioimaging applications, because it overlaps with the biological transparency window, as shown in Figure 1.4.2. Interestingly, it is possible to correlate the dimensions of the nanoparticle to the wavelength corresponding to the emission maximum thanks to an empirical formula described by Critchley *et al.* and here reported.[253]

$$d = 68.952 - 0.2136\lambda_{PL} + 1.717 \times 10^{-4}\lambda_{PL}^2$$

The emissive properties of CIS QDs show important differences with other direct band gap semiconductor nanoparticles.[252] From the emission dynamics perspective, while prototypical CdSe QDs show a lifetime of 10–30 ns at room temperature, emission decays are generally longer for ternary semiconducting nanocrystals: non-shelled CIS QDs usually display a biexponential decay,[257] with a shorter component in the range of $10^0 \div 10^1$ ns and a longer one in the order of 10^2 ns. Due to size inhomogeneities and the overlapping of various vibro-electronic transitions,[267] CIS QD emission bands are characterized by a higher FWHM (about 100 nm) when compared to conventional QDs. Further studies recently demonstrated that the preferential localization of the excitonic hole on Cu sites plays an essential role on the broadening of the photoluminescence signals.[297,298] Another considerable dissimilarity consists in usually high Stokes shifts (200-300 meV), caused by the presence of different electronic states involved in absorption and emission, which diminishes the probability of reabsorption.[299] Interestingly, the optical properties can be tuned not only by varying the nanoparticle size, but also modifying the composition and the metal-to-metal stoichiometry of the compound.[250] A blue-shift of both absorption and emission spectra occurs when decreasing the ratio [Cu]/[In].[282] Also, an increase of the band gap was reported. This was attributed to the strong contribution of Cu 3d-orbital to the valence band: a Cu deficiency results in a lowering of the occupied levels,[300] while

an enhancement of PLQY is observed (up to 30%)[252]. The dependence between PLQYs and [Cu]/[In] ratios relies on donor-acceptor pair luminescence mechanisms and the introduction of defects responsible of radiative decays.[262]

The PLQY drastically increases when CIS QDs is shelled with a higher band gap semiconductor (i.e., a type I core-shell QDs). For CP CIS QDs, PLQY is reported to enhance from 5-10% to ca. 70% with a ZnS shell,[257] and usually the short-lived emitting component is not detected. These aspects are connected with the suppression of surface states that act as trap for the charge carriers, either reducing the yield of radiative recombination *via* thermal decays or providing an alternative radiative relaxation path characterized by shorter lifetimes. Another consequence of a ZnS shell growth is the shift of the photoluminescence band at lower wavelengths. This effect is more pronounced with respect to Cd-based type I core-shell QDs (*e.g.*, for CIS/ZnS core/shell, the blue shift is 130 nm compared to the CIS emission, Δ=335 meV) and it is associated to the interdiffusion of Zn^{2+} into the core or a cation exchange.[301] Absorption and emission spectra can also be tuned in the Vis/NIR range by alloying CIS QDs with other semiconductors and elements, including Ag, Al and Zn.[302–304,305]

Copper indium sulphide quantum dots were also demonstrated to display an efficient electrochemiluminescence if paired with co-reactant (for example, TrPA) or moreover with an annihilation mechanism.[306] As reported for other quantum dots,[54] this emission is slightly red-shifted if compared to photoluminescence, because it is believed to originate from surface states.

The presence of defect and therefore of the shell has many repercussions in the different applications CIS QDs can achieve, as reported in the next paragraph.

1.5.4. Applications of CIS QDs

Among the numerous applications of CIS QDs, the most promising are photocatalysis, solar energy conversion (e.g. solar cells and luminescent solar concentrators), electroluminescent devices (LEDs) and bioimaging.[227,307] It is worth noting that several applications, such as LEDs and bioimaging, require high emission quantum yields, while other (solar cells and catalysis) need a good charge transport. This is important to be considered while synthesizing CIS QDs. As a matter of fact, the presence of a protecting shell undoubtedly enhances the PLQY, but could be

detrimental for charge separation; moreover, defects in the nanocrystal structure can disrupt the propagation of charge-carriers, while it is also well-known that defect-free nanoparticles are less luminescent (see Paragraph 1.5.3).[255,257]

Concerning photocatalysis, CIS QDs seem to be very appropriate, due to the high molar absorption coefficients in the visible spectral region. CIS QDs and CIS@ZnS QDs were studied for the photoinduced water-splitting and the generation of hydrogen.[308,309] Those nanocrystals were also evaluated as photosensitizers for TiO_2 nanoparticles in the process of degradation of organic pollutants: following the absorption of visible light, an electron passes from the conduction band of CIS QD to TiO_2, while the hole remains in the valence band of CIS. The electron drives the reduction of oxygen into superoxide and the hole the oxidation of water into OH radical. Both species can oxidize organic compounds.[310,311]

Solar cells based on CIS QDs, unfortunately, do not display high efficiencies, especially because of the natural presence of defects.[312,313] CIS QDs were introduced as inks for thin-film devices[314] or as dyes in DSSC (dye-sensitized solar cells).[315] Better results were obtained covering the surface with a CdS shell but suppressing the advantage of using non-toxic materials.[316] Concerning the solar energy conversion, CIS QDs can be very suitable emitters for luminescent solar concentrators (see Paragraph 1.4.1 for further details). In fact, like SiNCs, they can take advantage of a large Stokes shift, which prevents the reabsorption and allow to obtain a good transparency. The high molar absorption coefficient and PLQY (especially with a shell), render them more promising that Cd-based LSCs.[184,317,318]

The high Stokes shift is also important for electroluminescent devices. In contrast with other semiconducting nanoparticles, such as Si and Ge, CIS QDs show an efficient electroluminescence.[251] Despite the broad emission peak could not be considered suitable for high colour purity devices, this is interesting for producing white LEDs, where CIS QDs are used as light converter while paired with blue-emitting phosphors.[319] White LEDs were also obtained changing the ratio between copper and indium.[320]

Due to their peculiar properties, which make them similar to silicon nanocrystals, CIS QDs seem to be a valid alternative to Cd counterparts for bioimaging applications:

the low toxicity, the high photostability, PLQY and absorption, an emission that lays in the so-called biological window and long emission lifetimes (which can enable the time-gated detection, see Paragraph 1.4.2) are surely best appropriate for *in vivo* applications.[227,321] With respect to SiNCs, CIS QDs show also a good two-photons absorption, which overcomes the problem of the excitation in biological tissues.[280] The main applications were conducted for the targeting and visualization of tumour cells in mice,[251] sentinel lymph node[322] and vaccine tracking.[323] Multi-modal imaging was achieved coupling the nanoparticles with paramagnetic ions and the optical imaging with magnetic resonance imaging[324] or doping $CuInS_2$ with the radioactive isotope Cu-64 for positron emission tomography or Cherenkov energy transfer.[284] Theranostics was fulfilled by drug release[325,326,327] or phototherapy[328,329] coupled to optical imaging. A comprehensive study of the bioimaging applications of CIS QDs can be found in a review written by us.[227]

2. Functionalisation of Silicon Nanocrystals with acetylides

2.1. Introduction

In Paragraph 1.3.1, the advantages of the hydrosilylation in the presence of a radical initiator such as diazonium salts have been explained. The passivation with chlorosilanes, moreover, adds important benefits, especially in the chemical yield of functionalisation with chromophores.

If the reader imagined functionalising hydride-terminated SiNCs with only chromophores, he should assume that the steric hindrance of the organic molecules cannot allow an overall passivation of the surface. This could lead to a scarce dispersibility and an oxidation of the nanoparticle. This is the reason why in order to produce a light-harvesting antenna, the direct hydrosilylation with chromophores was always accompanied by the passivation with less hindered alkenes (e.g. dodecene) in a multicomponent one-pot reaction.[74,76]

It appears clear that this reaction is competitive between the two different alkenes, i.e. the chromophore and the "capping" alkene. Because of the steric hindrance, the efficiency of direct tethering of the chromophore will be inferior, and a lower amount of it will be attached to the surface of the nanoparticle (with a consequent waste of reagent).

A first passivation of the surface with chlorosilanes can overcome the issue: chlorosilane-passivated silicon nanocrystals are made react with the chromophore-containing nucleophile. The addition of the "capping" ligand can occur in a second time, being the surface already stabilised by the chlorosilane shell. In this case, the competition between the two molecules does not occur and the number of chromophores linked is higher with respect to the direct hydrosilylation (see Figure 2.1.1).

During my Bachelor's Degree Thesis project, I was able to synthesise silanols containing pyrene units and dodecyl(dimethyl)silanols respectively as the nucleophilic chromophore and the "capping" nucleophilic agent to add in a second stage. The subsequent reaction with 3 nm chlorosilane-passivated silicon nanocrystals yielded

light-harvesting systems with 13 units of pyrene (compared to the 6-8 units reported in the competitive approach[74]). This methodology was abandoned due to the scarce reaction yield for the production of silanols. Moreover, an alternative of pyrene was searched, due to the formation of excimers which reduces the efficiency of energy transfer to the nanocrystal.[75]

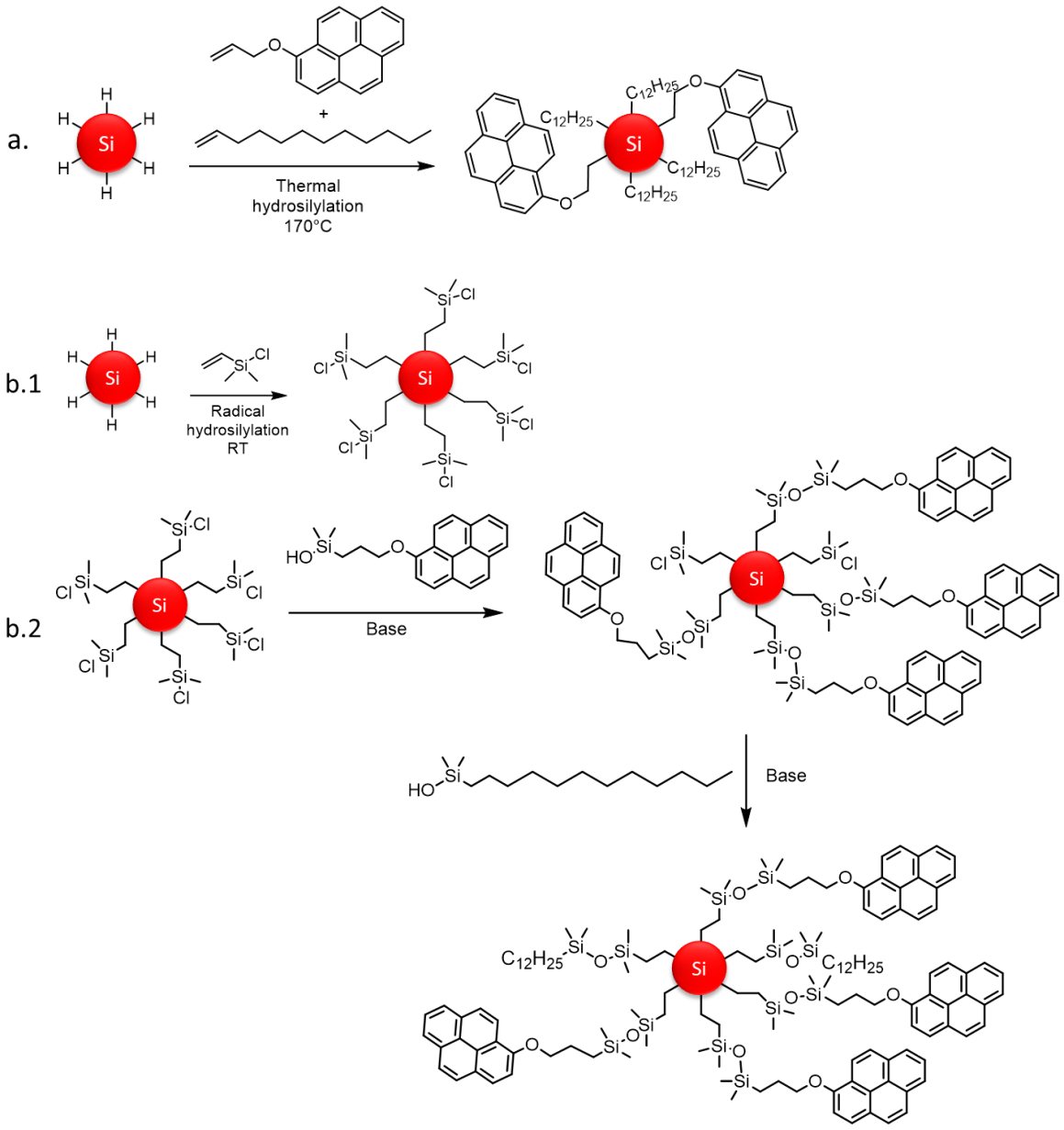

Figure 2.1.1 – (a) Competitive direct hydrosilylation of H-SiNCs with chromophores and capping alkene compared to post-functionalisation after (b.1) passivation of H-SiNCs with chlorosilanes and (b.2) subsequent addition of chromophore (here, pyrene silanol) and capping ligand (dodecyldimethylsilanol). The second approach allows to link a higher number of hindered fluorophores. The representations are simplified and do not comply with the scale proportions. From now on, only few ligands per nanocrystal will be drawn.

A more efficient approach consists in making chlorosilane-passivated SiNCs react with acetylides, i.e. deprotonated terminal alkynes. It is known that the C_{sp}-H is acidic towards strong bases such as lithium diisopropylamide (LDA)[330] and n-butyllithium (nBuLi)[331] with a pKa included in the range between 18 and 23.[332] The synthetic approach of functionalising chlorosilane-passivated SiNCs with acetylides was studied during my Master's Degree Thesis project and ameliorated in the first months of my PhD studies. The contents of this chapter have been reprinted and adapted with permission from reference [106]. Copyright 2019, American Chemical Society.

2.2. Results and Discussion

The first considered alkynes were 1-octyne and ((propargyloxy)methyl)diphenylanthracene (IUPAC name, 9-phenyl-10-(4-(prop-2-yn-1-yloxy)phenyl)anthracene, see Figure 2.2.1). Diphenylanthracene (DPA) was chosen as an alternative chromophore to pyrene due to the non-planarity of the molecule which cannot enable the formation of excimers.

The two alkynes were tested for the functionalisation of two different 4 nm sized SiNCs, i.e. octyne functionalised (Si-octyne) and DPA functionalised ones (Si-DPA), to compare the photophysical properties of nanoparticles linked to optically inactive ligands or chromophores. The synthetical approach for the synthesis of DPA bearing a terminal alkyne moiety is reported in the Experimental Section.

The first tests were conducted producing the acetylide in the presence of LDA in THF, followed by the addition of chlorosilane-passivated silicon nanocrystals, in inert moisture-free conditions. This approach was not efficient and therefore we decided to use a stronger base, nBuLi.

Moreover, the reaction's conditions were also modified in order to achieve a higher yield: the chosen solvent was dry toluene, the alkyllithium was activated by the addition of freshly distilled N,N,N',N'-tetramethylethylenediamine (TMEDA); the equivalents of reagents were increased by a 1.5-fold factor; the times and temperatures of the reaction steps were adapted in order to enhance the efficiency of the acid-base reactions and the nucleophilic substitutions between the acetylide and the chlorosilanes. Anyway, the chemical yields were scarce and an aggregation of SiNCs was observed.

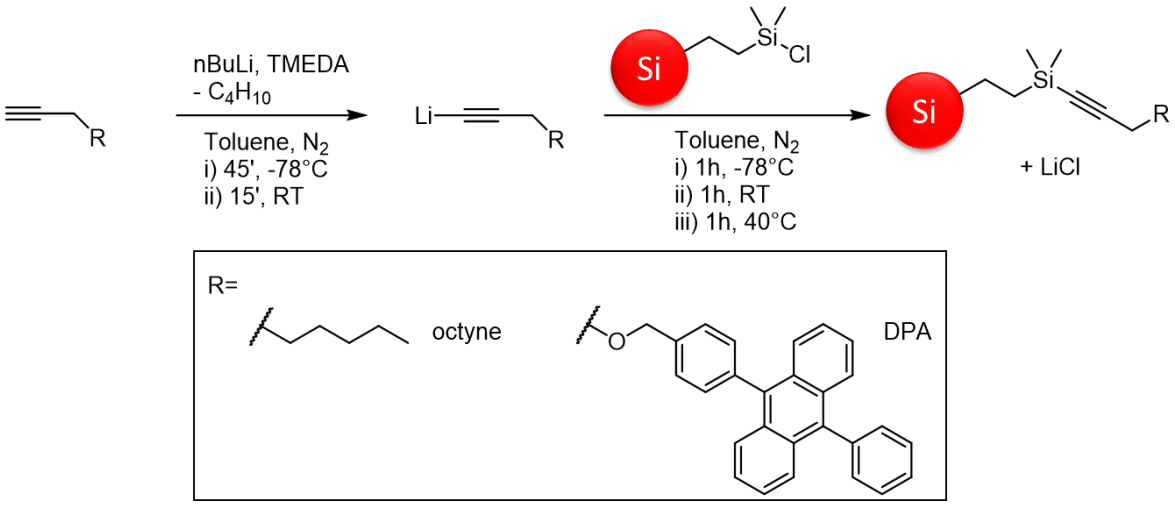

Figure 2.2.1 – Reaction scheme of the functionalisation of chlorosilane-passivated SiNCs in the presence of acetylides (i.e. 1-octyne or ((propargyloxy)methyl)diphenylanthracene).

A possible explanation to this could be due to the poor capping ability of the acetylides towards the SiNC's surface due to their weak nucleophilicity. This means that at the end of the reaction, several chlorosilanes are still present on the shell. In the presence of moisture and alcohols introduced during the work-up, chlorosilanes react yielding silanols or silyl ethers and hydrochloric acid. Being those species labile and unstable, they can react with each other forming siloxane bridges. This condensation leads to the aggregation and the precipitation of the nanoparticles (Figure 2.2.2).

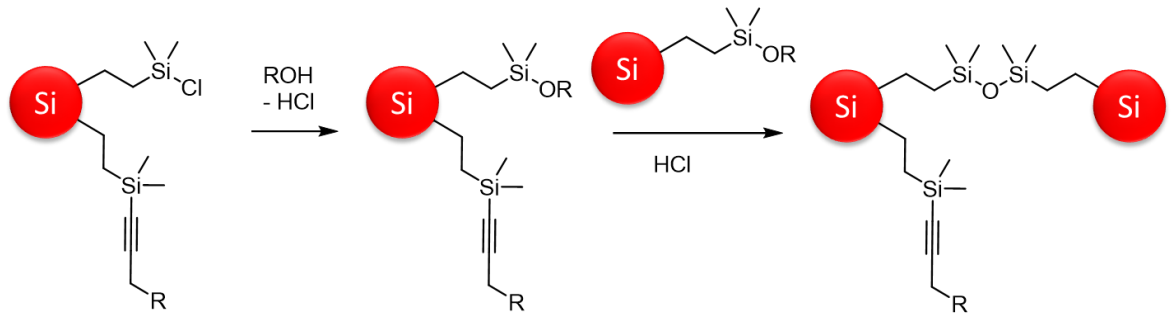

Figure 2.2.2 – Hypothetical mechanism of aggregation of poorly capped SiNCs.

This is the reason why we decided to add a further passivation step. At the end of the reaction, a nucleophilic reagent was added and let react overnight to complete the capping of the non-reacted chlorosilanes. This strategy was accomplished by adding a Grignard reagent (e.g. vinyl magnesium bromide in THF solution) or nBuLi (in the presence of a higher amount of TMEDA) in dry toluene at -78 °C. The so-obtained Si-DPA were characterised and used for the realization of LSCs[106] or studied as ECL emitters (see Chapter 6).[165]

An important characterisation technique used to assess the presence of ligands attached onto the surface of a nanoparticle is ^{1}H-NMR. The signals of the protons of the linked molecule appear broader than the detached one, as it is possible to see from Figure 2.2.3. This is due to a longer relaxation time caused by the hampered motions of the ligands grafted to the nanocrystal's surface.[105,106,109]

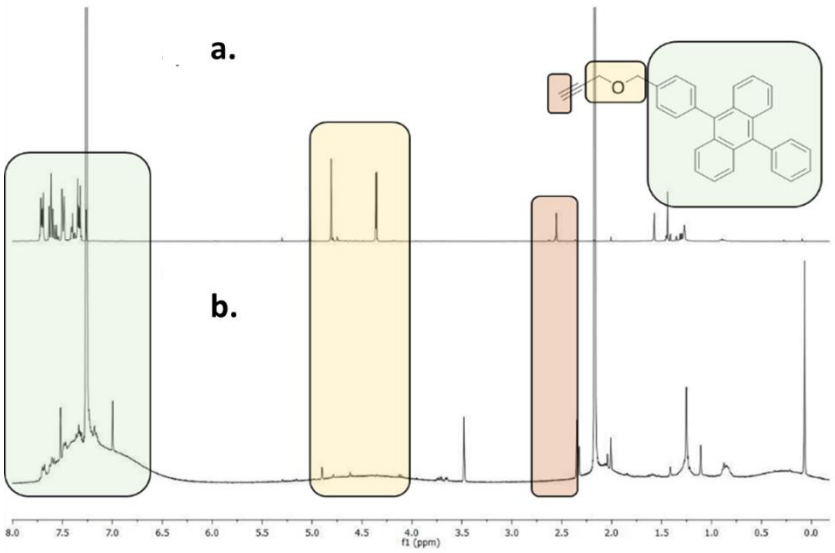

Figure 2.2.3 – ^{1}H-NMR spectra (400 MHz, $CDCl_3$, RT) of a) DPA, and b) Si-DPA.[106]

Photophysical characterisation is another useful tool to gain a deeper understanding of the systems. The absorption and emission spectra of Si-DPA, compared to dodecyl-passivated silicon nanocrystals in presence (Si+DPA) and in absence (Si) of detached DPA of the same concentration, are reported in Figure 2.2.4.

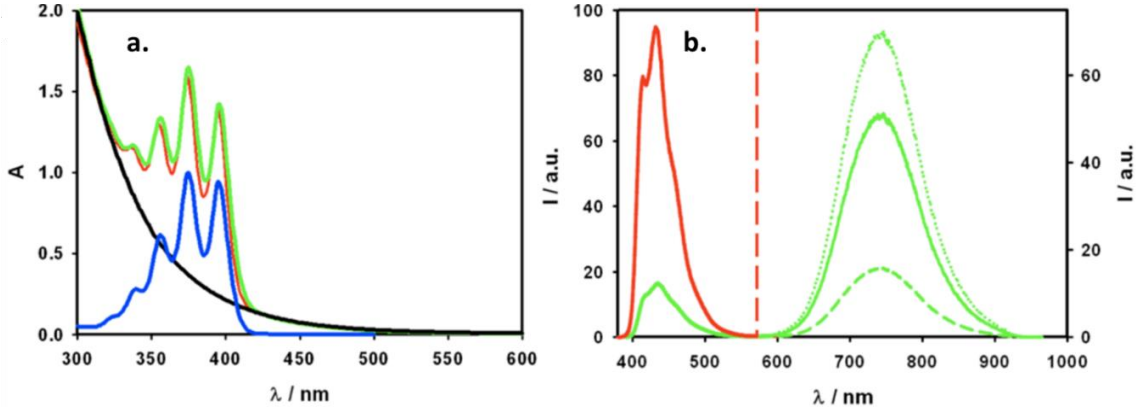

Figure 2.2.4 – (a) Absorption spectra of Si (black line), Si-DPA (green line), DPA (blue line), and a physical mixture of Si and DPA (Si+DPA, red line) with the same concentration as that of the covalent sample. (b) PL spectra of Si-DPA (green solid line, λ_{exc} = 375 nm) and Si+DPA (red line, only DPA contribution, λ_{em} = 390–580 nm) of two isoabsorbing solutions at the excitation wavelength of 375 nm. For comparison, the PL spectra of Si-DPA corresponding to 100% energy transfer (dotted green line) and 0% energy transfer (dashed green line) are reported. The samples are in air-equilibrated toluene.[106]

The absorption spectrum exhibits the typical featureless absorption of the silicon core gradually increasing in the UV region, as observed for the Si sample, plus the structured and sharp band of the diphenylanthracene chromophore limited to the UV-A region. The overall spectrum perfectly matches the one of the control sample constituted by a physical mixture of Si and DPA (Si+DPA, red line) with the same concentration, suggesting that no ground state interaction is affecting their optical properties. On the basis of the molar absorption coefficients of DPA ($\varepsilon_{375\ nm} = 1.4 \times 10^4$ M^{-1} cm^{-1}) and SiNCs ($\varepsilon_{430\ nm} = 1 \times 10^5$ M^{-1} cm^{-1} for 4-nm sized nanoparticles)[106], we can estimate an average number of about 80 DPA fluorophores per SiNC (see Appendix A.1 for further details about the computations), resulting in a strong enhancement of the absorption properties of the Si-DPA upon excitation in the $\lambda = 350–400$ nm region. Upon excitation at 375 nm, where most of the light (80%) is absorbed by DPA chromophores in the Si-DPA sample, two emission bands are observed (green line in Figure 2.2.4b): one structured-band centred at 440 nm and the other at about 750 nm. The high energy band is assigned to the diphenylanthracene fluorescence and the low energy band is due to the Si core emission, by comparison with the PL spectra of DPA and Si. Indeed, the band centred at 440 nm is observed also in the control sample Si+DPA, the lower intensity of DPA band in the covalent sample being due to a quenching process. The quenching efficiency is estimated to be 82% and it is due to a photoinduced energy transfer from diphenylanthracene to the Si core, as demonstrated by the sensitization of the Si core emission at 750 nm.

Indeed, a close match of the excitation spectrum performed at the SiNC emission ($\lambda_{em} = 750$ nm) and the absorption spectrum of Si-DPA is observed (Figure 2.2.5). The sensitisation efficiency is estimated to be 70% (see Appendix A.2), pointing to a very efficient energy transfer. The PL quantum yield (PLQY) of the SiNCs in the Si-DPA sample is measured upon selective excitation of the Si core at 460 nm: the resulting value is 26%, while the photoluminescence lifetime is 50 μs.

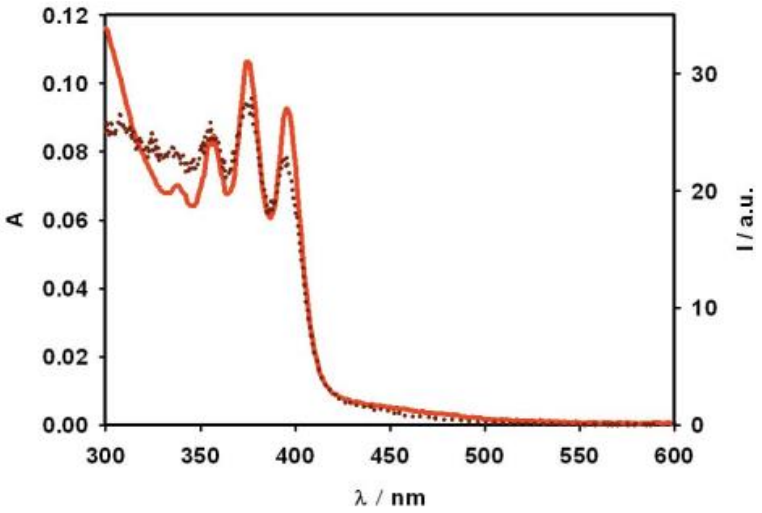

Figure 2.2.5 – Absorption spectrum (solid line) superimposed to excitation spectrum (dotted line, recorded at λ_{em} = 750 nm) of Si-DPA in air-equilibrated toluene.[106]

2.3. Conclusions

The biggest challenge in functionalizing SiNCs with chromophores, in order to ameliorate the optical properties of the quantum dot, is the competitive reaction between the hindered conjugated molecule and the capping ligand. This issue can be overcome by subsequent reaction of the fluorophore with the reactive groups exposed on the surface of the quantum dot, followed by the addition of the alkyl chain. We have proved that the best way to accomplish this is to firstly passivate the surface of the SiNCs with an electrophilic chlorosilane shell and to make it react with an acetylide derivative of the chromophore (e.g. diphenylanthracene). The final capping of the unreacted chlorosilane moieties is performed by the addition of nBuLi. The efficiency of this approach is verified by the higher number of attached fluorophores (80 on 4-nm SiNCs) if compared to the previously reported competitive strategy (60 on 5-nm SiNCs[74]).

Moreover, we found that DPA is a good choice as a chromophore to be linked onto SiNCs' surface. The high sensitization yield (70%) assessed also by excitation spectra shows the formation of a highly efficient light-harvesting antenna. The resulting system proves to be interesting for a variety of studies about the energy transfer dynamics,[333] and for various applications, from the conversion of solar light into electricity (in luminescent solar concentrators, see Figure 2.3.1),[106] to electrochemiluminescent devices (see Chapter 6).[165]

Figure 2.3.1 – From the left side, digital pictures of luminescent solar concentrators based on alkyl-passivated SiNCs, a physical mixture of SiNCs and diphenylanthracene, diphenylanthracene functionalised-SiNCs and diphenylanthracene, under 365-nm UV light.

2.4. Experimental Section

2.4.1. Materials and methods

All reagents were purchased from Sigma-Aldrich and used without further purification if not stated otherwise. Dry toluene was obtained via distillation over calcium chloride under nitrogen atmosphere. N,N,N',N'-tetramethylethylenediamine was refluxed over fresh KOH and distilled under nitrogen.

2.4.2. Synthesis of Si-DPA

2.4.2.1. Preparation of oxide-embedded SiNCs

Polymeric hydrogen silsesquioxane (HSQ) was prepared from $HSiCl_3$ following reported procedure,[82] dried under vacuum and transferred into a tube furnace. After purging with forming gas (95% N_2, 5% H_2), the tube furnace was heated to 1100 °C at a heating rate of 18 °C/min and then held at that temperature for an hour. The resulting dark solid was cooled to room temperature, manually reduced into brown powder using mortar and pestle and then transferred to a glass vial half filled with high-purity silica beads and mechanically shaken overnight with a vortex. The resulting homogeneous powder was stored in glass vials until further use.

2.4.2.2. Synthesis of hydride-terminated silicon nanocrystals (H-SiNCs)

Hydride-terminated silicon nanocrystals were liberated from the silica matrix through HF etching: 300 mg of oxide-embedded silicon nanocrystals were dispersed in a mixture composed of 3 mL of ethanol, 3 mL of bi-distilled water and 3 mL of a 49% solution of aqueous HF (Note: HF is lethal, handle it with extreme caution). The mixture was stirred for 1h and 30 minutes under ambient light at room temperature. The nanocrystals were extracted with toluene (3x10 mL) and then centrifuged three times in toluene (8000 rpm for 5 minutes). The nanocrystals were then transferred in a dry box.

2.4.2.3. Passivation with chloro(dimethyl)vinylsilane or dodecene

The nanocrystals were dispersed in 4 mL of dry toluene and separated in two 8 mL vials. Two milligrams of 4-decyldiazobenzene tetrafluoroborate (about 6 μmol) were added in each one. Afterwards, in a vial, 200 μL of chloro(dimethyl)vinylsilane (1.5 mmol) were introduced to obtain chlorosilane passivated silicon nanocrystals. In the other vial, 330 μL of 1-dodecene (1.5 mmol) were dropped, to passivate the nanocrystals with an alkyl chain. Both mixtures were stirred overnight at RT. The mixture of chlorosilane-passivated SiNCs was then filtered, concentrated at rotary evaporator, transferred again in the dry-box and diluted in 2 mL of dry toluene. The suspension of dodecyl-passivated nanocrystals was precipitated in an anti-solvent (methanol), was centrifuged three times washing with methanol. The precipitate was readily dissolved in 2 mL of toluene.

2.4.2.4. Synthesis of (4-(10-phenylanthracen-9-yl)phenyl)methanol

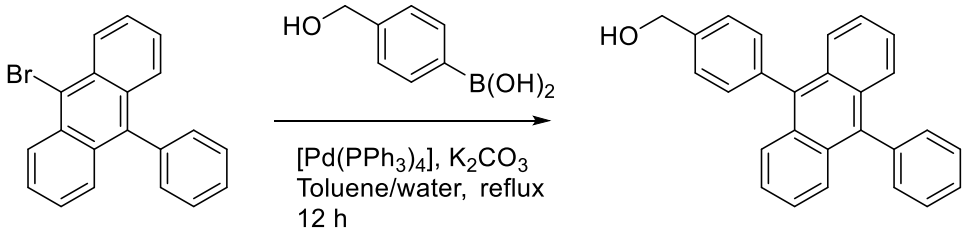

Synthesis of (4-(10-phenylanthracen-9-yl)phenyl)methanol was performed via Suzuki-Miyaura reaction conditions between 9-bromo-10-phenylanthracene and 4-(Hydroxymethyl)phenylboronic acid. To a suspension of degassed toluene (50.0 mL) and K_2CO_3 (12 mL of a 1.6 M solution), under nitrogen atmosphere, 9-bromo-10-phenylanthracene (1.7 g, 5.1 mmol), boronic acid (6.12 mmol, 1.2 equiv.) and a catalytic amount (1.5% m/m) of $[Pd(PPh_3)_4]$ were added. The resulting mixture was heated at 90 °C overnight, then cooled to room temperature, and solvents were removed under reduced pressure at 40 °C. The crude was purified via flash chromatography using toluene as eluent and applying a gradient with ethyl acetate to a final ratio of 70:30 (toluene:ethyl acetate). The product was recovered as pale yellow solid after evaporation of solvents, with a yield of 50%. GC-MS (EI): m/z 360.40.

^{1}H-NMR ($CDCl_3$, 400 MHz): 7.6 – 7.4 ppm (17 H, m); 4.90 ppm (1 H, s); 4.71 ppm (2 H, s).

2.4.2.5. Synthesis of 9-phenyl-10-(4-((prop-2-yn-1-yloxy)methyl)phenyl)anthracene

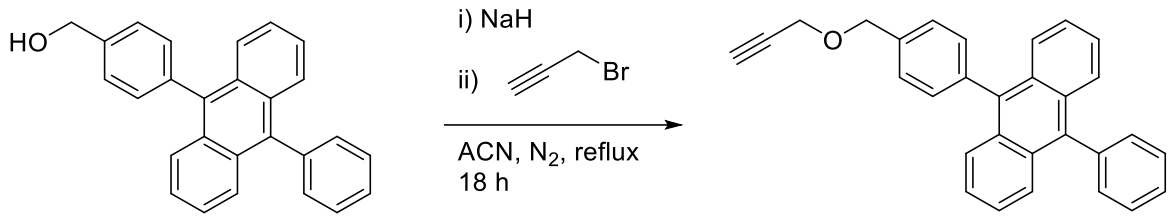

In a two-necked 100 mL round-bottom flask, under nitrogen atmosphere, 75 mL of acetonitrile were introduced to dissolve 1.4 g of (4-(10-phenylanthracen-9-yl)phenyl)methanol (4 mmol). Later, 290 mg of NaH 95% (12 mmol; *note*: sodium hydride reacts violently with moisture, must be handled under inert atmosphere) were introduced, and the mixture was heated to 78 °C. A solution of propargyl bromide (80% in toluene, 1.1 mL, 12 mmol) was added dropwise, and the mixture was stirred at reflux overnight. The reaction was quenched with water (100 mL) and then extracted with DCM (3x100 mL). The organic fraction was collected and dried over $MgSO_4$. A flash chromatography (toluene as eluent phase) was performed to isolate 0.96 g of product, a bright yellow solid (60% yield). GC-MS (EI): m/z 398.51.

^{1}H-NMR ($CDCl_3$, 400 MHz), δ: 8.0 – 7.0 ppm (17 H, m); 4.80 ppm (2 H, s); 4.36 ppm (2 H, d, J=4 Hz); 2.55 (1 H, t, J=4 Hz).

2.4.2.6. Functionalisation of silicon nanocrystals with alkynes

In a two-neck 25 mL round-bottom flask, dried and filled with nitrogen, 0.3 mmol of alkyne (1-octyne or 9-phenyl-10-(4-((prop-2-yn-1-yloxy)methyl)phenyl)anthracene) were introduced. The flask was transferred in a dry-box and 70 µL of N,N,N',N'-tetramethylethylenediamine (TMEDA, 0.45 mmol) and 3 mL of dry toluene were added. The flask was then removed from the dry-box and plugged to a Shlenk line filled with N_2. After having cooled the reaction down to -78 °C with a liquid nitrogen/acetone bath, 120 µL of n-butyllithium (2.5 M in hexanes, 0.3 mmol; *note*: n-butyllithium reacts violently with moisture, must be handled under inert atmosphere) were added dropwise, while stirring. The acetone bath was removed after 45 minutes, and the mixture was stirred for 15 minutes at room temperature. Again at -78 °C, a suspension of silicon nanocrystals in 2 mL of toluene was slowly added to the reaction mixture. One hour later, the acetone bath was removed and the reaction mixture was stirred for an hour at room temperature. Later, it was heated to 40 °C, and

stirred for another hour. The reaction was cooled again to -78 °C and a second amount of nBuLi (60 μL, 0.15 mmol) was added to complete the capping of the surface. The reaction was allowed to reach room temperature and stirred overnight. The introduction of 7 mL of a 1 M solution of HCl in MeOH made the nanocrystals precipitate. The precipitate was washed 3 times with methanol and separated from the supernatant by centrifuge (8000 rpm, 5 minutes). The nanocrystals were then dispersed in chloroform. For Si-DPA, a size exclusion chromatography over BioBeadsTM S-X1 Support (200-400 mesh) in chloroform was performed to ameliorate the purity of the sample.

3. Functionalisation of Silicon Nanocrystals with amines

3.1. Introduction

Among the principal issues regarding the application of silicon nanocrystals for diagnostic bioimaging, the poor colloidal stability in water and the low absorption profile are pivotal. To circumvent this problem, we believed that a functionalisation with primary or secondary amines could be effective: well-established coupling reactions with carboxyl groups allow to create amide bonds. Amide bonds are fairly stable in physiological conditions and can be used to post-functionalise silicon nanocrystals with a high variety of molecules, e.g. water-solubilising groups (such as poly(ethylene)glycol) and/or chromophores for the realisation of a light-harvesting antenna. This approach could be used also for tethering specific receptors, enabling an active targeting of tissues. Moreover, many biologically important molecules are sold as activated esters (e.g. NHS-esters) which are selectively reactive towards amines.

As stated in Paragraph 1.3.2, the functionalisation of SiNCs with amines is tricky, because the interaction between the nitrogen atom and the silicon lattice can compromise the typical optical properties of the quantum dot, suppressing the characteristic bright red long-lived photoluminescence useful for bioimaging purposes (see Paragraph 1.4.2) and producing a blue short-lived emission with a lower quantum yield. Therefore, no example of amine functionalised silicon nanocrystals with bright red and long-lived emission was reported before ours.[105] This approach was very challenging: firstly developed during my Master's Degree Thesis project, it gave positive outcomes during my first year of PhD. The contents of this chapter have been reproduced and adapted from reference [105] with permission from the Royal Society of Chemistry.

3.2. Results and Discussion

In light of the results obtained from the reaction between chlorosilane-passivated SiNCs and acetylides, we decided to extend this synthetical strategy also for functionalising the quantum dots with an amine bearing a terminal alkyne moiety, i.e. propargylamine (Figure 3.2.1). In order to avoid a possible direct contact between the nitrogen atom and the silicon core, a protection of the amine group was necessary.

The first choice of protective group fell on trimethyl silyl (TMS, Figure 3.2.1) a group known to protect alcohols from deprotonation and nucleophilic substitution.[334] The protection occurs in the presence of chlorotrimethylsilane and a non-nucleophilic base, while the cleavage is achieved in the presence of K_2CO_3 in methanol (the characteristic deprotection in the presence of fluoride must be avoided since it can damage SiNCs).

Figure 3.2.1 – Protection of propargylamine with chlorotrimethylsilane.

The further step is the deprotonation of the terminal alkyne in the presence of nBuLi and the successive nucleophilic substitution with chlorosilane-passivated silicon nanocrystals, as explained in Chapter 2. Unfortunately, this reaction was unsuccessful, because of the instability of TMS group at ambient conditions and the impossibility to store the protected amine.

Therefore, we decided to produce *in situ* the acetylide of the protected propargylamine, using hexamethyldisilazane (HMDS) as starting material (Figure 3.2.2). In this reaction, (1) HMDS was firstly deprotonated in the presence of nBuLi, producing a lithium amide. Therefore, (2) half an equivalent of propargyl bromide was introduced to generate (through a nucleophilic substitution and an acid-base reaction) the acetylide of the silane-protected propargyl amine. This (3) was made react with chlorosilane-passivated silicon nanocrystals. Afterwards, the sample was deprotected (4) with potassium carbonate, purified and suspended in ethanol. The occurrence of this reaction was confirmed by NMR characterisations on molecules, ninhydrin test, TLC; however, the obtained nanoparticles were blue short-lived emitting (Figure 3.2.2).

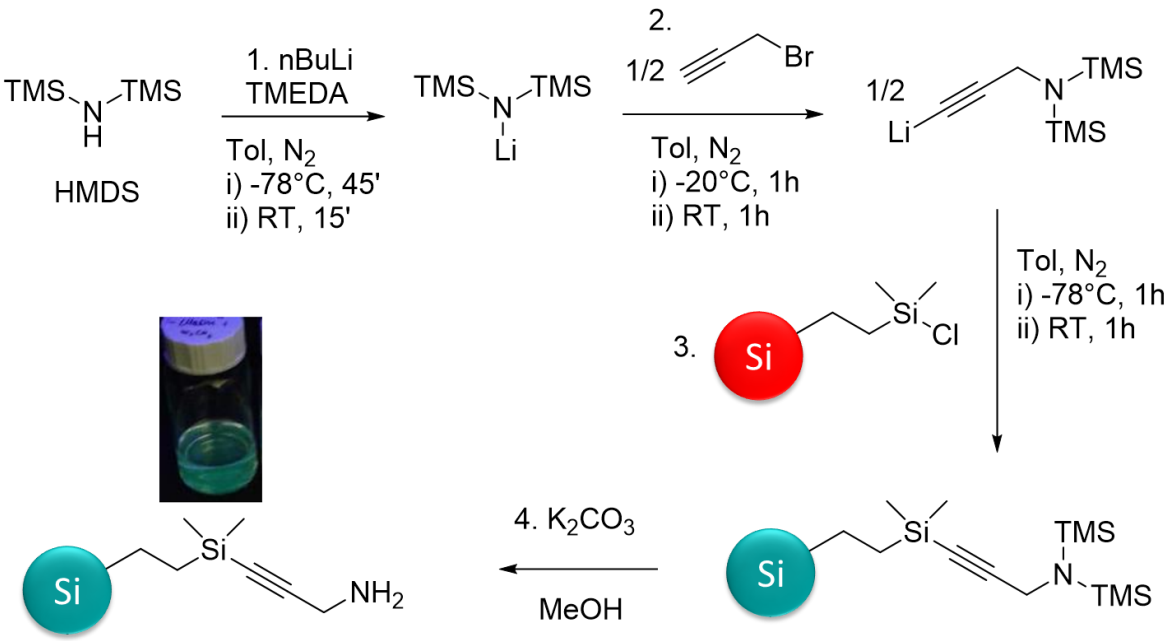

Figure 3.2.2 – Reaction scheme of functionalisation of silicon nanocrystals with amines using HMDS as starting material. Inset: photograph of an ethanol suspension of the produced SiNCs under 365 nm UV light.

We believe that, being TMS an unconventional protective group for amines, it could spontaneously cleave while working up. The presence of free deprotected amines could have interacted with the nanoparticles, introducing the defects responsible for the rising of the F band (see Paragraph 1.3.2 for further details). Therefore, our attention focussed on a different kind of protective group.

Trityl group (or triphenylmethyl group) is a well-known protecting group for amines. It is stable under the nucleophilic and basic conditions of the reaction, and it is labile in acidic conditions in which silicon nanocrystals are stable. Unlike TMS group, however, due to its huge size and the steric hindering, only one trityl group can protect one amine. If the molecule is a primary amine, only one of the two hydrogen atoms bonded to the nitrogen is replaced by the protecting group, as the other one is maintained (Figure 3.2.3 shows the mechanism for the protection of a primary amine such as propargylamine with tritylchloride).[334]

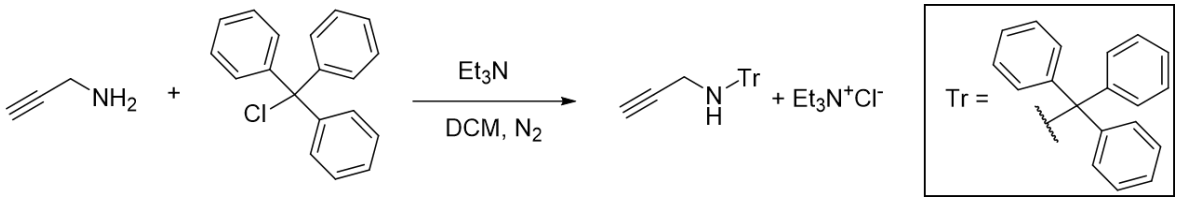

Figure 3.2.3 – Protection of propargylamine with tritylchloride.

The reaction on chlorosilane-passivated SiNCs was performed with the same procedure developed for Si-DPA, including the additional step of capping with nBuLi, being the ligand bulky and avoiding an overall passivation of the surface (see Chapter 2). The tritylamine-functionalised nanoparticles were washed with methanol, centrifuged and re-dispersed in chloroform, yielding a limpid yellowish suspension emitting red light under UV-light. Unfortunately, the nanoparticles precipitated over time.

The reason of this behaviour was associated to the ineffectiveness of the capping step with nBuLi. We believe that the presence of the hydrogen atom linked to the nitrogen of the protected amine could have influenced the procedure: at low temperatures, nBuLi could have deprotonated it instead of reacting with chlorosilanes. Moreover, the presence of a negative charge of the so-formed amide could have avoided the further approaching of nucleophilic agents to the near chlorosilanes. Therefore, some chlorosilanes remained unreacted and, working the reaction up, formed silanols, which could interact with other non-passivated nanoparticles, resulting in an aggregation (Figure 3.2.4).

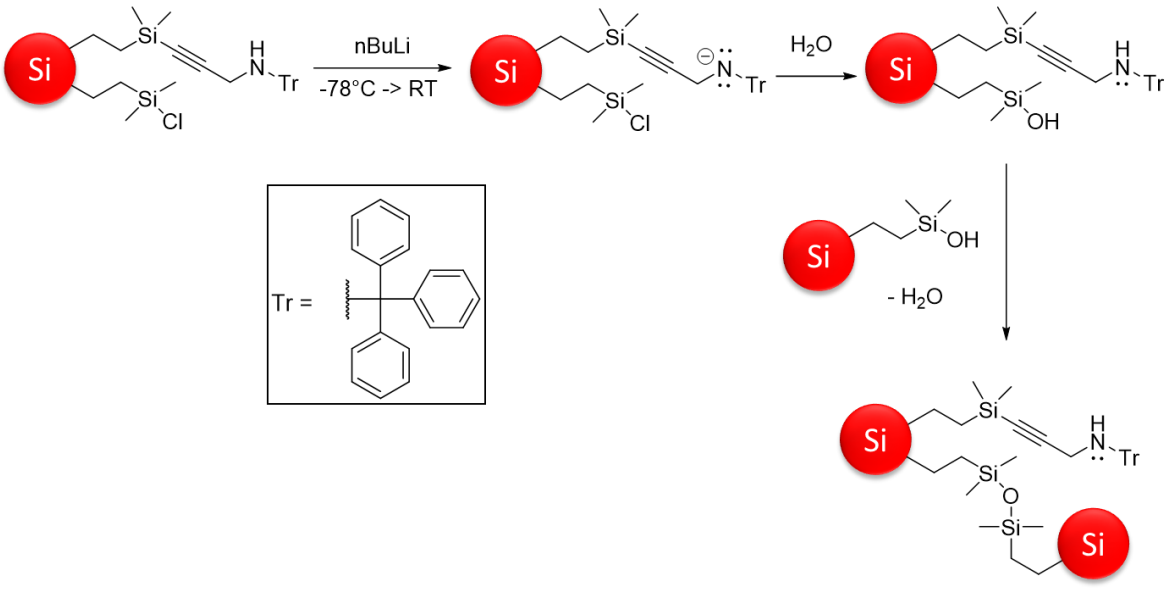

Figure 3.2.4 – Proposed mechanism for the aggregation of tritylamine-functionalised silicon nanocrystals.

Because the photophysical properties of the nanoparticles did not seem to be compromised, we assumed appropriate the choice of trityl as protective group for amines in the functionalisation. Considering that the main problem was related to the

acidic hydrogen linked to the nitrogen, we decided to substitute propargylamine with N-methylpropargylamine. In this case, its protection with trityl group does not leave acidic protons, except for the terminal alkyne one.[335] The overall reaction scheme is reported in Figure 3.2.5. The obtained nanoparticles were red emitting and well-dispersible in apolar solvents such as chloroform.

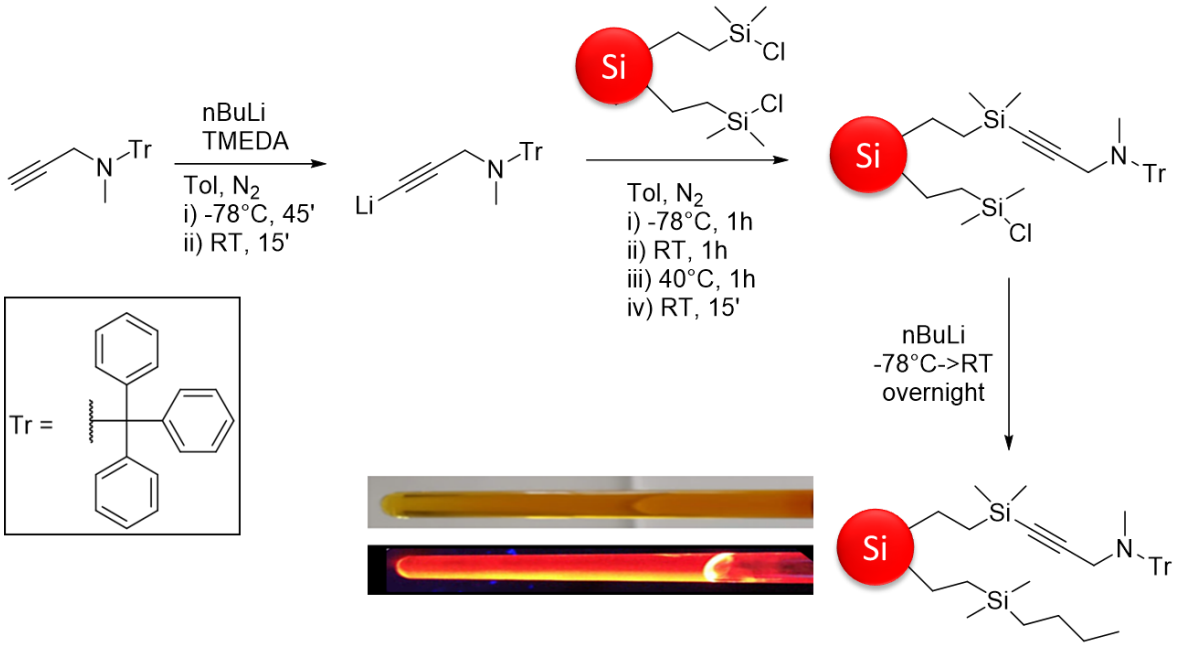

Figure 3.2.5 – Scheme of the effective reaction for functionalising silicon nanocrystals with tritylamines. Inset: photograph of a chloroform suspension of the produced SiNCs under ambient and 365 nm UV light.

The obtained nanoparticles were characterised qualitatively with ninhydrin test and ^{1}H-NMR.

A *ninhydrin test* is an assay used to detect the presence of amines. Primary amines react with ninhydrin, yielding a blue-coloured compound, secondary amines produce an orange compound and tertiary amines don't react.[336] The tritylamine-functionalised SiNCs did not display a colour change when exposed to the ninhydrin assay (spot A in Figure 3.2.6), as expected for a tertiary amine functionalization of the surface (see e.g., N-methyl-N-tritylpropargylamine, B in Figure 3.2.6).

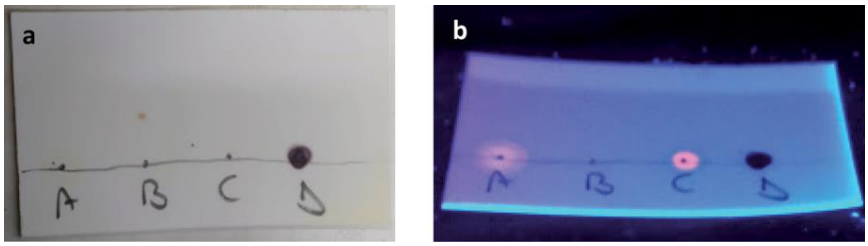

Figure 3.2.6 – Ninhydrin tests on TLC plates for different suspensions: (A) tritylamine-functionalised silicon nanocrystals, (B) a tertiary amine (here, N-methyl-N-tritylpropargylamine), (C) alkyl-passivated silicon nanocrystals (non-containing amines), (D) a primary amine (in this case, bis-aminopropyl polyethylene glycol) under (a) ambient or (b) 365 nm UV light.

^{1}H-NMR spectrum (Figure 3.2.7) confirms the presence of trityl group attached onto the surface of silicon nanoparticles. The broadening of the signals due to the longer relaxation times have already been reported also for Si-DPA (Chapter 2).

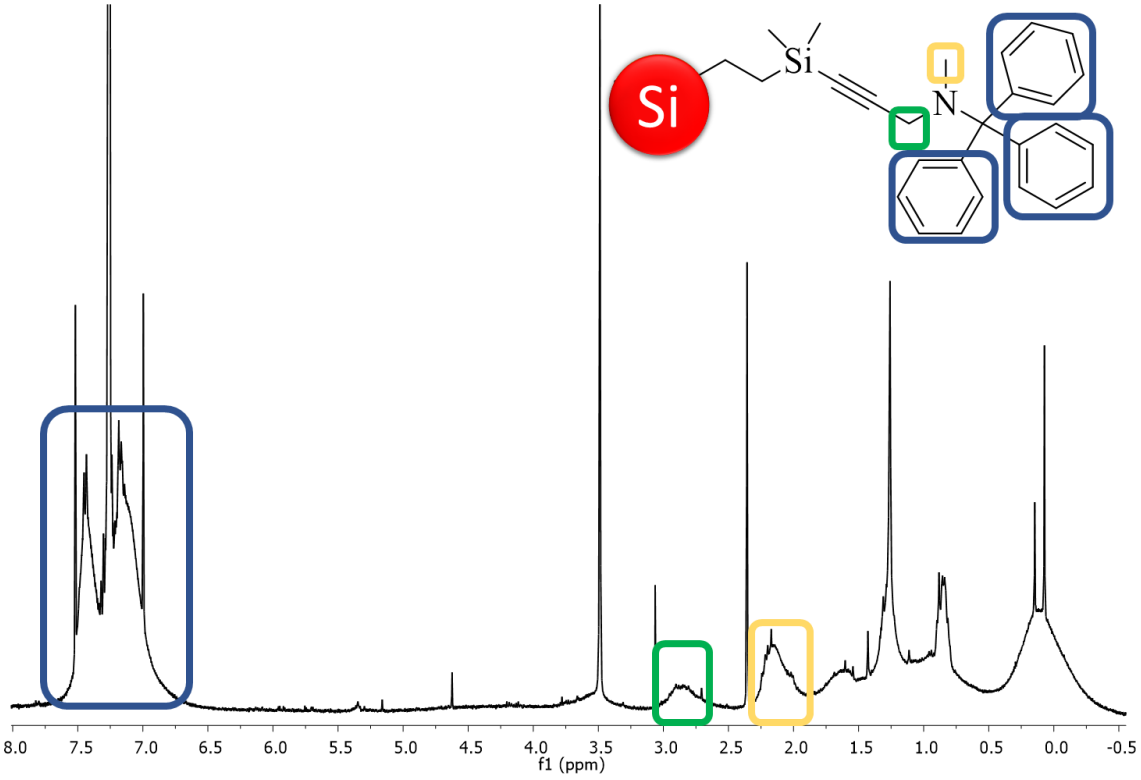

Figure 3.2.7 – ^{1}H-NMR spectrum of tritylamine-functionalised silicon nanocrystals (400 MHz, $CDCl_3$).

The cleavage of trityl group occurs in the presence of a quantitative amount of trifluoroacetic acid in chloroform, which leads to a precipitation of the nanocrystals in apolar solvents, due also to a protonation of the amines. After having washed the nanoparticles through centrifuge cycles, the sample was transferred in methanol, in which it was readily dispersible (Figure 3.2.8).

Figure 3.2.8 – Above, deprotection of tritylamine-functionalised silicon nanocrystals; below, photographs of ammonium functionalised silicon nanocrystals in chloroform (a) and in methanol under ambient (b) or 365 nm UV (c) light.

Also for deprotected amine-functionalised silicon nanocrystals, ninhydrin test (Figure 3.2.9) and ^{1}H-NMR spectrum (Figure 3.2.10) were performed, all of these confirming the fading of trityl group. Ninhydrin test assessed the presence of a secondary amine (yellowish coloration), while NMR spectrum is free of the aromatic signals of triphenylmethyl group.

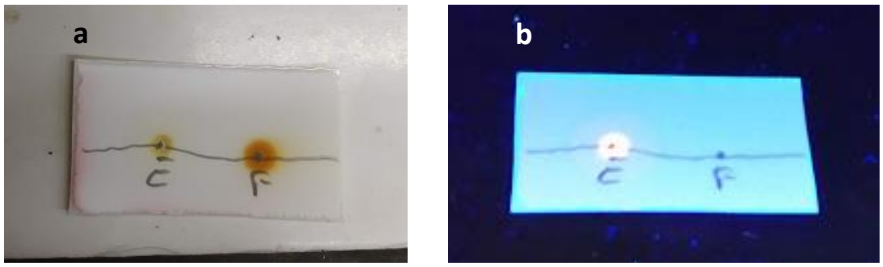

Figure 3.2.9 – (a) Ninhydrin test for (E) ammonium-functionalised silicon nanocrystals and (F) a secondary amine as comparison (N-methylpropargylamine); (b) TLC plate before the test under UV light.

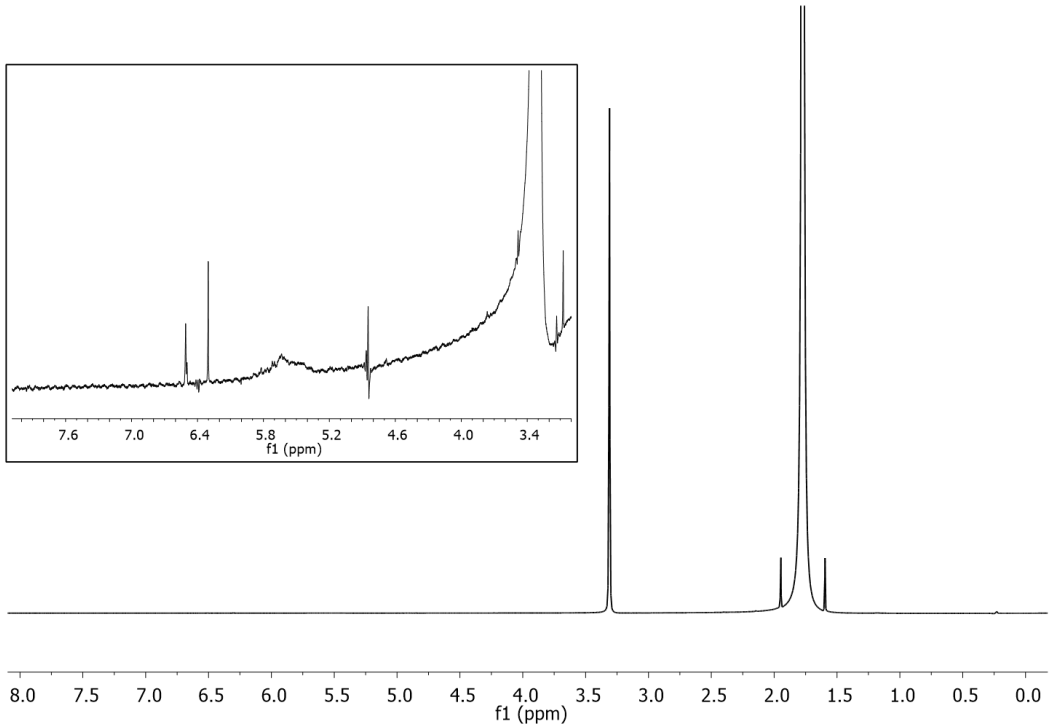

Figure 3.2.10 – ^{1}H-NMR spectra of ammonium-functionalised silicon nanocrystals (400 MHz, CD_3OD), with a 500x magnification in the inset, showing the absence of the aromatic signals.

The photophysical characterisation was performed on ammonium-terminated silicon nanocrystals dispersed in ethanol. The absorption spectrum (line blue in Figure 3.2.11a) exhibits the typical trend of the absorption of alkyl-passivated SiNCs, which gradually increases at lower wavelengths (see Paragraph 1.3.2). The emission band (red line in Figure 3.2.11a) is centred at about 750 nm with an emission quantum yield of 24% and an emission lifetime of 75 μs. Upon deprotonation of ammonium-terminated silicon nanocrystals with triethylamine (TEA) in chloroform, the absorption and emission spectra maintained the same shapes, but a decrease of the emission intensity was observed (Figure 3.2.11b), corresponding to an emission quantum yield of 4%.

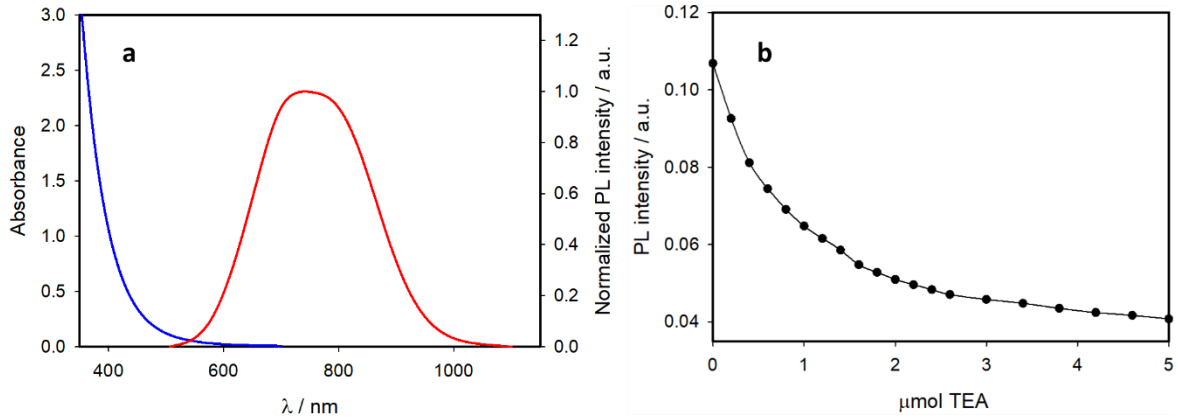

Figure 3.2.11 – (a) Absorption (blue line) and emission (red line) of ammonium-functionalised silicon nanocrystals in ethanol; (b) decay of the emission intensity upon addition of triethylamine (TEA).

This quenching process can be due to a photoinduced electron transfer between the silicon nanocrystal core and the terminal amine functionalities. The emission lifetime did not change significantly. This experimental finding is likely related to the fact that we cannot detect components shorter than 5 μs with this experimental setup and the observed intensity decay is related to the emission of excitons formed in the inner part of the nanocrystal core, that are not affected by the photoinduced electron transfer process.

We noticed that ammonium-terminated silicon nanocrystals are not dispersible in water if the counter anion is trifluoroacetate. Upon addition of HCl in methanol, anion exchange takes place, replacing the trifluoroacetate with chloride. The so-obtained nanocrystals were suspendable in water. The absorption and emission spectra of this sample are reported in Figure 3.2.12. The slight blue-shift observed in the photoluminescence (the emission band is centred at 675 nm) is probably due to oxidation of the surface caused by a non-homogeneous coating of the surface (see Paragraph 1.3.2 for further details). The emission quantum yield was equal to 5% and the emission lifetime was about 50 microseconds.

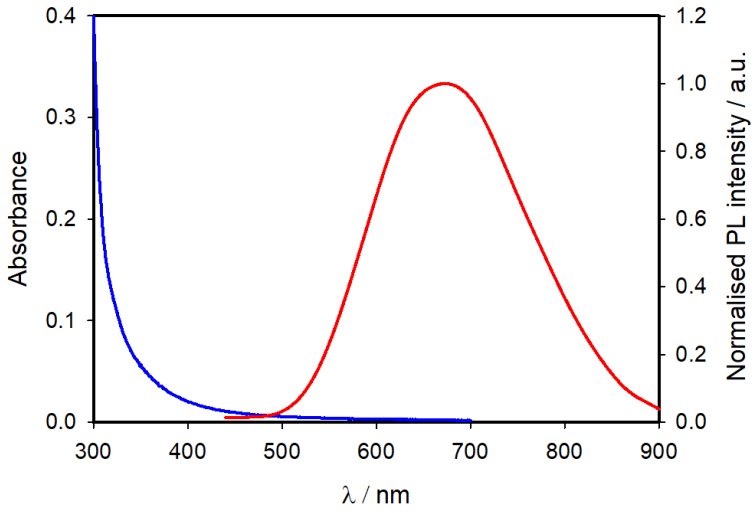

Figure 3.2.12 – Absorption (blue line) and emission (red line) spectra of ammonium-terminated silicon nanocrystals in water.

In light of biological applications, however, this colloidal stability in water was not further investigated. As a matter of fact, ammonium-terminated silicon nanocrystals are proven to be cytotoxic.[337] Therefore, we believe that the main purpose of amines on SiNCs is to link a most biocompatible polymer (e.g. poly(ethylene)glycol) through amide bonds.

The possibility to further functionalise the so-obtained SiNCs via amide coupling was tested by reaction with 1-pyrenebutyric acid in the presence of amide coupling reagents (1-cyano-2-ethoxy-2-oxoethylidenaminooxy) dimethylamino – morpholino – carbenium hexafluorophosphate and 1-ethyl-3- (3-dimethylaminopropyl)carbodiimide hydrochloride (COMU and EDC, as shown in Figure 3.2.13). The resulting SiNCs functionalised with pyrene chromophores (Si-py) were dispersed in DMF solution and the linkage of the chromophore was confirmed by photophysical characterisations (see below).

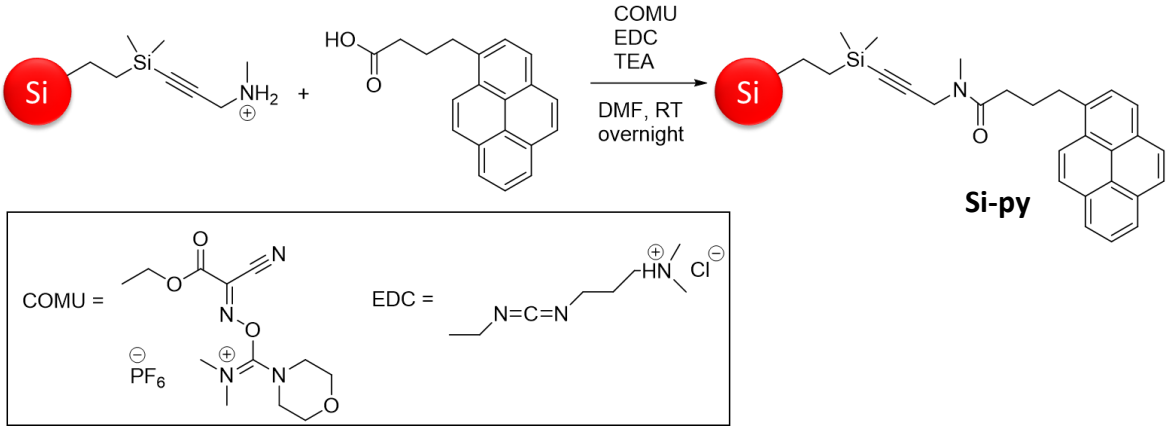

Figure 3.2.13 – Reaction scheme of the amide coupling between ammonium-terminated silicon nanocrystals and pyrenebutyric acid in the presence of COMU and EDC as coupling reagents in N,N-dimethylformamide (DMF).

The absorption spectrum of Si-Py (blue line in Figure 3.2.14) displays a trend associated to the sum of the absorption of the silicon core (red line) and the 1-pyrenebutyric acid one (green line), demonstrating that no significant interactions take place between the organic pyrene chromophore and the inorganic silicon core in the ground state. From these data, knowing the molar absorption coefficient for pyrenebutyric acid (3.7×10^4 $M^{-1}cm^{-1}$ at 344 nm, derived from spectrophotometric measurements) and that of the silicon core (1.0×10^5 $M^{-1}cm^{-1}$ computed at 430 nm,[73] where the absorption of the organic fluorophore does not occur) it is possible to estimate an average of 40 pyrene units per silicon nanocrystal (see Chapter 2 for further details about the computations).

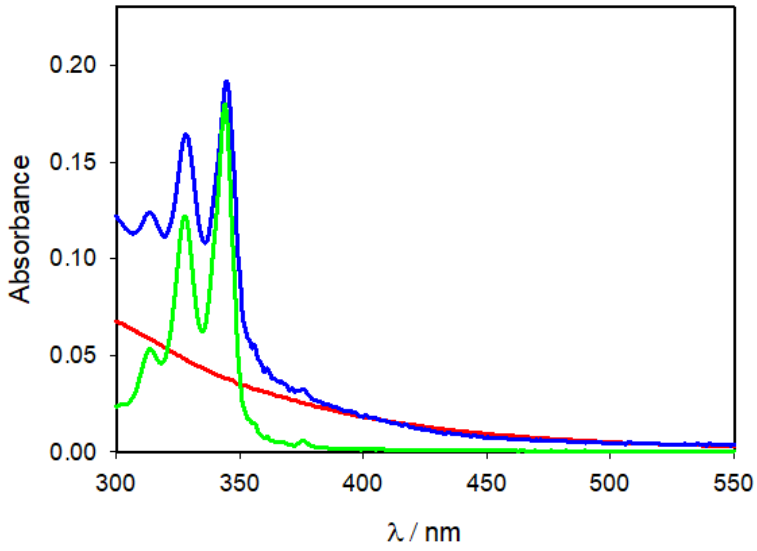

Figure 3.2.14 – Absorption spectra of Si-py (blue line), alkyl passivated silicon nanocrystals (in red) and 1-pyrenebutyric acid (green).

Upon excitation at 450 nm where only the silicon core absorbs light, the characteristic red luminescence is present (Figure 3.2.15a) with a photoluminescence quantum yield of 1.4%, which is increased up to 11% (τ = 20 μs) upon the addition of trifluoroacetic acid. This enhancement is compatible with the protonation of amine groups that prevent photoinduced electron transfer processes, as previously discussed for ammonium-terminated silicon nanocrystals.

Upon excitation at 340 nm, where 70% of light is absorbed by pyrene and 30% of light by the silicon core, the emission spectrum displays three main bands (Figure 3.2.15b) attributed to: (i) the pyrene monomer emission (380–420 nm, as confirmed by the emission spectrum of the 1-pyrenebutyric acid in blue); (ii) the emission of the pyrene excimer (centred at about 480 nm); (iii) the photoluminescence of the silicon nanocrystal (from 600 nm), which is better observed using a time-gated detection (dashed line in Figure 3.2.15b).

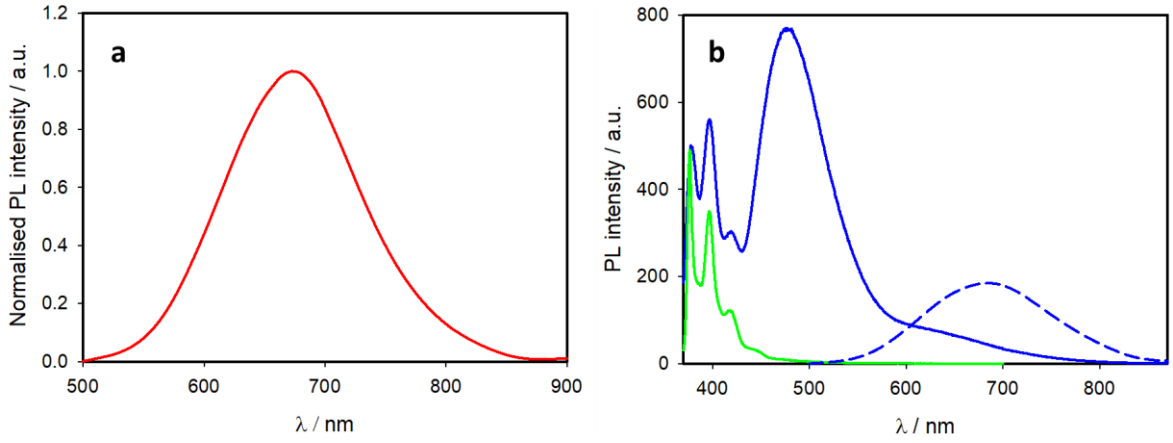

Figure 3.2.15 – (a) Emission spectrum of silicon core upon excitation at 450 nm; (b) emission spectra of Si-py (blue line) and 1-pyrenebutyric acid (green line) in DMF exciting at 340 nm and emission of Si-py (blue dashed line) with a time-gated detection of 50 microseconds (this emission is magnified).

The intense emission of the excimer is proof of the high number of pyrene units linked to the nanocrystals, as previously observed for pyrene-functionalised nanocrystals.[75] On the other hand, the emission of the pyrene monomer is strongly quenched (10-times). Indeed, the fluorescence lifetime of pyrene at 396 nm for Si-py in air-equilibrated dimethylformamide solution is 3.7 ns, compared to 37 ns for 1-pyrenebutyric acid under the same experimental conditions. The same value (3.7 ns) corresponds to the rise time in PL emission of the SiNCs at 700 nm upon excitation at

340 nm, which proves the occurrence of energy transfer from the pyrenes to the silicon core.

A further demonstration of the energy transfer between the organic chromophores and the silicon core is given by the excitation spectrum recorded at 700 nm (blue line in Figure 3.2.16), where only the nanocrystal contributes to the emission. The excitation spectrum shows a good match with the absorption spectrum (red line in Figure 3.2.16). The close match of the absorption and excitation spectra proves the occurrence of energy transfer with efficiency higher than 90%. The excitation spectrum was also measured for ammonium-terminated silicon nanocrystals mixed with free 1-pyrenebutyric acid in the appropriate ratios to match the Si-py absorbance profile. In this case, the excitation spectrum (green line in Figure 3.2.16) is superimposed onto the absorption spectrum of the ammonium-terminated SiNCs sample and no contribution from the pyrene chromophores is present. As previously observed,[74,75] in the physical mixture, excitation of pyrene does not result in sensitised emission of the SiNCs: the pyrene fluorescent excited state is short lived (tens of ns) and cannot interact with non-covalently bound SiNCs present in low concentration.

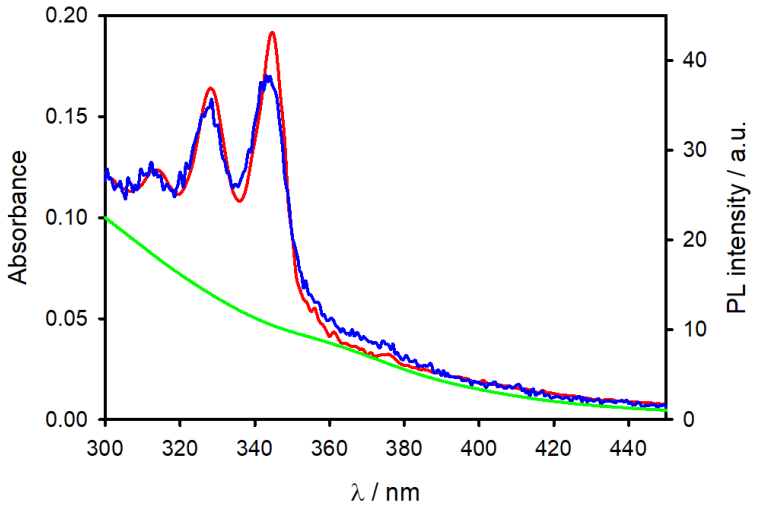

Figure 3.2.16 – Absorption (red line) and excitation spectra (blue line, λ_{em} = 700 nm, time-gated detection with delay = 50 μs and gate time = 1 ms) of Si-py in DMF. For comparison purposes, the excitation spectrum (green line) of a physical mixture of 1-pyrenebutyric acid and ammonium-terminated SiNCs under the same experimental conditions is shown.

It is worth noting that light-harvesting antennae based on silicon and pyrene were already reported by our group, where the functionalisation occurred *via* a competitive thermal hydrosilylation in the presence of 1-dodecene.[74,75] However, this sequential method allowed to link a higher number of chromophores with a lower amount of

pyrene (1.5% mol with respect to the previous synthesis). Moreover, this was the first example of light-harvesting antenna based on SiNCs suspendable in polar solvents.

This was also the first case of SiNCs functionalised with secondary amines with a long-lived bright red/NIR emission. Those nanoparticles are stable in ethanol for more than a year.

3.3. Conclusions

The functionalisation of SiNCs with amines is considered to be very convenient, especially thanks to the opportunity to perform an amide coupling. It could offer the possibility to link a wide variety of molecules, such as chromophores or bio-molecules, using a strategy that is well-known to chemists and bio-chemists. Unfortunately, even if several research groups managed to produce amine-terminated silicon nanocrystals, the optical properties of the quantum dots were compromised and became unsuited for bio-applications.

We developed a new strategy based on the protection of the amine with a hindered group (i.e trityl) followed by a passivation of chlorosilane moieties exposed on SiNCs surface, in a procedure which is reminiscent of the one described in Chapter 2. The so-obtained amine-functionalised SiNCs maintained excellent properties: a long-lived bright red photoluminescence and a good dispersibility in polar solvents.

Therefore, we demonstrated that it is possible to perform an amide coupling with chromophores, such as pyrene, derivatized with carboxylic groups. The resulting antenna shows an excellent sensitization efficiency and a stability in DMF for more than one year.

3.4. Experimental Section

All reagents were purchased from Sigma-Aldrich and used without further purification if not stated otherwise. Dry toluene was obtained via distillation over calcium chloride under nitrogen atmosphere. N,N,N',N'-tetramethylethylenediamine was refluxed over fresh KOH and distilled under nitrogen.

3.4.1. Synthesis of amine-functionalised SiNCs

3.4.1.1. Synthesis of N-methyl-N-tritylpropargylamine

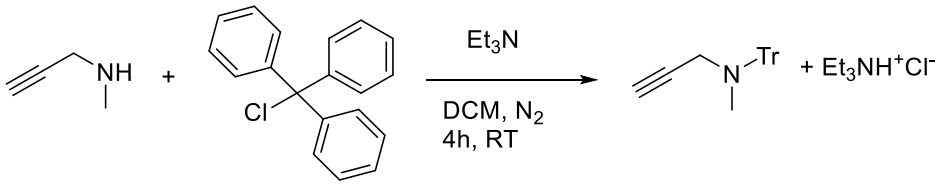

In a 25 mL two-necked flask, under a nitrogen atmosphere, 920 mg of tritylchloride (3.3 mmol, 1.1 eq.), 7 mL of anhydrous dichloromethane (DCM), 450 mL of anhydrous triethylamine (TEA, 333 mg, 3.3 mmol, 1.1 eq.) and 255 mL of N-methylpropargylamine (207 mg, 3 mmol, 1 eq.) were added in this order. After several minutes, the formation of a precipitate occurred (the ammonium salt). The mixture was stirred at room temperature for 4 hours under an inert atmosphere. The reaction was quenched with an aqueous solution of $NaHCO_3$ and diluted with another 5 mL of DCM. The organic phase was washed twice with water, collected, dried with Na_2SO_4 and concentrated at reduced pressure. TLC analysis (1:1 = cyclohexane:toluene as the eluent phase) showed two spots (Rf = 0, Rf = 0.8) upon developing with $KMnO_4$. The less polar one was identified as the product and the mixture was separated with flash chromatography using cyclohexane:toluene (1:1) as the eluent phase. The collected fractions gave a white crystalline solid (673 mg, yield: 72%).

GC-MS (EI): m/z 311. ^{1}H-NMR ($CDCl_3$, 400 MHz): 7.5 – 7.0 (15 H, m); 2.93 (2 H, br s); 2.25 (3 H, s); 2.19 (1 H, t).

3.4.1.2. Functionalisation of silicon nanocrystals with tritylamines

In a two-necked 25 mL round-bottom flask, dried and filled with nitrogen, 180 mg of N-methyl-N-tritylpropargylamine (0.6 mmol) were introduced. The flask was transferred into a dry-box and 140 mL of N,N,N',N'-tetramethylethylenediamine (TMEDA, 0.9 mmol, 105 mg) and 3 mL of dry toluene were added. The flask was then removed from the dry-box and was connected to a Schlenk line filled with N_2. After having cooled the reaction to -78 °C with a liquid nitrogen/acetone bath, 240 µL of n-butyllithium (nBuLi 2.5 M in hexanes, 0.6 mmol; *Attention*: pyrophoric! It must be handled under an inert atmosphere) were added dropwise, while stirring. The acetone bath was removed after 45 minutes, and the mixture was stirred for 15 minutes at room temperature. Again at -78 °C, the suspension of chlorosilane-passivated silicon

nanocrystals in 2 mL of toluene was slowly added to the reaction mixture. One hour later, the acetone bath was removed, and the reaction mixture was stirred for an hour at room temperature. Later, it was heated to 40 °C, and stirred for another hour. The reaction was cooled again to -78 °C and a second amount of nBuLi (120 µL, 0.3 mmol) was added to complete the capping of the surface. The reaction was allowed to reach room temperature and was stirred overnight.

The introduction of 7 mL of MeOH made the nanocrystals precipitate. The brownish precipitate was washed 3 times with methanol and separated from the supernatant by centrifugation (8000 rpm, 5 minutes). The obtained nanocrystals were dispersed in chloroform and the precipitate was filtered off.

3.4.1.3. Cleavage of trityl group for ammonium-terminated silicon nanocrystals

The suspension of tritylamine functionalised silicon nanocrystals was transferred into a 20 mL vial with a magnetic stir bar and was stirred slowly. Trifluoroacetic acid (TFA, 99%) was added dropwise carefully until the precipitation of silicon nanocrystals occurred (about 10 µL) due to the protonation of the amines. The suspension was let stir for 10 minutes. Then, the suspension was centrifuged, washing three times with chloroform (3×8000 rpm, 5 minutes) and the precipitate was dissolved in alcoholic solvent (ethanol, methanol), acetonitrile or N,N-dimethylformamide (DMF).

In order to obtain water-suspendable ammonium-terminated silicon nanocrystals, an excess of a HCl solution in methanol was added to a suspension of SiNCs in methanol. An excess of water was then introduced, and the suspension was filtered through 0.45 micrometre cut-off RC filters. The suspension was concentrated using a rotary evaporator to remove the methanol and the acid in excess.

3.4.1.4. Amide coupling with 1-pyrenebutyric acid

In a two-necked 25 mL round-bottom flask, under a nitrogen atmosphere, 7 mg of 1-pyrenebutyric acid (0.028 mmol) were dissolved in anhydrous DMF. Then, 9 µL of triethylamine (0.066 mmol, 6.6 mg), 5 µL of 1-ethyl-3-(3-dimethylaminopropyl) carbodiimide hydrochloride (EDC, 0.03 mmol, 4.4 mg) and 13 mg of (1-cyano-2-ethoxy-2-oxoethylidenaminooxy)dimethylamino – morpholino – carbenium hexa-fluorophosphate (COMU, 0.03 mmol) were added. The suspension was let stir for half

an hour at room temperature. Half a batch of ammonium-terminated silicon nanocrystals derived from the etching of 300 mg of silica-embedded SiNCs, dispersed in 2 mL of DMF, was added to the mixture, which was then let stir for 1 hour and a half. Thereafter, other 5 μL of EDC and 13 mg of COMU were added, and the mixture was let stir overnight. The addition of several mL of methanol made the nanocrystals precipitate. They were centrifuged five times with methanol (8000 rpm, 5 minutes) and the supernatant was dispersed in DMF.

4. Functionalisation of Silicon Nanocrystals *via* click-chemistry

4.1. Introduction

Despite the functionalisation with acetylides allowed to create efficient light-harvesting systems, it never worked for tethering poly(ethylene)glycol (from now on, PEG). PEG is a polymer frequently used for nanoparticles useful *in vivo*. It does not only enhance the colloidal stability in water, but it also permits a prolonged circulation time in the body.[338–341] As a matter of fact, it is well-known that when nanoparticles are administered, a variety of serum proteins (immunoglobulins, albumin, *et cetera*) bind to their surface. Those proteins are recognized by receptors overexposed on macrophage cell surfaces, which engulf the nanoparticle (in a process called phagocytosis) and remove them from circulation. The serum proteins which bind to the nanoparticles are also named "opsonins", and the process of adsorption is called "opsonization". PEG is shown to diminish the nonspecific interactions between the nanoparticle and the serum proteins, reducing opsonization.[342,343] Therefore, an increasing interest in the functionalisation of silicon nanocrystals with PEG has been shown.

Our attention was directed towards click-reactions. *Click chemistry* is defined as the ensemble of reactions characterized by a high yield, with no or less by-products easy to remove and simple to carry out.[344] In particular, we focussed on the click-reaction occurring between thiols and alkenes (for this reason it is also called *thiol-ene click reaction*).[345] In the presence of a radical initiator such as AIBN (azobisisobutyronitrile), the labile bond S-H of thiol is subject to a homolytic fission which generates a tihyl radical (i), which adds to the carbon-carbon double bond of the alkene (ii). This process leads to the formation of a radical on the adjacent carbon (iii), which cleaves another sulphur-hydrogen bond (iv), and the chain propagation occurs (Figure 4.1.1).

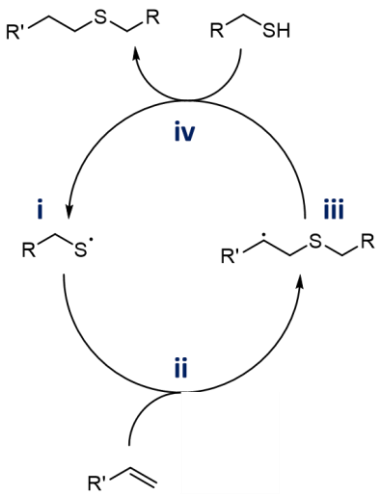

Figure 4.1.1 – Schematic representation of the steps for thiol-ene click reaction.

Our strategy involved the reaction between terminal alkenes overexposed on SiNCs' surface and PEG bearing a thiol moiety. The resulting nanoparticles were water-suspendable and were tested for time-gated detection bioimaging. The contents of this chapter have been reprinted and adapted with permission from reference [104] with permission from the Royal Society of Chemistry.

4.2. Results and Discussion

In order to accomplish the reaction, SiNCs were functionalised with overexpressed carbon-carbon double bonds. This can be achieved by a direct hydrosilylation between H-SiNCs and dienes.[218] The main drawback of this approach consists in a parasite hydrosilylation process which involves both the extremities of the diene, functionalising the nanocrystals with purely alkyl chains.

Therefore, we decided to passivate 4 and 5 nm H-SiNCs with chlorosilanes (as performed in the previous cases) which were subsequently made react with allyl magnesium bromide (Figure 4.2.1). The nucleophilic substitution with the Grignard reagent yields alkene-terminated SiNCs (Si-allyl).

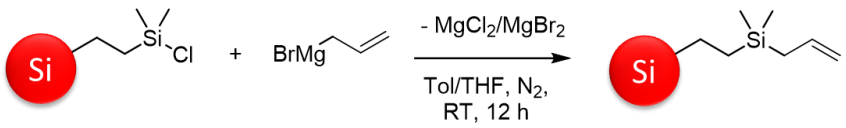

Figure 4.2.1 – Functionalisation of SiNCs with double bonds.

Moreover, PEG (mean MW = 2,000 Da) bearing a thiol moiety (PEG-SH) was synthesized through Fischer esterification between poly(ethylene)glycol and

mercaptopropionic acid (see Experimental Section for further details).[346] The thiol-ene click reaction was then performed and PEGylated SiNCs were produced (Figure 4.2.2).

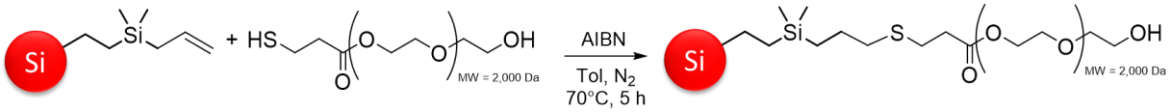

Figure 4.2.2 – Thiol-ene click reaction for the functionalisation of silicon nanocrystals with PEG.

The so-obtained nanocrystals were dispersible in toluene, ethanol and water (Figure 4.2.3).

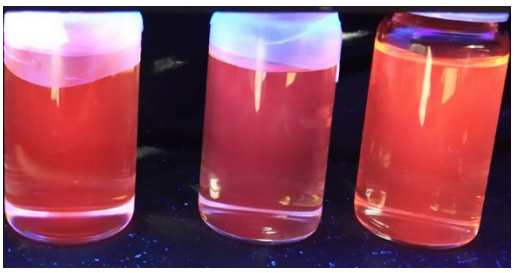

Figure 4.2.3 – From left to right, photographs of vials containing PEGylated SiNCs in toluene, ethanol and water under 365 nm UV light.

In the same way, the functionalisation of double bond-terminated SiNCs with thiols bearing an amino moiety was tested. The reaction with amino-terminated PEG-SH did not occur. We believe that the basicity of the amine could have interfered with the reaction. However, functionalisation with cysteamine hydrochloride yielded blue-emitting nanoparticles (Figure 4.2.4).

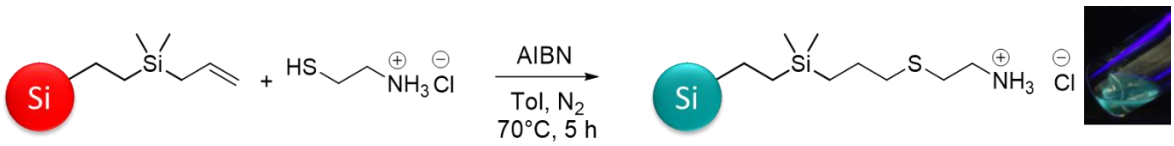

Figure 4.2.4 – Thiol-ene click reaction for the functionalisation of silicon nanocrystals with cysteamine. No characterization was performed on the resulting nanoparticles, whose structure is hypothesized.

Because of the maintaining of good optical properties, only PEGylated SiNCs (from now on, Si-PEG) were deeply characterised.

The absorption spectra of Si-PEG exhibit an unstructured absorption profile that is characteristic of Si nanocrystals (solid lines in Figure 4.2.5a). The photophysical data reported in Figure 4.2.5b for Si-allyl and Si-PEG in toluene demonstrate that the

radiative transition is characterized by the same energy, similar photoluminescence intensity decays (τ) and a decrease of the photoluminescence quantum yield (PLQY) in the case of 4 nm SiNCs. This decrease of PLQY with no effect on the lifetime might be indicative of the complete quenching of part of the nanocrystal ensemble (corresponding to lifetimes shorter than 5 μs). This effect can be ascribed to partial surface oxidation during the click reaction of the fraction of nanocrystals with incomplete surface functionalization in Figure 4.2.1, as previously reported by some of us in a different post-functionalisation reaction of SiNCs.[96] The photophysical properties of Si-PEG in distilled water are reported in Figure 4.2.5: bright red to NIR emission (λ_{max} = 735 and 945 nm) are observed for average core diameters of 4 and 5 nm, respectively.

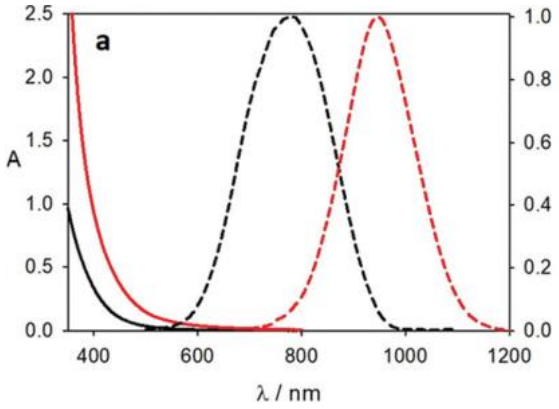

b

		Diameter = 4 nm			Diameter = 5 nm		
SiNC	Solvent	λ_{max} (nm)	PLQY	τ (μs)	λ_{max} (nm)	PLQY	τ (μs
Si-allyl	Toluene	770	0.41	74	955	0.30	135
Si-PEG	Toluene	770	0.20	68	950	0.29	130
Si-PEG	Water	735	0.16	60	945	0.18	120

Figure 4.2.5 – (a) Absorption (solid lines) and normalized photoluminescence spectra (dashed lines) of Si-PEG nanocrystals in water with an average diameter of the silicon core of 4 nm (black-line) and 5 nm (red-line); (b) Photoluminescence band maximum (λ_{max}), quantum yield (PLQY) and lifetime (τ) of Si-PEG and Si-allyl in toluene or distilled water. The reported diameters are referred to the silicon core.

Dynamic light scattering (DLS) analysis was used to evaluate the hydrodynamic volumes of Si-PEG in water and their stability as a function of time. The results indicate diameters of around (30 ± 10) nm for both 4 and 5 nm Si-PEG nanoparticles, as shown in Figure 4.2.6. No significant change was observed over a one-week time interval, demonstrating no aggregation. Even the optical properties do not change with time: the samples remained transparent for several months when stored at room temperature. Moreover, the photoluminescence lifetime of a Si-PEG sample in distilled water shows no change in a 1-day range and in blood serum at 37 °C, suggesting that the PEG surface functionalization was able to prevent interaction with serum proteins.

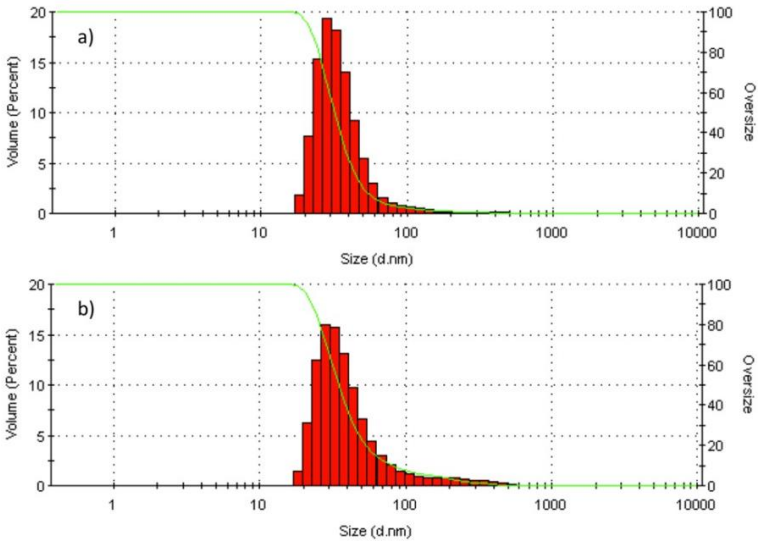

Figure 4.2.6 – Dynamic light scattering analysis of (a) 3 nm and (b) 5 nm Si-PEG nanocrystals in water.

The pH dependence on the optical properties is also a fundamental issue for luminescent probes: at basic pH (>8) a significant decrease of lifetime was observed and lifetime changes were not fully reversible upon acidification to the initial pH value. In contrast, at acidic pH, we observed a significant and fully reversible increase of lifetime (Figure 4.2.7), suggesting the possibility of implementing a pH sensor based on the luminescence lifetime of Si-PEG. It is worth noting that the lifetimes reported in Figure 4.2.6 are lower than the value reported in distilled water (Figure 4.2.5b) and this is due to the effect of ionic strength in aqueous solution. In addition, the photoluminescence lifetime was proven not to be affected by the oxygen concentration, whose presence may affect the signal detected and reduce the reliability of the sensor.

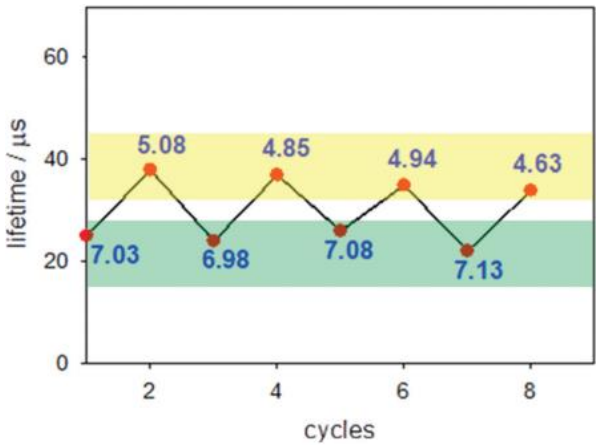

Figure 4.2.7 – Luminescence lifetimes as a function of pH (values reported in blue) in successive additions of HCl and KOH to a 7.5 × 10^{-7} M solution of 4 nm Si-PEG in water. λ_{exc} = 365 nm; λ_{em} > 550 nm.

4.3. Conclusions

The functionalisation of nanomaterials with poly(ethylene)glycol (i.e. pegylation) is of paramount importance for the implementation in biological systems. Because bioimaging is believed to be one of the most promising applications of SiNCs, their pegylation has been intensively studied. In particular, a good coverage of the surface is requested, and this appears to be quite difficult if considering the high hinderance of PEG. Therefore, we focussed our attention on *click chemistry reactions*, which are renowned for their high yield and simplicity. One of them is the *thiol-ene coupling*, for which the conditions are well-tolerated by silicon nanocrystals.

We developed a strategy in which the nanoparticles are functionalised with a terminal alkene and PEG is bearing a thiol moiety. Their reaction in presence of a radical initiator (AIBN) activated by quite low temperatures (70 °C) allows to obtain water-suspendable nanocrystals with a good stability and quantum yield.

Thanks to a collaboration with Dartmouth College, we assessed their utilization *in vivo*, showing that these systems can perform a passive targeting of tumours in mice. Moreover, their visualization is highlighted taking advantage of the long emission lifetimes of the quantum dots: the time-gated detection enhances the signal to noise ratio of a 3-fold factor with respect to steady-state measurements, allowing a good separation of the contributions (see Figure 4.3.1 that displays subcutaneously injected Si-PEG upon excitation at 457 nm).

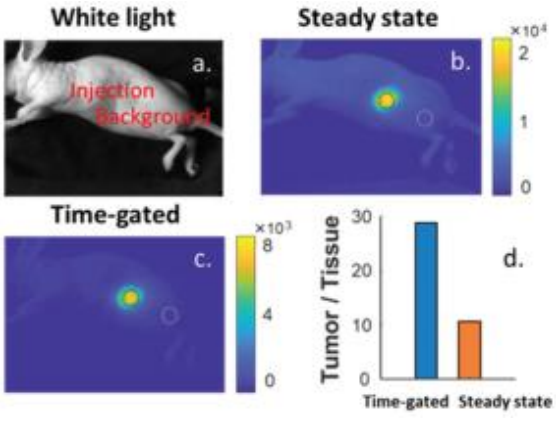

Figure 4.3.1 – Advantages of time-gated imaging. Si-PEG (1.5 μM) were subcutaneously injected into athymic nude mice; (a) white light image indicating the location of injection and location of quantitation of background luminescence; (b) steady state fluorescence imaging of SiNCs; (c) time-gated luminescence imaging; (d) difference in the signal to background ratio afforded by time-gated imaging (delay 10 μs).

The main disadvantages of this procedure are related to the impossibility to co-functionalise the nanocrystal with chromophores achieving a light-harvesting antenna (this is due to the low stability of conjugated systems towards the click reaction) and to the presence of an ester bond in PEG-SH, which is less stable in physiological environment than amides. Therefore, we addressed our attention on procedures which could allow to overcome those issues.

4.4. Experimental Section

All reagents were purchased from Sigma-Aldrich and used without further purification if not stated otherwise. Dry toluene was obtained via distillation over calcium chloride under nitrogen atmosphere.

4.4.1. Synthesis of Si-PEG

4.4.1.1. Synthesis of PEG-SH

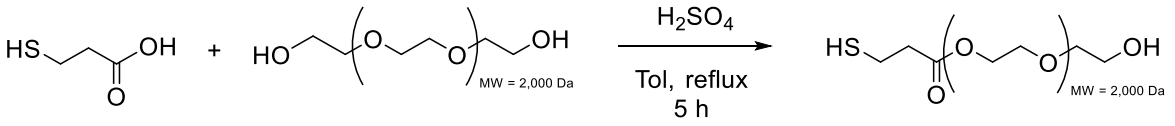

Mercaptopoly(ethylene glycol) (PEG-SH) was prepared as follows:[346] 4.4 g of poly(ethylene glycol), MW=2,000 (PEG) was introduced in a three-necked flask equipped with a stirrer and a condenser. 50 mL of dry toluene were added to dissolve the PEG, then 261 µL (3 eq.) of 3-mercaptopropionic acid and few drops of sulfuric acid were added. The flask was heated to reflux with an oil bath overnight, under nitrogen. The reaction was then checked with TLC and cooled to room temperature. The reaction solution was concentrated under reduced atmosphere, then diethyl ether was added to precipitate the product. The product was transferred on a Gooch filter and washed three times with diethyl ether, dried under vacuum and collected as a white waxy solid 1.4 g (yield 32%).

^{1}H-NMR ($CDCl_3$, 400 MHz): 4.26 – 4.23 ppm (2 H, m), 3.62 ppm (200 H, s), 2.75 ppm (2 H, m), 2.66 ppm (2 H, t, J = 7.3 Hz), 1.66 ppm (1 H, t, J = 8.3 Hz).

4.4.1.2. Synthesis of Si-allyl

Allyl terminated nanocrystals were prepared through the Grignard nucleophilic addition to the chlorosilane passivated SiNCs. In particular, 0.2 mL allyl magnesium bromide (1 M solution in diethyl ether) was added to the chlorosilane passivated SiNCs

solution and left stirring overnight at room temperature. While the addition of the Grignard reagent results in a turbid solution for 5 nm SiNCs, no significant effect was observed on the 4 nm nanocrystals other than the quenching of the typical red emission under UV light excitation. The samples are then extracted from the glove-box and acidified MeOH (0.5mL HCl in 20 mL of MeOH) is added to quench the residual Grignard and precipitate the nanocrystals. The dispersion is then precipitated and washed three times with MeOH, then dissolved again in toluene and stored in vials for further use. Proton NMR measurements of Si-allyl were conducted and proton signals from the double bonds appeared around 6 ppm confirming the functionalization.[104]

4.4.1.3. Synthesis of Si-PEG through thiol-ene click reaction

A batch of allyl functionalised SiNCs was dissolved in 10 mL of toluene, then 1g of PEG-SH was added. After the PEG is completely dissolved, 15 mg of AIBN (azobisisobutyronitrile) was added to start the thiol-ene click reaction. The solution was purged with nitrogen for 20 min under ultrasonication to remove oxygen traces, then heated for 4h at 70 °C. After cooling to room temperature, the suspension became slightly turbid. The sample was dried under vacuum, suspended in ethanol, then dried again and dissolved in distilled water. The ethanol addition is essential to maintain the colloidal stability of the resulting sample. A drastic change in polarity of the solvent from toluene to bi-distilled water might induce aggregation of functionalised SiNCs. The excess PEG and the residual AIBN were removed by either dialysis (RC dialysis tube, Millipore, MW cutoff = 14,000 Da) or high-pressure filtration (RC filter, Amicon® Stirred Cells, MW cutoff = 14,000 Da). Finally, the sample is filtered over 0.22 μm RC syringe filter and stored at room temperature. Slight aggregation occurs over the course of several weeks in concentrated solution, but not in diluted solutions (10^{-4} – 10^{-5} M). ^{1}H-NMR spectrum of functionalised SiNCs shows new signals of methylene protons in proximity to the thiol-ether group, which is formed upon click reaction between allyl functionalised SiNCs and PEG-SH.

^{1}H-NMR ($CDCl_3$, 400 MHz): 4.17 ppm (2 H, m), 3.59 ppm (186 H, m), 2.83 ppm (2 H, m), 2.66 ppm (2 H, m), 2.56 ppm (2 H, t), 1.63 ppm (2 H, m).

5. Functionalisation of Silicon Nanocrystals with carboxylic acids

5.1. Introduction

As explained in Chapter 3, post-functionalisation of SiNCs through amide bonds could avoid several issues for the applications *in vivo* of the nanoparticles. In the same chapter, SiNCs were functionalised with amines and the ligands were introduced as carboxyl derivatives. This approach was successful but expensive in time: each reaction on SiNCs, from hydride-terminated to amide-functionalised ones, takes one day. Easier approaches for achieving the grafting of amines on SiNCs have been being studied.

Another strategy which could allow the formation of amides is the functionalisation of silicon nanocrystals with carboxylic acids, which can further react with biologically important molecules containing amines. In order to reduce the reaction times, our attention focussed on the direct functionalisation of H-SiNCs with carboxyl compounds. However, the direct hydrosilylation with carboxylic acids showed some issues: the resulting nanoparticle is too polar to be suspended in toluene[222] (the typical reaction solvent) and the hydrosilylation with acrylic acid and 10-undecenoic acid in the presence of diazonium salts wasn't successful. If the hydrosilylation was conducted in co-presence of 1-dodecene, the grafting of 10-undecenoic acid occurred in different ratios, but the nanoparticles were suspendable in solvents characterised by different polarity, rendering the purification process hard. Moreover, the emission quantum yield was low in polar solvents and a slight blue-shift occurred (probably due to the oxidation of the surface, see Paragraph 1.3.2).

Therefore, we studied a new strategy involving a protected carboxylic acid. The resulting nanoparticles were completely functionalised with carboxyl groups, red-emitting and with high emission quantum yields in ethanol.

5.2. Results and Discussion

As reported in Chapter 3, the choice of the suitable protective group should consider its stability in the reaction conditions in which SiNCs are exposed and must be cleavable in a non-harmful ambient for the nanoparticles. For instance, we noticed

that SiNCs are more stable in the presence of acids such as TFA. Our decision was directed to tert-butyl (tBu) group. The reaction (*Steglich esterification*) between a carboxylic acid (here, 10-undecenoic acid) and tert-butanol, in the presence of dicyclohexylcarbodiimide (DCC) and a non-nucleophilic base such as dimethylaminopyridine (DMAP) yields tert-butyl 10-undecenoate.[347] Because of the presence of side-products which render the mixture difficult to purify, it is also possible to obtain the same molecule converting 10-undecenoic acid to 10-undecenoyl chloride with thionyl chloride and making tert-butanol react with the acyl chloride in presence of diisopropylethylamine (DIPEA), adapting a procedure widely found in literature.[348–350] The deprotection from tert-butyl group and the regeneration of the carboxylic acid occurs in presence of an excess of trifluoroacetic acid in chloroform.[334]

Therefore, the strategy involved (i) the protection of 10-undecenoic acid; (ii) the hydrosilylation on H-SiNCs and (iii) the deprotection (Figure 5.2.1). Afterwards, trials of amide coupling were performed.

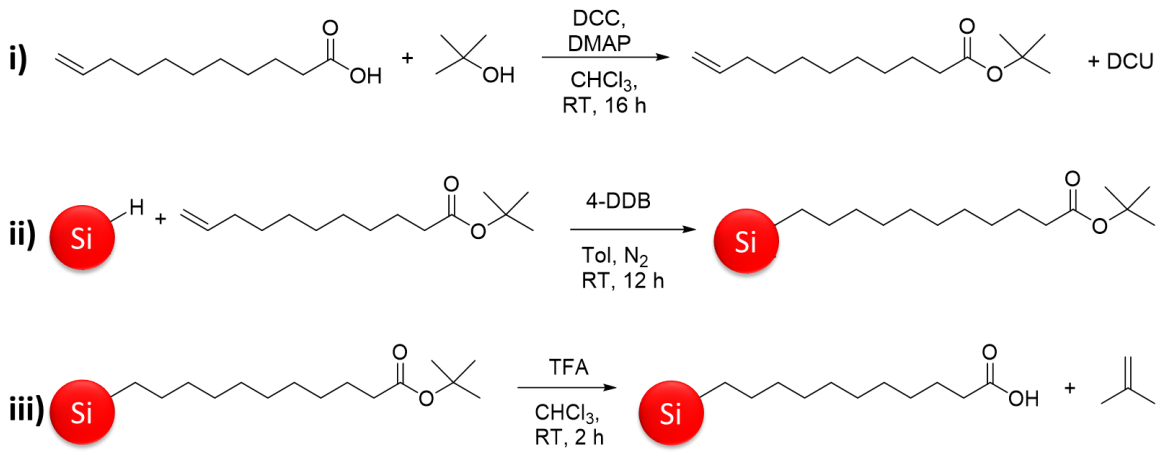

Figure 5.2.1 – Adopted strategy for the functionalisation of silicon nanocrystals with carboxylic acids: (i) protection of 10-undecenoic acid with tert-butanol; (ii) radical-initiated hydrosilylation; (iii) deprotection.

Tert-butyl esters let the nanocrystals be suspended in apolar solvents, such as toluene and chloroform, but not in polar ones as methanol. This allows to perform the purification of the hydrosilylation reaction through precipitation in CH_3OH and subsequent centrifugation. The so-obtained nanocrystals are usually quenched, but the luminescence is recovered over time or deprotecting the nanoparticles.

The precipitation of the nanoparticles in chloroform during the deprotection is one proof of the presence of polar carboxylic acids on their surface. However, the

nanoparticles can be maintained suspended if the amount of TFA is high. Consequently, a real proof of the cleavage of tBu group is given by ^{1}H-NMR spectra collected before and after the deprotection.

The ^{1}H-NMR spectrum of tert-butyl ester-functionalised SiNCs is reported in Figure 5.2.2. The main signals lay at 2.17 ppm (2 hydrogens in alfa position with respect to the carboxyl group), 1.57 and 1.2 ppm (broad signals related to the hydrogens of the alkyl chain linked to the nanoparticle) and 1.44 ppm (highlighted in the figure). The latter singlet represents the signal due to the 9 hydrogens of tert-butyl group. This signal will be crucial for the determination of the number of ligands connected to the surface of each nanoparticle (*vide infra*).

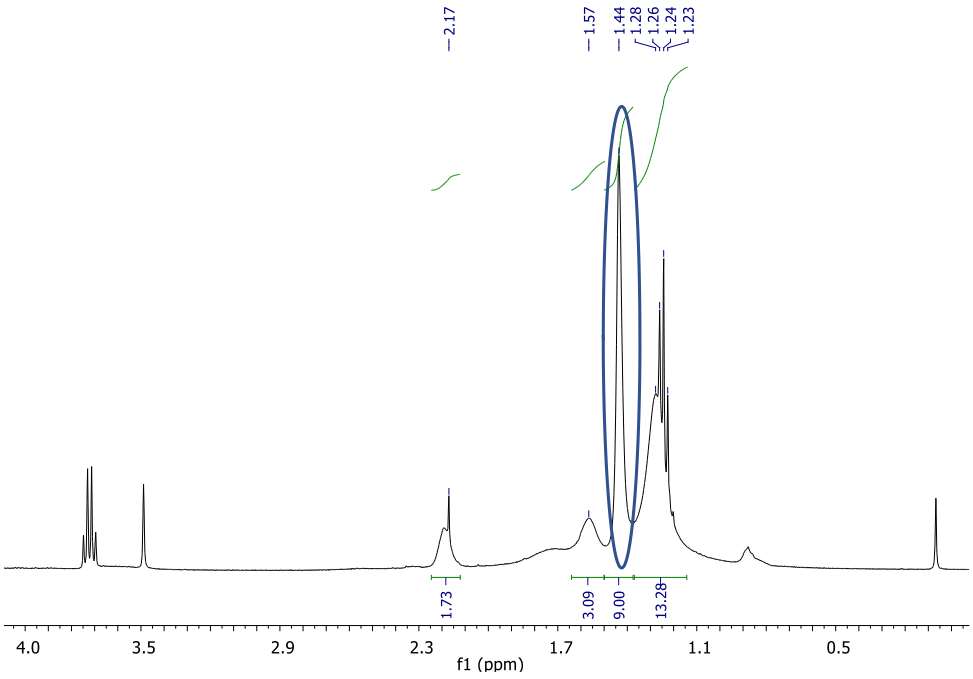

Figure 5.2.2 – ^{1}H-NMR spectrum (400 MHz, $CDCl_3$) of tert-butyl ester-functionalised SiNCs.

After the deprotection, the nanocrystals were dispersed in a mixture 1:2 chloroform-d:methanol-4d. The resulting NMR spectrum (Figure 5.2.3) shows the reduction (or the fading) of the peak related to tBu.

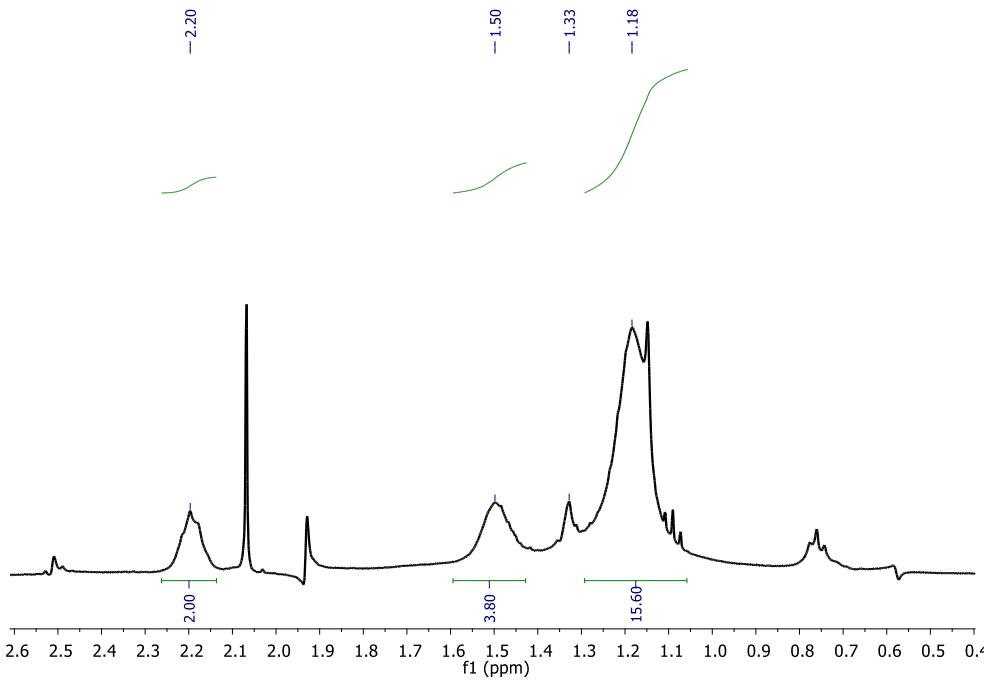

Figure 5.2.3 – ^{1}H-NMR spectrum (400 MHz, 1:2=$CDCl_3$:CD_3OD) of acid-functionalised SiNCs.

The photophysical characterization of the tert-butyl ester-passivated SiNCs was performed in toluene, while the deprotected sample was studied in ethanol. While the absorption spectra are well-overlapped (blue lines in Figure 5.2.4), the emission spectrum of the deprotected sample (solid dark red line) is blue-shifted by about 10 nm with respect to the protected one (dashed red line), which is index of a slight oxidation of the surface, as reported in literature.[130] However, both emission quantum yield and lifetimes are increased for the deprotected sample (respectively, 22% and 87 μs *versus* 19% and 77 μs of the tert-butyl ester passivated one). This behaviour is unusual for nanoparticles dispersed in more polar solvents, where the optical properties are usually compromised.

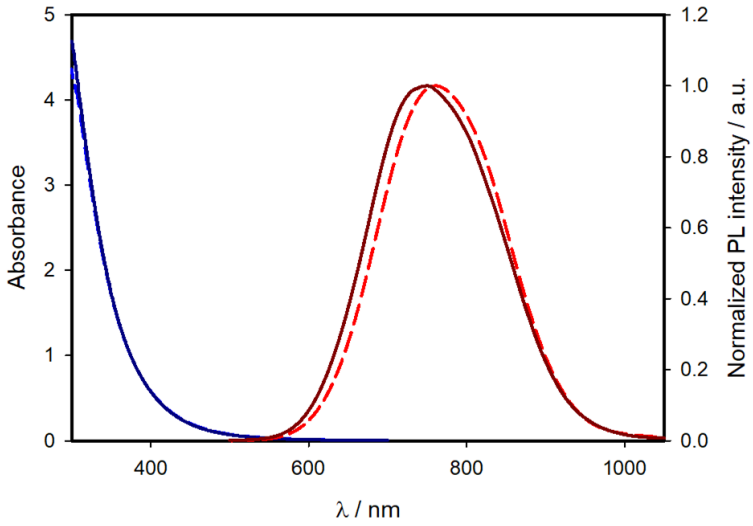

Figure 5.2.4 – Absorption (blue lines) and emission (red lines, exciting at 450 nm) spectra of tert-butyl ester-functionalised SiNCs in toluene (dashed lines) or carboxylic acid-functionalised SiNCs in ethanol (solid dark lines).

The amidation processes were more challenging. Different routes have been attempted, using a high variety of amide coupling reagents, namely COMU and EDC (already used for amine functionalised SiNCs, see Chapter 3), or HBTU (i.e. Hexafluorophosphate Benzotriazole Tetramethyl Uronium), a salt widely used to graft amines onto carboxylic acid terminated dendrimers.[351] However, the first trials were unsuccessful, due to the presence of residual TFA that can compete with the carboxylic acid of SiNCs. This issue was initially overcome by reducing the amount of TFA concentrating numerous times the deprotected sample at rotary evaporator, or washing and filtrating with toluene, until the pH of the suspension was as neutral as possible.

Despite the taken precautions to ameliorate the reaction conditions, the amide couplings continued to be unsuccessful. Even using different coupling reagents, modifying the concentration of the starting materials, using various types of amines, from the most hindered bis-amino poly(ethylene)glycol, to the nucleophilic propargylamine, the reaction did not occur or compromised the emission of the nanoparticles. We attributed most of the causes to the poor suitability of the solvent. As a matter of fact, we chose DMF, which is the only solvent able to dissolve each component of the reaction mixture and it is highly recommended for amidations. However, it seems to damage the optical properties of SiNCs, quenching and/or blue-

shifting the emission, is difficult to remove and must be fresh, or can degrade into diethylamine. Substituting DMF with THF, the nanoparticles tended to aggregate.

Moreover, in literature, only few examples of carboxylic acid-functionalised SiNCs are coupled to amines. Usually, they are water-suspendable quantum dots and the amide coupling step is performed in presence of EDC and (Sulfo-)NHS in water.[132,352] The bonded amine was usually a protein or, more generally, a biomolecule, so the researchers haven't been focussed on the amount of linked molecules. This suggested that this kind of reactions are not very suitable for the functionalisation of acid SiNCs.

Therefore, a new synthetical route was adopted in order to activate the carboxylic moiety.

5.2.1. Amide coupling *via* formation of acyl chlorides

Specifically, the acyl chloride is far more reactive towards amines with respect to carboxylic acids activated with amide coupling reagents. Acyl chlorides can be produced *in situ* from carboxylic acids in the presence of oxalyl chloride or thionyl chloride.[348–350] In particular, the reaction between R-COOH and $SOCl_2$ can be described as follows:

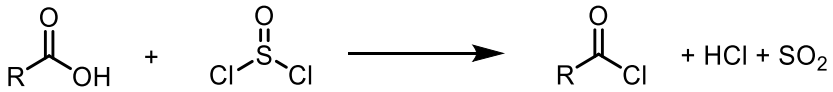

The driving force is the production of gaseous SO_2 and HCl which can be moved away from the reaction mixture. This reaction can be catalysed in the presence of few drops of DMF, which enables the formation of the Vilsmeier-Haak intermediate.[353] $SOCl_2$ can be used in stoichiometric amount or in excess (as a solvent or co-solvent). The typical solvents for the reaction are toluene or DCM. THF is also indicated as a possibility, even if someone claims to avoid it because it can polymerize in the presence of acid.[354] If $SOCl_2$ is used in high amount, it should be moved away from the reaction before the next step. Usually, thionyl chloride is evaporated at reduced pressure (290 mbar @ 40 °C) washing with toluene (azeotropic removal).[355]

The next step is the reaction with a primary amine, which leads to an amide bond, as described:

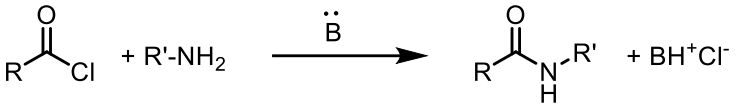

In order to neutralize the hydrochloric acid produced (which can protonate the primary amine and make it unreactive towards the electrophilic acyl chloride), a tertiary amine should be added. TEA or DIPEA are the best choices, while DMAP is known to react violently with the acyl chloride and should be added in catalytical amounts.[356] The base can also react with the acyl chloride yielding reactive ketenes.

When applying to silicon nanocrystals, the main concerns are related to the solvent. Thionyl chloride should be avoided as pure solvent, because it must be completely removed from the reaction mixture before adding the amines. This could lead to a precipitation of the nanoparticles at rotary evaporator which can result in an irreversible aggregation. On the other hand, the solvents that are suggested for the reaction are apolar and cannot stabilize the acid-functionalised SiNCs. For this reason, we decided to passivate the surface of H-SiNCs with an equimolar mixture of 1-dodecene and tert-butyl 10-undecenoate. The deprotection with TFA produces silicon nanocrystals functionalised with a mixture of pure dodecyl chains and carboxylic acids (from now on Si-DDE:COOH) that are suspendable also in non-polar solvents.

Another issue was related to the amine to be linked. In order to understand if the amidation effectively occurs, as we did for amine terminated SiNCs (Chapter 3), we decided to tether an amino derivative of pyrene, assessing then the presence of amide bond through excitation spectra. In Figure 5.2.5 the entire procedure, which has been studied and adapted on model compounds, is shown.

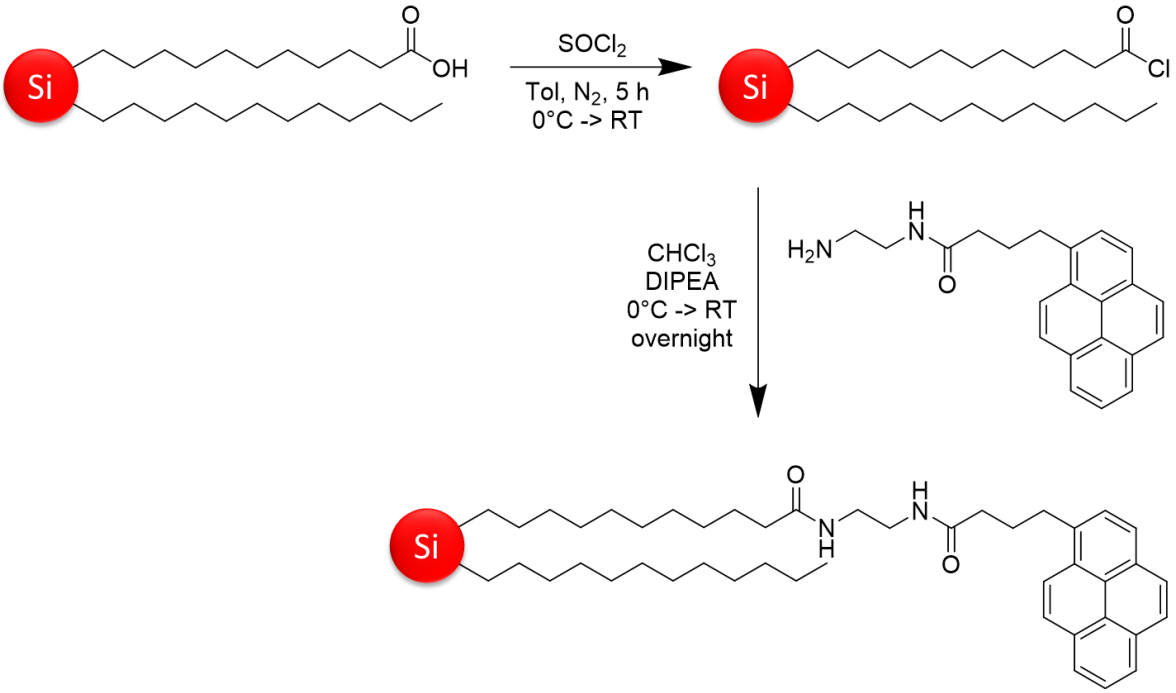

Figure 5.2.5 – Strategy for coupling carboxylic acid functionalised SiNCs with amines.

Even though for the entire duration of the reaction the nanocrystals were well-suspendable, after the purification by SEC, only a small batch was obtained, affecting the chemical yield of the amide coupling. Figure 5.2.6 collects the absorption, excitation and time-gated emission spectra of the sample. There are many similarities to the ones described in Chapter 3 (from Figure 3.2.15 to Figure 3.2.17), confirming the occurrence of the energy transfer from pyrene to the silicon and therefore the success of the functionalization. This is clear from the excitation spectrum recorded at 700 nm (red line, Figure 5.2.6) that shows the contribution of the pyrene absorption (e.g. the peaks at 325 nm and 345 nm) to the emission of the inorganic core. However, the overlap with the absorption spectrum (black line) is not so good and this is probably due to two reasons: (i) part of the pyrene in the sample is detached from the nanocrystal, and this does not provide energy transfer; (ii) the efficiency of energy transfer is low because of the long distance between the attached chromophore and the silicon.

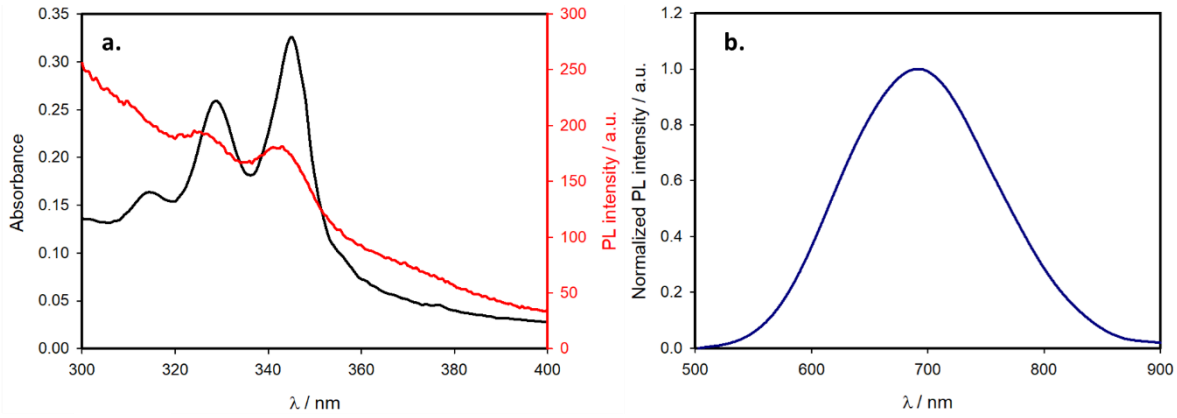

Figure 5.2.6 – (a) Absorption (black line) and excitation (red line, recorded at 700 nm) spectra of SiNCs functionalised with pyrene via *acyl chloride in chloroform; (b) normalized photoluminescence intensity recorded exciting at 345 nm with a time-gated detection (delay of 50 microseconds).*

The amount of detached pyrene can be estimated analyzing the emission lifetimes (τ) of pyrene. The ligand has a τ in $CHCl_3$ equal to 15 ns, while in the SiNCs suspension, the emission intensity decay can be described with a bi-exponential function:

$$I = B_1 e^{-t/\tau_1} + B_2 e^{-t/\tau_2},$$

where:

- τ_1 = 5 ns and B_1 = 0.016

- τ_2 = 15 ns and B_2 = 0.039

Obviously, the second term is related to the detached pyrene, while the first one, with an inferior lifetime, is referred to the bonded (i.e. quenched) pyrene. From the pre-exponential factors it is possible to compute the amount of linked chromophore over the total number of pyrene in the suspension (the formula is strictly valid for diluted suspensions):

$$n_{pyrene,linked} = \frac{16}{16+39} \cdot n_{pyrene,total} = 30\% \cdot n_{pyrene,total}$$

Knowing the molar absorption coefficient of pyrene (3.7×10^4 $M^{-1}cm^{-1}$ at 344 nm) and the silicon core (1.0×10^5 $M^{-1}cm^{-1}$ at 430 nm)[73] it is possible to estimate a total of 30 pyrene units either attached or detached per silicon nanocrystal, about 9 of which (*id est* the 30%) are linked to each nanoparticle.

This low number is due to the reduced amount of reactive units (i.e. carboxylic acids) on SiNCs (because of the co-passivation with dodecene) and the poor reliability of the reaction. Therefore, we decided to switch our attention on different functionalization strategies.

5.2.2. Determination of the number of ligands per nanocrystal

An important factor for the evaluation of the efficiency of functionalisation is surely related to the determination of the number of ligands tethered on the surface of the SiNC. In literature, the only way found to compute that is TGA (thermogravimetric analysis): the loss of the mass occurring at temperatures lower than 400 °C is related to the oxidation to CO_2 of alkyl chains.[73] Comparing the percentage of loss of this mass to the mass of the nanoparticle (whether the molecular weights of the ligand and SiNC are known), it is possible to estimate the desired value.

For different nanoparticles, this has been assessed also by spectrometric analysis, such as colorimetric assays and emission spectra (e.g. ninhydrin[357] and fluorescamine[358] are used for the quantification of amino groups on silica nanoparticles) or NMR in the presence of standards. To the best of our knowledge, these approaches weren't used to determine the amount of non-chromophoric units linked to silicon nanocrystals. Unfortunately, the NMR signals are usually broadened, non-specific and difficult to distinguish.

However, tert-butyl group seems to be valid for the purpose: as it is possible to see from Figure 5.2.2, the signal is quite sharp (it is a singlet and the distance from the nanoparticle renders this group less affected by the hindrance of the motions), intense (it corresponds to 9 equivalent hydrogens) and specific (1.44 ppm in $CDCl_3$, 400 MHz).[347]

Our strategy consisted in performing ^{1}H-NMR spectrum of a well-known volume of a dispersion in chloroform-d of tert-butyl functionalised SiNCs in the presence of a standard (here, dimethylformamide and pyrene) in order to determine the overall amount of ligands in the sample. From the absorption spectrum of the same sample (being careful about the dilutions), knowing the molar absorption coefficient of the nanoparticles, it was possible to estimate the number of nanocrystals. The desired value is the ratio.

Firstly, we performed the absorption spectrum of a 2.4 mL chloroform suspension of tert-butyl ester functionalised SiNCs (derived from the etching of 100 mg of $Si@SiO_2$ powder). The absorbance at 430 nm was 1.18. Assuming a molar absorption coefficient of 1×10^5 $M^{-1}cm^{-1}$ for 4 nm sized SiNCs at the considered wavelength,[106] it is possible to compute a number of 28 nmols of SiNCs in the sample.

The sample was concentrated and re-dispersed in 700 µL of deuterated chloroform. A known amount of pyrene and DMF were then introduced in order to obtain a solution of 4.9 mM and 6.7 mM respectively. The ^{1}H-NMR spectrum is reported in Figure 5.2.7.

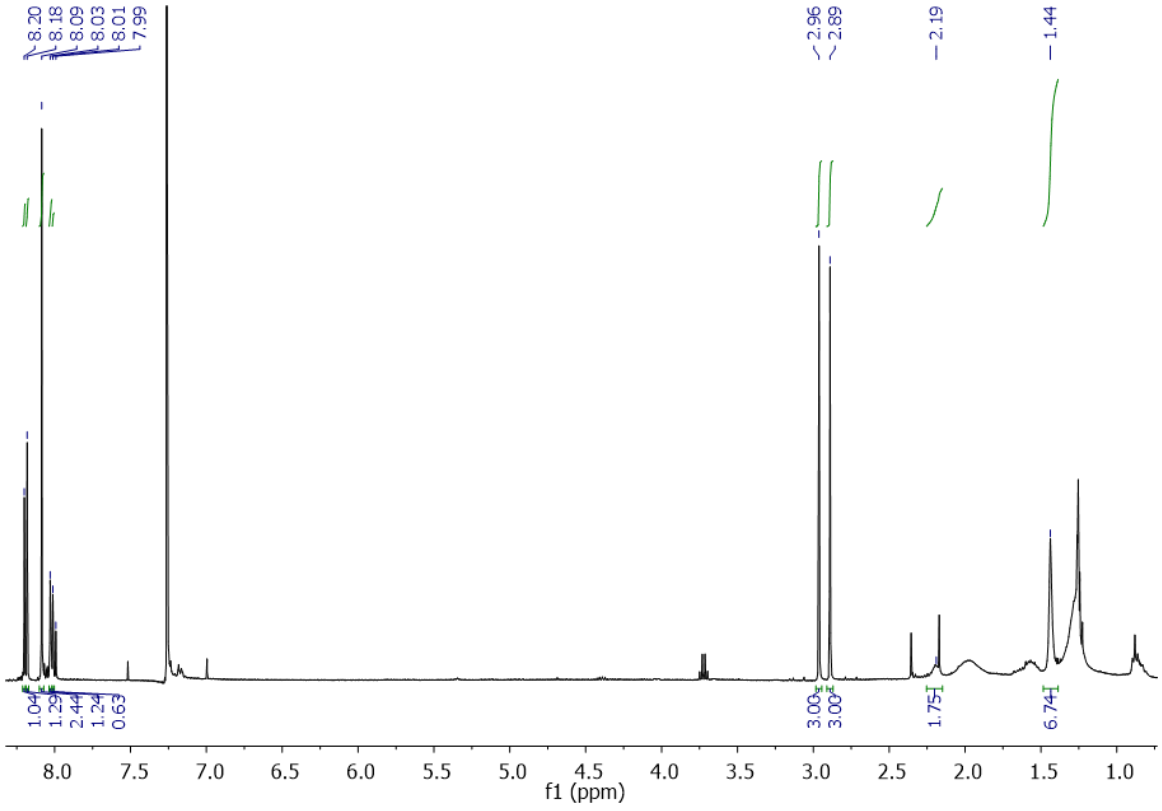

Figure 5.2.7 – ^{1}H-NMR spectrum (400 MHz, $CDCl_3$) of 700 microliters of a suspension containing 28 nmols of tert-butyl functionalised SiNCs, 4.9 mM of pyrene and 6.7 mM of pyrene.

Using DMF as standard (δ = 2.89 ppm, s, 3H; 2.96 ppm, s, 3H; 8.01 ppm, s, 1H), it is possible to estimate an amount of ligands equals to 3.64 µmols; using pyrene (δ = 7.99 ppm, m, 2H; 8.09 ppm, m, 4H; 8.19 ppm, m, 4H), the desired value equals to 4.4 µmols. Considering a solid non-volatile compound as a better standard, we decided to continue with this number for the ratio.

Therefore, about 160 ligands are estimated to be linked per 4-nm sized nanocrystal.

5.3. Conclusions

The direct functionalisation of silicon nanocrystals with carboxylic acids usually leads to an oxidation of the surface of the nanoparticle, with a consequent blue-shift of the photoluminescence. One way to avoid this is to protect the carboxylic moiety with an ester that is easily cleavable. We found that tert-butyl esters possess the desired characteristics and the hydrosilylation of tert-butyl undecenoate with H-SiNCs in the presence of diazonium salts occurs with high yields.

The so-obtained nanoparticles terminate with a group (-C-$(CH_3)_3$) whose signal at ^{1}H-NMR is facile to distinguish. This allows a computation of the number of attached ligands per nanoparticle in the presence of a standard (e.g. pyrene) and knowing the amount of SiNCs in the sample (obtained from absorption spectroscopy) without the use of less common techniques in an organic chemistry laboratory such as TGA.

The deprotection produces carboxylic acid functionalised SiNCs with a bright red emission, with long lifetimes and a dispersibility in polar solvents such as ethanol.

The step further, i.e. the amide coupling, is still challenging and no investigated strategies allows to obtain a high yield of amidation.

5.4. Experimental Section

All reagents were purchased from Sigma-Aldrich and used without further purification if not stated otherwise. Dry toluene was obtained via distillation over calcium chloride under nitrogen atmosphere.

5.4.1. Functionalisation of silicon nanocrystals with carboxylic acids

5.4.1.1. Protection of 10-undecenoic acid: tert-butyl undecenoate

Tert-butyl undecenoate was synthesised with two different approaches: via acyl chloride and by Steglich esterification. Both are reported.

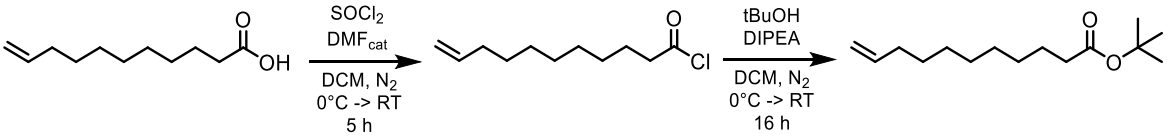

Via acyl chloride. In a 100 mL two-necked round-bottomed flask, desiccated and under inert atmosphere, 2.760 g of 10-undecenoic acid (15 mmol) were dissolved in 5

mL of anhydrous dichloromethane (DCM). At 0 °C, 1.1 mL of thionyl chloride ($SOCl_2$, 15 mmol) and a catalytic amount of N,N-dimethylformamide (DMF) were added dropwise and the mixture allowed to heat up to room temperature and let stir for 5 h under a nitrogen flux. Therefore, 20 mL of anhydrous dichloromethane were added, before cooling the mixture down to 0 °C. N-ethyl-N,N-diisopropylamine (DIPEA, 11 mL, 60 mmol) and tert-butanol (tBuOH, 6 mL, 60 mmol) were carefully introduced (*caution!* The reaction produces heat and gas), and the mixture let stir overnight at room temperature. The reaction was quenched with a saturated $NaHCO_3$ aqueous solution and the organic phase extracted three times with $NaHCO_{3(aq)}$ and one with water. A flash chromatography over silica (100% toluene, R_f = 0.8) was performed to isolate 1.7 g of a brown oil (yield 67%).

GC-MS (EI): m/z 240. ^{1}H-NMR ($CDCl_3$, 400 MHz): 5.8 ppm (1 H, m); 4.93 ppm (2 H, dd); 2.18 ppm (2 H, t); 2.03 ppm (2 H, m); 1.56 ppm (2 H, t); 1.43 ppm (9 H, s); 1.36 ppm (2 H, m); 1.27 ppm (8 H, s).

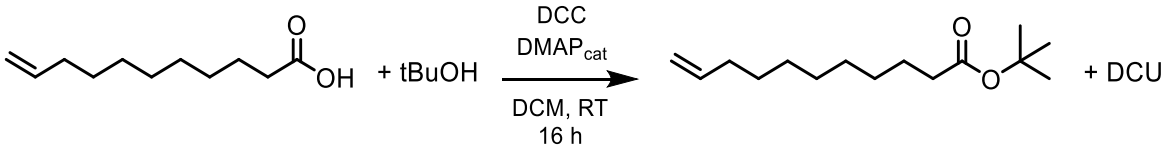

Steglich esterification. In a 100 mL one-necked round-bottomed flask, 3 g of 10-undecenoic acid (16 mmol), 20 mL of chloroform, 3.3 mL of tert-butanol (34 mmol) and 650 mg of DMAP (5 mmol) were introduced and the mixture was let stir. Afterwards, a solution of 4 g of DCC in 20 mL of chloroform was added dropwise and the mixture let stir for further 16 h at room temperature and ambient atmosphere. The precipitation of the dicyclohexylurea was a symptom of the occurring of the reaction. The white solid was filtered off with a Gouch filter and the liquid washed three times with water. The organic phase was collected, dried over Na_2SO_4 and purified by flash chromatography (100% toluene as eluent phase). 3 g of a viscous liquid were obtained (yield 80%). GC-MS and ^{1}H-NMR were identical to the ones of the previous reaction.

5.4.1.2. Hydrosilylation and deprotection to obtain all-carboxylic acid-terminated SiNCs

In a dry-box, in a 8 mL vial were introduced 720 mg of tert-butyl undecenoate (3 mmol). A dispersion of H-SiNCs derived from the etching of 300 mg of $Si@SiO_2$ powder

in 2 mL of toluene was added. Finally, 2 mg of 4-DDB were added to initiate the hydrosilylation. The suspension became darker and limpid in few hours, but it was let stir overnight.

The addition of 20 mL of methanol made the nanocrystals precipitate. They were centrifuged 3 times (8000 rpm, 5') and suspended in 2 mL of chloroform.

The deprotection consisted in the addition of 1 mL of TFA (however, the ratio v/v chloroform/TFA was maintained of 2:1) and the suspension was let stir for 2 hours at room temperature at ambient atmosphere.

Afterwards, the suspension was concentrated under reduced pressure and toluene was added to make the nanocrystals precipitate. The nanoparticles were centrifuged 3 times in toluene (8000 rpm, 5'), until no TFA was present. The nanocrystals were re-dispersed in a more polar solvent (AcOEt, DMF, ethanol).

5.4.1.3. Hydrosilylation and deprotection to obtain SiNCs passivated with acid and dodecene

The procedure to obtain Si-DDE:COOH, that is silicon nanocrystals passivated with an equimolar amount of carboxylic acid and dodecyl chain is the same described in Paragraph 5.3.1.2, but 240 mg of tert-butyl undecenoate (1 mmol) and 200 µL of 1-dodecene (1 mmol) were used to cap a batch of H-SiNCs obtained from the etching of 300 mg of $Si@SiO_2$ powder.

The purification process was performed exclusively by size exclusion chromatography (200-400 mesh) in distilled chloroform.

The deprotection was conducted in a mixture 2:1 of chloroform/TFA for 2 hours at room temperature. TFA was removed at rotary evaporator introducing toluene and concentrating 5 times. The sample was then redispersed in toluene.

5.4.2. Functionalisation of silicon nanocrystals with amides *via* acyl chloride

5.4.2.1. Synthesis of tert-butyl (2-(4-(pyren-1-yl)butanamido)ethyl)carbamate

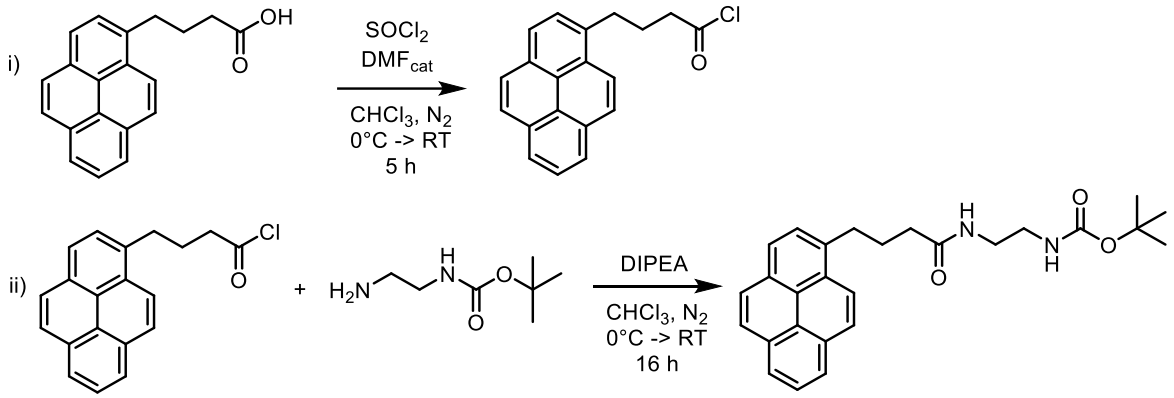

Pyrene butyric acid (288 mg, 1 mmol) was introduced in a 25 mL anhydrous two-necked round-bottom flask under inert atmosphere and 5 mL of anhydrous DCM were introduced. At 0 °C, thionyl chloride (74 µL, 1 mmol) was carefully added, followed by a catalytic amount of anhydrous DMF. After 15 minutes, the colour of the mixture changed and pyrene was well-dissolved into it. The mixture was let stir for 5 h at room temperature under a continuous nitrogen flux. Therefore, at 0 °C, DIPEA (550 µL, 3 mmol) were carefully added, while a production of gas evolved and the colour of the mixture became darker (probably due to the formation of ketenes). Subsequently, N-Boc-ethylenediamine (350 µL, 2.2 mmol) was introduced and the mixture let stir overnight at room temperature.

The reaction was quenched adding a saturated solution of $NaHCO_3$. The organic phase was separated and washed 3 times with $NaHCO_{3(aq)}$. $CHCl_3$ was evaporated at reduced pressure, yielding a dark solid. Flash chromatography (7:3=AcOEt:cyclohexane, Rf = 0.3 under 365 nm UV light) was performed to isolate a yellow solid (165 mg, 0.38 mmol, yield 38%).

^{1}H-NMR ($CDCl_3$, 400 MHz): 8.3 – 7.8 ppm (9 H, m); 6.29 ppm (1 H, bs); 5.02 ppm (1 H, bs); 3.4 – 3.2 ppm (4 H, m); 2.25 ppm (2 H, t); 2.16 ppm (2 H, t); 2.04 ppm (2 H, m); 1.37 ppm (9 H, s).

5.4.2.2. Synthesis of N-(2-aminoethyl)-4-(pyren-1-yl)butanamide

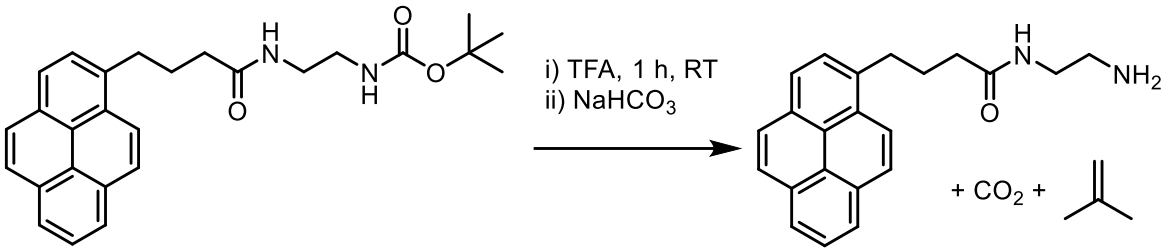

A procedure found in literature was followed.[359] (2-(4-(pyren-1-yl)butanamido)ethyl)carbamate (165 mg, 0.38 mmol) was dissolved in 4 mL of TFA at room temperature for 1 h. The solution was concentrated and then an aqueous saturated solution of $NaHCO_3$ (20 mL) were added. The product was extracted in chloroform washing 3 times with $NaHCO_{3(aq)}$. 106 mg (0.32 mmol) of N-(2-aminoethyl)-4-(pyren-1-yl)butanamide were obtained (85% yield).

^{1}H-NMR ($CDCl_3$, 400 MHz): 8.5 – 7.8 ppm (9 H, m); 5.94 ppm (1 H, bs); 3.37 ppm (2 H, t); 3.25 ppm (2 H, t); 2.28 ppm (2 H, t); 2.20 ppm (2 H, t); 1.97 ppm (2 H, bs).

5.4.2.3. Synthesis of pyrene-functionalised SiNCs

The 3 mL toluene suspension of Si-DDE:COOH was introduced in a two-necked round-bottom flask, filled with nitrogen. At 0 °C, 2 mL of $SOCl_2$ was added dropwise. The mixture was allowed to reach room temperature and let stir 3 h, leaving a flux of nitrogen flowing. Therefore, the suspension was concentrated at rotary evaporator (70 mbar @ 40 °C) and 3 mL of toluene were added. The suspension was concentrated again and redispersed in 3 mL of chloroform. 0.4 mmol of DIPEA (100 µL) and a suspension of N-(2-aminoethyl)-4-(pyren-1-yl)butanamide (0.2 mmol, 60 mg) in 1 mL of anhydrous THF were added dropwise at 0 °C. The ice bath was then removed and the mixture let stir overnight.

The suspension was quenched with TFA and filtrated (syringe and PTFE filter 0.2 µm), concentrated and redispersed in a little amount of chloroform. A SEC (200-400 mesh) in chloroform was performed to isolate a yellowish suspension.

6. ECL of chromophore-functionalised SiNCs

6.1. Introduction

In Paragraph 1.3.3 I briefly discussed the electrochemical properties of silicon nanocrystals, including their ECL behaviour. It is interesting that despite the advantage of using non-toxic nanomaterials, the ECL of silicon-based nanomaterials was not investigated in depth. Bard and co-workers pioneering reported the generation of ECL from blue-photoluminescent SiNCs, whose signal was, contrary to photoluminescence, size-independent.[54] Afterwards, Dong *et al.*[163,164] investigated the ECL biosensing applications of water-suspendable SiNCs, which were, however, synthesized with a severely criticized approach[62,63] and therefore it is not possible to correlate the ECL signal to silicon effectively. Porous silicon ECL was studied more extensively, but only few ECL cycles were stable and reproducible because of an irreversible oxidation.[360–365]

When we firstly synthesized DPA-functionalised SiNCs (see Chapter 2) we were curious about their ECL behaviour: both SiNCs and diphenylanthracene[149] are known to display electrochemiluminescence, and therefore we wondered if those emissions are influenced by the presence of each component, as it happens for photoluminescence (see Chapter 2).

Subsequently, we demonstrated that the electrochemigenerated emissions from the organic shell and the inorganic nanoparticle act independently: at different potentials it is possible to observe only one emission. Species like this one are known as "dual-potential" systems,[366–371] and have been investigated as ratiometric sensors, by recording the ECL intensities at the different potentials and calculating their ratio.

The advantages of DPA-functionalised SiNCs over the already existing systems, such as a unique heterosupramolecular species which act uniquely at negative potentials and a pair of ECL signals which can be in principle varied accordingly with the size of the nanoparticle and the type of attached chromophores, have been collected in one work of ours.[165] The contents of this chapter have been reprinted and adapted with permission from reference [165]. Copyright 2021, American Chemical Society.

6.2. Results and Discussion

In order to assess the effect of the chromophore and the dimensions on the ECL signal, we synthesised DPA-functionalised and dodecyl-passivated SiNCs with a diameter of 3 or 4 nm. The size of the core was modulated with the temperature of decomposition of the hydrogen silsesquioxane precursor (see Paragraph 1.3.1 for further details). The functionalisation with DPA has already been described in Chapter 2 and will be proposed in the Experimental Section of this chapter too. The passivation with a dodecyl chain, instead, was performed by direct hydrosilylation of hydride terminated silicon nanocrystals in the presence of diazonium salts (see Paragraph 1.3.1). For simplicity purposes, we will address to 3-nm sized dodecyl-passivated and diphenylanthracene-functionalised SiNCs respectively as **Si_{3nm}-DDE** and **Si_{3nm}-DPA**. In the same way, **Si_{4nm}-DDE** and **Si_{4nm}-DPA** are referred to 4-nm sized SiNCs. Figure 6.2.1 represents a schematisation of the different functionalised nanoparticles.

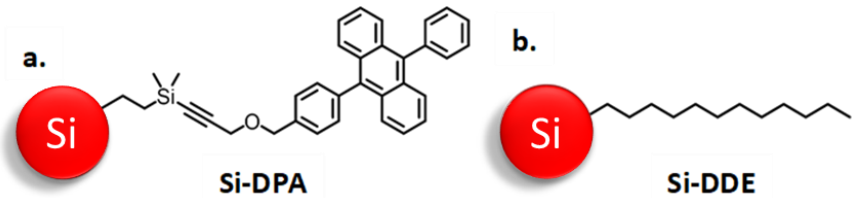

Figure 6.2.1 – Schematic representation of (a) 9,10-Diphenylanthracene-functionalized silicon nanocrystals (Si-DPA) and (b) dodecyl-passivated silicon nanocrystals (Si-DDE). For simplicity purposes, only one ligand per nanocrystal has been drawn.

At the beginning, to verify the reproducibility of the photoluminescence properties for nanoparticles with different sizes, a photophysical characterisation was performed on the samples. The absorption spectra of diphenylanthracene-functionalised SiNCs in tetrahydrofuran (solid blue lines in Figure 6.2.2) show the contribution of DPA (the absorption spectrum of the ligand alone is given in Figure 6.2.2, black line) with sharp peaks in the interval 350-410 nm and a tail due to silicon nanocrystals extending up to 550 nm. From the absorption spectra we can evaluate that 80 DPA units are linked per **Si_{4nm}-DPA** and 35 per **Si_{3nm}-DPA**, as an average (further details can be found in Chapter 2 and in the Appendix A.1). This results in an enhancement in the absorbance between 350 and 410 nm. The energy transfer to the silicon core, which has already been described in Chapter 2, occurs with an efficiency of 70%, followed by a sensitised emission of the inner silicon nanoparticle at 800 nm (solid red lines in Figure 6.2.2). This system acts as a light-harvesting antenna characterised by a brightness superior

to the alkyl-passivated silicon nanocrystals' one (exciting at 373 nm, DPA functionalisation led to a nearly 150% brightness enhancement in THF for **$Si_{4\,nm}$-DPA**).

Concerning the photoluminescence (red lines in Figure 6.2.2), it is possible to notice that dodecyl-passivated SiNCs are characterised by a blue-shifted emission with respect to DPA functionalised samples (this behaviour has been noticed also for pyrene-functionalised SiNCs).[74] The same occurs for smaller nanoparticles with the same functionalisation, confirming the size-dependency of the emission. In THF, the emission quantum yields (Φ) of the nanocrystals are, respectively:

a) Φ (**Si_{4nm}-DDE**) = 25%
b) Φ (**$Si_{4\,nm}$-DPA**) = 11%
c) Φ (**Si_{3nm}-DDE**) = 10%
d) Φ (**Si_{3nm}-DPA**) = 1%

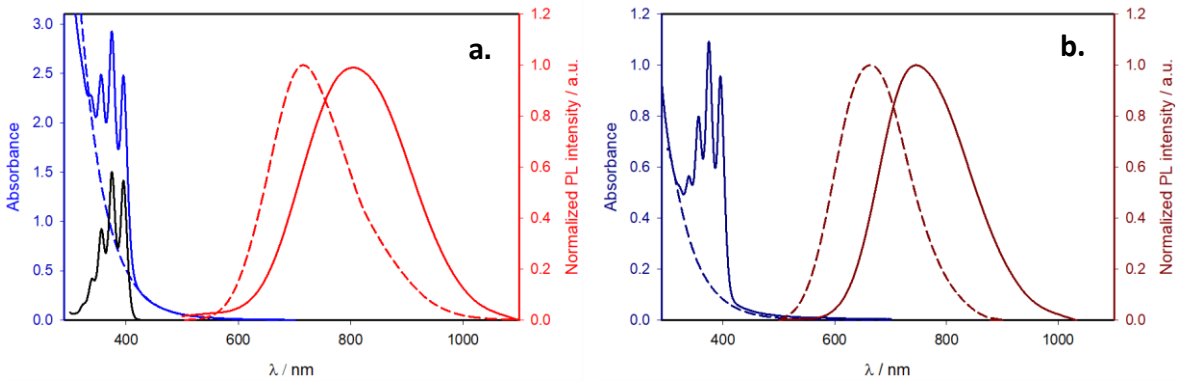

Figure 6.2.2 – Absorption (blue lines) and normalized photoluminescence spectra (red lines, excitation at 400 nm) of THF suspension of (a) 4-nm and (b) 3-nm sized DPA-functionalized SiNCs (solid lines) and dodecyl-passivated SiNCs (dashed lines). For comparison purposes, the absorption spectrum of DPA (black line) has been included in panel a.

The setup and the instrumentation used for electrochemistry measurements are described in the Experimental Section of this chapter. The first ones were performed in dichloromethane (DCM), using tetrabutylammonium hexafluorophosphate ($TBAPF_6$) as electrolyte and tripropylamine (TrPA) as coreactant. TrPA was chosen because it is known to act as coreactant for the ECL of porous silicon at positive potentials.[360] A cyclic voltammetry was performed (from OCV to 1.8 V vs Ag QRE back to 0 V vs Ag QRE). The electrochemiluminescence was collected with a P980 photomultiplier detector. The CVs and ECL signals are reported in Figure 6.2.3a and b respectively for dodecyl and DPA-functionalised SiNCs.

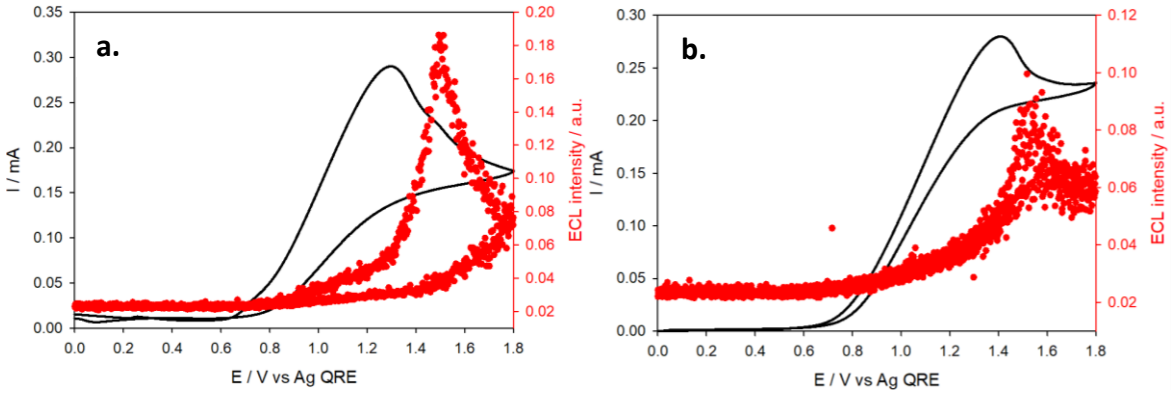

Figure 6.2.3 – Cyclic voltammetry (black lines) and ECL intensity (red dotted lines) of (a) ***Si$_{4\ nm}$-DDE*** *and (b)* ***Si$_{4\ nm}$-DPA*** *in DCM with TrPA as coreactant (first cycle).*[165]

The first cycle of ECL measurements for each sample showed a single oxidation peak at about 1.3-1.4 V vs Ag QRE followed by a single ECL peak assigned to the silicon core emission. For DPA-functionalised SiNCs sample, the signals are lower, probably due to the steric hindrance of the organic chromophore which avoids the approaching of the coreactant to the surface of the emitting nanocrystal. DPA, moreover, does not seem to participate to the electrochemiluminescence process in the considered experimental conditions. After the first cycle, a precipitation of Ag in the solution and an aggregation of the two samples were observed. The ECL signal for each dropped in the second cycle, even if the photoluminescence of the nanocrystals was still maintained. We believe that the oxidative conditions are not suitable for silicon quantum dots.

Therefore, the ECL measurements for dodecyl and DPA-functionalized SiNCs were replicated in different experimental conditions. Firstly, a different coreactant, benzoyl peroxide (BPO), was chosen instead of TrPA. This reagent is known to act as ECL coreactant with a so called "reductive-oxidation" mechanism with aromatic species.[372] At cathodic potentials, BPO is irreversibly reduced and it decomposes in a strong oxidizing species (benzoyloxy radical, PhCOO·), which is able to react with aromatic compounds reduced at the working electrode, yielding their corresponding excited state.

Moreover, tetrahydrofuran (THF) was chosen as solvent as the photoluminescence emission quantum yield of silicon nanocrystals are high, it is possible to introduce a lower amount of electrolyte and it is known to well dissolve every component of the mixture.

Cyclic voltammetries (from OCV to -2.5 V or -2.7 V vs Ag QRE and back to 0 V) were performed for equimolar suspensions of nanoparticles and are reported in Figure 6.2.4.

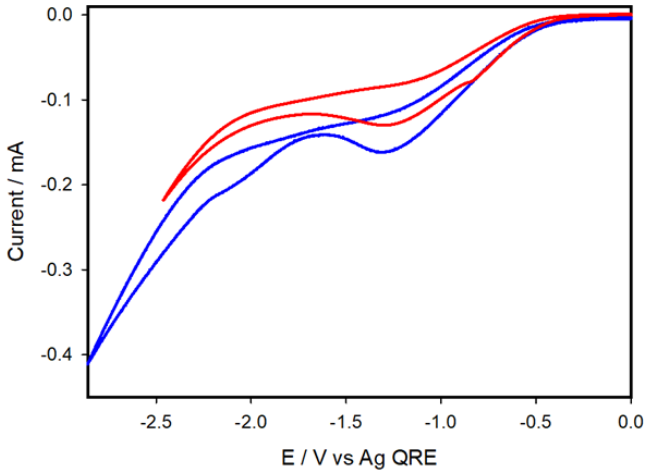

Figure 6.2.4 - Cyclic voltammograms of ***$Si_{3\ nm}$-DDE*** *(red line) and* ***$Si_{3\ nm}$-DPA*** *(blue line) in THF in the presence of BPO. Scan rate: 0.1 V/s.*

Due to the high concentration of BPO with respect to silicon nanoparticles and DPA only BPO reduction is visible (peak potential at -1.3 V, in accordance with the data found in literature[372]). The corresponding ECL signals are reported in Figure 6.2.5.

For 4-nm sized SiNCs (Figure 6.2.5a and b), electrochemiluminescence is observed at -2.0 V. For the **$Si_{4\ nm}$-DPA** sample (Figure 6.2.5b), a further ECL signal happens with maximum at -2.4 V. These two signals are attributed to SiNC and DPA electrogenerated emission, respectively. Indeed, upon registering ECL with a 550-nm cutoff filter, which eliminates the DPA emission, only the ECL signal at -2.0 V was observed (red dotted line in Figure 6.2.5b) as occurs for **$Si_{4\ nm}$-DDE** (Figure 6.2.5a). Performing the same measurements on 3-nm sized nanoparticles (Figure 6.2.5c and d for **$Si_{3\ nm}$-DDE** and **$Si_{3\ nm}$-DPA**, respectively), the ECL behaviour is similar to that observed for 4-nm nanoparticles apart from the fact that the emission associated to the silicon nanoparticle occurs at a lower potential (with a maximum comprised between -1.2 and -1.4 V). This behaviour has been attributed to the different dimension of the nanoparticles.

Under these experimental conditions, SiNCs are stable since repeated cycles of CV and ECLs are reproducible. To assess this, chronoamperometry and the trend of the ECL signal over cycles were performed and can be found in Figure 6.2.6.

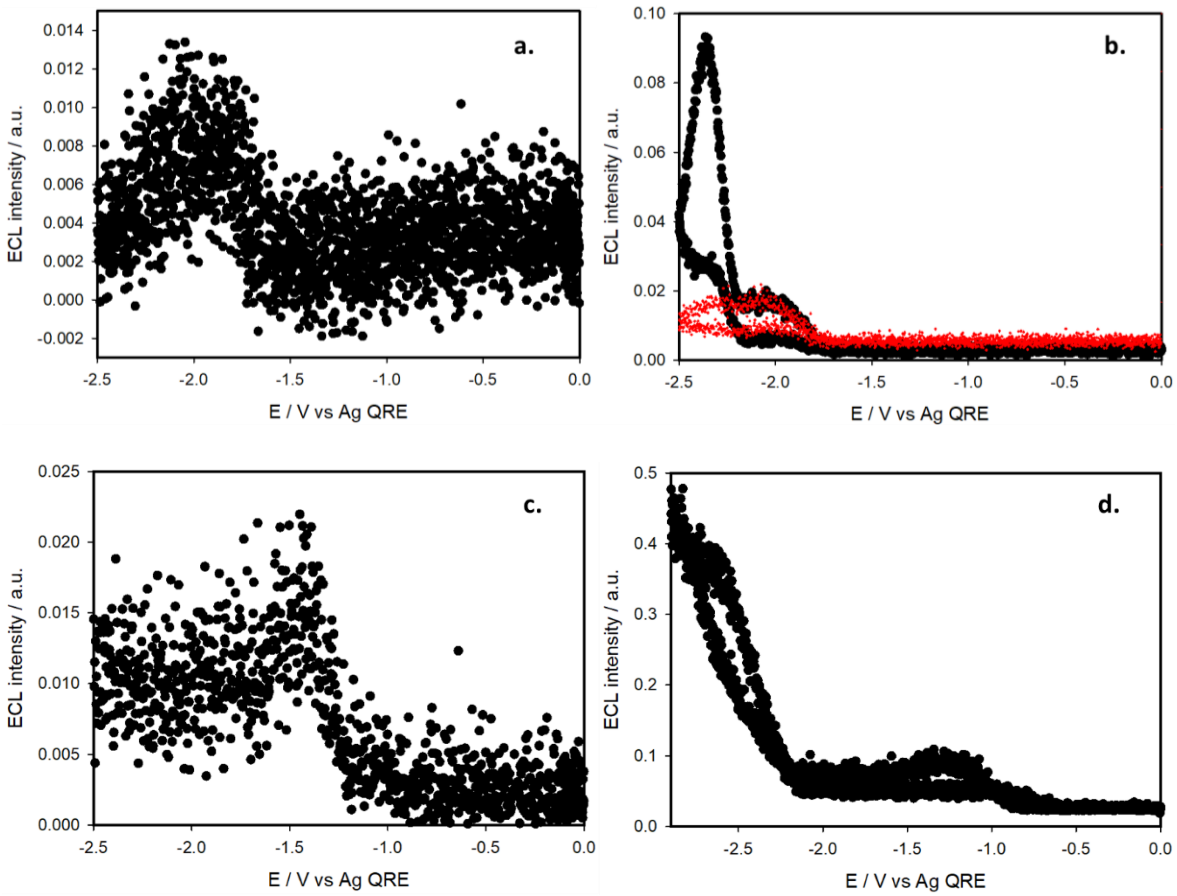

Figure 6.2.5 – ECL intensity of (a) ***Si$_{4\text{-}nm}$-DDE****, (b)* ***Si$_{4\ nm}$-DPA****, (c)* ***Si$_{3\ nm}$-DDE****, and (d)* ***Si$_{3\ nm}$-DPA*** *in THF with BPO as coreactant (first cycle). Scan rate: 0.1 V/s. Panel b reports also the ECL intensity registered with a 550-nm cutoff filter.*

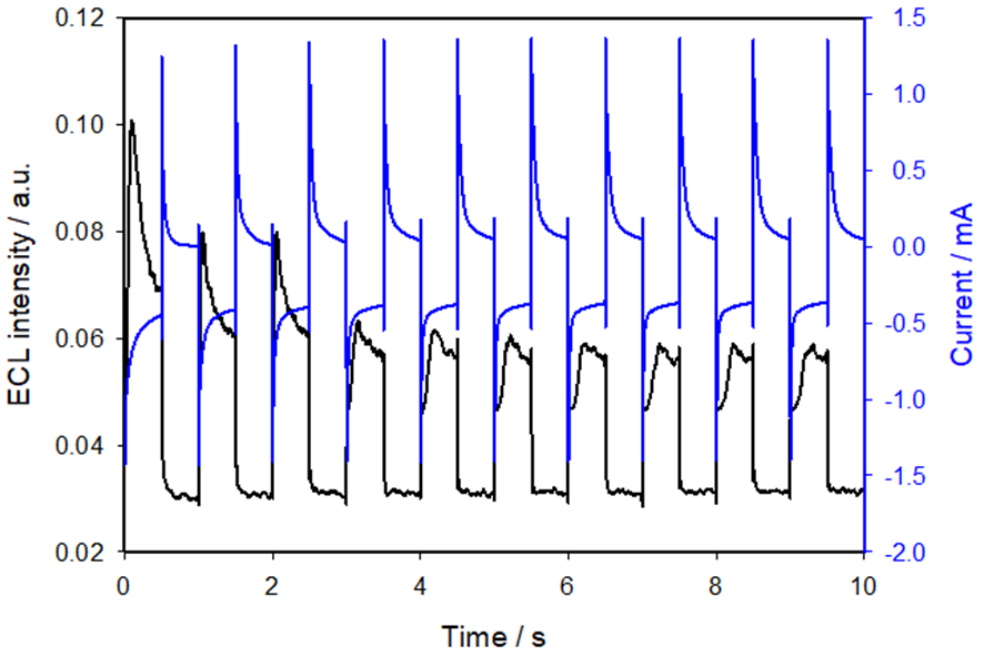

Figure 6.2.6 – Chronoamperometry (blue line) and ECL intensity (black line) over time of ***Si$_{3\ nm}$-DDE*** *in THF in the presence of 10 mM BPO. Steps of 0.5 s, alternating -2.5 V and 0 V.*

It is worth noting that, for the samples functionalised with diphenylanthracene (Figure 6.2.5c and d) the emission of silicon is far less intense than DPA's one. This is probably due to the high number of DPA units per SiNC, which enhances the probability for the coreactants to encounter the organic fluorophore, and the steric hindrance of DPA which does not facilitate the diffusion of the coreactants towards the silicon surface. On the other hand, the emission of the silicon is enhanced compared to the dodecyl-passivated samples (Figure 6.2.5a and c). A possible explanation is the different passivating molecules: 1-dodecene or chloro(dimethyl)vinylsilane for the first step of passivation with diphenylanthracene. The capping with the chlorosilane can result in a lower surface coverage compared to the alkyl chain, resulting in a better accessibility for the BPO coreactant in the diphenylanthracene containing sample.

In order to understand if silicon ECL is influenced by DPA, as it occurs for photoluminescence, ECL spectra were performed at different potentials (-2.0 V, -2.4 V and -2.5 V vs Ag QRE for **$Si_{4\ nm}$-DPA**, -2.0 and -2.7 V for **$Si_{3\ nm}$-DPA**). The emissions are collected in Figure 6.2.7.

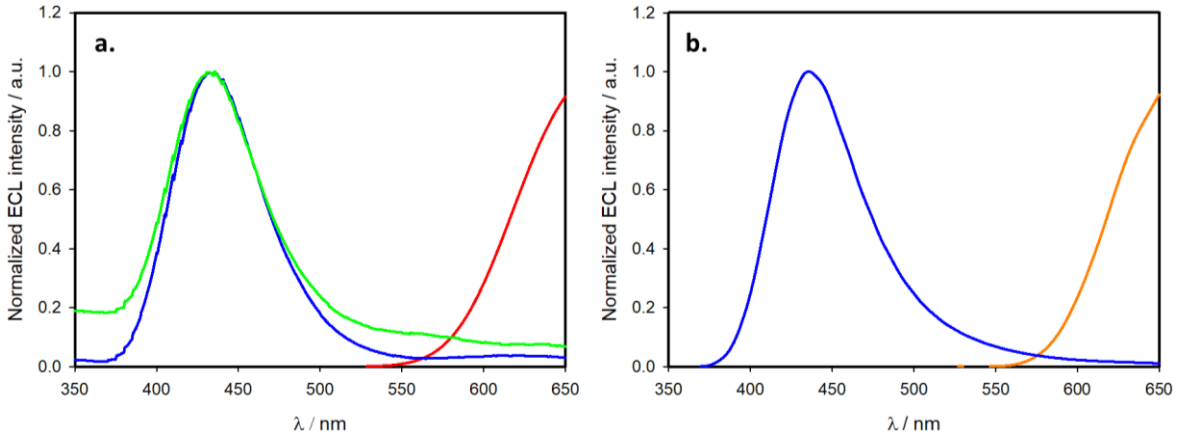

*Figure 6.2.7 – ECL spectra of (a) **$Si_{4\ nm}$-DPA** sample in THF with BPO as coreactant recorded at -2.0 V (red line), -2.4 V (blue line) and -2.5 V (green line) vs Ag QRE, (b) **$Si_{3\ nm}$-DPA** at -2.0 V (orange line) and -2.7 V (blue line).*

For the spectra recorded at -2.0 V, a single emission band is visible and it is associated to the silicon nanoparticle luminescence (red line in Figure 6.2.7a and orange line in Figure 6.2.7b). Unfortunately, the emission maximum is outside the sensitivity range of the photomultiplier used for ECL experiments, so that a direct comparison with the photoluminescence spectrum reported in Figure 6.2.2 is not possible. The DPA emission is not visible, confirming that at the potential under

consideration, the organic chromophore is not reduced. Only the SiNC is reduced, the benzoyloxy radical reaches the quantum dot and the exciton is formed.

It is interesting however that the ECL spectrum of SiNCs (Figure 6.2.7) is reminiscent of their PL spectrum (Figure 6.2.2), even if only the high energy part can be observed in the ECL experiment for the different detector sensitivity. On the other hand, Bard[54] reported a strongly red-shifted ECL spectrum for SiNCs compared to their PL spectrum: this shift was attributed to different emissive states, in particular from the surface, where the energy gap was smaller.

Performing the measurements at lower potentials, the obtained ECL spectra look different (Figure 6.2.7, blue and green lines). In each case, only one significant emission is shown and it is attributed to the DPA. To verify this, cyclic voltammetry (from OCV to -2.5 V vs Ag QRE and back to 0 V) and the ECL spectrum were performed on an 80 µM solution of 9,10-diphenylanthracene in THF containing 10 mM BPO and 300 mg of $TBAPF_6$ at a scan rate of 0.1 V/s. The results and are reported in Figure 6.2.8a and b respectively.

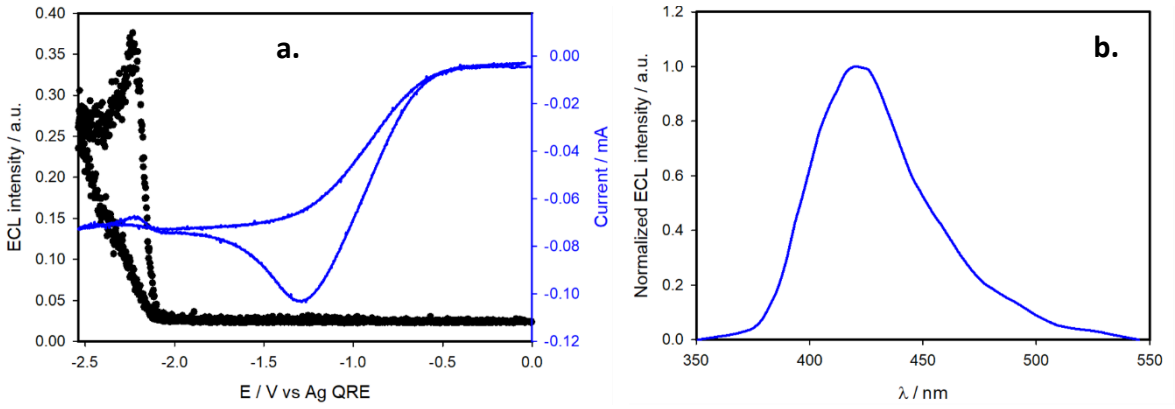

Figure 6.2.8 – (a) ECL intensity (black dots) of DPA in THF with BPO as coreactant (first cycle) and cyclic voltammograms (blue line) obtained with a scan rate of 0.1 V/s. (b) ECL spectrum recorded at -2.5 V vs Ag QRE.

Unlike photoexcitation, the experiment suggests that the antenna effect does not take place in consequence of the electrogenerated excitation of DPA. Our explanation is that at potentials more negative than -2.4 V vs Ag QRE, both the organic chromophore and the silicon nanocrystal are reduced. Benzoyloxy radical, before reaching the surface of silicon quantum dot, encounters the reduced DPA and generates its excited state. The energy transfer process to the SiNC does not occur, likely made unfavourable by the presence of extra electrons in the conduction band of silicon, and the emission

of DPA can take place without being affected (a schematisation of the occurring processes is reported in Figure 6.2.9).

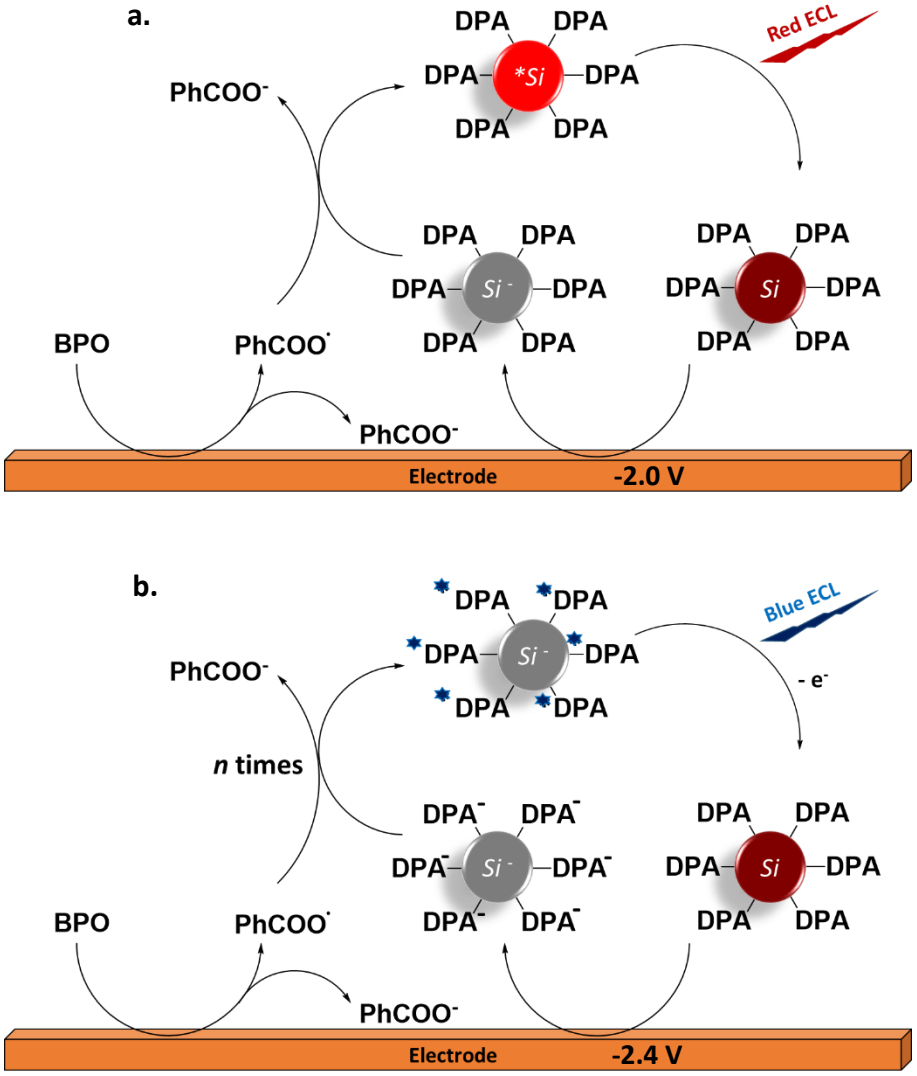

Figure 6.2.9 – Mechanism of electrochemiluminescence of diphenylanthracene-functionalised SiNCs at (a) -2.0 V and (b) -2.4 V with BPO as coreactant.

6.3. Conclusions

After having analysed the photophysical properties of diphenylanthracene-functionalised SiNCs, we were aimed to assess also the ECL behaviour. While the photoluminescence of the organic chromophore is influenced by the presence of the inorganic nanoparticle (i.e. it is quenched) and *vice versa* (the band edge luminescence of the quantum dot is sensitised), we observed that the electrochemigenerated luminescences act independently. Therefore, it is possible to separate the emissions of the SiNC or the diphenylanthracene performing the measurements at different

potentials. Systems like this fall under the definition of dual-potential ECL emitters. The peculiarity of this one is the sign of the applied potentials at which the ECLs occur, which is always cathodic. This is important if the electrochemical stability of the solvent does not allow to span a wide range of potentials.

A further step of investigation could be the functionalisation of SiNCs with chromophores that are reduced at less negative potentials. In this case, there would be a situation in which the organic moiety is excited while the inner nanoparticle is at its ground state. Similar situations are difficult to obtain by photoexcitation. If quenching occurred, that could be useful to study the dynamics of energy transfer to silicon nanocrystals.

6.4. Experimental Section

All reagents were purchased from Sigma-Aldrich and used without further purification if not stated otherwise. Dry toluene was obtained via distillation over calcium chloride under nitrogen atmosphere. N,N,N',N'-tetramethylethylenediamine was refluxed over fresh KOH and distilled under nitrogen.

6.4.1. Synthesis of silicon nanocrystals

Despite the general syntheses have already been described in Chapter 2, several differences concerning the obtainment of smaller nanoparticles and dodecyl-passivated ones are included. Therefore, the procedures will be briefly written.

6.4.1.1. Preparation of oxide-embedded and hydride-terminated silicon nanocrystals

Hydrogen silsesquioxane (HSQ) was prepared from $HSiCl_3$ as starting material following a reported procedure,[73] dried under vacuum and transferred into a tube furnace. After purging with reducing gas (95% N_2, 5% H_2), the tube furnace was heated to 1100 °C or 1025 °C at a rate of 18 °C/min and then held at that temperature for an hour. The resulting solid was cooled to room temperature, manually and mechanically reduced into brown powder (that is $Si@SiO_2$, i.e. SiNCs embedded in a silica matrix) and stored in a glass vial. The sizes of the nanoparticles obtained by this process were determined by the temperature of annealing of HSQ, as reported in literature.[79] At 1100 °C, SiNCs with a diameter of about 4 nm were obtained, while at 1025 °C, nanoparticles with about 3-nm diameter were formed.

Hydride-terminated silicon nanocrystals were liberated from the silica matrix by HF etching (***caution!*** *HF is very dangerous and must be handled very carefully!)*: 300 mg of oxide-embedded silicon nanocrystals were dispersed in a mixture composed of 3 mL of ethanol, 3 mL of bi-distilled water and 3 mL of a 49% solution of aqueous HF. The mixture was stirred for 90 minutes under ambient light at room temperature. The nanocrystals were extracted with toluene (3x10 mL) and then centrifuged three times in toluene (8000 rpm for 5 minutes). The nanocrystals were then transferred in a dry box.

6.4.1.2. Passivation with chloro(dimethyl)vinylsilane or 1-dodecene (Si-DDE)

The nanocrystals were dispersed in 4 mL of dry toluene and split in two portions. Two milligrams of 4-decyldiazobenzene tetrafluoroborate (about 6 μmol) were added in each one. Afterwards, in a mixture, 200 μL of chloro(dimethyl)vinylsilane (1.5 mmol) were introduced to obtain chlorosilane-passivated silicon nanocrystals. In the other one, 330 μL of 1-dodecene (1.5 mmol) were dropped, to passivate the nanocrystals with an alkyl chain. Both mixtures were stirred overnight at room temperature. The mixture of chlorosilane-passivated SiNCs was then filtered, concentrated at reduced pressure, transferred again in the dry-box, diluted with 2 mL of dry toluene and conserved for a further functionalization. The suspension of dodecyl-passivated nanocrystals was precipitated by adding methanol and centrifuged three times washing with methanol. The precipitate was dissolved in dichloromethane (DCM) or inhibitor-free tetrahydrofuran (THF), obtaining **Si_{3nm}-DDE** and **Si_{4nm}-DDE** indicating dodecyl-passivated SiNCs with an average diameter of 3 or 4 nm.

6.4.1.3. Functionalisation of silicon nanocrystals with diphenylanthracene (Si-DPA)

0.3 mmol of 9-phenyl-10-(4-((prop-2-yn-1-yloxy)methyl)phenyl)anthracene were introduced in a flask containing 0.45 mmol of N,N,N',N'-tetramethylethylenediamine (TMEDA) and 3 mL of dry toluene. At -78 °C, 0.3 mmol of n-butyllithium (nBuLi) 2.5 M in hexanes were added dropwise under inert atmosphere (***caution!*** *n-butyllithium is pyrophoric!*). The mixture was stirred for 45 minutes at -78 °C and 15 minutes at room temperature. Again at -78 °C, a suspension of chlorosilane-passivated silicon nanocrystals in toluene was slowly added to the reaction mixture. One hour later, the reaction mixture was stirred for an hour at room temperature. Later, it was heated to

40 °C, and stirred for another hour. At -78 °C a second amount of nBuLi (0.15 mmol) was added before letting the mixture stir overnight at room temperature. The reaction was quenched with several mL of a 1 M solution of HCl in MeOH. The precipitate was washed 3 times with methanol, centrifuging (8000 rpm, 5 minutes) and then dispersed in chloroform. A size exclusion chromatography over BioBeadsTM S-X1 Support (200-400 mesh) was performed to isolate a brown limpid suspension, yielding the Si-DPA samples (**Si_{3nm}-DPA** or **Si_{4nm}-DPA** for, respectively, diphenylanthracene-functionalised SiNCs with an average diameter of 3 or 4 nm). ^{1}H-NMR ($CDCl_3$, 400 MHz) was used to assess the occurring of the functionalisation (Chapter 2). The sample was then dispersed in DCM or inhibitor-free THF.

6.4.2. ECL apparatus and ECL measurements

ECL and electrochemical measurements were carried out with an AUTOLAB electrochemical station (Ecochemie, Mod. PGSTAT 30). The ECL signal generated by performing the potential step program was measured with a photomultiplier tube (PMT, Hamamatsu P980) placed, at a constant distance in front of the working electrode, under the cell and inside a homemade dark box. A voltage in the range 550−750 V was supplied to the PMT. The light/current/voltage curves were recorded by collecting the preamplified PMT output signal (by an ultralow noise Acton research model 181) with the second input channel of the ADC module of the AUTOLAB instrument. ECL spectra have been recorded by inserting the same PMT in a dual-exit monochromator (ACTON RESEARCH model Spectra Pro2300i) and collecting the signal as described at a fixed voltage vs Ag QRE. Photocurrent detected at PMT was accumulated for 1-3 s, depending on the emission intensity, for each monochromator wavelength step (usually 1 or 2 nm).

For ECL measurements, a cylindrical three electrodes electrochemiluminescence cell with PTFE stopcock and a Schlenk-like connection to the vacuum-inert gas line was used. As working electrode, platinum was chosen, as quasi-reference electrode, silver, and as counter electrode, a spiral-shaped platinum wire.

For the measurements in dichloromethane (DCM), a batch of dodecyl-passivated or DPA-functionalised SiNCs derived from the etching of 100 mg of $Si@SiO_2$ powder in 3 mL of DCM (about 1 µM) was introduced in the cell. 500 mg of $TBAPF_6$ (0.4 M) and 50 µL of tripropylamine (TrPA) (0.08 M) were subsequently added. The suspension was

degassed with Ar. For the measurements in tetrahydrofuran (THF), the same procedure was performed, but 300 mg of $TBAPF_6$ (0.25 M) and 10 mg of benzoyl peroxide, BPO, (10 mM) were added instead in 3 mL of solvent. In each solution, two or three records were made to check the temporal stability of the system investigated.

7. Light-harvesting antennae based on CIS@ZnS QDs

7.1. Introduction

As reported in Paragraph 1.5, I exploited the period that I spent at the University of Leeds, in Dr. Kevin Critchley's Molecular and Nanoscale Physics group, learning how to synthesize copper indium sulphide (CIS) quantum dots. The main difference in the physics between CIS QDs and SiNCs is the nature of the band gap, which is direct for the former, indirect for the latter. A direct band gap renders the transitions in absorption more favourable, yielding nanoparticles with a higher molar absorption coefficient over the entire visible spectral range. The reader will remember that this is the main issue of silicon quantum dots, from which the necessity of introducing chromophores onto their surface and the formation of light-harvesting antennae.

The method I was taught to synthesize CIS QDs is a *heating-up* procedure, in which the components of the nanoparticles (the precursors of copper and indium) are mixed together, dissolved in an alkyl thiol and a non-coordinating high-boiling solvent. At temperatures higher than 180 °C, the thiol decomposes providing sulphide anions. At 200 °C, the nucleation occurs and the nanoparticles grow until the reaction mixture is immersed in a cold-water bath. The so-obtained nanoparticles are low emissive, due to the presence of surface trap state. The growth of a ZnS shell (the resulting core-shell nanoparticles will be indicated as CIS@ZnS QDs) can drastically improve the photoluminescence quantum yield, also by a 10-folder factor, or even more. Details on the synthesis can be found in Paragraph 1.5.2 and in the Experimental Section of the current chapter. The mentioned synthesis allows to obtain nanoparticles stabilized with purely alkyl chains provided by the thiol reagent. For this reason, the nanoparticles are suspendable only in non-polar solvents like toluene or chloroform.

Among the various strategies adopted to transfer the CIS QDs in aqueous phase (described more in detail in Paragraph 1.5.2), ligand exchange is one of the most exploited.[227] In particular, the replacement of the native thiol with dihydrolipoic acid or a derivative (usually an ester or an amide of a poly(ethylene)glycol) is well-suited, due to the higher stabilization that the two anchoring thiol moieties provide.[321,322,373]

Unfortunately, the examples reported in literature show a severe decrease of the emission quantum yield, even in the case of CIS with a ZnS shell.

In this context, the enhancement of the brightness provided by the coating of the nanoparticle's surface with appropriate chromophores can be pivotal. However, despite only few examples of hybrid organic-inorganic CIS QDs are reported, the emissive properties of the inner nanoparticle did not improve or even deteriorated.[325–327,374,375] For instance, a quenching of the CIS QDs occurred *via* Forster resonance energy transfer,[375] or electron transfer,[325] while the photoluminescence was recovered when the chromophore was separated.

We described for the first time the functionalisation of CIS and CIS@ZnS QDs with a pyrene-containing dihydrolipoamide. The resulting nanoparticles are characterised by a superior absorption below 350 nm and a sensitised emission of the CIS QD upon pyrene excitation due to energy transfer from the organic chromophore towards the quantum dot. This represents the first example of a light-harvesting antenna based on copper indium sulphide quantum dots with enhanced brightness compared to the corresponding sample without pyrene chromophores at the surface. The contents of this chapter have been reprinted and adapted with permission from reference [376] with permission from the Royal Society of Chemistry.

7.2. Results and Discussion

Copper indium sulphide (CIS) QDs with or without a ZnS shell (hereafter named **CIS@ZnS QDs** and **CIS QDs**, respectively) were synthesized according to a heating-up procedure adapted from literature.[257] The produced nanoparticles were stabilized and coated with an organic shell composed of 1-octanethiol, which allows a good dispersibility in non-polar solvents like chloroform. Afterwards, a partial ligand exchange with 6,8-dimercapto-N-(pyren-1-ylmethyl)octanamide (compound **2**) was performed. This molecule was chosen since it contains a dihydrolipoic acid-derivative moiety and therefore possesses two thiol groups that reinforce the interaction with the surface of the nanoparticle and therefore allows a more efficient replacement with the native mono-thiol ligand.[251] This was obtained firstly by amide coupling between lipoic acid and 1-pyrenemethylamine, followed by reduction of the sulphur-sulphur bond. The overall synthetical procedure is represented in Figure 7.2.1. Ligand exchange was accomplished on both shelled and pristine quantum dots, yielding the samples named **CIS@ZnS-py QDs** and **CIS-py QDs**, respectively.

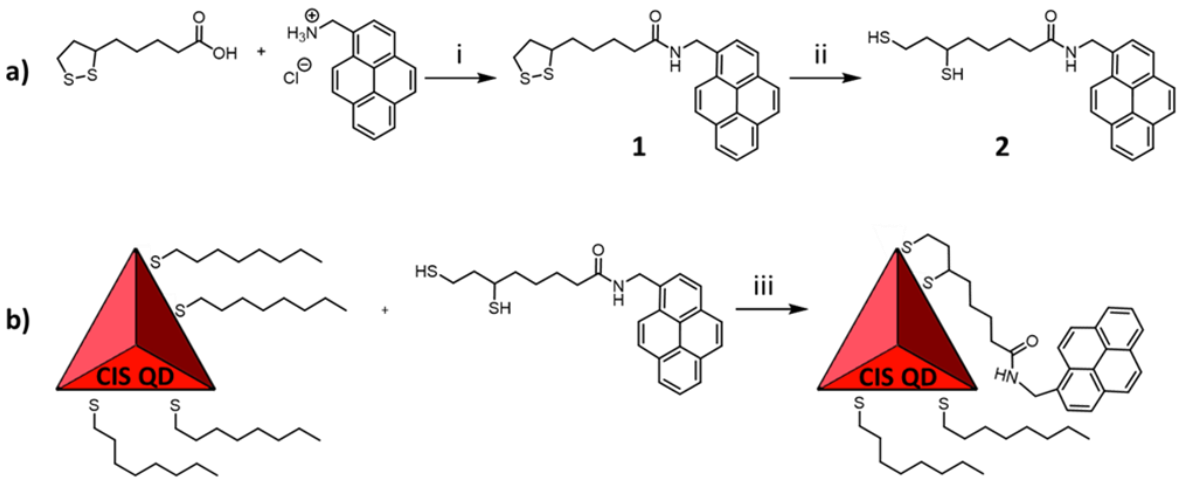

Figure 7.2.1 – Schematic representation of the adopted strategy to functionalize copper indium sulphide QDs with pyrene. (a) The synthesis of the ligand involves firstly an amide coupling between (±)-α-lipoic acid and 1-pyrenemethylamine hydrochloride, yielding compound 1, followed by the reduction of the S-S bond, producing compound 2 (reaction conditions: i – HBTU, EDC, DIPEA, in DMF, 1 day; ii – $NaBH_4$ in DMF/water, 4 hours). (b) Ligand exchange to 1-octanethiol passivated CIS QDs or CIS@ZnS QDs (iii – chloroform, overnight) For simplicity purposes, few ligands per nanocrystal have been drawn.

The high magnification STEM image of the sample **CIS@ZnS QDs** is reported in Figure 7.2.2 a. The chalcopyrite crystalline phase was determined by high resolution micrographs and select area electron diffraction (SAED) evaluation (Figure 7.2.2 b).

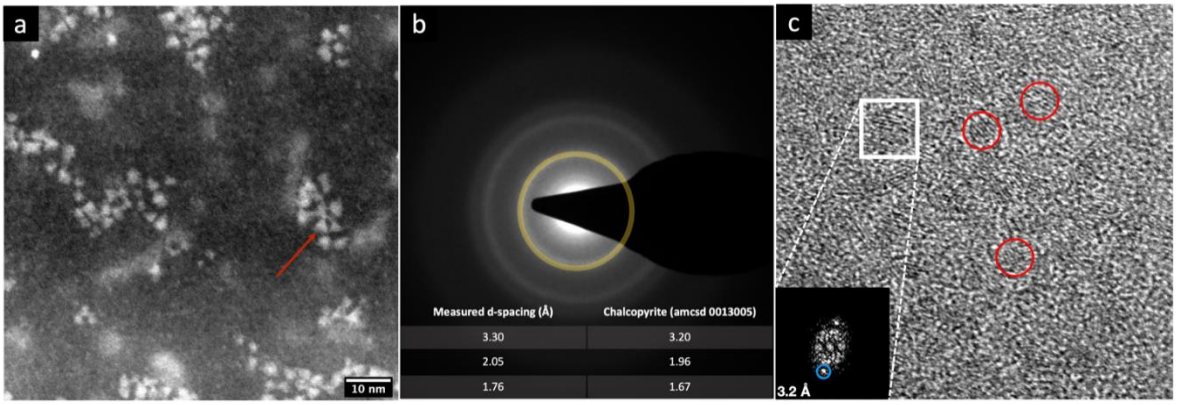

*Figure 7.2.2 – (a) High magnification STEM micrographs of the **CIS@ZnS QDs**; (b) Selected area electron diffraction (SAED) of **CIS@ZnS QDs**; (c) high resolution (HR) TEM image of **CIS@ZnS QDs**. The FFT (fast Fourier transform) in the inset refers to the zone highlighted with the white square.*

The distribution of the particles dimension is quite heterogenous with values from 2.5 nm up to 4 nm. The morphological characterization shows a triangular shape, particularly evident for some of the nanoparticles (see for example the one indicated by the red arrow in Figure 7.2.2 a), consistent with the tetrahedral shape previously reported in literature.[257] High resolution micrograph (Figure 7.2.2 c) confirms the

crystalline character of the nanoparticles (indicated by the red circles). The lattice spacing of 0.32 nm reported in the fast Fourier Transform inset (relative to the particle in the white square in Figure 7.2.2 c) is compatible with a tetragonal chalcopyrite phase.

^{1}H-NMR spectroscopy was used to verify the presence of pyrene attached onto CIS QDs surface. Figure 7.2.3 shows the overlap between the spectrum of compound **1** (green line) and **CIS@ZnS-py QDs** (red line) in $CDCl_3$.

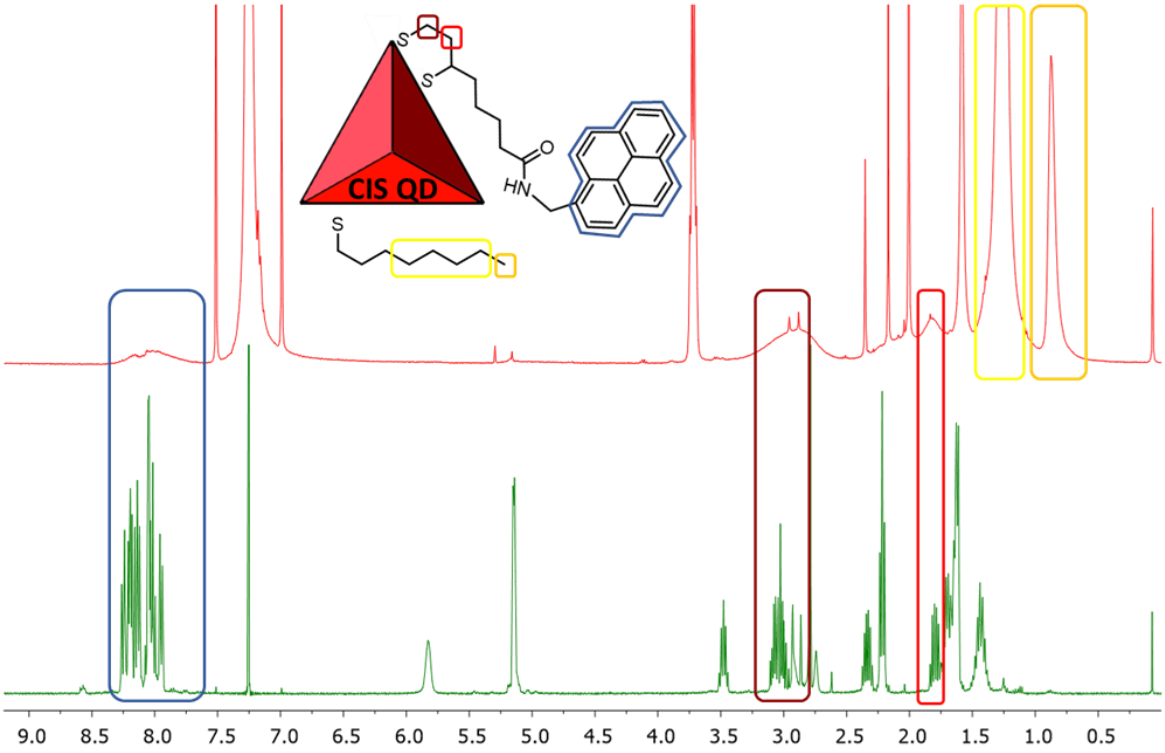

*Figure 7.2.3 – ^{1}H-NMR (400 MHz, $CDCl_3$) spectra of compound **1** (green line) and **CIS@ZnS-py** (red line), which is schematized in the inset. The principal signals are highlighted to show the broadening of the peaks related to the attached molecules.*

The principal peaks are highlighted and associated to the protons of the molecule represented in the inset. The chemical shifts of the aromatic protons occur at around 7.7-8.3 ppm; at 3.0-3.5 ppm it is possible to distinguish the signal due to the hydrogens in alpha position with respect to the sulphur atoms, at 2.0-2.2 ppm the band related to the protons linked to the carbon in proximity of the carboxylic group, while at about 1.2-1.4 ppm, the signals of the alkyl thiol chain are predominant, indication of a non-complete replacement of the native ligand. It is worth noting that the signals related to the hydrogens of the ligand attached to the quantum dot appear broadened due to the restricted motions that cause an enhancement of the relaxation times, as we also

observed in previous works.[105,106] For comparison purposes, the NMR spectrum of the physical mixture compound **2 – CIS@ZnS QDs** is reported in Figure 7.2.4, which shows the structure of the multiplicity of the detached ligands.

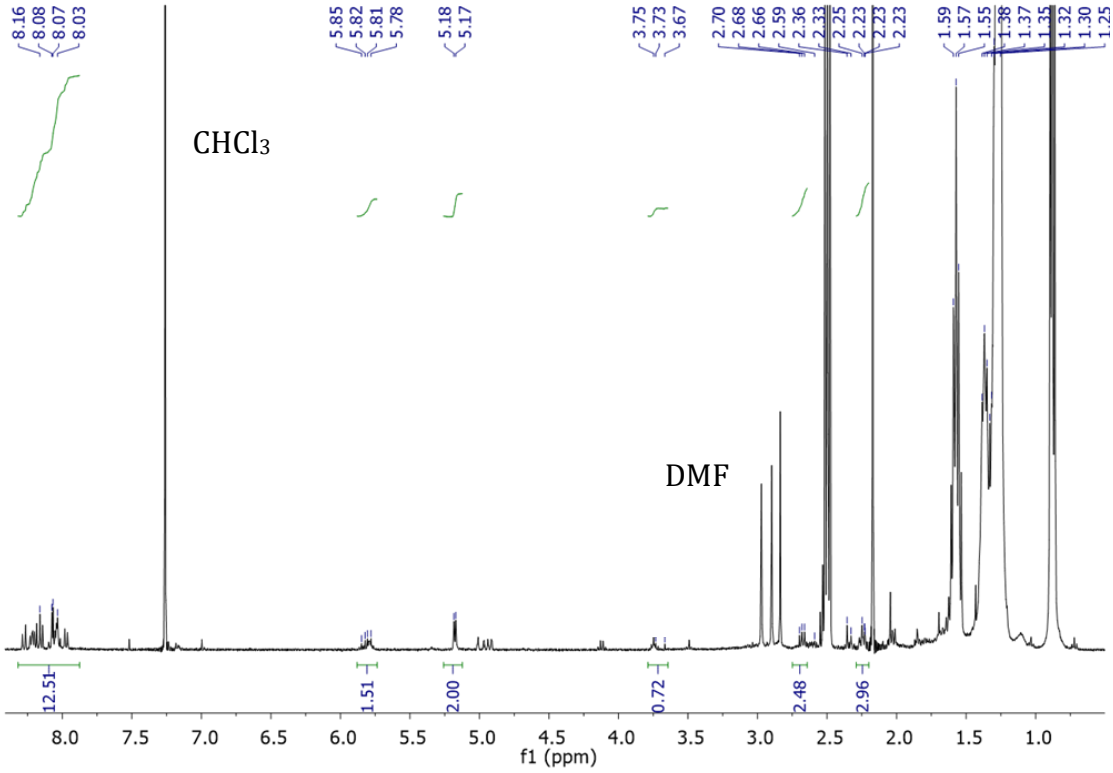

*Figure 7.2.4 – ^{1}H-NMR ($CDCl_3$, 400 MHz) spectrum of a mixture of free compound **2** and **CIS@ZnS QDs**.*

The absorption spectra of all the investigated sample of CIS QDs (Figure 7.2.5) show the characteristic shoulder that corresponds to the band gap transition.

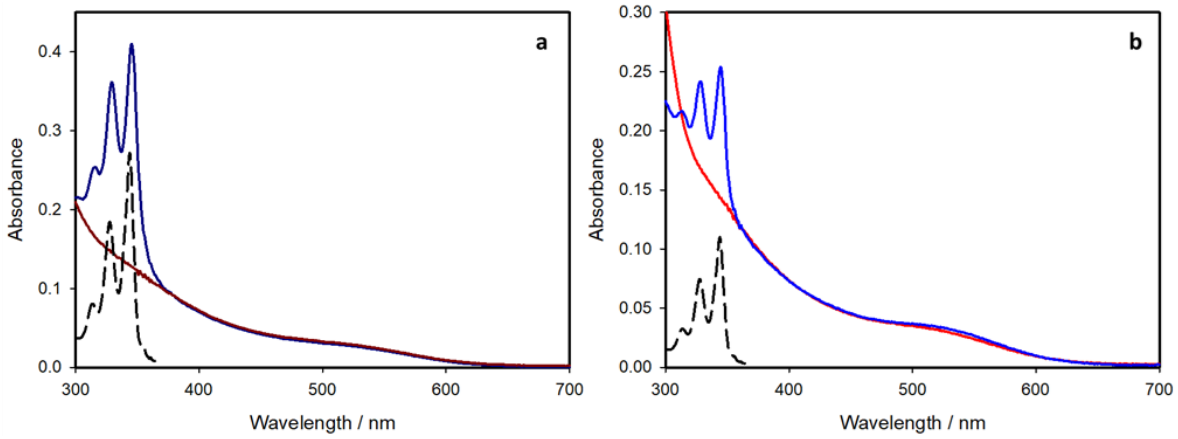

*Figure 7.2.5 – Absorption spectra of (a) **CIS QDs** (dark red line) and **CIS-py QDs** (dark blue line) and (b) **CIS@ZnS QDs** (red line) and **CIS@ZnS-py QDs** (blue line) in chloroform, compared to the absorption spectrum of pyrene (black dashed line).*

To better determine the corresponding wavelength, the local minimum of the second derivative of the spectra in the range 400-600 nm was evaluated, according to a procedure reported in literature.[253] In every case, the electronic transition occurs at 530 nm, corresponding to an energy gap of about 2.3 eV.

In the case of the pyrene-functionalized samples (blue lines), the typical absorption features of CIS QDs are overlapped to those of pyrene, clearly visible at 300-350 nm (black dashed lines). Since each component maintains its own absorption properties, no significant interaction occurs between the organic chromophore and the inorganic nanoparticle in the ground state.

The average number of chromophores per nanocrystal can be estimated by the absorption spectra, if the molar absorption coefficients (ε) of the present species are known. The molar absorption coefficient of the pyrene-based ligand is 4×10^4 $M^{-1}cm^{-1}$ at 345 nm. For CIS QDs, we relied on the work from Booth et al.[253] who correlated the photophysical properties of copper indium sulphide quantum dots to their size. From their formula (reported in Paragraph 1.5.3), it was possible to estimate the diameter of the CIS core for the samples, which is 3.6 nm and 2.7 nm for the shell-free and the ZnS-coated samples, respectively, which is in good accordance with the data obtained by TEM analysis. Moreover, the molar absorption coefficient can be computed at 530 nm (i.e. the first electronic transition), using the formula reported also in Paragraph 1.5.3, which is:

$$\varepsilon_{CIS\ QD}(530\ nm) = (830)d^{3.7}$$

where d is the diameter in nanometers and the result is expressed in $M^{-1}cm^{-1}$. Consequently, at 530 nm, where pyrene does not absorb, the molar absorption coefficients for **CIS QDs** and **CIS@ZnS QDs** are 9.5×10^4 $M^{-1}cm^{-1}$ and 3.3×10^4 $M^{-1}cm^{-1}$, respectively. From these data the average number of pyrene moieties per nanocrystals is estimated to be about 20 for **CIS-py QDs** and 3 for **CIS@ZnS-py QDs**. In our opinion, this discrepancy can be due to a different surface reactivity towards the dihydrolipoamide either because of the different composition exposed ($CuInS_2$ or ZnS), or because of the different dimensions of the nanoparticles.[377]

Exciting at 450 nm, where the pyrene chromophores do not absorb, the emissions recorded from the nanocrystals possess a bell-shaped band centred at about 710 nm

for the shell-free quantum dots and 650 nm for the ZnS-coated ones (Figure 7.2.6). This blue-shift is well-known for such core-shell QDs and is associated to an interdiffusion of zinc ions into the CIS core[301] and an etching of the core material.[257]

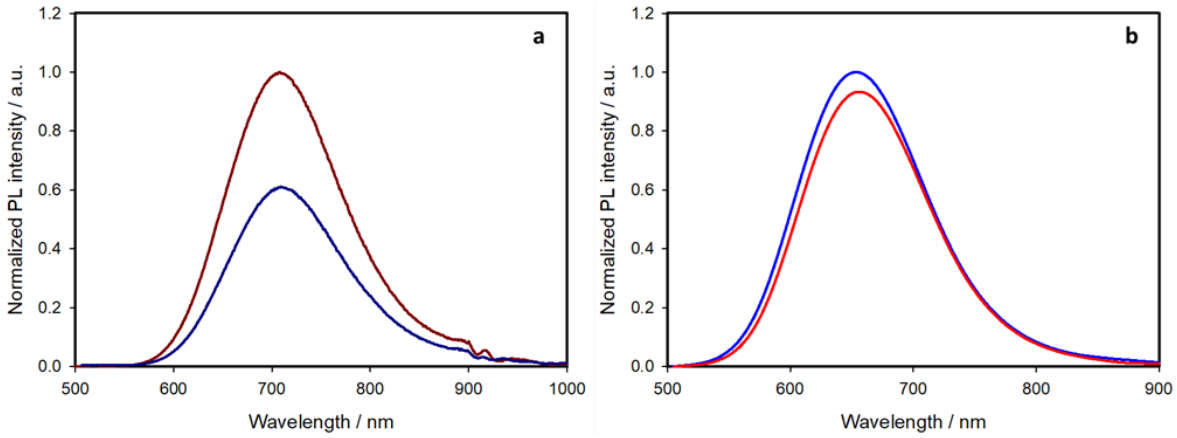

Figure 7.2.6 – Emission spectra corrected for the emission quantum yields of (a) ***CIS QDs*** *(dark red line) and* ***CIS-py QDs*** *(dark blue line) and (b)* ***CIS@ZnS QDs*** *(red line) and* ***CIS@ZnS-py QDs*** *(blue line) in chloroform, exciting at 450 nm. The relative intensities in each panel reflect the corresponding emission quantum yields.*

The photophysical data of the samples recorded are collected in Table 7.2.1.

Table 7.2.1 – Main photophysical properties of the studied quantum dots in air-equilibrated chloroform suspension.

	Pyrene emission		**Quantum dot emission**		
	λ_{em} (nm)	τ (ns)[a]	λ_{em} (nm)	τ (ns)[b]	PLQY (%)[c]
CIS QDs	-	-	710	70	1.9
CIS-py QDs	395	1.4 (0.08) 20 (0.02)	710	50	1.2
CIS@ZnS QDs	-	-	650	350	28
CIS@ZnS-py QDs	395	1.0 (0.04) 20 (0.01)	650	260	30

[a] Excitation at 340 nm, emission at 390 nm (pre-exponential factor between brackets). [b] Weighted average lifetime, excitation at 405 nm, emission at the corresponding maximum. [c] Excitation at 450 nm.

It is possible to notice a remarkable increase in the emission quantum yield when coating the nanocrystals with a ZnS shell, as frequently reported in the literature.[250,252,257] Two opposite behaviours are observed after ligand exchange. For the pristine nanoparticles, the emission quantum yield slightly decreases, as already reported in the literature, a phenomenon associated to the introduction of surface defects.[250,272,378] On the other hand, the quantum yield of the shelled sample slightly increased.

Exciting at 345 nm, where also pyrene absorbs, the situation is quite different (Figure 7.2.7) and two additional bands appear. A structured band due to the emission

of pyrene monomer is visible with maximum at about 400 nm, while a broad band peaked at 480 nm can be correlated to the emission of the excimer of pyrene (its lifetime was measured and resulted in 30 ns).

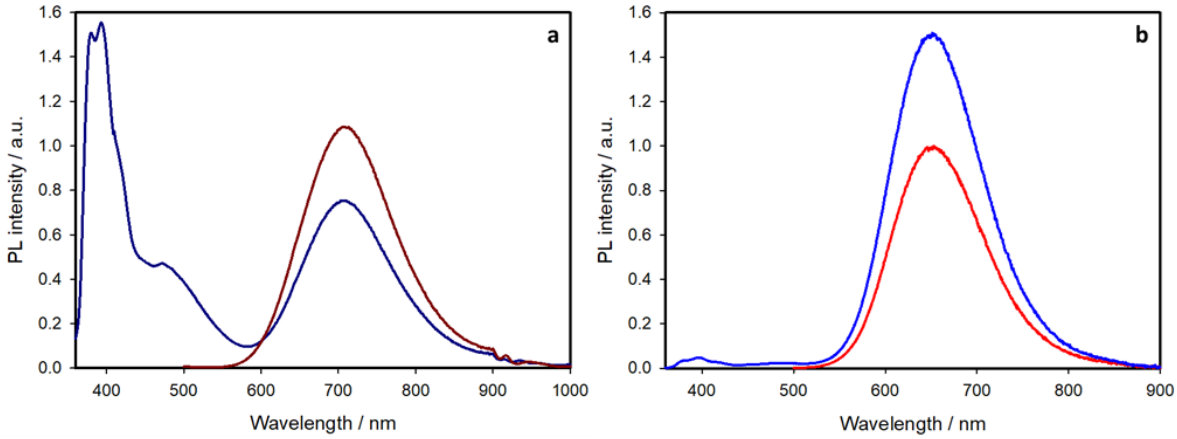

Figure 7.2.7 – Emission spectra of equimolar suspensions of (a) ***CIS QDs*** *(dark red line) and* ***CIS-py QDs*** *(dark blue line) and (b)* ***CIS@ZnS QDs*** *(red line) and* ***CIS@ZnS-py QDs*** *(blue line) in chloroform, exciting at 345 nm. The emission spectra in (a) are magnified by a 16 factor for comparison purposes.*

For a solution of free pyrene chromophores, excimer emission is observed only at concentration higher than about 10^{-4} M.[379] In the present case, the sample concentration is inferior to 5×10^{-5} M and the presence of the excimer is related to their close proximity, symptom of a high number of attached chromophores, as also reported for other pyrene-functionalized quantum dots.[75,105]

The pyrene monomer emission is strongly quenched for both samples. This is confirmed by the lifetime measurements reported in Table 7.2.1. For both pyrene-containing samples, the emission decay at 395 nm (upon excitation at 340 nm) can be fitted with a bi-exponential function: the shorter component (ca. 1 ns) corresponds to the quenched pyrene chromophores attached at the nanocrystal surface and the long component (20 ns) corresponds to that of the free pyrene ligand (compound **2**) in air-equilibrated chloroform (τ = 20 ns). The quenching efficiency is ca. 95% for both the samples, while the kinetic rate constants for the quenching process are 6.6×10^{8} s^{-1} and 9.5×10^{8} s^{-1} for the shell-free and the core-shell system, respectively, as estimated by the comparison of the emission lifetimes (see Appendix A.3 for further details on the calculations). The presence of free pyrene ligand is expected since the binding of the ligand and the nanocrystal surface is dynamic, as previously reported for typical quantum dots,[7,380–383] and an equilibrium between free and attached chromophores is

contemplated. From the pre-exponential factors of the two lifetimes, we can estimate that the free pyrene ligand is around 20% for both samples.

The above-discussed quenching process of the pyrene emission is related to energy transfer from the pyrene chromophore to the CIS core, as demonstrated by the excitation spectra performed at an emission wavelength of 700 nm. Figure 7.2.8 displays the excitation spectra of the pyrene-functionalized samples (blue lines) compared to the chromophore-free samples (red lines) and their absorption spectra (green lines).

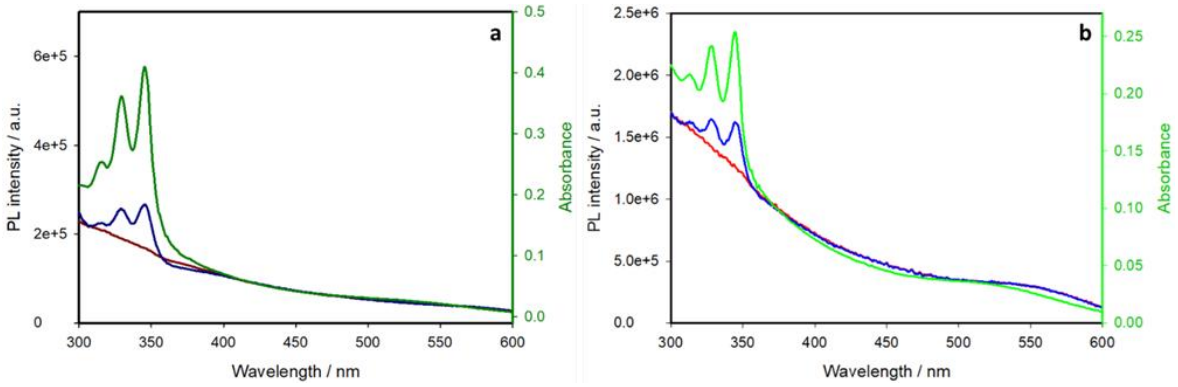

Figure 7.2.8 – Excitation spectra of (a) ***CIS QDs*** *(dark red line) and* ***CIS-py QDs*** *(dark blue line) compared to the absorption spectrum of* ***CIS-py QDs*** *(green line) and (b)* ***CIS@ZnS QDs*** *(red line) and* ***CIS@ZnS-py QDs*** *(blue line) with the absorption profile of* ***CIS@ZnS-py QDs*** *in chloroform (excitation spectra recorded at the maximum emission wavelength).*

The pyrene-functionalized samples show the characteristic pyrene absorption peaks in the range 300-350 nm, demonstrating that the emission of the inner CIS QD is sensitized by pyrene: excitation of the organic chromophore at wavelengths lower than 350 nm results in an energy transfer to the nanoparticle, which emits at ca. 700 nm. This is, to the best of our knowledge, the first case of an efficient light-harvesting antenna based on copper indium sulphide quantum dots.

Interestingly, the brightness (relative to the emission at 700 nm upon excitation at 345 nm) is higher for the pyrene-functionalized nanoparticles with an increase of 50% for the core-shell sample. On the contrary, the emission of the shell-free sample did not receive benefits by the enhanced absorption, because of the lower emission quantum yield of the nanoparticle, highlighting the importance of coating the quantum dot with a ZnS layer. It is interesting to notice that **CIS@ZnS QDs** enhance their emissive properties after ligand exchange: most of the literature examples report an opposite

trend because ligand exchange causes the introduction of defective states.[281] In our opinion, this was possible due to (i) a partial exchange of the native alkyl thiol ligands, (ii) the linkage with an efficient chromophore and (iii) the presence of a protective ZnS shell.

The introduction of a higher amount of pyrene chromophore was also attempted: the reaction with a 4-times higher concentration of compound 2 yielded **CIS@ZnS QDs** functionalized with 13 pyrene units, suggesting that a control on the amount of the linked chromophore can be performed during the ligand exchange procedure. However, the signal of the excimer emission due to the high amount of chromophore was predominant. Therefore, also the energy transfer efficiency was compromised.

7.3. Conclusions

We have successfully functionalized copper indium sulphide quantum dots and their core-shell analogues, namely **CIS@ZnS QDs**, with a dihydrolipoamide derivative bearing a pyrene moiety. The resulting systems act as light-harvesting antennae (see Figure 7.3.1): pyrene increases the absorption properties and sensitizes the emission of the quantum dot at 700 nm. In particular, for the ZnS coated sample, we observed a substantial improvement of the photoluminescence properties of the quantum dot, with an increase of the brightness up to 50% when exciting at 345 nm. We believe that this is particularly advantageous for water-suspendable systems, since PLQY of quantum dots usually decreases when transferred in polar solvents.[378,384,385] The enhanced absorption, along with the energy transfer process to the quantum dot can compensate this effect.

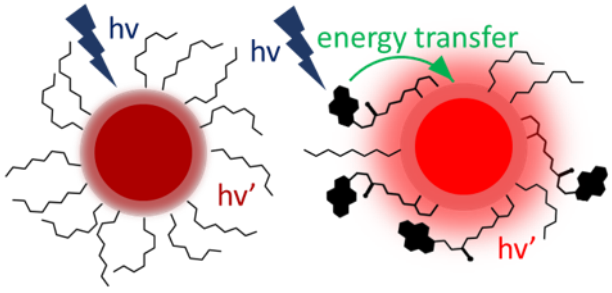

Figure 7.3.1 – Light-harvesting antenna based on pyrene-functionalised CIS QDs (on the right) compared to alkyl-chain-passivated CIS QDs (on the left). Upon excitation of pyrene, an efficient energy transfer occurs, yielding a brighter emission of the inner quantum dot.

7.4. Experimental Section

7.4.1. Materials and methods

CuI (99.998%), $(AcO)_3In$ (99.99%), 1-octanethiol (97%), 1-octadecene (90%), zinc stearate were purchased from Fisher Scientific; chloroform (ACS), methanol (ACS), N,N-dimethylformamide (anhydrous), $NaBH_4$ (99%), (±)-alpha-lipoic acid, 1-pyrenemethylamine hydrochloride, N-ethyl-N′-(3-dimethylaminopropyl)carbodiimide hydrochloride (EDC) and N,N,N′,N′-tetramethyl-O-(1H-benzotriazol-1-yl)uronium hexafluorophosphate (HBTU), N,N-diisopropylethylamine and the other reagents were purchased from Sigma-Aldrich and used without further purification, unless stated otherwise.

7.4.2. Synthesis of CIS-py and CIS@ZnS-py QDs

7.4.2.1. Synthesis of alkyl thiol-coated CIS and CIS@ZnS QDs

The synthesis of the quantum dots was adapted from strategies reported in literature.[257] Briefly, copper(I) iodide (0.25 mmol) and indium(III) acetate (0.25 mmol) were suspended in 4 mL of 1-octanethiol and 6 mL of 1-octadecene in a three-necked 100 mL round-bottomed flask equipped with condenser. In a 50 mL round-bottomed flask, zinc stearate (0.5 mmol) was suspended in 2 mL of 1-octanethiol and 2 mL of 1-octadecene. The suspensions were purged twice under two vacuum/nitrogen flux cycles for an hour. The temperatures were raised respectively to 120 °C and 150 °C to complete the dissolution of the solids. After 30 minutes, the flask containing copper and indium precursors was heated up to 210 °C, noticing the change in color (from yellow to orange to red to dark red). The suspension was let stir for 45 minutes and then quenched by dipping the flask in a cold-water bath.

An aliquot (1 mL) of the suspension was separated, diluted with chloroform (1:1) and acetone (10:1) was added to make the nanocrystals precipitate. The suspension was centrifuged (2 times, 8000 rpm, 10 minutes each), the supernatant discarded and the precipitate dissolved in chloroform, yielding the **CIS QDs** sample.

The temperature of the flask was then raised up to 150 °C. Then, the suspension containing zinc stearate was added to the nanocrystals' dispersion. The mixture was stirred for half an hour. Then, the temperature was raised up to 200 °C to make the shell grow. The reaction was quenched one hour later and purified as described for the

non-shelled nanocrystals, obtaining the **CIS@ZnS QDs** sample. It is worth noting that both the samples are stabilized in apolar solvents thanks to a 1-octanethiol organic shell.

7.4.2.2. Synthesis of 5-(1,2-dithiolan-3-yl)-N-(pyren-1-ylmethyl)pentanamide

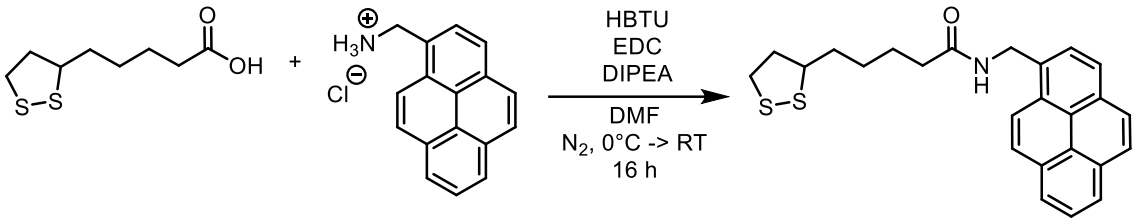

5-(1,2-dithiolan-3-yl)-N-(pyren-1-ylmethyl)pentanamide (Compound **1** in the main text) was obtained by amidation coupling between (±)-α-lipoic acid and 1-pyrenemethylamine hydrochloride in the presence of N-ethyl-N′-(3-dimethylaminopropyl)carbodiimide hydrochloride (EDC) and N,N,N′,N′-tetramethyl-O-(1H-benzotriazol-1-yl)uronium hexafluorophosphate (HBTU), as follows. 1-pyrenemethylamine hydrochloride (1 mmol) was dispersed in anhydrous N,N-dimethylformamide (DMF, 15 mL) under nitrogen atmosphere. Therefore, N,N-diisopropylethylamine (6 mmol) was dropped until complete dissolution of the solid. (±)-α-lipoic acid (1 mmol) was added, followed by HBTU (1.5 mmol) and EDC (1.5 mmol). The reaction was stirred overnight at room temperature under inert atmosphere. The mixture was diluted with 1 M $HCl_{(aq)}$ and extracted in chloroform. The organic phase was separated and washed twice with 1 M $HCl_{(aq)}$, water, twice with 1 M $KOH_{(aq)}$. The organic phase was separated, dried over sodium sulfate and the solvent removed under reduced pressure. Further purification was not necessary, yielding a bright yellow solid (99% yield).

^{1}H-NMR ($CDCl_3$, 400 MHz): 8.25 – 7.95 ppm (9 H, m); 5.8 ppm (1 H, bs); 5.1 ppm (2 H, d); 3.5 ppm (1 H, m); 3.0 ppm (2 H, t); 2.2 ppm (2 H, t); 1.8 ppm (2 H, m); 1.6-1.4 ppm (6 H, m).

LC-MS (ESI, m/z) = found 420.2 ($M + H^+$).

7.4.2.3. Synthesis of 6,8-dimercapto-N-(pyren-1-ylmethyl)octanamide

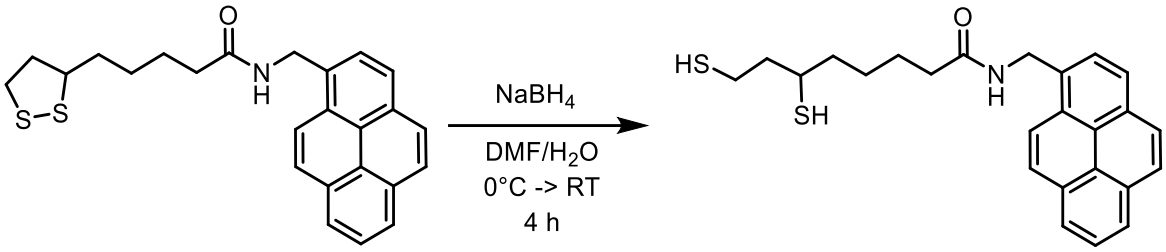

6,8-dimercapto-N-(pyren-1-ylmethyl)octanamide (compound **2**) was obtained by reduction of disulfide bond with sodium borohydride. In particular, compound **1** was dissolved in a 75:25 mixture of DMF/H_2O. At 0 °C, carefully, $NaBH_4$ (3 mmol) was added. The cold bath was removed 10 minutes later and the mixture was let stir for 4 hours at room temperature. The suspension became clearer. Then 10% $HCl_{(aq)}$ was added until the pH was almost equal to 1. The mixture was extracted in chloroform, washing 3 times with acidic water and 3 times with bi-distilled water. The organic phase was dried over sodium sulfate, concentrated, suspended in $CDCl_3$ (the complete removal of solvent was detrimental for the redissolution of the solid) and transferred into a vial filled with nitrogen as a clear yellow solid (>90% yield). The compound was stored in a refrigerator at 4 °C.

^{1}H-NMR ($CDCl_3$, 400 MHz): 8.25 – 7.95 ppm (9 H, m); 5.9 ppm (1 H, bs); 5.1 ppm (2 H, d); 3.7 ppm (1 H, m); 2.6 ppm (2 H, m); 2.19 ppm (2 H, t); 1.8 ppm (2 H, m); 1.8 – 1.4 ppm (8 H, m).

LC-MS (ESI, m/z) = found 422.0 ($M + H^+$).

7.4.2.4. Ligand exchange strategy

To obtain the sample functionalized with pyrene, partial ligand exchange with 6,8-dimercapto-N-(pyren-1-ylmethyl)octanamide was accomplished. **CIS@ZnS QDs** and **CIS QDs** batches were precipitated and centrifuged in methanol (8000 rpm, 10 minutes) and redispersed in distilled chloroform. About 0.04 mmol of 6,8-dimercapto-N-(pyren-1-ylmethyl)octanamide were added in ca. 10^{-5} mmol of each sample and the suspensions let stir overnight at room temperature. The purification was accomplished by centrifuging in methanol or acetone and by size-exclusion chromatography. The obtained samples were stored at 4 °C.

Final considerations and perspectives

In conclusion, new synthetical strategies have been developed for the functionalisation of silicon nanocrystals and copper indium sulphide quantum dots. The syntheses were designed in order to introduce new functionalities and properties to the nanoparticles. Therefore, I was able to obtain efficient light-harvesting antennae and dual-potential electrochemiluminescent systems, by tethering chromophores onto the surface of the quantum dot, or transfer the nanoparticles in a different solvent, preserving their optical properties. By summarizing, SiNCs were functionalised with acetylides containing a chromophore or an amine, or directly passivated with tert-butyl esters that can be easily cleaved to carboxylic acids. The functionalisation with a terminal double bond was developed to link thiols through click chemistry, yielding water-suspendable PEGylated SiNCs. CIS QDs were functionalised with a pyrene-containing dihydrolipoamide, generating the first example of light-harvesting antenna based on those quantum dots. This was accomplished by partial ligand exchange with the native alkyl thiol ligand.

This was undoubtedly challenging, due to the numerous reaction conditions that can damage the nanoparticle (i.e. quenching, shifting the emission spectrum, etching the inorganic core). I don't deny that a lot of work must still be done in order to couple those routes. For instance, the production of a water-suspendable light-harvesting antenna based on SiNCs or CIS QDs, which is pivotal for the realisation of bioimaging contrast agents or biosensors, is still an issue. More in particular, future work should be addressed on the co-functionalisation of the nanoparticles, in order to achieve multiple tasks by using the same system. In the biomedical field, this could enable active targeting, multi-modal imaging and even theranostics.

As far as I am concerned, the development of novel functionalisation strategies should be considered also for an application that was not discussed in depth in this thesis, which is photocatalysis. While quantum dots have been increasingly studied for photochemical reactions, the implementation of a coupling with organic and inorganic mediators could provide an added benefit if compared to the separated systems, as this dissertation proved valid for ECL systems and LSCs active materials.

I strongly believe that this elaborate, which does not only list my successes but also my failures, can be a great help for scientists who want to engage in the research of quantum dots for their numerous applications. In the same way, I am convinced that the collaboration among specialists with different backgrounds should be improved and the barriers in Science reduced to a minimum.

Appendix – Experimental techniques

A.1. Electronic Absorption Spectroscopy

Steady-state UV-Visible absorption spectra are the result of electronic transitions taking place when photons are absorbed by species at their ground state, generating excited states.[379] Each species possesses its own absorption spectrum and from this it is possible to gain information on the difference in energy of the excited and ground states (equal to the energy of the photon requested for the transition, as expressed by the resonance law), the geometry of the potential energy surfaces involved (expressed by the Frank Condon factor), the allowability of the transition (indicated by the intensity of the absorption, related to the molar absorption coefficient and therefore to the kinetic constant rate of the absorption process), *et cetera*.

During my thesis project, the absorption spectra were acquired with a Perkin Elmer λ650, a double-beam spectrophotometer equipped with tungsten and deuterium lamps for the scan of visible (350-900 nm) and UV (190-350 nm) spectral range respectively. The scheme of the instrument is represented in Figure A1.

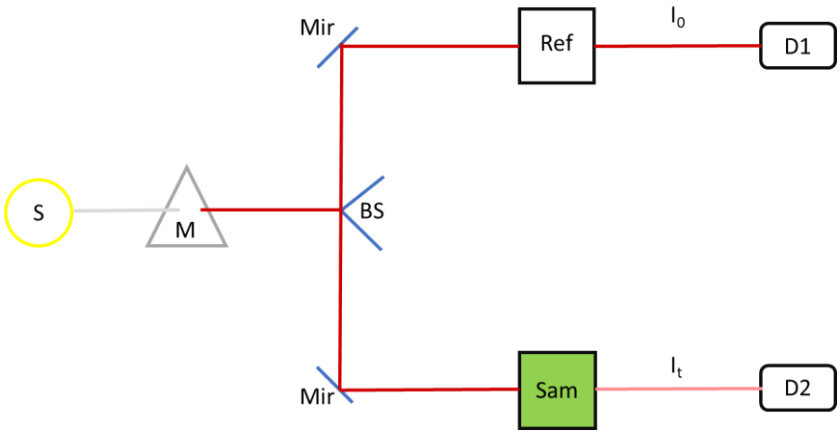

Figure A1 – Schematic diagram of double-beam UV-Visible spectrophotometer equipped with: S: light source(s), M: monochromator (in the present case, a diffraction grating), BS: a beam splitter, M: optical components like mirrors that deviate the beam without affecting the intensity of the incoming light (for simplicity purposes, only two mirrors have been drawn), the sample (Sam) or reference (Ref) cuvette holders and the detectors (D1 and D2) for the registration of the intensities of the beams, indicated as I_t and I_0 respectively.

Briefly, the analysing light beam is split in two parts after the monochromator that selects the measuring wavelength. The beams pass through the blank and the sample and are directed to two identical detectors (usually photomultiplier tubes, PMT). The

simultaneous registration of the intensities of the light transmitted by the reference (I_0) and the sample (I_t) avoids the risk of fluctuation of the lamp or the detection system.

UV-Visible spectroscopy allows to perform quantitative measurements thanks to the Lambert-Beer law, that correlates the absorbance (A, that is the logarithm of the ratio between I_0 and I_t) to the concentration of the sample (c, expressed in molarity) through the optical path (b, in cm) and the molar absorption coefficient (ε, in $M^{-1}cm^{-1}$):

$$A = \varepsilon bc$$

Computation of the number of chromophores per nanoparticle

In Chapter 2, it has been claimed that about 80 units of diphenylanthracene (DPA) per 4-nm sized silicon nanocrystal (SiNC) are linked.

This estimation was obtained knowing the molar absorption coefficient of DPA at 375 nm ($\varepsilon_{DPA,\ 375\ nm} = 1.4 \times 10^4\ M^{-1}cm^{-1}$) and 4-nm sized SiNC at 430 nm ($\varepsilon_{Si,\ 430\ nm} = 1 \times 10^5\ M^{-1}cm^{-1}$).[106] Therefore, the following formula was used, that is the ratio between the concentration of DPA in the sample Si-DPA and the concentration of nanoparticles in the same sample:

$$n_{DPA/Si} = \frac{c_{DPA}}{c_{Si}} = \frac{A_{DPA}(375\ nm)/\varepsilon_{DPA}(375\ nm)}{A_{Si}(430\ nm)/\varepsilon_{Si}(430\ nm)}$$
$$= \frac{[A_{Si-DPA}(375\ nm) - A_{Si}(375\ nm)]/\varepsilon_{DPA}(375\ nm)}{A_{Si}(430\ nm)/\varepsilon_{Si}(430\ nm)}$$

where c represents the concentration, A the absorbance at the given wavelength and A_{Si}(375 nm) is the absorbance of an equimolar suspension of Si-DDE at 375 nm. It is worth noting that at 375 nm, both SiNCs and DPA absorb, and therefore the subtraction of the quantum dot contribution is necessary to provide the estimation of the chromophore concentration. In the present case:

- $A_{Si\text{-}DPA}$ (375 nm) = 1.5
- A_{Si} (375 nm) = 0.4
- A_{Si} (430 nm) = 0.10

The same procedure can be applied to different chromophores (e.g. pyrene) and CIS QDs, by knowing their molar absorption coefficients.

A.2. Emission Spectroscopy

For luminescent samples, emission spectroscopy can provide important information on the nature of the emitting excited state which deactivate to the ground state.[379] Steady-state emission spectroscopy measurements are performed with a spectrofluorimeter, whose scheme is shown in Figure A2.

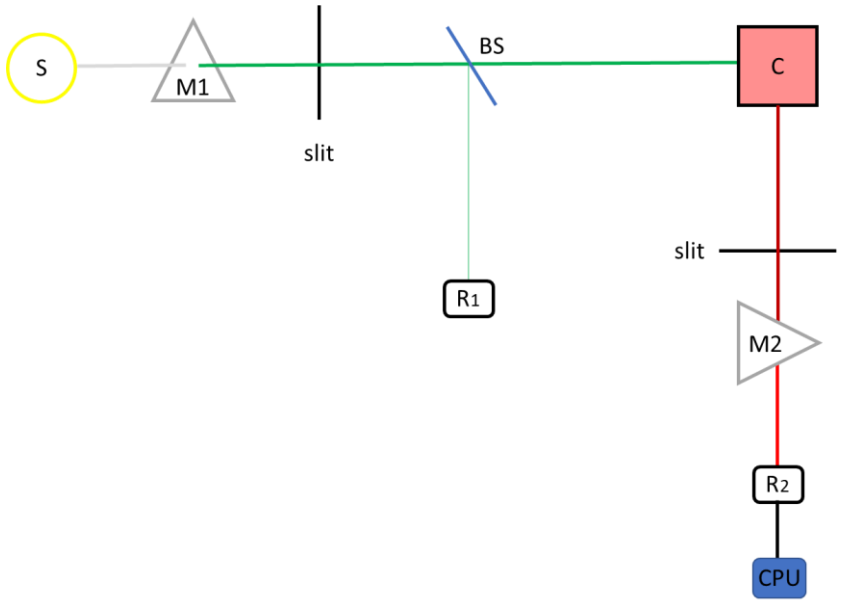

Figure A2 – Schematic diagram of a spectrofluorimeter. S represents the light source, M1 the excitation monochromator, BS a beam splitter that sends part of the excitation light towards a reference detector (R_1), C the cuvette holder of the sample, M2 the emission monochromator, R_2 the detector (usually a photomultiplier tube), CPU the computer that collects the data and controls the set-up parameters, including the modality of registration, the slits, the wavelengths selected by the monochromators, et cetera.

The source is generally a xenon arc lamp whose spectrum is continuous in the range 250-1000 nm. The excitation monochromator is used to select the wavelength of the light for the excitation of the sample, while the emission one selects the wavelength of the emitted light observed by the detector. Modern instruments are equipped with a reference detector used to monitor part of the exciting beam, in order to correct automatically the signal recorded for variations in source intensity.

It is worth noting that the emitted light is recorded from the central area of the sample cell with a 90° angle with respect to the excited beam, in order to minimize the amount of excitation light directed towards the PMT.

Several instruments allow to record time-resolved spectra, by the use of a pulsed lamp. This permits to discriminate phosphorescence spectra from fluorescence

spectra, therefore long-lived emissions from short-lived ones, and to collect long emission lifetimes (usually in the range 10 μs – 100 s, see Paragraph A.3).

Typical spectrofluorimeters allow to record emission spectra and excitation spectra. To obtain emission spectra, the excitation monochromator is kept at a fixed wavelength, usually at a maximum of the absorption spectrum of the sample, while the emission monochromator scans a spectral range at higher wavelengths. On the contrary, for excitation spectra, the emission monochromator is fixed (usually at the maximum emission wavelength of the sample) while the excitation monochromator scans the wavelength range corresponding to the absorption profile of the sample. Because the higher excited states are completely converted to the lowest emitting excited state for Kasha's rule, the profile of the excitation spectrum overlaps the absorption spectrum of the sample (if the photoluminescence intensity is directly proportional to the absorbance, that is for diluted samples with A<0.1). Excitation spectra are useful to separate the absorption contribution of different emissive species in a sample, or to assess the occurring of energy transfer processes.

During my project, emission and excitation spectra were recorded with a Perkin-Elmer LS55 equipped with a Hamamatsu R928 phototube, an Edinburgh FS5 with a PMT980 and an InGaAs detector for visible and NIR spectral range, respectively and an Edinburgh F900 equipped with a liquid-nitrogen cooled germanium detector for high sensitive detection of NIR emission. Correction of the emission spectra for detector sensitivity in the 550-1000 nm spectral region was performed by a calibrated lamp.[379,386]

Emission Quantum Yield

The emission quantum yield (or, in the case of photoproduced excited states, photoluminescence quantum yield, PLQY or Φ) is an important parameter for the characterization of luminescent species, and it is defined as follows:

$$\Phi = \frac{Number\ of\ emitted\ photons}{Number\ of\ absorbed\ photons}$$

Mathematically, the PLQY is the product of the efficiencies of the processes that follow the photoexcitation and lead to the radiative deactivation to the ground state.

For simple systems, for example in which the emitting state is directly generated by irradiation, this value equals the efficiency of the radiative deactivation of this state.[379]

A simple way to measure the PLQY is the method of Demas and Crosby,[387] a relative method based on the comparison with the solution of a compound whose emission quantum yield is stable and known. The choice of the reference should consider the absorption and emission features of the samples, that should be similar to the ones of the standards. For instance, among the various references, during my thesis project, $[Ru(bpy)_3]Cl_2$ in water (PLQY = 0.04) and 1,1',3,3,3',3'-hexamethyl indotricarbocyanine iodide in ethanol (PLQY = 0.30) were used as standards.

Operatively, the luminescence spectra of the sample and of the reference are recorded over their whole wavelength range under the same experimental conditions (e.g. emission wavelength range, excitation wavelength, slits width). The spectra are then corrected for the instrumental response and PLQY can be obtained from the following formula:

$$\Phi = \Phi_R \frac{S}{S_R} \frac{A_R}{A} \frac{n^2}{n_R^2}$$

In this formula, the subscript R refers to the quantities related to the reference; S represents the area below the recorded emission spectrum; A the absorbance at the excitation wavelength; n is the refraction index of the solvent.

It is worth pointing out that the expressed formula is strictly valid if the photoluminescence intensity is directly proportional to the absorbance, where A<0.1. Otherwise, geometrical factors of the apparatus can affect the computation and these should be taken into account. If diluted solutions cannot be used, it is possible to match the absorption spectra at the excitation wavelength (the best choice requires that two spectra at this wavelength were as flat as possible, to reduce the errors on the absorbance). In this case, the previous formula can be reduced to:

$$\Phi = \Phi_R \frac{S}{S_R} \frac{n^2}{n_R^2}$$

Evaluation of the enhancement of the brightness

The brightness B of a system is defined as the product between the sensitized emission quantum yield (Φ) of this system and the molar absorption coefficient at the

excitation wavelength. For example, in order to compute the enhancement of the brightness of 4-nm sized diphenylanthracene-functionalised quantum dots (**Si$_{4\ nm}$-DPA**) at 373 nm, with respect to the pristine alkyl-passivated system (**Si$_{4\ nm}$-DDE**) this ratio has been computed:

$$\frac{B_{Si4\ nm-DPA}}{B_{Si4\ nm-DDE}} = \frac{\Phi_{sens,Si4\ nm-DPA}}{\Phi_{Si4\ nm-DDE}} \times \frac{\varepsilon_{Si4\ nm-DPA}(373\ nm)}{\varepsilon_{Si4\ nm-DDE}(373\ nm)}$$

For equimolar suspensions of **Si$_{4\ nm}$-DPA** and **Si$_{4\ nm}$-DDE**, the molar absorption coefficients can be replaced with the absorbances at the considered wavelengths. The same results can be obtained by exciting two equimolar suspensions of **Si$_{4\ nm}$-DPA** and **Si$_{4\ nm}$-DDE** at 373 nm and dividing the area below the curve related to the emissions of the silicon.

Evaluation of the sensitisation efficiency

To estimate the sensitisation efficiency of Si-DPA (η_S, Chapter 2) we registered PL spectra of two chromophore-functionalised samples displaying the same absorbance at the following excitation wavelengths:

- 375 nm, where most of the light (80%) is absorbed by DPA;

- 430 nm, where only the silicon core is absorbing light.

By keeping the experimental conditions constant and correcting for the incident photon flux using an air-equilibrated aqueous solution of $[Ru(bpy)_3]^{2+}$ at the two different wavelengths, the sensitisation efficiency can be evaluated as follows:

$$\eta_S = \frac{\int_{550\ nm}^{1000\ nm} I_{Si-DPA} - \int_{550\ nm}^{1000\ nm} I_{0\%}}{\int_{550\ nm}^{1000\ nm} I_{100\%} - \int_{550\ nm}^{1000\ nm} I_{0\%}}$$

where I_{Si-DPA} is the PL spectrum of the sample Si-DPA upon excitation at 375 nm, $I_{100\%}$ is the PL spectrum of the sample Si-DPA upon excitation at 430 nm and $I_{0\%}$ represents the amount of light emitted by the silicon core upon its direct excitation at 375 nm.

A.3. Lifetime Measurements

If the reader considered that, after the absorption of a photon, a species *A* is lead to an excited state **A*, he should assume that this can undergo different deactivation

paths, in competition with each other. Each deactivation process is characterised by a specific rate constant, k_i. Assuming only "n" first-kinetic order processes, for simplicity purposes, the lifetime (τ) of $*A$ is defined as:

$$\tau(*A) = \frac{1}{\sum_{i=1}^{n} k_i}$$

It is obvious that a mathematical treatment of the kinetic of the depopulation of $*A$, that is the variation of its concentration, $[*A]$, over time, leads to:

$$\frac{d[*A]}{dt} = -\sum_{i=1}^{n} k_i[*A] = -\frac{1}{\tau(*A)}[*A]$$

The resolution of the differential equation leads to:

$$[*A](t) = [*A]_0 e^{-t/\tau(*A)},$$

where $[*A]_0$ represents the initial concentration of $*A$, before the deactivation paths occurred.

This formula indicates that another way to define $*A$ lifetime is the time that takes so that the concentration of A in its excited state is reduced by a factor e. Therefore, it is possible to measure the lifetime of an excited state of a species by recording the trend of its concentration over time. "Time-domain measurements" techniques are based on this. If the excited state is emissive, because the concentration of the species in the excited state is directly proportional to the number of emitted photons, an easy way to compute the lifetime is to record the trend of the luminescence intensity (I) over time. The previous equation can be then written as follows:

$$I(t) = I_0 e^{-t/\tau(*A)},$$

where I_0 represents the photoluminescence intensity recorded at the initial time.

It is worth noting that in more complex cases, multiexponential cases can be observed. For instance, if two independent luminescent species (1 and 2) are present in the same sample, the intensity decay is reduced to:

$$I(t) = B_1\, e^{-\frac{t}{\tau_1}} + B_2\, e^{-\frac{t}{\tau_2}},$$

where τ_1 and τ_2 are the lifetimes of the two species and B_1 and B_2 their photoluminescence intensities recorded at the initial time. B_1 and B_2 are also called

"pre-exponential factors" and depend on the emission quantum yields of the emitting species, their emission intensity at the measuring wavelength and their concentration.[379]

Two main methods have been used to measure emission lifetimes and are known as "gated-sampling" and "time-correlated single-photon counting".

Gated Sampling

This technique is used in several commercial spectrofluorimeters equipped with a pulsed xenon lamp (see Paragraph A.2) and allows to determine lifetimes ranging from 10 μs to 100 s approximately. After the excitation pulse, the emission intensity of the sample is measured after a certain delay time, t_1, comprised in a time window called *gate time*, which must be short with respect to the sample lifetime. The measurement is then repeated several times, progressively shifting the gate time toward increasing delay times (t_2, t_3, … t_n) until the end of the decay is reached. By plotting the recorded emission intensities as a function of the delay time, the decay curve is obtained.[379] Emission intensity decay measurements in the range 10 μs to 1 s were also performed on a homemade time-resolved phosphorimeter.

Time-Correlated Single-Photon Counting

Time-Correlated Single-Photon Counting (TCSPC) is a time-domain technique useful to acquire lifetimes ranging from about 0.5 ns to 20 μs. It relies on the probability that a single photon emitted by a sample is detected by a high-gain PMT. The block diagram of a single-photon counting apparatus is shown in Figure A3.

In principle, to obtain a reliable decay, the measurements require a high number of excitation-emission cycles. For each cycle, an excitation flash is emitted by a pulsed source (nowadays compact lasers are widely available), producing a certain number of excited states in the sample. The same flash (or the laser pulse voltage) is revealed by a detection system (D_{start} in the Figure) generating a potential ramp that linearly increases in a time-to-amplitude converter (TAC). This potential ramp can stop if a certain temporal interval passes without any stop signal is detected. On the contrary, if a single photon emitted by the sample is detected by a second photomultiplier (D_{stop}), this cycle stops at a certain potential value. The TAC sends this signal to a multichannel analyser that collects the "counts" in a certain number of channels (for example 4056)

each of which corresponds to a particular range of time (e.g. 0.10 ns): in other words, the value of the potential at the end of the cycle is converted in time units (e.g. 5.2 ns) and is counted in its specific channel (5.1-5.2 ns). The cycles restart and the new signals are collected in the multichannel analyser until a specific condition is reached (for example, the counts reached 1000 in one channel). A CPU analyses and fits the obtained data. At the end, the multichannel analyser produces a histogram showing how many times a single photon was seen by the D_{stop} at a given temporal interval.

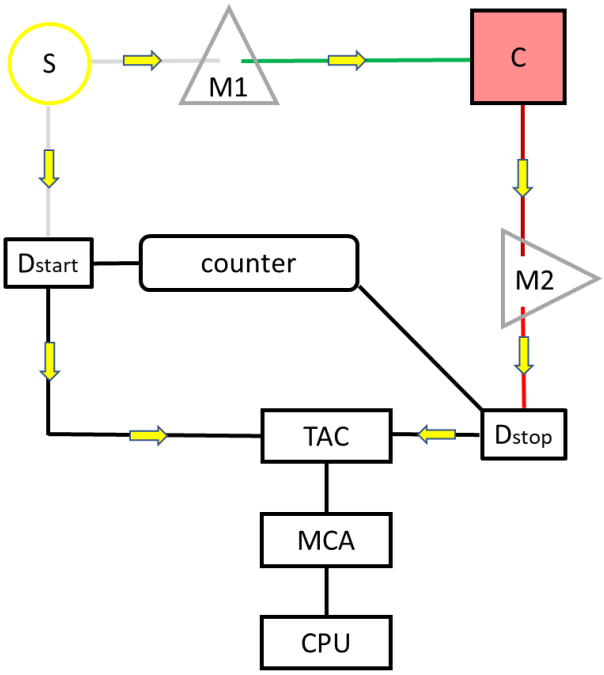

Figure A3 – Block diagram of a single-photon counting apparatus. S is the pulsed source (usually a laser), M1 and M2 are the excitation (if any) and emission monochromators, respectively, C the sample cell, D_{start} and D_{stop} are the photomultipliers that start and stop the electronic timing unit, TAC represents a time-to-amplitude converter, MCA a multichannel analyser and CPU the computer.

For statistical reasons, the so-obtained curve overlaps well with the real intensity decay only if less than 2 photons out of 100 are detected before the potential ramp of the TAC ends. To do this, the monochromators slits must be well regulated.

TCSPC technique allows also a mathematical deconvolution of the emission decay from the collected profile, separating the contribution of the lamp. By doing this, emission lifetimes down to hundreds of picoseconds can be determined.[379] *Time correlating single photon counting* technique was performed on an Edinburgh F900 spectrofluorometer equipped with a pulsed laser.

Computation of the quenching efficiency of a fluorophore

The quenching efficiency (η_q) of a fluorophore (for instance, pyrene) linked to a nanoparticle (e.g. CIS QDs) is defined as:

$$\eta_q = \frac{k_q}{k_q + \sum k}$$

where k_q represents the first-kinetic order constant of the quenching process and $\sum k$ the sum of the kinetic constants related to the other deactivation pathways of the excited fluorophore. In particular, expressing the emission lifetimes of the detached (i.e. not quenched) fluorophore (τ_0) and the linked (i.e. quenched) one (τ) as a function of the kinetic constants, it is possible to obtain:

$$\tau_0 = \frac{1}{\sum k} \quad and \quad \tau = \frac{1}{k_q + \sum k}$$

From the last equation it is possible to express k_q as a function of τ and τ_0:

$$k_q = \frac{1}{\tau} - \sum k = \frac{1}{\tau} - \frac{1}{\tau_0}$$

By substituting the equations into the first expression, it is possible to correlate the quenching efficiency of the fluorophore to the emission lifetimes of the quenched and free ligand:

$$\eta_q = \left(\frac{1}{\tau} - \frac{1}{\tau_0}\right)\tau = 1 - \frac{\tau}{\tau_0}$$

A.4. Dynamic Light Scattering

Dynamic light scattering (DLS) is a technique used to estimate the hydrodynamic diameter of a nanoparticle, assuming it possesses a spherical shape. DLS relies on the measurements of the intensity fluctuations of a scattered light during time.

In principle, the nanoparticles randomly move in the suspension, subject to Brownian motions. An incident light (usually a monochromatic laser beam) is directed towards the nanoparticles that scatter the ray towards a detector (usually at 173°). The beams scattered from different nanoparticles will undergo constructive or destructive interferences due to the relative position of the nanoparticles. Since the nanoparticles

are moving, the overall intensity of the detected light will be subject to fluctuations during time.

DLS analyses the intensity fluctuation over time *via* an algorithm called *correlation function*, $G(\tau)$, that measures how long the intensity is maintained during time. In other words, if the nanoparticles move slower, the correlation will be maintained for a longer time. On the contrary, if the nanoparticles move faster, the oscillation between constructive and destructive interferences of the scattered beams will change rapidly. For the simplest case in which a single population (monomodal distribution) is present and the correlation function can be fitted as a mono-exponential decay (cumulants analysis), $G(\tau)$ can be expressed as:

$$G(\tau) = A[1 + Bexp(-2Dq^2\tau)],$$

where A and B are factors that represent the baseline and intercept of the correlation function respectively, q is a quantity that takes into account the refractive index of the suspension, the wavelength of the laser and the scattering angle, τ the sample time of the correlator and finally D, the translational diffusional coefficient.

The diffusion coefficient is related to the size of the nanoparticles, as expressed by the Stokes-Einstein equation:

$$d_H = \frac{kT}{3\pi\eta D},$$

where d_H is the hydrodynamic diameter, k the Boltzmann constant, T the temperature and η the dispersant viscosity at the given temperature.

Therefore, by recording the fluctuations of the scattered light intensity and by applying the Stokes-Einstein equation, DLS can provide a measure of the hydrodynamic diameter of the nanoparticles.

The analysis provides a size distribution of the nanoparticles in intensity and a polydispersity index, which is representative of the width of the distribution. Since the intensity of Rayleigh scattering depends on the diameter of the particles elevated to 6, in the case of a high number of populations, the number of the smaller nanoparticles can be underestimated. A volume distribution can provide a more realistic representation (since the dependence is now on the radius of the nanoparticles elevated to 3).

During my PhD studies, DLS analyses were conducted on a Malvern ZetaSizer Nano Series instrument with a 633 nm laser diode. A schematic block representation is shown in Figure A4. Samples were housed in disposable polystyrene cuvettes of 1 cm optical path length.

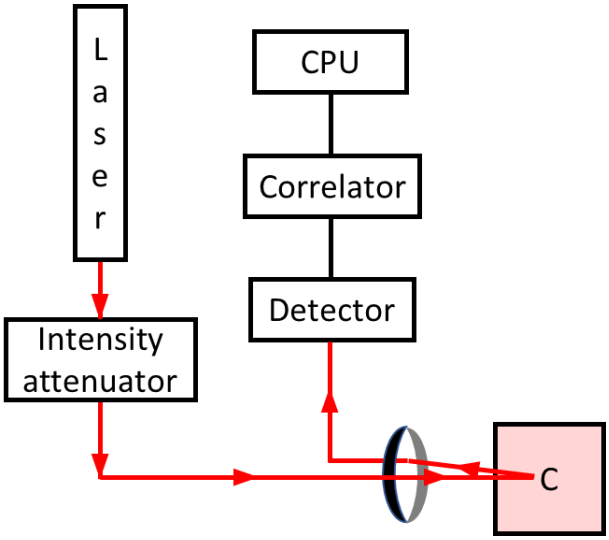

Figure A4 – Block diagram of a Nano ZetaSizer instrument configuration. It is worth noting that the scattered light from the sample C is recorded at an angle of 173°.

A.5. Nuclear Magnetic Resonance

All the ^{1}H-NMR spectra acquired during the PhD studies were recorded on a Varian Inova 400 (400 MHz) spectrometer, which uses a pulse system with a Fourier transform to collect simultaneously the overall spectrum. The instrument produces a magnetic field of 9.4 T using a superconductor magnet immersed in liquid helium (4 K) dewar immersed in a liquid nitrogen (77 K) dewar to avoid a rapid evaporation of helium. The sample is inserted inside the probe, where the homogeneity of the magnetic field is assured by shim coils.

The Larmor frequency of the proton (i.e. the frequency requested to invert the spin) is:

$$\nu = \gamma \frac{B_0}{2\pi}$$

γ is the gyromagnetic ratio, and B_0 the applied magnetic field. Magnet coils around the sample can generate the radiofrequency requested to invert the spin of the protons whose precession axes were aligned to the magnetic field direction. The examination of the relaxation process of the protons to the initial state allows to obtain the free

induction decay that by Fourier transform analysis can provide the NMR spectrum in frequency domain.[388]

The utility of the measure relies on the effective resonance frequency of the different protons depending on their local chemical environment, ν_{eff}:

$$\nu_{eff} = \gamma \frac{B_0(1-\sigma)}{2\pi}$$

Here, σ represents the shield factor that takes into account the effect of the local environment. The differences from the original applied radiofrequency, for protons, are in the range of a few parts per million (ppm), which is the typical way to express the chemical shift of the protons (δ), using the signal of tetramethylsilane (TMS) as reference.

$$\delta\ (ppm) = \frac{\nu_{proton}(Hz) - \nu_{TMS}(Hz)}{\nu_{applied}(Hz)} \cdot 10^6$$

It is worth noting that the utility of using this notation relies on the independency from the radiofrequency applied by the instrument, permitting a direct comparison among spectra collected with different apparatuses.

In each experimental part of this thesis, data are reported as follows: chemical shift, multiplicity (s = singlet, d =doublet, t = triplet, q = quartet, br = broad, m = multiplet), coupling constants (Hz).

A.6. Mass spectrometry

Mass spectroscopy (MS) is a widely used technique in synthesis laboratories, due to the information on the mass and, to a lesser extent, on the structure of the molecule that is provided. The principle of mass spectroscopy is quite simple: the examined compound is ionized (different ionization methods are available), the ions fragments are separated according to their mass over charge ratio (which involves an ion separation method) and the counts of each mass/charge unit is recorded as a spectrum. A mass spectrometer is usually coupled to a chromatographic instrument that provides a separation of the compounds in the sample before the ionization is performed. Typically, gas chromatography (GC-MS) or high-performance liquid chromatography (HPLC-MS) are implemented.[388]

Ionization methods are generally divided into two main categories: hard or soft. Hard methods provide a more extensive fragmentation with respect to soft ones. Electron impact (EI) is one example of the former case. Vapor phase sample molecules are bombarded with high energy electrons (usually 70 eV). The interaction with the molecule leads to a first ejection of an electron, yielding a radical cation known as "molecular ion". The amount of energy of the electron flux is sufficient to break the covalent bonds of the molecular cation, generating new cationic species that are directed towards the detector. This kind of fragmentation is highly reproducible and characteristic of the compound. Therefore, the comparison of the obtained spectrum with a library of mass spectra can be useful to identify the compound. Electron spray ionization (ESI) is considered a soft method. The sample is introduced in the ionization system as a solution (usually eluted from a liquid chromatograph) through a stainless-steel capillary. A nebulizing gas (e.g. nitrogen) surrounds the tip, which is maintained at high potential with respect to a counter-electrode. As the solution is ejected from the capillary, an aerosol of charged droplets forms and the nebulizing gas drives the effluent towards the mass spectrometer. The solvent evaporates, leading to a shrinking of the charged droplets. When the charge becomes more concentrated, the electrostatic repulsion of the sample ions enhances until a "Coulombic explosion" occurs, liberating the ions into the vapor phase and directing them towards the mass analyser. ESI method is useful for non-volatile compounds.

The mass analyser separates the mixture of ions generated by the ionization system according to their mass/charge ratio, therefore providing the mass spectrum. Quadrupole mass analysers consist of four cylindrical rods mounted parallel to each other at the corners of a square. A constant DC voltage and an alternate radiofrequency voltage is applied to the rods. The sample ions pass through the space among the rods and are subject to the electric fields. Only ions with a certain mass/charge ratio possess a stable trajectory and are directed to the detector, while the other ones are deflected. By modifying the applied radiofrequency it is possible to scan ions with different mass/charge ratio.

The schematic diagram of a mass spectrometer is shown in Figure A5.

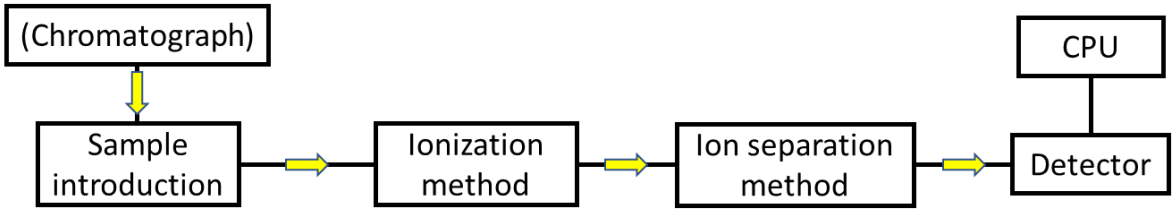

Figure A5 – Block diagram of a mass spectrometer (also implemented with a chromatograph).

During my PhD studies, GC-MS analyses were obtained using an Agilent Technologies GC-6850 MS-5975 equipped with EI (70 eV) ionization system, single quadrupole analyser, and HP5 5% Ph-Me Silicon. LC-electrospray ionization mass spectra were obtained with an Agilent Technologies MSD1100 single-quadrupole mass spectrometer.

A.7. Cyclic Voltammetry and Chronoamperometry

Cyclic voltammetry (CV) is an electrochemical measurement in which the working electrode potential is increased linearly over time. Moreover, after a predetermined potential is reached, the working electrode potential is ramped in the opposite direction, until the initial potential is reached again. The current intensity at the working electrode is plotted against the potential, generating the cyclic voltammogram.[389]

Chronoamperometry, on the other hand, measures the current intensity at the working electrode as a function of time, while a potential step is applied for a specific time to perform a reaction. A switch of potentials between 0 V and the potential in exam is usually performed to better understand the stability of the faradic process.

The measures were carried in DCM or THF solution at room temperature using a Ecochemie, Mod. PGSTAT 30 AutoLab instrument. A cylindrical three-electrode electrochemiluminescence cell with a poly(tetrafluoroethylene) (PTFE) stopcock and a Schlenk-like connection to the vacuum–inert gas line was used. As a working electrode, platinum was chosen, as a quasi-reference electrode, silver was chosen, and as a counter electrode, a spiral-shaped platinum wire was chosen.

In such system, the current flows from the working to the counter electrodes, while the potential applied to the working electrode is referred to the reference electrode.

The solution contained tetrabutylammonium hexafluorophosphate as electrolyte to diminish the resistivity of the suspension and to minimize the mass transfer effects.

The suspension was degassed with argon and the cell kept under inert atmosphere to minimize the presence of oxygen, which can react under the potentials under examination.

A.8. Transmission Electron Microscopy

High Resolution Transmission Electron Microscopy (HR-TEM) and Scanning Transmission Electron Microscopy (STEM) was carried out by a FEI Tecnai F20 instrument, equipped with a Schottky emitter and operated at 120 keV. EDX spectra were collected by focusing the beam on the region of interest and registered with an EDAX Phoenix spectrometer equipped with an ultra-thin window detector. Different instrument setups are employed to obtain selected area diffraction (SAED), or high resolution micrographs and scanning transmission micrographs.[390] The samples were prepared by drop casting on a CVD graphene coated TEM grid, in order to enhance the nanocrystals' contrast due to the low thickness and atomic weight of the substrate. The TEM is provided with a Gatan MSC794 CCD camera, Fischione High Angle Annular Dark Field STEM detector and double tilt specimen holder. The preparation of the sample usually consists in casting few drops of the sample solution on carbon coated copper TEM grids. The solvent is then removed by vacuum pumping the grid or by rapid heating over the solvent boiling point.

Bibliography

1 C. Kittel, *An Introduction to Solid State Physics*, John Wiley & Sons, 8th ed., 2004.

2 B. R. Hoffmann, *Angew. Chemie Int. Ed. English*, 1987, **26**, 846–878.

3 H. P. Myers, *Introductory Solid State Physics*, Taylor & Francis, 2nd ed., 1997.

4 G. Sun, *The intersubband approach to Si-based lasers*, INTECH Open Access Publisher, 2010.

5 V. Balzani, A. Credi and M. Venturi, *Molecular Devices and Machines: Concepts and Perspectives for the Nanoworld*, Wiley-VCH, Weinheim, 2nd ed., 2008.

6 C. Buzea, I. Pacheco and K. Robbie, *Biointerphases*, 2007, **2**, MR 17.

7 S. Silvi and A. Credi, *Chem. Soc. Rev.*, 2015, **44**, 4275–4289.

8 C. Burda, X. Chen, R. Narayanan and M. A. El-Sayed, *Chem Rev*, 2005, **105**, 1025–1102.

9 M. El-Sayed, *Acc. Chem. Res*, 2004, **37**, 326–333.

10 G. Wannier, *Phys. Rev.*, 1937, **52**, 191.

11 A. Smith and S. Nie, *Acc. Chem. Res.*, 2009, **43**, 190–200.

12 Efros and Efros., *Sov. Phys. Semicond*, 1982, **16**, 772–775.

13 C. B. Murray, D. J. Norris and M. G. Bawendi, *J. Am. Chem. Soc.*, 1993, **115**, 8706–8715.

14 J. Yang, J. Wang, K. Zhao, T. Izuishi, Y. Li, Q. Shen and X. Zhong, *J. Phys. Chem. C*, 2015, **119**, 28800–28808.

15 H. K. Jun, M. A. Careem. and A. K. Arof, *Renew. Sustain. Energy Rev.*, 2013, **22**, 148–167.

16 W. H. Badaway, *J. Adv. Res.*, 2015, **6**, 123–132.

17 J. Duan, H. Zhang, Q. Tang, B. He and L. Yu, *J. Mater. Chem. A*, 2015, **3**, 17497–17510.

18 S. Emin, S. P. Singh, L. Han, N. Satoh and A. Islam, *Sol. Energy*, 2011, **85**, 1264–

1282.

19 L. Qian, Y. Zheng, J. Xue and P. H. Holloway, *Nat. Photonics*, 2011, **5**, 543–548.

20 V. Wood and V. Bulovic, *Nano Rev.*, 2010, **1**, 5202.

21 C. L. J. Shen, Y. Zhu, *Chem. Commun*, 2012, **48**, 3686 – 3699.

22 K. M. et al. Parida, *Int. J. Hydrogen Energy*, 2017, **42**, 9467–9481.

23 B. Bajorowicz, M. P. Kobylański, A. Gołąbiewska, J. Nadolna, A. Zaleska-Medynska and A. Malankowska, *Adv. Colloid Interface Sci.*, 2018, **256**, 352–372.

24 M. Chern, J. C. Kays, S. Bhuckory and A. M. Dennis, *Methods Appl. Fluoresc.*, 2019, **7**, 012005.

25 I. V. Martynenko, A. P. Litvin, F. Purcell-Milton, A. V. Baranov, A. V. Fedorov and Y. K. Gun'ko, *J. Mater. Chem. B*, 2017, **5**, 6701–6727.

26 T. Pellegrino, S. Kudera, T. Liedl, A. Munoz-Javier, L. Manna and W. . Parak, *Small*, 2005, **1**, 48–63.

27 X. Michalet, F. F. Pinaud, L. A. Bentolila, J. M. Tsay, S. Doose, J. J. Li, G. Sundaresan, A. M. Wu, S. S. Gambhir and S. Weiss, *Science*, 2005, **307**, 538–544.

28 S. S. Wu, J. Z. Zhang, X. H. Yu, Y. Cao and H. J. Wang, *RSC Adv.*, 2014, **4**, 63502–63507.

29 Y. Fu, M. S. Jang, T. Wu, J. H. Lee, Y. Li, D. S. Lee and H. Y. Yang, *Carbohydr. Polym.*, 2019, **224**, 115174.

30 M. L. Steigerwald and L. E. Brus, *Annu. Rev. Mater. Sci.*, 1989, **19**, 471.

31 G. Markovich, C. P. Collier, S. E. Henrichs, F. Remacle, R. D. Levine and J. D. Heath, *Acc. Chem. Res*, 1999, **32**, 415.

32 R. M. Penner, *Chem. Res.*, 2000, **33**, 78.

33 F. W. Wise, *Acc. Chem. Res*, 2000, **33**, 773.

34 A. Chen, S. Li, L. Huang and D. Pan, *Nanoscale*, 2014, **6**, 1295–1298.

35 H. Zhong, S. S. Lo, T. Mirkovic, Y. Li, Y. Ding, Y. Li and G. D. Scholes, *ACS Nano*, 2010, **4**, 5253–5262.

36 A. N. Beecher, X. Yang, J. H. Palmer, A. L. LaGrassa, P. Juhas, S. J. L. Billinge and J. S. Owen, *J. Am. Chem. Soc.*, 2014, **136**, 10645–10653.

37 J. E. B. Katari, V. L. Colvin and A. P. Alivisatos, *J. Phys. Chem.*, 1994, **98**, 4109–4117.

38 J. Chang and E. R. Waclawik, *Cryst. Eng. Comm.*, 2013, **15**, 5612–5619.

39 A. Kharkwal, S. N. Sharma, K. Jain and A. K. Singh, *Mat. Chem. Phys.*, 2014, **144**, 252–262.

40 X. Peng, J. Wickham and A. P. Alivisatos, *J. Am. Chem. Soc.*, 1998, **120**, 5343–5344.

41 B. R. Pamplin, *Crystal Growth*, 1975.

42 X. Peng, J. Wickham and A. P. Alivisatos, *J. Am. Chem. Soc.*, 1998, **120**, 5343.

43 A. Mielnik-Pyszczorski, K. Gawarecki and P. Machnikowski, *Sci. Rep.*, 2018, **8**, 2873.

44 J. W. Haus, H. S. Zhou, I. Honma and H. Komiyama, *Phys.Rev. B*, 1993, **47**, 1359.

45 P. Reiss, M. Protière and L. Li, *Small*, 2009, **5**, 154–168.

46 A. R. Kortan, R. Hull, R. L. Opila, M. G. Bawendi, M. L. Steigerwald, P. J. Carroll and L. E. Brus, *J. Am. Chem. Soc.*, 1990, **112**, 1327–1332.

47 M. Dasog, J. Kehrle, B. Rieger and J. G. C. Veinot, *Angew. Chemie Int. Ed.*, 2015, **54**, 2–20.

48 M. Montalti, A. Cantelli and G. Battistelli, *Chem. Soc. Rev.*, 2015, **44**, 4853–4921.

49 D. L. Anderson, *Theory of the Earth*, Blackwell Scientific Publications, 1989.

50 N. Shirahata, J. Nakamura, J. Inoue, B. Ghosh, K. Nemoto, Y. Nemoto, M. Takeguchi, Y. Masuda, M. Tanaka and A. Ozin, *Nano Lett.*, 2020, **20**, 1491–1498.

51 M. H. Mobarok, T. K. Purkait, M. A. Islam, M. Miskolzie and J. G. C. Veinot, *J. Angew Chem, Int Ed.*, 2016, 6169–6173.

52 A. G. Cullis and L. T. Canham, *Nature*, 1991, **353**, 335 – 338.

53 R. Mazzaro, F. Romano and P. Ceroni, *Phys. Chem. Chem. Phys.*, 2017, **19**, 26507–26526.

54 Z. Ding, B. M. Quinn, S. K. Haram, L. E. Pell, B. A. Korgel and A. J. Bard, *Science*, 2002, **296**, 1293–1298.

55 K. Dohnalova, T. Gregorkiewicz and K. Kusova, *J. Phys. Condens. Matter*, 2014, **26**, 173201.

56 B. F. P. McVey and R. D. Tilley, *Acc. Chem. Res*, 2014, **47**, 3045–3051.

57 B. F. P. McVey, S. Prabakar, J. J. Gooding and R. D. Tilley, *Chempluschem*, 2017, **82**, 60–73.

58 L. Canham, *Faraday Discuss.*, 2020, **222**, 10–81.

59 J. Choi, N. S. Wang and V. Reipa, *Langmuir*, 2007, **23**, 3388 – 3394.

60 A. S. Heintz, M. J. Fink and B. S. Mitchell, *Adv. Mater.*, 2007, **19**, 3984 – 3988.

61 J. L. Wilbrink, *Faraday Discuss.*, , DOI:10.1039/C9FD00099B.

62 J. L. Z. Ddungu, S. Silvestrini, A. Tassoni and L. De Cola, *Faraday Discuss.*, 2020, **222**, 350–361.

63 B. V. Oliinyk, D. Korytko, V. Lysenko and S. Alekseev, *Chem Mater*, 2019, **31**, 7167–7172.

64 R. K. Baldwin, K. A. Pettigrew, E. Ratai, M. P. Augustine and S. M. Kauzlarich, *Chem Commun*, 2002, 1822–1823.

65 M. Sletnes, J. Maria, T. Grande, M. Lindgren and M. A. Einarsud, *Dalt. Trans.*, 2014, **43**, 2127–2133.

66 J. H. Warner, A. Hoshino, K. Yamamoto and R. D. Tilley, *Angew. Chem. Int. Ed.*, 2005, **44**, 4550–4554.

67 A. Shiohara, S. Prabakar, A. Faramus, C. Y. Hsu, P. S. Lai, P. T. Northcote and R. D. Tilley, *Nanoscale*, 2011, **3**, 3364–3370.

68 C. S. Yang, R. A. Bley, S. M. Kauzlarich, H. W. H. Lee and R. G. Delgado, *J. Am. Chem. Soc.*, 1999, **91**, 5191–5195.

69 M. T. Atkins, M. C. Cassidy, M. Lee, S. Ganguly, C. M. Marcus and M. S. Kauzlarich, *ACS Nano*, 2013, **7**, 1609–1617.

70 L. Mangolini, E. Thimsen and U. Kortshagen, *Nano Lett.*, 2005, **5**, 655–659.

71 X. D. Pi, R. W. Liptak, J. D. Nowak, N. P. Wells, C. B. Carter, S. A. Campbell and U. Kortshagen, *Nanotechnology*, 2008, **19**, 245603.

72 C. M. Hessel, E. J. Henderson and J. G. C. Veinot, *Chem. Mater.*, 2006, **18**, 6139–6146.

73 C. M. Hessel, D. Reid, M. G. Panthani, M. R. Rasch, B. W. Goodfellow, J. Wei, H. Fujii, V. Akhavan and B. A. Korgel, *Chem. Mater*, 2012, **24**, 393–401.

74 M. Locritani, Y. Yu, G. Bergamini, M. Baroncini, J. K. Molloy, B. A. Korgel and P. Ceroni, *J. Phys. Chem. Lett.*, 2014, **5**, 3325–3329.

75 R. Mazzaro, M. Locritani, J. K. Molloy, M. Montalti, Y. Yu, B. A. Korgel, G. Bergamini, V. Morandi and P. Ceroni, *Chem. Mater.*, 2015, **27**, 4390–4397.

76 A. Fermi, M. Locritani, D. Carlo, M. Pizzotti, S. Caramori, Y. Yu, B. A. Korgel and P. Ceroni, *Faraday Discuss.*, 2015, **185**, 481–495.

77 M. B. Brook, *Silicon in Organic Organometallic and Polymer Chemistry*, John Wiley and Sons, Inc.: New York.

78 B. Arkles, L. K. Berry, D. H. Figge, R. J. Composto, T. Chiou, H. Colazzo and W. E. Wallace, *Sol-Gel Sci. Technol.*, 1997, **8**, 465.

79 R. J. Clark, M. Aghajamali, C. M. Gonzalez, L. Hadidi, M. A. Islam, M. Javadi, H. Mobarok, T. K. Purkait, C. J. T. Robidillo, R. Sinelnikov, A. N. Thiessen, J. Washington, H. Yu and J. G. C. Veinot, *Chem Mater*, 2017, **29**, 80–89.

80 E. J. Henderson, J. A. Kelly and J. G. C. Veinot, *Chem Mater*, 2009, 5426–5434.

81 J. A. Kelly, E. J. Henderson and J. G. C. Veinot, *Chem. Commun.*, 2010, **46**, 8704.

82 J. G. C. Veinot, E. J. Henderson and C. M. Hessel, *IOP Conf. Ser. Mater. Sci. Eng*, 2009, **6**, 012017.

83 I. Höhlein, A. Angı, R. Sinelnikov, J. G. C. Veinot and B. Rieger, *Chem. Eur. J.*, 2015, **21**, 2755–2758.

84 M. Dasog, G. B. De los Reyes, L. V. Titova, F. A. Hegmann and J. G. C. Veinot, *ACS Nano*, 2014, **8**, 9636– 9648.

85 M. Dasog, K. Bader and J. G. C. Veinot, *Chem. Mater.*, 2015, **27**, 1153–1156.

86 Y. Nakajima and S. Shimada, *RSC Adv.*, 2015, **5**, 20603–20616.

87 T. Schulz and T. Strassner, *J. Organomet. Chem.*, 2013, **744**, 113–118.

88 L. N. Lewis, *J. Am. Chem. Soc.*, 1990, **112**, 5998–6004.

89 R. D. Tilley, J. H. Warner, K. Yamamoto, I. Matsui and H. Fujimori, *Chem Commun*, 2005, 1833–1835.

90 J. H. Warner, H. Rubinsztein-dunlop and R. D. Tilley, *J. Phys. Chem. B Lett.*, 2005, **109**, 19064–19067.

91 R. Boukherroub, S. Morin, F. Bensebaa and D. D. M. Wayner, *Langmuir*, 1999, **15**, 3831–3835.

92 R. L. Cicero, M. R. Linford and C. E. D. Chidsey, *Langmuir*, 2000, **16**, 5688–5695.

93 J. M. Buriak, M. P. Stewart, T. W. Geders, M. J. Allen, H. C. Choi, J. Smith, D. Raftery and L. T. Canham, *J. Am. Chem. Soc.*, 1999, **121**, 11491–11502.

94 J. M. Schmeltzer, L. A. Porter, M. P. Stewart and J. M. Buriak, *Langmuir*, 2002, **18**, 2971–2974.

95 M. R. Linford, P. . Fenter, P. M. Eisenberger and C. E. D. Chidsey, *J. Am. Chem. Soc.*, 1995, **117**, 3145–3155.

96 L. Ravotto, Q. Chen, Y. Ma, S. A. Vinogradov, M. Locritani, G. Bergamini, F. Negri, Y. Yu, B. A. Korgel and P. Ceroni, *Chem*, 2017, **2**, 550–560.

97 Z. Yang, M. Iqbal, A. R. Dobbie and J. G. C. Veinot, *J. Am. Chem. Soc.*, 2013, **135**, 17595–17601.

98 J. A. Kelly and J. G. C. Veinot, *ACS Nano*, 2010, **4**, 4645–4656.

99 J. A. Kelly, A. M. Shukaliak, M. D. Fleischauer and J. G. C. Veinot, *J. Am. Chem. Soc.*, 2011, **133**, 9564–9571.

100 T. K. Purkait, M. Iqbal, M. H. Wahl, K. Gottschling, C. M. Gonzalez, M. A. Islam and J. G. C. Veinot, *J. Am. Chem. Soc.*, 2014, **136**, 17914–17917.

101 Y. Yu, C. M. Hessel, T. D. Bogart, M. G. Panthani, M. R. Rasch and B. A. Korgel,

Langmuir, 2013, **29**, 1533–1540.

102 M. A. Islam, R. Sinelnikov, M. A. Howlader, A. Faramus and J. G. C. Veinot, *Chem. Mater.*, 2018, **30**, 8925–8931.

103 D. Wang and J. M. Buriak, *Langmuir*, 2006, **22**, 6214 – 6221.

104 F. Romano, S. Angeloni, G. Morselli, R. Mazzaro, V. Morandi, J. R. Shell, X. Cao, B. Pogue and P. Ceroni, *Nanoscale*, 2020, **12**, 7921–7926.

105 G. Morselli, F. Romano and P. Ceroni, *Faraday Discuss.*, 2020, **222**, 108–121.

106 R. Mazzaro, A. Gradone, S. Angeloni, G. Morselli, P. G. Cozzi, F. Romano, A. Vomiero and P. Ceroni, *ACS Photonics*, 2019, **6**, 2303–2311.

107 I. M. D. Höhlein, J. Kehrle, T. Helbich, Z. Yang, J. G. C. Veinot and B. Rieger, *Chem. - A Eur. J.*, 2014, **20**, 4212–4216.

108 T. T. Koh, T. Huang, J. Schwan, P. Xia, S. T. Roberts, L. Mangolini and M. L. Tang, *Faraday Discuss.*, 2020, **222**, 190–200.

109 I. M. D. Hohlein, J. Kehrle, J. G. C. Veinot and B. Rieger, *Nanoscale*, 2015, **7**, 914–918.

110 K. Dohnalova, A. N. Poddubny, A. A. Prokofiev, W. D. A. de B. M., C. P. Umesh, J. M. Paulusse, H. Zuilhof and T. Gregorkiewicz, *Light Sci. Appl.*, 2013, **2**, 47.

111 Y. Yu, G. Fan, A. Fermi, R. Mazzaro, V. Morandi, P. Ceroni, D.-M. Smilgies and B. A. Korgel, *J. Phys. Chem.*, 2017, **121**, 23240–23248.

112 M. L. Mastronardi, F. Maier-Flaig, D. Faulkner, E. J. Henderson, C. Kübel, U. Lemmer and G. A. Ozin, *Nano Lett.*, 2011, **12**, 337–342.

113 I. Sychugov, A. Fucikova, F. Pevere, Z. Yang, J. G. Veinot and J. Linnros, *ACS Photonics*, 2014, **1**, 998–1005.

114 R. Anthony and U. Kortshagen, *Phys. Rev. B Condens. Matter Mater. Phys.*, 2009, **80**, 115407.

115 A. N. Thiessen, M. Ha, R. W. Hooper, H. Yu, A. O. Oliynyk, J. G. C. Veinot and V. K. Michaelis, *Chem. Mater.*, 2019, **31**, 678–688.

116 A. Thiessen, L. Zhang, A. Oliynyk, H. Yu, K. O'Connor, A. Meldrum and J. G. C. Veinot, *Chem. Mater.*, 2020, **32**, 6838–6846.

117 K. A. Pettigrew, Q. Liu, P. P. Power and S. M. Kauzlarich, *Chem. Mater.*, 2003, **15**, 4005–4011.

118 K. Dohnalova, A. Fucıkova, C. P. Umesh, J. Humpolıckova, J. M. J. Paulusse, J. Valenta, H. Zuilhof, M. Hof and T. Gregorkiewicz, *Small*, 2012, **8**, 3185–3191.

119 M. Rosso-Vasic, E. Spruijt, B. van Lagen, L. De Cola and H. Zuilhof, *Small*, 2008, **4**, 1835–1841.

120 G. B. Teh, S. Nagalingam, R. D. Tilley, S. Ramesh and Z. Y. S. Lim, *Phys. Chem.*, 2009, **223**, 1417–1426.

121 D. Neiner, H. W. Chiu and S. M. Kauzlarich, *J. Am. Chem. Soc.*, 2006, **128**, 11016–11017.

122 I. Jia, X. Zhang, P. Lin, Z. Anthony, R. Kortshagen, U. Huang, S. Puthen-Veettil, B. Conibeer and G. PerezWurfl, *RSC Adv.*, 2015, **5**, 55119–55125.

123 M. C. Beard, K. P. Knutsen, P. Yu, J. M. Luther, Q. Song, W. K. Metzger, R. J. Ellingson and A. J. Nozik, *Nano Lett.*, 2007, **7**, 2506–2512.

124 K. Y. Cheng, R. Anthony, U. R. Kortshagen and R. J. Holmes, *Nano Lett.*, 2011, **11**, 1952–1956.

125 S. L. Brown, J. B. Miller, R. J. Anthony, U. R. Kortshagen, A. Kryjevski and K. E. Hobbie, *ACS Nano*, 2017, **11**, 1597–1603.

126 D. Jurbergs, E. Rogojina, L. Mangolini and U. Kortshagen, *Appl. Phys. Lett.*, 2006, **8**, 233116.

127 M. Sykora, L. Mangolini, R. D. Schaller, U. Kortshagen, D. Jurbergs and V. I. Klimov, *Phys. Rev. Lett*, 2008, **100**, 1–4.

128 W. Sun, C. Qian, L. Wang, M. Wei, M. L. Mastronardi, G. Casillas, J. Breu and G. A. Ozin, *Adv. Mater.*, 2015, **27**, 746–749.

129 M. V. Wolkin, J. Jorne, P. M. Fauchet, G. Allan and C. Delerue, *Phys. Rev. Lett.*, 1999, **82**, 197–200.

130 R. Sinelnikov, M. Dasog, J. Beamish, A. Meldrum and J. G. C. Veinot, *ACS Photonics*, 2017, **4**, 1920–1929.

131 W. J. I. Debenedetti, S. K. Chiu, C. M. Radlinger, R. J. Ellison, B. A. Manhat, J. Z. Zhang, J. Shi and A. M. Goforth, *J. Phys. Chem. C*, 2015, **119**, 9595–9608.

132 C. J. T. Robidillo, M. A. Islam, M. Aghajamali, A. Faramus, R. Sinelnikov, X. Zhang, J. Boekhoven and J. G. C. Veinot, *Langmuir*, 2018, **34**, 6556–6569.

133 M. Dasog, Z. Yang, S. Regli, T. M. Atkins, A. Faramus, M. P. Singh, E. Muthuswamy, S. M. Kauzlarich, R. D. Tilley and J. G. C. Veinot, *ACS Nano*, 2013, **7**, 2676–2685.

134 G. B. De los Reyes, M. Dasog, M. Na, L. V. Titova, J. G. C. Veinot and F. A. Hegmann, *Phys. Chem. Chem. Phys*, 2015, **17**, 30125–30133.

135 K. Dohnalova, K. Zidek, L. Ondic, K. Kusova, O. Cibulka and I. Pelant, *J. Phys. D Appl. Phys.*, 2009, **42**, 135102.

136 W. D. A. M. de Boer, D. Timmerman, K. Dohnalova, I. N. Yassievich, H. Zhang, W. J. Buma and T. Gregorkiewicz, *Nat. Nanotechnol*, 2010, **5**, 878–884.

137 L. Wang, Q. Li, H.-Y. Wang, J.-C. Huang, R. Zhang, Q.-D. Chen, H.-L. Xu, W. Han, Z.-Z. Shao and H.-B. Sun, *Light Sci. Appl.*, 2015, **4**, e245.

138 P. Galar, T. Popelar, J. Khun, I. Matulkova, I. Nemec, K. Dohnalova Newell, A. Michalcova, V. Scholtz and K. Kusova, *Faraday Discuss.*, 2020, **222**, 240–257.

139 A. N. Thiessen, T. K. Purkait, A. Faramus and J. G. C. Veinot, *Phys. Status Solidi Appl. Mater. Sci.*, 2018, **215**, 1–5.

140 F. Romano, Y. Yu, B. A. Korgel, G. Bergamini and P. Ceroni, *Top. Curr. Chem.*, 2016, **374**, 89–106.

141 D. Beri, M. Jakoby, I. A. Howard, D. Busko, B. S. Richards and A. Turshatov, *Dalt. Trans.*, 2020, **49**, 2290–2299.

142 P. Xia, E. K. Raulerson, D. Coleman, C. S. Gerke, L. Mangolini, M. L. Tang and S. T. Roberts, *Nat. Chem.*, 2020, **12**, 137–144.

143 A. J. Bard, *Electrogenerated chemiluminescence*, Marcel Dekker: New York, 2004.

144 M. M. Richter, *Chem. Rev.*, 2004, **104**, 3003–3036.

145 Z. Liu, W. Qi and G. Xu, *Chem Soc Rev*, 2015, **44**, 3117–3142.

146 Y. Yuan, S. Han, L. Hu, S. Parveen and G. Xu, *Electrochim. Acta*, 2012, **82**, 484–492.

147 G. Valenti, E. Rampazzo, S. Kesarkar, D. Genovese, A. Fiorani, A. Zanut, F. Palomba, M. Marcaccio, F. Paolucci and L. Prodi, *Coord. Chem. Rev.*, 2018, **367**, 65–81.

148 G. Valenti, E. Rampazzo, E. Biavardi, E. Villani, G. Fracasso, M. Marcaccio, F. Bertani, D. Ramarli, E. Dalcanale, F. Paolucci and L. Prodi, *Faraday Discuss.*, 2015, **185**, 299.

149 D. J. Vinyard, S. Su and M. M. Richter, *J. Phys. Chem. A*, 2008, **112**, 8529–8533.

150 S. Carrara, F. Arcudi, M. Prato and L. De Cola, *Angew. Chem. Int. Ed.*, 2017, **56**, 4757–4761.

151 F. Pinaud, L. Russo, S. Pinet, I. Gosse, V. Ravaine and N. Sojic, *J. Am. Chem. Soc.*, 2013, **135**, 5517–5520.

152 S. Kesarkar, S. Valente, A. Zanut, F. Palomba, A. Fiorani, M. Marcaccio, E. Rampazzo, G. Valenti, F. Paolucci and L. Prodi, *J. Phys. Chem. C*, 2019, **123**, 5686–5691.

153 L. Zhang and S. Dong, *Anal. Chem.*, 2006, **78**, 5119–5123.

154 W. J. Miao, *Chem. Rev.*, **108**, 2506–2553.

155 A. Fiorani, J. P. Merino, A. Zanut, A. Criado, G. Valenti, M. Prato and F. Paolucci, *Curr. Opin. Electrochem.*, 2019, **16**, 66–74.

156 P. Bertoncello and P. Ugo, *ChemElectroChem*, 2017, **4**, 1663–1676.

157 Z. Cao, Y. Shu, H. Qin, B. Su and X. Peng, *ACS Cent. Sci.*, 2020, **6**, 1129–1137.

158 S. Chen, R. S. Ingram, M. J. Hostetler, R. W. Pietron, J.J.Murray, T. G. Schaaff, J. T. Khoury, M. M. Alvarez and R. L. Whetten, *Science*, 1998, **280**, 2098–2101.

159 A. Arrigo, R. Mazzaro, F. Romano, G. Bergamini and P. Ceroni, *Chem. Mater.*, 2016, **28**, 6664–6671.

160 I. N. Germanenko, S. Li and M. S. El-Shall, *J. Phys. Chem. B*, 2001, **105**, 59–66.

161 C. M. Gonzalez, M. Iqbal, M. Dasog, D. G. Piercey, R. Lockwood, T. M. Klapotke and

J. G. C. Veinot, *Nanoscale*, 2014, **6**, 2608.

162 A. Nguyen, C. M. Gonzalez, R. Sinelnikov, W. Newman, S. Sun, R. Lockwood, J. G. C. Veinot and A. Meldrum, *Nanotechnology*, 2016, **27**, 105501.

163 Y. Dong, J. Wang, Y. Peng and J. Zhu, *Biosens. Bioelectron.*, 2017, **89**, 1053–1058.

164 Y. Dong, J. Wang, Y. Peng and J. Zhu, *Biosens. Bioelectron.*, 2017, **94**, 530–535.

165 G. Morselli, F. Romano, G. Valenti, F. Paolucci and P. Ceroni, *J. Phys. Chem. C*, 2021, **125**, 5708–5714.

166 M. Dutta, L. Thirugnanam, P. Van Trinh and N. Fukata, *ACS Nano*, 2015, **9**, 6891–6899.

167 F. Priolo, T. Gregorkiewicz, M. Galli and T. F. Krauss, *Nanute Nanotech.*, 2014, **9**, 19–32.

168 C. M. Chuang, P. R. Brown, V. Bulovic and M. G. Bawendi, *Nat. Mater.*, 2014, **13**, 796–801.

169 M. T. Trinh, R. Limpens, W. D. A. M. De Boer, J. M. Schins, L. D. A. Siebbeles and G. T., *Nat. Photonics*, 2012, **6**, 316–321.

170 D. Timmerman, J. Valenta, K. Dohnalova, W. D. A. M. De Boer and T. Gregorkiewicz, *Nat. Nanotechnol.*, 2011, **6**, 710–713.

171 S. Coe, W. Woo, G. M. Bawendi and V. Bulovic, *Nature*, 2002, **420**, 800–803.

172 Y. Shirasaki, G. J. Supran, M. G. Bawendi and V. Bulovic, *Nat. Photonics*, 2013, **7**, 13–23.

173 V. I. Klimov, A. A. Mikhailovsky, S. Xu, A. Malko, J. A. Hollingsworth, C. A. Leatherdale, H. J. Eisler and M. G. Bawendi, *Science*, 2000, **290**, 314–317.

174 H. J. Eisler, V. C. Sundar, M. G. Bawendi, M. Walsh, H. I. Smith and V. Klimov, *Appl. Phys. Lett.*, 2002, **80**, 4614 – 4616.

175 N. N. Ledentsov, *Semicond. Sci. Technol.*, 2011, **26**, 014001.

176 M. A. Islam, T. K. Purkait and J. G. C. Veinot, *J. Am. Chem. Soc.*, 2014, **136**, 15130–15133.

177 D. Mosconi, D. Mazzier, S. Silvestrini, A. Privitera, C. Marega, L. Franco and A. Moretto, *ACS Nano*, 2015, **9**, 4156 – 4164.

178 C. M. Gonzalez and J. G. C. Veinot, *J. Mater. Chem. C*, 2016, **4**, 4836–4846.

179 J. M. Elzerman, R. Hanson, L. H. W. Van Beveren, B. Witkamp, L. M. K. Vandersypen and L. P. Kouwenhoven, *Nature*, 2004, **430**, 431 – 435.

180 S. Y. Weinstein, C. S. Hellberg and J. Levy, *Phys. Rev. A*, 2005, **72**, 020304.

181 J. S. Batchelder, H. Zewai and T. Cole, *Appl. Opt*, 1979, **18**, 3090–3110.

182 W. H. Weber and J. Lambe, *Appl. Opt*, 1976, **15**, 2299–2300.

183 A. Goetzberger and W. Greubel, *Appl. Phys.*, 1977, **14**, 123–139.

184 F. Meinardi, H. McDaniel, F. Carulli, A. Colombo, V. K., N. S. Makarov, R. Simonutti, V. I. Klimov and S. Brovelli, *Nat. Nanotechnol.*, 2015, **10**, 878–885.

185 H. Li, K. Wu, J. Lim, H.-J. Song and V. I. Klimov, *Nat. Energy*, 2016, **1**, 16157.

186 M. R. Bergren, N. S. Makarov, K. Ramasamy, A. Jackson, R. Guglielmetti and H. McDaniel, *ACS Energy Lett.*, 2018, **3**, 520–525.

187 F. Meinardi, F. Bruni and S. Brovelli, *Nat. Rev. Mater.*, 2017, **2**, 17072.

188 M. G. Debije and P. P. C. Verbunt, *Adv. Energy Mater.*, 2012, **2**, 12–35.

189 F. Meinardi, S. Ehrenberg, L. Dhamo, F. Carulli, M. Mauri, F. Bruni, R. Simonutti, U. Kortshagen and S. Brovelli, *Nat. Photonics*, 2017, **11**, 177–186.

190 S. K. E. Hill, R. Connell, C. Peterson, J. Hollinger, M. A. Hillmyer, U. Kortshagen and V. E. Ferry, *ACS Photonics*, 2019, **6**, 170–180.

191 S. K. E. Hill, R. Connell, J. Held, C. Peterson, L. Francis, M. A. Hillmyer, V. E. Ferry and U. Kortshagen, *ACS Appl. Mater. Interfaces*, 2020, **12**, 4572–4578.

192 M. Montalti, L. Prodi, E. Rampazzo and N. Zaccheroni, *Chem. Soc. Rev.*, 2014, **43**, 4243–4268.

193 B. Y. S. Kim, J. T. Rutka and W. C. W. Chan, *N Engl. J. Med.*, 2010, **363**, 2434–2443.

194 S. Kunjachan, J. Ehling, G. Storm, F. Kiessling and T. Lammers, *Chem. Rev.*, 2014, **115**, 10907.

195 T. M. Allen and P. R. Cullis, *Science*, 2004, **303**, 1818–1822.

196 R. Langer, *Nature*, 1998, **392**, 5–10.

197 B. R. Smith and S. S. Gambhir, *Chem. Rev.*, 2017, **117**, 901–986.

198 Y. Wang, R. Hu, G. Lin, I. Roy and K. T. Yong, *ACS Appl. Mater. Interfaces*, 2013, **5**, 2786–2799.

199 P. Raghavendra and T. Pullaiah, in *Advances in Cell and Molecular Diagnostics*, 2018, pp. 85–111.

200 C. Li and Q. Wang, *ACS Nano*, 2018, **12**, 9654–9659.

201 Q. T. Nguyen, E. S. Olson, T. A. Aguilera, T. Jiang, M. Scadeng, L. G. Ellies and R. Y. Tsien, *Proc. Natl. Acad. Sci.*, 2010, **107**, 4317–4322.

202 R. Weissleder, *Nat. Biotechnol.*, 2001, **19**, 316–317.

203 M. Y. Berezin and S. Achilefu, *Chem Rev*, 2010, **110**, 2641–2684.

204 F. Peng, Y. Su, Y. Zhong, C. Fan, S.-T. Lee and Y. He, *Acc. Chem. Res.*, 2014, **47**, 612–623.

205 J. Pang, Y. Su, Y. Zhong, F. Peng, B. Song and Y. He, *Nano Res.*, 2016, **9**, 3027–3037.

206 F. Erogbogbo, K.-T. Yong, I. Roy, R. Hu, W.-C. Law, W. Zhao, H. Ding, F. Wu, R. Kumar, M. T. Swihart and P. N. Prasad, *ACS Nano*, 2011, **5**, 413–423.

207 Y. Su, X. Ji and Y. He, *Adv. Mater.*, 2016, **28**, 10567–10574.

208 X. Ji, H. Wang, B. Song, B. Chu and Y. He, *Front. Chem.*, 2018, **6**, 1–9.

209 Y. J. Liu, F. Erogbogbo, K.-T. Yong, L. Ye, J. Liu, R. Hu, H. Chen, Y. Hu and P. N. P. Yang, J. Yang, I. Roy, N. A. Karker, M. T. Swihart, *ACS Nano*, 2013, **7**, 7303–7310.

210 L. De Cola and H. Stephan, *Nanoscale*, 2018, **10**, 9799–10298.

211 H. S. Choi, W. Liu, P. Misra, E. Tanaka, J. P. Zimmer, B. I. Ipe, M. G. Bawendi and J. V. Frangioni, *Nat. Biotechnol.*, 2007, **25**, 1165–1170.

212 Y. Li, L. Sun, M. Jin, Z. Du, X. Liu, C. Guo, Y. Li and P. Huang, *Toxicol. Vitr.*, 2011, **25**, 1343–1352.

213 D. Napierska, L. C. J. Thomassen, V. Rabolli, D. Lison, L. Gonzalez, M. Kirsch-volders, J. A. Martens and P. H. Hoet, *Small*, 2009, **5**, 846–853.

214 Y. Pan, S. Neuss, A. Leifert, M. Fischler, F. Wen, U. Simon, G. Schmid, W. Brandau and W. Jahnen-dechent, *Small*, 2007, **3**, 1941–1949.

215 T. H. L. A. Shiohara, S. Hanada, S. Prabakar, K. Fujioka and P. T. N. and R. D. T. K. Yamamoto, *J. Am. Chem. Soc.*, 2010, **132**, 248–253.

216 S. Bhattacharjee, I. M. C. M. Rietjens, M. P. Singh, T. M. Atkins, T. K. Purkait, Z. Xu, S. Regli, A. Shukaliak, R. J. Clark, B. S. Mitchell, G. . Alink, A. T. M. Marcelis, M. J. Fink, J. G. C. Veinot, S. M. Kauzlarich and H. Zuilhof, *Nanoscale*, 2013, **5**, 4870–4883.

217 C. M. Hessel, M. R. Rasch, J. L. Hueso, B. W. Goodfellow, V. A. Akhavan, P. Puvanakrishnan, J. W. Tunnel and B. A. Korgel, *Small*, 2010, **6**, 2026–2034.

218 C. J. T. Robidillo, M. Aghajamali, A. Faramus, R. Sinelnikov and J. G. C. Veinot, *Nanoscale*, 2018, **10**, 18706–18719.

219 H. Li, X. He, Z. Kang, H. Hui, Y. Liu, J. Liu, S. Lian, C. H. A. Tsang, X. Yang and S.-T. Lee, *Angew. Chemie - Int. Ed.*, 2009, **48**, 128–132.

220 Z. F. Li and E. Ruckenstein, *Nano Lett.*, 2004, **4**, 1463–1467.

221 Y. He, Y. Zhong, F. Peng, X. Wei, Y. Su, Y. Lu, S. Su, W. Gu, L. Liao and S.-T. Lee, *J. Am. Chem. Soc.*, 2011, **133**, 14192–14195.

222 R. J. Clark, M. K. M. Dang and J. G. C. Veinot, *Langmuir*, 2010, **26**, 15657–15664.

223 C. W. Hsu, D. Septiadi, C. H. Lai, P. Chen, P. H. Seeberger and L. De Cola, *Chempluschem*, 2017, **82**, 660–667.

224 J. H. Ahire, M. Behray, C. A. Webster, Q. Wang, V. Sherwood, N. Saengkrit, U. Ruktanonchai, N. Woramongkolchai and Y. Chao, *Adv. Healthc. Mater*, 2015, **4**, 1877–1886.

225 K. K. Chen, K. Liao, G. Casillas, Y. Li and G. A. Ozin, *Adv. Sci.*, 2016, **3**, 1500263.

226 J. G. Croissant, Y. Fatieiev and N. M. Khashab, *Adv. Mater.*, 2017, **29**, 1604634.

227 G. Morselli, M. Villa, A. Fermi, K. Critchley and P. Ceroni, *Nanoscale Horizons*,

2021, **6**, 676–695.

228 E. J. New, D. Parker, D. G. Smith and J. W. Walton, *Curr. Opin. Chem. Biol.*, 2010, **14**, 238–246.

229 L. Sun, R. Wei, J. Feng and H. Zhang, *Coord. Chem. Rev.*, 2018, **364**, 10–32.

230 A. J. Amoroso and S. J. A. Pope, *Chem Soc Rev*, 2015, **44**, 4723–4742.

231 N. Ohta and Y. Li, *ACS Photonics*, 2017, **4**, 1306–1315.

232 J. Joo, X. Liu, V. R. Kotamraju, E. Ruoslahti, Y. Nam and M. J. Sailor, *ACS Nano*, 2015, **9**, 6233–6241.

233 W. Yang, P. K. Srivastava, S. Han, L. Jing, C. Tu and S. Chen, *Anal. Chem.*, 2019, **91**, 5499–5503.

234 C. Wang, Z. Wang, T. Zhao, Y. Li, G. Huang, B. D. Sumer and J. Gao, *Biomaterials*, 2018, **157**, 62–75.

235 Q. T. Nguyen and R. Y. Tsien, *Nat. Rev. Cancer*, 2013, **13**, 653–662.

236 S. G. Burke S, *Biochem Soc Trans*, 2009, **37**, 318–322.

237 F. D. Dip, T. Ishizawa, N. Kokudo and R. J. Rosenthal, *Fluorescence Imaging for Surgeons*, Springer, 2015.

238 S. Gioux, H. S. Choi and J. V. Frangioni, *Mol. Imaging*, 2010, **9**, 237–255.

239 H. S. Choi and J. V Frangioni, *Mol. Imaging*, 2010, **9**, 291–310.

240 A. V Dsouza, E. R. Henderson, K. S. Samkoe, B. W. Pogue, A. V Dsouza, H. Lin, E. R. Henderson, K. S. Samkoe and B. W. Pogue, *J. Biomed. Opt.*, 2016, **21**, 080901-1–15.

241 M. L. J. Landsman, G. Kwant, G. A. Mook and W. G. Zijlstra, *J. Appl. Physiol.*, 1976, **40**, 575–583.

242 P. Meershoek, G. H. Kleinjan, E. M. K. Wit, M. N. Van Oosteromon, D. M. Van Willigen, K. P. Bauwens, A. M. Mottrie, E. J. Van Gennep, H. G. Van Der Poel, F. W. B. Van Leeuwen, O. Academy and V. Hospital, *J. Nucl. Med.*, 2018, 1–15.

243 H. Guosong, L. A. Alexander and D. Hongjie, *Nat. Biomed. Eng.*, 2017, **1**, 0010.

244 P. Liu, X. Mu, X. Zhang and D. Ming, *Bioconjug. Chem.*, 2020, **31**, 260–275.

245 Y. Zhong, Z. Ma, F. Wang, X. Wang, Y. Yang, Y. Liu, X. Zhao, J. Li, H. Du, M. Zhang, Q. Cui, S. Zhu, Q. Sun, H. Wan, Y. Tian, Q. Liu, W. Wang, K. C. Garcia and H. Dai, *Nat. Biotechnol.*, 2019, **37**, 1322–1331.

246 Y. Fan, P. Wang, Y. Lu, R. Wang, L. Zhou, X. Zheng, X. Li, J. A. Piper and F. Zhang, *Nat. Nanotechnol.*, 2018, **13**, 941–946.

247 H. Zhang, Y. Fan, P. Pei, C. Sun, L. Lu and F. Zhang, *Angew. Chem. Int. Ed.*, 2019, **58**, 10153–10157.

248 M. Howard, B. J. Zern, A. C. Anselmo, V. V. Shuvaev, S. Mitragotri and V. Muzykantov, *ACS Nano*, 2014, **8**, 4100–4132.

249 X. Gao, Y. Cui, R. M. Levenson, L. W. K. Chung and S. Nie, *Nat. Biotechnol.*, 2004, **22**, 969–976.

250 A. D. P. Leach and J. E. Macdonald, *J. Phys. Chem. Lett.*, 2016, **7**, 572–583.

251 J. Kolny-Olesiak and H. Weller, *ACS Appl. Mater. Interfaces*, 2013, **5**, 12221–12237.

252 H. Zhong, Z. Bai and B. Zou, *J. Phys. Chem. Lett.*, 2012, **3**, 3167–3175.

253 M. Booth, A. P. Brown, S. D. Evans and K. Critchley, *Chem. Mater.*, 2012, **24**, 2064–2070.

254 W. J. Yue, S. K. Han, R. X. Peng, W. Shen, H. W. Geng, F. Wu, S. W. Tao and M. T. Wang, *J. Mater. Chem.*, 2010, **20**, 7570– 7578.

255 R. Xie, M. Rutherford and X. Peng, *J. Am. Chem. Soc.*, 2009, **131**, 5691–5697.

256 D. Deng, Y. Chen, J. Cao, J. Tian, Z. Qian, S. Achilefu and Y. Gu, *Chem. Mater.*, 2012, **24**, 3029–3037.

257 L. Li, A. Pandey, D. J. Werder, B. P. Khanal, J. M. Pietryga and V. I. Klimov, *J. Am. Chem. Soc.*, 2011, **133**, 1176–1179.

258 J. J. M. Binsma, L. J. Giling and J. Bloem, *J. Cryst. Growth*, 1980, **50**, 429–436.

259 S. L. Castro, S. G. Bailey, R. P. Raffaelle, K. K. Banger and F. A. Hepp, *Chem. Mater.*,

2003, **15**, 3142–3147.

260 D. Pan, L. An, Z. Sun, W. Hou, Y. Yang, Z. Yang and Y. Lu, *J. Am. Chem. Soc.*, 2008, **130**, 5620–5621.

261 H. Y. Ueng and H. L. Hwang, *J. Phys. Chem. Solids*, 1989, **50**, 1297–1305.

262 B. Chen, H. Zhong, W. Zhang, Z. A. Tan, Y. Li, C. Yu, T. Zhai, Y. Bando, S. Yang and B. Zou, *Adv. Funct. Mater.*, 2012, **22**, 2081–2088.

263 X. Shen, E. A. Hernández-Pagan, W. Zhou, Y. S. Puzyrev, J. C. Idrobo, J. E. Macdonald, S. J. Pennycook and S. T. Pantelides, *Nat. Commun.*, 2014, **5**, 1–6.

264 S. T. Connor, C. M. Hsu, B. D. Weil, S. Aloni and Y. Cui, *J. Am. Chem. Soc.*, 2009, **131**, 4962–4966.

265 C. Xia, J. D. Meeldijk, H. C. Gerritsen and C. De Mello Donega, *Chem. Mater.*, 2017, **29**, 4940–4951.

266 S. L. Castro, S. G. Bailey, R. P. Raffaelle, K. K. Banger and A. F. Hepp, *Chem. Mater.*, 2003, **15**, 3142–3147.

267 S. L. Castro, S. G. Bailey, R. P. Raffaelle, K. K. Banger and A. F. Hepp, *J. Phys. Chem. B*, 2004, **108**, 12429–12435.

268 X. Bai, F. Purcell-milton and Y. K. Gun, *Nanomaterials*, 2019, **9**, 85.

269 F. Bensebaa, C. Durand, A. Aouadou, L. Scoles, X. Du, D. Wang and Y. Page, *J. Nanoparticle Res.*, 2009, **12**, 1897–1903.

270 Q. Liu, Z. Zhao, Y. Lin, P. Guo, S. Li, D. Pan and X. Ji, *Chem. Commun.*, 2011, **47**, 964–966.

271 S. Liu, H. Zhang, Y. Qiao and X. Su, *RSC Adv.*, 2012, **2**, 819–825.

272 M. Booth, R. Peel, R. Partanen, N. Hondow, V. Vasilca, L. J. C. Jeuken and K. Critchley, *RSC Adv.*, 2013, **3**, 20559–20566.

273 A. Nag, M. V Kovalenko, J. S. Lee, W. Liu, B. Spokoyny and D. V Talapin, *J. Am. Chem. Soc.*, 2011, **133**, 10612–10620.

274 R. Marin, A. Vivian, A. Skripka, A. Migliori, V. Morandi, F. Enrichi, F. Vetrone, P.

Ceroni, C. Aprile and P. Canton, *ACS Appl. Nano Mater.*, 2019, **2**, 2426–2436.

275 H. Nakamura, W. Kato, M. Uehara, K. Nose, T. Omata, S. Otsuka-Yao-Matsuo, M. Miyazaki and H. Maeda, *Chem. Mater.*, 2006, **18**, 3330–3335.

276 K. E. Hughes, S. R. Ostheller, H. D. Nelson and D. R. Gamelin, *Nano Lett.*, 2019, **2**, 1318–1325.

277 Y. A. Wang, X. Zhang, N. Bao, B. Lin and A. Gupta, *J. Am. Chem. Soc.*, 2011, **133**, 11072–11075.

278 Q. Liu, Z. Zhao, Y. Lin, P. Guo, S. Li, D. Pan and X. Ji, *Chem. Commun.*, 2011, **47**, 964–966.

279 J. Y. Chang, G. R. Chen and J. D. Li, *Phys. Chem. Chem. Phys.*, 2016, **18**, 7132–7140.

280 X. Tang, W. Cheng, E. S. G. Choo and J. Xue, *Chem. Commun.*, 2011, **47**, 5217–5219.

281 Z. Long, W. Zhang, J. Tian, G. Chen, Y. Liu and R. Liu, *Inorg. Chem. Front.*, 2021, **8**, 880–897.

282 Y. Chen, S. Li, L. Huang and D. Pan, *Inorg. Chem.*, 2013, **52**, 7819–7821.

283 S. Liu, H. Zhang, Y. Qiao and X. Su, *RSC Adv.*, 2012, **2**, 819–825.

284 W. Guo, X. Sun, O. Jacobson, X. Yan, K. Min, A. Srivatsan, G. Niu, D. O. Kiesewetter, J. Chang and X. Chen, *ACS Nano*, 2015, **9**, 488–495.

285 T. Jiang, J. Song, H. Wang, X. Ye, H. Wang, W. Zhang, M. Yang, R. Xia, L. Zhu and X. Xu, *J. Mater. Chem. B*, 2015, **3**, 2402–2410.

286 W. W. Xiong, G. H. Yang, X. C. Wu and J. J. Zhu, *ACS Appl. Mater. Interfaces*, 2013, **5**, 8210–8216.

287 L. Li, T. J. Daou, I. Texier, T. T. K. Chi, N. Q. Liem and P. Reiss, *Chem. Mater.*, 2009, **21**, 2422–2429.

288 J. Choi, W. Choi and D. Y. Jeon, *ACS Appl. Nano Mater.*, 2019, **2**, 5504–5511.

289 G. Gabka, P. Bujak, K. Giedyk, K. Kotwica, A. Ostrowski, K. Malinowska, W. Lisowski, J. W. Sobczak and A. Pron, *Phys. Chem. Chem. Phys.*, 2014, **16**, 23082–23088.

290 W. Guo, N. chen, Y. Tu, C. Dong, B. Zhang, C. Hu and J. Chang, *Theranostics*, 2013, **3**, 99–108.

291 E. S. Speranskaya, N. V. Beloglazova, S. Abé, T. Aubert, P. F. Smet, D. Poelman, I. Y. Goryacheva, S. De Saeger and Z. Hens, *Langmuir*, 2014, **30**, 7567–7575.

292 M. F. Foda, L. Huang, F. Shao and H. Y. Han, *ACS Appl. Mater. Interfaces*, 2014, **6**, 2011–2017.

293 C. Xia, W. Wu, T. Yu, X. Xie, C. Van Oversteeg, H. C. Gerritsen and C. De Mello Donega, *ACS Nano*, 2018, **12**, 8350–8361.

294 J. Niezgoda and M. Harrison, *Chem. Mater.*, 2012, **24**, 3294–3298.

295 S. Zott, K. Leo, M. Ruckh and H. W. Schock, *J. Appl. Phys.*, 1997, **82**, 356– 367.

296 S. L. Castro, S. G. Bailey, R. P. Raffaelle, K. K. Banger and A. F. Hepp, *J. Phys. Chem. B*, 2004, **108**, 12429–12435.

297 S. O. M. Hinterding, M. J. J. Mangnus, P. T. Prins, H. J. Jöbsis, S. Busatto, D. Vanmaekelbergh, C. De Mello Donega and F. T. Rabouw, *Nano Lett.*, 2021, **21**, 658–665.

298 K. E. Knowles, H. D. Nelson, T. B. Kilburn and D. R. Gamelin, *J. Am. Chem. Soc.*, 2015, **137**, 13138–13147.

299 A. Anand, M. L. Zaffalon, G. Gariano, A. Camellini, M. Gandini, R. Brescia, C. Capitani, F. Bruni, V. Pinchetti, M. Zavelani-Rossi, F. Meinardi, S. A. Crooker and S. Brovelli, *Adv. Funct. Mater.*, 2020, **30**, 1–13.

300 S. B. Zhang, S. H. Wei, A. Zunger and H. Katayama-Yoshida, *Phys. Rev. B Condens. Matter Mater. Phys.*, 1998, **57**, 9642–9656.

301 J. Park and S. W. Kim, *J. Mater. Chem.*, 2011, **21**, 3745–3750.

302 J. Zhang, R. Xie and W. Yang, *Chem Mater*, 2011, **23**, 3357–3361.

303 Z. Liu, A. Tang, M. Wang, C. Yang and F. Teng, *J Mater Chem C*, 2015, **3**, 10114–10120.

304 S. Y. Yoon, J. H. Kim, E. P. Jang, S. H. Lee, D. Y. Jo, Y. Kim, Y. R. Do and H. Yang, *Chem. Mater.*, 2019, **31**, 2627–2634.

305 D. Pan, D. Weng, X. Wang, Q. Xiao, W. Chen, C. Xu, Z. Yang and Y. Lu, *Chem Commun*, 2009, **28**, 4221–4223.

306 X. Long, X. Tan, Y. He and G. Zou, *J. Mater. Chem. C*, 2017, **5**, 12393–12399.

307 M. V. Kovalenko, L. Manna, A. Cabot, Z. Hens, D. V. Talapin, C. R. Kagan, V. I. Klimov, A. L. Rogach, P. Reiss, D. J. Milliron and E. Al., *ACS Nano*, 2015, **9**, 1012–1057.

308 I. Tsuji, H. Kato, H. Kobayashi and A. Kudo, *J. Phys. Chem. B*, 2005, **109**, 7323–7329.

309 L. Zheng, Y. Xu, Y. Song, C. Wu, M. Zhang and Y. Xie, *Inorg. Chem.*, 2009, **48**, 4003–4009.

310 Y. Lin, F. Zhang, D. Pan, H. Li and Y. Lu, *J. Mater. Chem.*, 2012, **22**, 8759–8763.

311 F. Shen, W. Que, Y. Liao and X. Yin, *Ind. Eng. Chem. Res.*, 2011, **50**, 9131–9137.

312 Z. Pan, I. Mora-Sero, Q. Shen, H. Zhang, Y. Li, K. Zhao, J. Wang, X. Zhong and J. Bisquert, *J. Am. Chem. Soc.*, 2014, **136**, 9203–9210.

313 J. Y. Chang, L. F. Su, C. H. Li, C. C. Chang and J. M. Lin, *Chem. Commun.*, 2014, **48**, 4848–4850.

314 L. Li, N. Coates and D. Moses, *J. Am. Chem. Soc.*, 2009, **132**, 22–23.

315 K. T. Kuo, D. M. Liu, S. Y. Chen and C. C. Lin, *J. Mater. Chem.*, 2009, **19**, 6780–6788.

316 J. Luo, H. Wei, Q. Huang, X. Hu, H. Zhao, R. Yu, D. Li, Y. Luo and Q. Meng, *Chem. Commun.*, 2013, **49**, 3881–3883.

317 X. M. Hu, R. D. Kang, Y. Y. Zhang, L. G. Deng, H. Z. Zhong, B. S. Zou and L. J. Shi, *Opt. Express*, 2015, **23**, A858–A867.

318 K. E. Knowles, T. B. Kilburn, D. G. Alzate, S. McDowall and D. R. Gamelin, *Chem. Commun.*, 2015, **51**, 9129–9132.

319 Y. Zhang, C. Xie, H. Su, J. Liu, S. Pickering, Y. Wang, W. W. Yu, J. Wang, Y. Wang, J. Hahm, N. Dellas, S. E. Mohney and J. Xu, *Nano Lett.*, 2011, **11**, 329–332.

320 W. Song and H. Yang, *Chem. Mater.*, 2012, **24**, 1961–1967.

321 L. Li, T. J. T. Daou, I. Texier, T. K. Chi, T. T. Kim Chi, N. Q. Liem and P. Reiss, *Chem. Mater.*, 2009, **21**, 2422–2429.

322 T. Pons, E. Pic, N. Lequeux, E. Cassette, L. Bezdetnaya, F. Guillemin, F. Marchal and B. Dubertret, *ACS Nano*, 2010, **4**, 2531–2538.

323 M. G. Panthani, T. A. Khan, D. K. Reid, D. J. Hellebusch, M. R. Rasch, J. A. Maynard and B. A. Korgel, *Nano Lett.*, 2013, **13**, 4294–4298.

324 C. Y. Cheng, K. L. Ou, W. T. Huang, J. K. Chen, J. Y. Chang and C. H. Yang, *ACS Appl. Mater. Interfaces*, 2013, **5**, 4389–4400.

325 X. Gao, Z. Liu, Z. Lin and X. Su, *Analyst*, 2014, **139**, 831–836.

326 A. A. P. Mansur, J. C. Amaral-Júnior, S. M. Carvalho, I. C. Carvalho and H. S. Mansur, *Carbohydr. Polym.*, 2020, **247**, 116703.

327 Z. Lin, Q. Ma, X. Fei, H. Zhang and X. Su, *Anal. Chim. Acta*, 2014, **818**, 54–60.

328 Y. Feng, L. Liu, S. Hu, Y. Liu, Y. Ren and X. Zhang, *RSC Adv.*, 2016, **6**, 55568–55576.

329 G. Lv, W. Guo, W. Zhang, T. Zhang, S. Li, S. Chen, A. S. Eltahan, D. Wang, Y. Wang, J. Zhang, P. C. Wang, J. Chang and X. J. Liang, *ACS Nano*, 2016, **10**, 9637–9645.

330 H. G. Viehe, *Angew. Chemie*, 1969, **84**, 170–179.

331 M. M. Midland, J. I. McLoughlin and R. T. J. Werley, *Org. Synth.*, 1990, **68**, 14.

332 A. J. Kresge, P. Pruszynski, P. J. Stang and B. L. Williamson, *J. Org. Chem.*, 1991, **56**, 4808–4811.

333 K. Kůsová, T. Popelář, I. Pelant, G. Morselli, S. Angeloni and P. Ceroni, *J. Phys. Chem. C*, 2021, **125**, 2055–2063.

334 P. G. M. Wuts, in *Greene's Protective Groups in Organic Synthesis*, 2014, pp. 1086–1087.

335 A. D. Lebsack, J. T. Link, L. E. Overman and B. A. Stearns, *J. Am. Chem. Soc.*, 2002, **124**, 9008–9009.

336 M. Friedman and L. D. Williams, *Bioorg. Chem.*, 1974, **3**, 267–280.

337 S. Bhattacharjee, L. H. J. De Haan, N. M. Evers, X. Jiang, A. T. M. Marcelis, H. Zuilhof,

I. M. C. M. Rietjens and G. M. Alink, *Part. Fibre Toxicol.*, 2010, **7**, 1–12.

338 P. Opanasopit, M. Nishikawa and M. Hashida, *Crit. Rev. Ther. Drug Carr. Syst.*, 2002, **19**, 191–233.

339 D. Bazile, C. Prudhomme, M. T. Bassoullet, M. Marlard, G. Spenlehauer and M. Veillard, *J. Pharm. Sci.*, 1995, **84**, 493–498.

340 Y. Li, X. Pei, Z. Zhang, Z. Gu, W. Zhou, J. Yuan, J. Zhou, J. Zhu and X. Gao, *J. Control. Release*, 2001, **71**, 203–211.

341 R. Kumar, I. Roy, T. Ohulchanskky and L. Vathy, *ACS Nano*, 2010, **4**, 699–708.

342 M. J. Roberts, M. D. Bentley and J. M. Harris, *Adv. Drug Deliv. Rev.*, 2002, **54**, 459–476.

343 J. V Jokerst, T. Lobovkina, R. N. Zare and S. S. Gambhir, *Nanomedicine*, 2011, **6**, 715–728.

344 H. C. Kolb, M. G. Finn and K. B. Sharpless, *Angew. Chem. Int. Ed.*, 2001, **40**, 2004–2021.

345 C. E. Hoyle and C. N. Bowman, *Angew. Chemie - Int. Ed.*, 2010, **49**, 1540–1573.

346 Y. J. Du and J. L. Brash, *J. Appl. Polym. Sci.*, 2003, **90**, 594–607.

347 M. A. Reichle and B. Breit, *Angew. Chem.*, 2012, **124**, 5828–5832.

348 J. Clayden, N. Greeves, S. Warren and P. Wothers, *Organic Chemistry*, Oxford University Press, 1 ed., 2001.

349 L.-H. Zhang, J. C. Chung, T. D. Costello, I. Valvis, P. Ma, S. Kauffman and R. Ward, *J. Org. Chem.*, 1997, **62**, 2466.

350 L. A. Carpino, B. J. Cohen, J. Stephens, K. E., Y. Sadat-Aalaee, J.-H. Tien and D. C. Langridge, *J. Org. Chem.*, 1986, **51**, 3732.

351 L. E. Sinks, E. Roussakis, T. V. Esipova and S. A. Vinogradov, *J. Vis. Exp.*, 2010, **37**, 1731.

352 F. Erogbogbo, C. A. Tien, C. W. Chang, K. T. Yong, W. C. Law, H. Ding, I. Roy, M. T. Swihart and P. N. Prasad, *Bioconjug. Chem.*, 2011, **22**, 1081–1088.

353 H. H. Bosshard, R. Mory, M. Schmid and H. Zollinger, *Helv. Chim. Acta*, 1959, **42**, 1653–8.

354 G. Pruckmayr, P. Dreyfuss and M. P. Dreyfuss, in *Kirk-Othmer Encyclopedia of Chemical Technology*, John Wiley & Sons, Inc, 1996.

355 X. Wang, S. O. De Silva, J. N. Reed, R. Billadeau, E. J. Griffen, A. Chan and V. Snieckus, *Org. Synth.*, 1996, **72**, 163.

356 U. Ragnarsson and L. Grehn, *Acc. Chem. Res.*, 1998, **31**, 494.

357 Y. Sun, F. Kunc, V. Balhara, B. Coleman, O. Kodra, M. Raza, M. Chen, A. Brinkmann, G. P. Lopinski and L. J. Johnston, *Nanoscale Adv.*, 2019, **1**, 1598–1607.

358 Y. Chen and Y. Zhang, *Anal. Bionalaytical Chem.*, 2011, **399**, 2503–2509.

359 J. P. Holland, V. Fisher, J. A. Hickin and J. M. Peach, *Eur. J. Inorg. Chem.*, 2010, **2010**, 48–58.

360 Y. Mo, F. Li, B. Zheng, S. Yang, H. Yuan and Y. Guo, *Electroanalysis*, 2012, **24**, 1887–1894.

361 W. H. Green, E. J. Lee, J. M. Lauerhaas, T. W. Bitner and M. J. Sailor, *Appl. Phys. Lett.*, 1995, **67**, 1468–1470.

362 J. Tan, L. Xu, T. Li, B. Su and J. Wu, *Angew. Chem. Int. Ed.*, 2014, **53**, 9822–9826.

363 H. C. Choi and J. M. Buriak, *Chem. Mater.*, 2000, **12**, 2151–2156.

364 Y. Cui, J. Jin, X. Chen and J. Wu, *ACS Sens.*, 2018, **3**, 1439–1444.

365 L. T. Canham, *Appl. Phys. Lett.*, 1990, **57**, 1046–1048.

366 H. Chen, W. Li, Q. Wang, X. Jin, Z. Nie and S. Yao, *Electrochim. Acta*, 2016, **214**, 94–102.

367 H. Zhao, R. Liang, J. Wang and J. Qiu, *Chem. Commun.*, 2015, **51**, 12669–12672.

368 X. Fu, X. Tan, R. Yuan and S. Chen, *Biosens. Bioelectron.*, 2017, **90**, 61–68.

369 P. Wu, X. Hou, J. Xu and H. Chen, *Nanoscale*, 2016, **8**, 8427–8442.

370 H. Zhang, M. Wu, J. Xu and H. Chen, *Anal. Chem.*, 2014, **86**, 3834–3840.

371 X. Feng, N. Gan, H. Zhang, Q. Yan, T. Li, Y. Cao, F. Hu, H. Yu and Q. Jiang, *Biosens. Bioelectron.*, 2015, **74**, 587–593.

372 G. Valenti, C. Bruno, S. Rapino, A. Fiorani, E. A. Jackson, L. T. Scott, F. Paolucci and M. Marcaccio, *J. Phys. Chem. C*, 2010, **114**, 19467–19472.

373 J. Feng, M. Sun, F. Yang and X. Yang, *Chem. Commun.*, 2011, **47**, 6422–6424.

374 P. Ilaiyaraja, P. S. V. Mocherla, T. K. Srinivasan and C. Sudakar, *ACS Appl. Mater. Interfaces*, 2016, **8**, 12456–12465.

375 C. Xia, W. Wang, L. Du, F. T. Rabouw, D. J. Van Den Heuvel, H. C. Gerritsen, H. Mattoussi and C. De Mello Donega, *J. Phys. Chem. C*, 2020, **124**, 1717–1731.

376 G. Morselli, A. Gradone, V. Morandi and P. Ceroni, *Nanoscale*, 2022, **14**, 3013–3019.

377 L. Liu, X. Zhang, L. Ji, H. Li, H. Yu, F. Xu, J. Hu, D. Yang and A. Dong, *RSC Adv.*, 2015, **5**, 90570–90577.

378 N. Tsolekile, S. Parani and M. C. Matoetoe, *Nano-Structures & Nano-Objects*, 2017, **12**, 46–56.

379 V. Balzani, P. Ceroni and A. Juris, *Photochemistry and Photophysics - Concepts, Research, Applications*, Wiley-VCH, 1 ed., 2015.

380 M. Green, *J. Mater. Chem.*, 2010, **20**, 5797–5809.

381 A. Loiudice, O. Segura Lecina, A. Bornet, J. M. Luther and R. Buonsanti, *J. Am. Chem. Soc.*, 2021, **143**, 13418–13427.

382 R. R. Knauf, J. C. Lennox and J. L. Dempsey, *Chem. Mater.*, 2016, **28**, 4762–4770.

383 W. Liu, A. B. Greytak, J. Lee, C. R. Wong, J. Park, L. F. Marshall, W. Jiang, P. N. Curtin, A. Y. Ting, D. G. Nocera, D. Fukumura, R. K. Jain and M. G. Bawendi, *J. Am. Chem. Soc.*, 2010, **132**, 472–483.

384 H. T. Uyeda, I. L. Medintz, J. K. Jaiswal, S. M. Simon and H. Mattoussi, *J. Am. Chem. Soc.*, 2005, **127**, 3870–3878.

385 A. D. P. Leach and J. E. Macdonald, *J. Phys. Chem. Lett.*, 2016, **7**, 572–583.

386 M. Montalti, A. Credi, L. Prodi and M. T. Gandolfi, *Handbook of photochemistry*, Taylor & Francis, 3 ed., 2006.

387 G. Crosby and J. Demas, *J. Phys. Chem.*, 1971, **75**, 991–1024.

388 R. M. Silverstein, F. X. Webster and D. J. Kiemle, *Spectrometric identification of organic compounds*, John Wiley and Sons, 7th edn., 2005.

389 A. J. Bard and L. R. Faulkner, *Electrochemical methods*, John Wiley and Sons, 2nd edn., 2001.

390 D. B. Williams and C. B. Carter, *Transmission Electron Microscopy*, Springer.